University of Liège

Aerospace and Mechanical Engineering Department
Space Structures and Systems Laboratory

Centre Spatial de Liège

Space Thermal Analysis through Reduced Finite Element Modelling

Thesis submitted in fulfilment of the requirements for the degree of
Doctor in Engineering Sciences

by

Lionel Jacques, Ir.

October 2016

Author's contact details

Lionel JACQUES

Centre Spatial de Liège
University of Liège

Liège Science Park
Avenue du Pré-Aily
4031 Angleur, Belgium

e-mail: ljacques@ulg.ac.be
phone: +32 43 82 46 42

Members of the Examination Committee

Prof. Pierre ROCHUS (President of the Committee)
University of Liège - Centre Spatial de Liège (Liège, Belgium)
e-mail: prochus@ulg.ac.be

Prof. Gaëtan KERSCHEN (Advisor)
University of Liège (Liège, Belgium)
e-mail: g.kerschen@ulg.ac.be

Prof. Eric BECHET (Co-advisor)
University of Liège (Liège, Belgium)
e-mail: eric.bechet@ulg.ac.be

Prof. Ryszard BIALECKI
Silesian University of Technology (Gliwice, Poland)

Dr. Harrie ROOIJACKERS
ATG Europe, seconded to European Space Agency (Noordwijk, The Netherlands)

Prof. Olivier BRULS
University of Liège (Liège, Belgium)

Prof. Jean-Jacques EMBRECHTS
University of Liège (Liège, Belgium)

Abstract

The finite element method (FEM) is widely used in mechanical engineering, in particular for structure design. However, it is not often exploited for the thermal analysis of space structures for which the use of the lumped parameter method is still commonplace. To alleviate the computational burden of the FEM for thermal analyses involving conduction and radiation, an innovative global conductive-radiative reduction scheme based on the clustering of the finite element mesh is presented. The proposed method leads to a significant reduction of the number of radiative exchange factors (REFs) to compute and size of the corresponding matrix. It further keeps accurate conduction information by introducing the concept of physically meaningful super nodes associated to the clusters from which are derived the reduced conductive couplings.

To complement the reduction of the number of faces, an improved Monte Carlo ray tracing algorithm is developed. It provides better accuracy and convergence rate than the classic Monte Carlo method. The algorithm is adapted to the partitioned FE mesh and includes quadrics fitting for accurate normal representation.

The resulting conductive-radiative reduced model is solved using standard iterative techniques and the detailed mesh temperatures, recovered from the super nodes temperatures, can be directly exploited for thermo-mechanical analysis. The proposed global reduction method is validated on several space structures and is benchmarked against ESATAN-TMS, the standard thermal analysis software used in the European aerospace industry.

Keywords: [Space, Thermal, Finite Element, Reduction, Monte Carlo ray tracing]

Acknowledgements

Before all else, I would like to express my sincere gratitude to my advisor Prof. Gaëtan Kerschen for his priceless guidance throughout this journey. I would also thank my co-advisor Eric Béchet for his regular inputs and his external point of view.

Besides my advisors, I would like to thank the rest of my thesis committee, Prof. Olivier Brüls, Prof. Pierre Rochus and Tanguy Thibert who provided regular feedback about my work.

I am also pleased to acknowledge Prof. Ryszard Bialecki from the Silesian University of Technology in Poland, Dr. Harrie Rooijackers from the European Space Agency (ESA), Prof. Jean-Jacques Embrechts from the Montefiore Institute of the ULg for accepting to participate in the examination committee of this doctoral thesis.

In particular, I would like to thank Dr. Harrie Rooijackers, Dr. Olivier Pin, Head of the Thermal Control Section at ESA and Charles Stroom, retired Head of the Analysis and Verification Section at ESA for their careful review and valuable inputs to the historical review of space thermal analysers.

For the friendly working atmosphere, I wish to thank all my friends and colleagues from the Centre Spatial de Liège (CSL) and from the Space Structures and Systems Laboratory (S3L) between which I shared my time during these four years.

In particular, I would like to thank Jean-Philippe Halain and Aline Hermans with whom I had the chance to work on the EUI instrument and its door mechanisms, including the calls overnight to follow the thermal vacuum tests of the instrument. I wish also to thank Benoit Marquet for his laugh and for involving me in the development of the Sentinel 4 UVN CAA mechanism.

I am also deeply indebted to Tanguy Thibert for the numerous fruitful talks we had about thermal model reduction and to Luc Masset who laid the foundations of the Isocell method for ray tracing.

This research was undertaken with the financial support of the Belgian National Fund for Scientific Research (FNRS) as a FRIA grant that I gratefully acknowledge.

I would like to say thank you to my family and friends for their continuous support and encouragements.

Last and foremost, this dissertation would not have been possible without you, Géraldine, your love, support and understanding. Without you I would not have had the strength to embark on this journey in the first place, you gave me the spark I needed to take the first step. I dedicate this work to our first child, Adam who kept me awake during the writing of this manuscript.

Contents

Contents **xi**

List of Acronyms **xv**

Introduction **1**

1 Background on space structure thermal modelling **5**
1.1 Introduction 6
1.1.1 The thermal analysis workflow 6
1.1.2 A brief history of space thermal analysers 8
1.1.3 Chapter outline 11
1.2 Review of radiative heat transfer 11
1.2.1 Thermal radiation quantities 11
1.2.2 Black body radiation 14
1.2.3 The case of diffuse emitter/absorber 16
1.2.4 Surface properties 16
1.2.5 Exchange factors 19
1.3 Monte Carlo ray tracing 23
1.3.1 Random samples generation 25
1.3.2 The cosine distribution law 26
1.3.3 Accuracy control 27
1.4 Lumped parameter method and finite element method for heat transfer . . 28
1.4.1 Energy conservation 28
1.4.2 Lumped parameter method 29
1.4.3 Finite element method 30
1.4.4 Comparison 32
1.5 Thermal model reduction 35
1.6 Concluding remarks 36

2 Quasi Monte Carlo ray tracing for radiative heat transfer **37**
2.1 Introduction 38
2.2 Direction sampling strategies 39
2.2.1 Nusselt's analogy and Malley's method 40
2.2.2 Hemisphere stratified sampling 40
2.2.3 Isocell stratified sampling 41
2.2.4 Low-discrepancy sequence 43
2.2.5 Comparison and application to point-wise view factors 44
2.2.6 Conclusions 49

2.3 Surface sampling strategies . . . 50
2.3.1 Random sampling and area preserving mapping . . . 50
2.3.2 Coupled and segregated low-discrepancy sequence . . . 54
2.3.3 Uniform sampling . . . 54
2.3.4 Gauss sampling . . . 55
2.3.5 Comparison and application to surface-to-surface exchange factors . 55
2.3.6 Influence of thermo-optical properties . . . 61
2.3.7 Conclusions . . . 62
2.4 Sampling strategies for orbital heat fluxes . . . 64
2.4.1 Introduction . . . 64
2.4.2 Orbital heat fluxes key equations . . . 68
2.4.3 Planet-focused sampling and derivation of ray energy . . . 71
2.4.4 Application to albedo heat flux over a flat plate . . . 76
2.5 Additional variance reduction and MCRT acceleration techniques . . . 79
2.5.1 Reciprocity and closure enforcement . . . 79
2.5.2 Space partitioning . . . 81
2.5.3 Intersections computation . . . 83
2.6 Concluding remarks . . . 86

3 Benchmarking quasi-Monte Carlo ray tracing 88
3.1 Introduction . . . 89
3.2 Perpendicular cylinders . . . 89
3.2.1 Radiative exchanges factors . . . 89
3.2.2 Orbital heat fluxes . . . 90
3.2.3 Radiative equilibrium temperatures . . . 90
3.3 Solar Orbiter EUI entrance baffle . . . 92
3.3.1 EUI and the Solar Orbiter Mission . . . 93
3.3.2 Radiative exchanges factors . . . 94
3.3.3 Orbital heat fluxes . . . 94
3.3.4 Radiative equilibrium temperatures . . . 95
3.4 Sentinel 4 UVN baffle LPM model . . . 97
3.4.1 The Sentinel 4 mission, UVN instrument and CAA mechanism . . . 97
3.4.2 Radiative exchanges factors . . . 97
3.4.3 Orbital heat fluxes . . . 98
3.4.4 Radiative equilibrium temperatures . . . 99
3.5 Space subdivision . . . 100
3.6 Concluding remarks . . . 100

4 Finite element mesh clustering and super nodes 102
4.1 Introduction . . . 103
4.2 The clustering process . . . 104
4.2.1 K-means clustering seeding . . . 105
4.2.2 Greedy region growing clustering . . . 107
4.2.3 Cluster boundary smoothing . . . 108
4.3 The conductive reduction process . . . 109
4.3.1 Super node definition, reduction and recovery . . . 109
4.3.2 Augmented conduction matrix local inversion . . . 111

4.4 Validation . . . 113
4.4.1 The one-dimensional conductive beam . . . 113
4.4.2 The one-dimensional conductive-radiative beam . . . 115
4.4.3 The circular radiating fin . . . 118
4.5 Concluding remarks . . . 120

5 Partitioned mesh ray tracing with quadrics fitting 121
5.1 Introduction . . . 122
5.2 Quadric super faces . . . 123
5.2.1 Quadrics fitting . . . 123
5.2.2 Surface and direction sampling . . . 125
5.2.3 Ray-quadric intersection . . . 128
5.3 Planar super faces . . . 130
5.4 Performance assessment . . . 130
5.5 Concluding remarks . . . 133

6 Radiative-conductive thermal model reduction applied to space structures 134
6.1 Introduction . . . 135
6.2 MTG BTA . . . 136
6.3 EUI entrance baffle . . . 138
6.4 Concluding remarks . . . 143

Conclusions 146

A Integration limits for orbital heat fluxes computation 150

Bibliography 154

List of Publications 182

List of Acronyms

A.U.	Astronomical unit
BOL	beginning of life
BTA	Back telescope assembly
CAD	Computer-aided design
CFD	Computational fluid dynamics
CSL	Centre Spatial de Liège
EOL	End of life
ESA	European Space Agency
ESTEC	European Space Research and Technology Centre
EUI	Extreme-UV imager
FDM	Finite difference method
FE	Finite element
FEM	Finite element method
FFM	Far-field method
GMM	Geometrical mathematical model
IR	Infrared
LP	Lumped parameter
LPM	Lumped parameter method
LSE	Line sum error
MCRT	Monte Carlo ray-tracing
MTG	Meteosat third generation
NUSD	Non-uniform space subdivision
OHF	Orbital heat flux
PDF	Probability distribution function
PFHS	Planet-focused Halton sampling
POD	Proper orthogonal decomposition
REF	Radiative exchange factor
S/C	Spacecraft
SN	Super-node
TMM	Thermal mathematical model
USD	Uniform space subdivision
UV	Ultraviolet

Introduction

Starting with the first supersonic flight in October 1947 followed ten years later by the first artificial satellite, engineers were challenged to design structures exposed to increasingly severe thermal environments [1]. The difficulty in predicting the temperatures further complicated the tasks as confirmed by the comparison between the predicted and measured temperatures of Explorer-1, the first US satellite [2]. From then on, thermally induced deformations, stresses and vibrations were the subject of many books [3–8] and of a NATO report [9]. One celebrated example is the pointing error of the Hubble Space Telescope generated by the thermally-induced vibrations of the solar arrays [10–12].

Fortunately, the advent of computers stimulated the development of mathematical tools and computational techniques for solving partial differential equations to meet the needs of engineers. The two major techniques were the well-known and older finite difference method introduced in 1928 [13, 14], also called lumped parameter method (LPM) in the frame of space thermal analysis, and the newer finite element method (FEM) introduced in the mid-1950s in the structural engineering field [15, 16] and in the mid-1960s for thermal analysis [17]. Already in the early 1980s and although Emery *et al.* [18] concluded that no method was really superior to the other in the frame of heat transfer, the FEM was soon expected to replace the LPM for thermal analysis to have a common model for thermal and structural analyses [19].

As of today, scientific requirements continuously demand for more accurate space instruments [20–24] and engineers are facing evermore complex opto-thermo-mechanical challenges [25, 26] while ensuring the robustness and reliability of the design. Aerospace is not the only field where structures are exposed to a harsh thermal environment. High temperature applications involving radiation are also more and more often encountered in the rapidly evolving energy sector. In this respect, solar tower power plant receivers constitute perfect examples with temperature exceeding 400 °C on the receiver tubes [27, 28]. A similar trend is observed in which the quest for efficiency and power leads to ever higher temperatures, larger receivers involving more thermo-mechanical challenges.

Despite Thornton's expectations in the 1980s [19], the FEM is widely used in mechanical engineering but not yet often for thermal engineering of space structures where the LPM is still dominant [29–33]. Using two different methods for thermal and structural analyses calls for building two separate models with different meshes. Temperatures computed with the LPM then need to be extrapolated to the structural mesh to perform coupled analyses. Achieving today's thermo-mechanical requirements with such an inefficient workflow therefore becomes more and more challenging.

The main reason preventing the use of the FEM for thermal analyses is the presence of radiative heat transfer involving huge non sparse matrices containing the radiative exchange factors (REFs). Temperature fields being usually smoother than mechanical stress fields, space structure thermal models are hundreds or thousands times smaller than

mechanical models in terms of number of nodes. The number of REFs being proportional to the square of the number of elements, this translates into a reduction of 10^4 to 10^6 in terms of number of REFs to compute. Able to deal with realistic surface properties, the most general and efficient method to compute REFs is Monte Carlo ray tracing (MCRT) [34–36]. Even though, achieving meaningful REFs results with such a large number of elements would require too many rays to be fired.

The lack of accuracy of industrial FE mesh surface constitutes a second disadvantage of the FEM in the presence of specular reflections. The difficulty to implement user logic such as thermostats, controller, heat pipes with the FEM also favours the use of the LPM [31]. While they provide primitive shells for accurate ray tracing, currently-used thermal analysis software too frequently involve awkwardness and error-prone manual input because of the lack of interaction with CAD and FE models and quite deficient pre- and post-processing user interfaces [33, 37–41]. Table 1 summarises the advantages and drawbacks of the FEM versus the LPM.

		FEM		**LPM**
Number of nodes		$10^4 - 10^6$		$10^1 - 10^4$
Radiative links computation	✗	Prohibitive	✓	Affordable
Conductive links computation	✓	Automatic	✗	Manual, error-prone
Surface accuracy for ray-tracing	✗	FE facets	✓	Primitives
User-defined components	✗	Difficult	✓	Easy
Thermo-mechanical analysis	✓	Same mesh	✗	Extrapolation

Table 1 – Comparison between the FEM and the LPM.

There were several attempts in introducing the FEM for space thermal analysis. They are however still based on a different mesh than the structural model [32, 42] and thus require a dedicated thermal model due to the low number of elements used in practice to limit the number of REFs. For instance in [43], structural-thermal-optics-performance-gravity analyses of the LISA (Laser Interferometer Space Antenna) mission were performed using the FEM but the number of radiative couplings proved to be the bottleneck and filtering was required. Discarding REFs smaller than a given threshold or aggregating them to a special node is often employed, but the error increases too rapidly if a sufficiently high number of REFs are dropped to significantly reduce the computation time, as shown in [44]. This approach obviously also requires the computation of the REFs before discarding them and only reduces the size of the thermal model to solve.

The original idea of grouping the finite elements into radiation super elements and primitives was introduced ten years ago in some FE codes [45]. In that method, radiative links and orbital heat fluxes are redistributed onto the fine mesh with some weighting scheme and the detailed model is solved. This feature limits the use of structural meshes since even if the radiation super element REFs computation time is reduced, their redistribution onto the detailed mesh generates again too many inter-element REFs.

Contributions of the Thesis

Table 1 highlighted the differences between the FEM and the LPM but it also revealed the complementarity of both methods. The overall goal of this doctoral thesis is thus to re-unify LPM with FEM through a global reduction scheme taking the advantages and addressing the drawbacks of both methods.

The first hurdle to tackle is the radiative couplings computation by MCRT. Two general approaches can be considered to alleviate this problem:

- either reduce the number of rays fired from each face for a given accuracy and confidence level;
- or decrease the number of faces by grouping the FE external facets into clusters.

The first approach requires to improve the accuracy and convergence rate of MCRT. One possible way is to consider quasi-Monte Carlo methods [46–48]. Unlike the classical Monte Carlo method which relies on a sequence of pseudo-random numbers, the quasi-Monte Carlo method exploits for instance low-discrepancy sequences. Sobol and Halton sequences were exploited in MCRT problems [49, 50] to generate more uniform sampling directions. Another quasi-Monte Carlo approach for generating more uniform samples over the integration domain is to use stratified sampling [46, 48, 51]. Stratified sampling consists in dividing the integration domain into *strata* which are randomly sampled independently to avoid aliasing.

In this context, the first contribution of the research is to improve the direction sampling of MCRT through the recently-developed isocell disc sampling method [52]. Specifically, more uniformly-shaped strata than in the hemisphere method presented in [53] are sought. In addition, the spatial sampling of the emitting face [54] and its interaction with direction sampling will be studied in detail, something which has been rarely carried out in the literature. The ultimate goal of this first part is to provide a combined direction and surface sampling strategy that is general, robust and exhibit better accuracy and convergence rate for the REFs computation. From this perspective, the proposed coupled 4-dimensional Halton sampling strategy proves to offer the best results. This sampling strategy is then adapted to the computation of orbital heat fluxes, namely solar, planetary albedo and infrared heat fluxes.

As introduced above, the temperature field is usually much smoother than the deformation field and a thermal model therefore requires a much coarser mesh than a mechanical model. Hence, the second main contribution consists in finite element mesh clustering to reduce the number of REFs to compute to an affordable amount and to decrease the size of the associated non-sparse matrix. The idea behind the clustering process is to use the mesh of the structural finite element model. Using the same mesh for structural and thermal analyses rather than building a separate model first reduces the thermal model pre-processing time but also smoothes the thermo-structural analysis process [55], being of paramount importance for space structure design. This scheme avoids the awkward extrapolation of the temperature coming from a coarser mesh [56]. The proposed method relies on the detailed mesh clustering to reduce the radiative terms and introduces the concept of super-node associated to the clusters for the conductive reduction. This addresses the second row of Table 1 by generating accurate conductive links. Prior to the clustering step, specific critical surfaces can be fitted with quadrics to increase the accuracy of the REFs, in particular when specular surfaces impinged by collimated environmental heat

fluxes such as sunlight need to be computed. MCRT with FE mesh and quadrics solves the third drawback mentioned in Table 1. After the generation of the reduced radiative and conductive links between the super nodes, user-defined logic involving the super nodes can be added to the reduced model in the exact same way as with the LPM, preserving the advantage of LPM given in the fourth row of Table 1. The coupled reduced model is solved with standard techniques to obtain the super nodes temperature. The temperatures of the underlying detailed structural finite element mesh are then recovered from the super node temperatures through the inverse reduction procedure and ready to be used for the thermo-structural analysis. This final step solves the last issue encountered with LPM and mentioned in the last row of Table 1.

Outline of the manuscript

Chapter 1 first recalls the basics of radiative and conductive heat transfer and presents the current practices in space structure thermal analysis. It highlights the strengths and weaknesses of LP and FE methods pointed out above.

Chapter 2 addresses the MCRT improvement techniques. Several direction and surface sampling schemes are studied along with the interaction between each other. In particular, the isocell and Halton samplings strategies are discussed and a robust coupled direction-surface sampling is derived and validated. The proposed sampling scheme is also applied to optimise orbital heat fluxes computation. Some general ray-tracing acceleration techniques that are also implemented in our algorithm such as space partitioning and efficient ray-intersection computation are finally described at the end of the chapter.

Chapter 3 then presents several full-scale benchmarking cases. In particular, two space structures currently developed at the *Centre Spatial de Liège* are studied.

The second approach to reduce the REFs computation time is presented in Chapter 4. The detailed FE mesh clustering scheme is discussed and the super node concept is defined. The detailed mesh matrix reduction is developed to derive the super-nodes conductive links.

Chapter 5 focuses on accurate surface ray tracing. The quadrics fitting step is presented followed by the adaptation of the ray tracing algorithm presented in Chapter 2 to the partitioned mesh.

Chapter 6 finally combines the developments presented in the preceding chapters to form the overall reduction process. The procedure is applied to two full-scale space structures also developed at the *Centre Spatial de Liège* namely one entrance baffle of the Extreme-UV imager on-board the Solar Orbiter mission and the structure of the Back Telescope Assembly on-board Meteosat Third Generation.

Conclusions are eventually drawn and the different contributions of this thesis are discussed. Some perspectives and research directions for future developments are also proposed.

Background on space structure thermal modelling

1

Abstract

This first chapter lays the foundations of space structure thermal analysis. It recalls the basics of radiative and conductive heat transfer in the context of space thermal modelling. In particular, the Monte Carlo ray tracing, lumped parameter and finite element methods are introduced. The weaknesses of current space thermal modelling practices are presented and the need for alternative techniques is highlighted.

1.1 Introduction

The purpose of the thermal control system is to ensure that all components of the instrument or spacecraft remain within their allowable temperature limits for all operating modes and at any time of the mission including ground test campaigns. To this aim, the thermal engineer is required to construct several thermal models to iteratively assess and refine the thermal design. The overall objective of the thermal engineer developing a thermal model is to achieve a given accuracy for the minimum cost. Costs are related to time and can be divided in two classes: development and use of the model [33, 57]. From a global perspective, the objective of this dissertation is twofold: increasing the accuracy and reducing the model development costs while maintaining reasonable computation times.

1.1.1 The thermal analysis workflow

In the frame of spacecraft and space instrument design, the thermal analysis workflow, *i.e.* the development and use of the model, typically consists of the key steps [31, 33, 58] represented in Figure 1.1. The first step starts with the construction of the Geometrical Mathematical Model (GMM), that is needed for the LPM radiative analysis. Building the GMM requires as input the geometry, thermo-optical properties of the exposed surfaces and the orbital and attitude parameters. It further needs the nodal breakdown solely determined by the engineer. A radiative solver processes the GMM to generate the radiative couplings between the nodes (commonly referred to as *GR*'s) and the planetary and solar heat fluxes if any. The GMM outputs serve as input to the Thermal Mathematical Model (TMM). In addition, the TMM requires the material bulk properties to derive the nodal capacitances and conductive couplings (commonly referred to as *GL*'s) from the same nodal breakdown. The boundary conditions, internal heat dissipation (*e.g.* electrical dissipation) and user logic (*e.g.* thermostats, control loops,...) are also integrated in the TMM. There is no direct link between the GMM and the TMM. The TMM is a pure mathematical representation of the system under study and the GMM is not mandatory. For simple systems, radiative couplings can be computed by hand to be directly integrated in the TMM. A dedicated LPM solver computes not only the temperatures but also heat flows between the nodes and group of nodes. It is worth mentioning here that thermal engineers usually tend to care more about heat flows than really accurate temperatures [31]. If thermo-mechanical analyses are necessary, the temperatures are mapped to a structural finite element mesh. This mapping step is not straightforward since the two models are based on dissimilar meshes and some TMM nodes are not necessarily related to a geometrical component in the GMM. As stated in [59], their is no standard tool and many individual aerospace companies have spent time and money over the years to develop their own internal tools to solve this issue. Even though the European Space Agency developed SINAS [56, 60] to translate ESATAN LPM temperature to MSC Nastran, it is not automatic and space companies like OHB System AG, Thales Alenia Space and many others keep developing their own custom tools [61–64].

To cover the numerous operational modes and environments the spacecraft or instrument thermal design has to cope with, a worst case approach is adopted. A hot and a cold case are traditionally defined to obtain temperature lower and upper bounds [33, 58, 65].

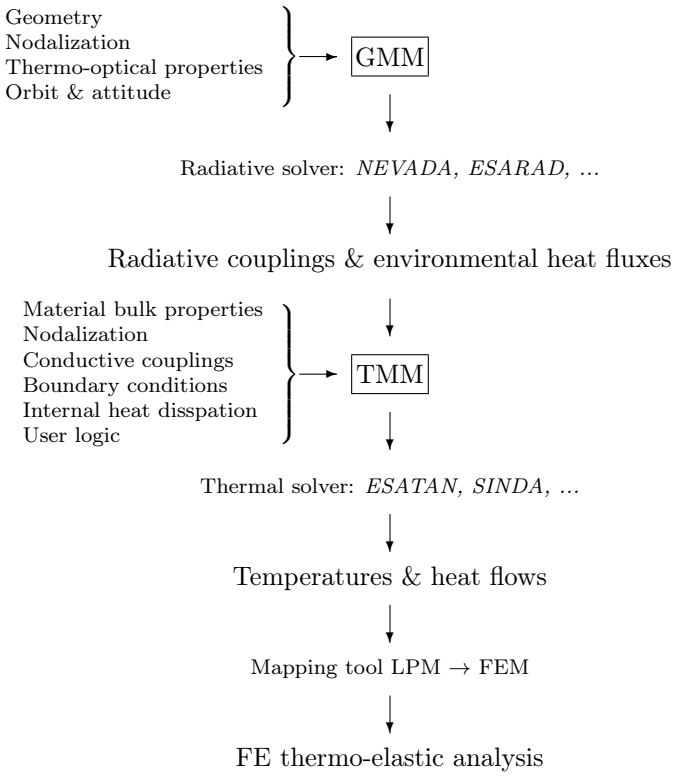

Figure 1.1 – Typical LPM thermal model construction flow.

This means that two separate models are built: the hot case model typically considering end-of-life (EOL) thermo-optical properties (absorption usually tends to increase as surface properties degrade over time in orbit), maximum dissipation and orbital heat fluxes and the cold case model conversely considering beginning-of-life (BOL) thermo-optical properties, minimum dissipation and orbital heat fluxes. In addition, models are marred by uncertainties coming from various sources that can be divided into three categories: physical parameters (material and surface properties, dissipation, contact conductances, dimensions, control logic set-points,...), environmental parameters (solar, planetary and aero-thermal heat fluxes, orbital and attitude parameters, test facility parameters,...) and modelling parameters (isothermal elements, radiative and conductive coupling errors, solver accuracy,...) [33, 58, 66, 67]. These uncertainties are added to the nominal computed temperatures in the hot and cold cases to derive the predicted temperature range. The modelling philosophy thus demands at least two models that are run many times to assess the uncertainties. Since the design is an iterative process interacting with other subsystems, the whole thermal analysis process is repeated many times in the course of the instrument or spacecraft development. Hence, the cost of generating and running the model is largely augmented by the number of times it has to be repeated. Decreasing the cost of one or more steps can lead to a significant global time reduction.

Figure 1.2 summarises the uncertainty and margin philosophy. It shows that on top of the predicted temperature range, test acceptance or qualification margins are added to demonstrate the robustness of the design. Decreasing the modelling uncertainties can ultimately decrease the acceptance and qualification temperature range and increase the design robustness.

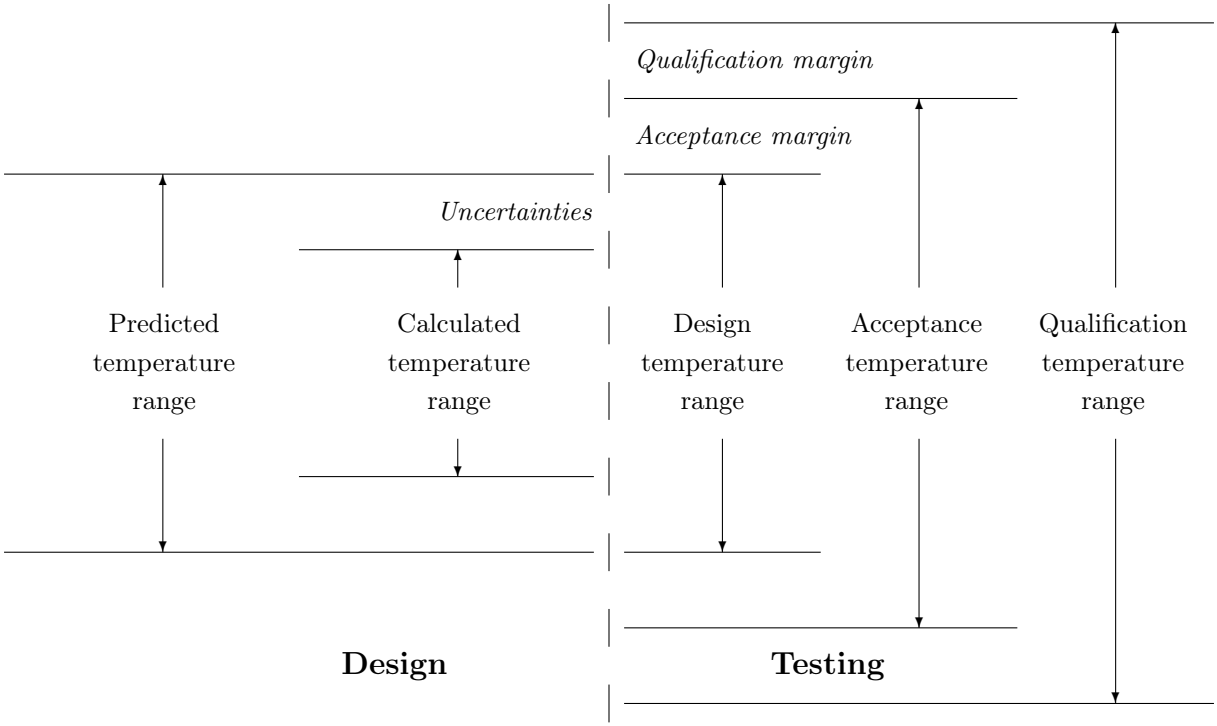

Figure 1.2 – Typical temperature margin philosophy with hot case temperatures in the upper part and cold case temperatures in the lower part of the diagram.

1.1.2 A brief history of space thermal analysers

The first large-scale aerospace thermal analysis computer code was originally developed by J. D. Gaski [68] in 1966 under the name CINDA (Chrysler Improved Numerical Differencing Analyzer) which soon became SINDA (Systems Improved Numerical Differencing Analyzer) [69] when further improved by TRW Inc. under a NASA contract. SINDA and its descendants remain today's most widely used thermal solver in the western aerospace industry [33, 70]. Before the advent of the first radiative solvers in the mid 1960s, thermal engineers used analytical formulae to compute the radiative couplings, only available for some simple configurations. For more complex geometries, form factometers (or view factor meters, that are gridded parabolic mirrors) were used on reduced or full scale models [71, 72] to derive the view factors. To help with the computation of radiative couplings and environmental heat fluxes, TRASYS (Thermal Radiation Analysis System) was developed in the 1960s by Martin Marietta Corp. in support of NASA Johnson Space Center [73]. It inherited from the development of several other computer programs such as LOHARP (Lockheed Orbital Heat Rate Program), MTRAP (Martin Marietta Thermal Radiation Analyzer Program) or MRI program (Midwest Research Institute program) that were already used for various space programs. For instance, the Phase A thermal analysis in 1966 of the Large Space Telescope (which eventually became the Hubble Space Telescope) was performed with LOHARP [74] and the external radiation absorbed by the Apollo spacecraft was computed with MRI [73]. TRASYS already included mixed diffuse-specular effect. At the same time, the European Space Agency Technical Center (ESTEC) revised LOHARP and distributed it under the name VWHEAT.

Monte Carlo methods were introduced in nuclear engineering during the 1940s and

were first used for solving thermal radiation problems in the early 1960s by Fleck [75] and Howell [76, 77]. In the aerospace industry, Monte Carlo ray tracing was introduced in the 1970s with the NEVADA code (Net Energy Verification And Determination Analyzer, developed by Turner Associates Consultants) [33, 78]. The Monte Carlo method rapidly convinced of its superiority and versatility as mentioned in [79] where it is compared to experimental data performed on the Space Shuttle heat rejection system and to traditional methods. In TRASYS, some MCRT capabilities were implemented in the 1980s [80, 81]. MCRT is now integrated in most of space thermal analysis tools.

In parallel, between 1965 and 1970, NASA led the development of its structural analysis FEM based computer code called NASTRAN (NASA STRuctural ANalysis program), further conducted by MacNeal-Schwendler Corporation (MSC) [82]. Under the initiative of the Structural-Thermal-Optical Program (STOP) by NASA Goddard Space Flight Center in 1969, thermal analysis capabilities were added to NASTRAN (NASTRAN thermal analyzer) with the aim of integrating thermal, structural and optical analyses [83–87].

When the Spacelab project started around 1977, the European Space Agency (ESA) distributed SINDA and LOHARP to the European space industry. At the same period, ESTEC (European Space Research and Technology Centre, technical heart of ESA) decided to start the development of its own thermal analyser that would rely on the layout of SINDA with data blocks and operation blocks. Up to then, most analysers considered the input data as a single monolithic model. Integrating different models together therefore required very strict agreements between parties on model data such as node numbers or variable names. Hence, the main new feature would be the ease of model combination into a tree-like structure without requiring any modification of the constituent separate models. The second major feature would be to follow the structured programming technique introduced by E. W. Dijkstra [88, 89], *i.e.* structured FORTRAN. Structured programming avoids the `GO TO` loops and enforces declaring all variables to enhance the maintainability of the software. The first release of the ESATAN (European Space Agency Thermal Analysis Network) tool for TMM processing became available in the early 1980s [90–93]. ESARAD followed a few years later [94–98]. The development of ESATAN and ESARAD was left to the Mechanical Engineering Laboratory (MEL) of the British General Electric Company (GEC) in Leicester. For internal usage, the MEL had already developed MELTAN, yet another SINDA derivative, before being entrusted with the development of ESATAN and ESARAD.

Actually, ESATAN and ESARAD were just the first steps of the more ambitious MANIP project driven by C. Stroom of ESA to create a combined software integrating thermal and radiative analysis in one tool [72, 99]. Similar to MANIP, Polytan was another feasibility study to try to combine both mathematical and physical model developments in one tool [100]. ESATAN and ESARAD are now integrated into a single software suite renamed ESATAN-TMS and developed by ITP Engines UK Ltd., the descendent of the MEL [101].

In Europe, the two major space companies developed their own thermal analysis tools: Thermica™ developed by Airbus Defence and Space [102] in the same period as ESARAD and which is now also integrated in the MSC software suite [103], Coratherm (renamed E-Therm) developed by Thales Alenia Space (Alcatel Space) [63, 104, 105]. ALTAN (ALenia Themal ANalyzer) was developed by Alenia Spazio [106] but is no longer main-

tained since Alenia Spazio merged with Alcatel Space which are now part of the Thales Alenia Space group. Outside Europe, other thermal analysis software suites include: TSS (Thermal Synthesis System, now Thermal Software System) developed by Spacedesign Corp. [107], Thermal Desktop, an AutoCAD based software developed by Cullimore and Ring Technologies, Inc. (C&R Tech.®) integrating the radiation engine RadCAD and thermal solver SINDA [108, 109], I-DEAS™TMG (Thermal Model Generator) developed by MAYA HTT Ltd., now also embedded into the Siemens PLM software suite as NX™space system thermal and ITAS (Integrated Thermal Analysis System) once developed by Analytix Corp. [110]. Besides the aerospace industry, the energy sector also needed thermal solvers including radiative heat transfer capabilities. For instance COYOTE, developed by D. Gartling from Sandia National Laboratories [111, 112] in the late 1970s, includes a radiation solver limited to diffuse grey surfaces and is based on the CHAPARRAL Library for view factor computation [113]. We restrict ourselves to non-participating media and we do not mention more specific techniques and software involving radiative heat transfer in participating media that are for instance needed in combustion problems.

As mentioned in the introduction, from its early developments the FEM was expected to replace the LPM for thermal analysis [19]. A comprehensive survey of computer programs for heat transfer available in the early 1980s, including SAMCEF (*Système pour l'Analyse des Milieux Continus par Eléments Finis*) developed at the University of Liège, is available in [114, 115] and [116]. It points out that FEM and LPM were equally applied to solve heat transfer problems but that only few of them had radiative exchange factor computing capabilities and even less if temperature mapping to structural analysis was required.

Bringing together the advantages of FEM and LPM is not a new idea. In 1993, a hybrid solution combining MITAS (Martin Marietta's version of SINDA) with I-DEAS or PATRAN for conductive link generation and TRASYS for orbital heat fluxes and radiative exchange factors computation was proposed [117] where the finite element nodes correspond to the LPM nodes. Another example of such a combination is provided in [32, 118]: FEMAP pre- and post-processing capabilities were combined to Thermal Desktop radiative solver. Finite elements were also introduced in TSS in 1997 [119]. Some finite elements functionalities were also added to ESATAN-TMS r3 in 2010 [120–122] but are not yet mature since complex geometries cannot be handled and automatic mesh generation is not yet provided.

In [42, 123], a p-version of the FEM was developed to handle radiative heat exchanges. Instead of refining the model mesh, p-FEM increases the degree of the shape functions. Then, the traditional assumption that surfaces are isothermal to compute the radiative exchange factors which is inconsistent with the FEM is eliminated. Again, this approach is not compatible with sharing the same mesh for structural and thermal analysis.

Due to the numerous different thermal analysis tools, exchanging thermal models and data is still not straightforward despite the many attempts in developing post-processing tools like ESATAP [124] or GAETAN (General and Automated Environment for Thermal Analysis Network) [125], or standard format like the well-known STEP-TAS developed by ESA in the late 90s [126–128] and other specific import-export routines between ESARAD and TMG or TSS [129], SINDA and ESATAN.

This review did not cover the specialised tools developed for studying thermal pro-

tection systems during re-entry or aero-breaking manoeuvres and ablation modelling is still an active research area [130–132]. Multiphase fluid loop analysis tools such as FHTS (Fluid Heat Transport System) [133] for ESATAN or FLUINT (Fluid Integrator) [134] for SINDA were also not covered.

1.1.3 Chapter outline

After this brief introduction setting up the background of space thermal analysis, the related computer codes and the different tentative of merging FEM with LPM, Section 1.2 reviews some fundamentals of radiative heat transfer to define the various concepts of view factors, radiative exchange factors, thermo-optical properties used later in this manuscript. The Monte Carlo method applied to ray tracing to derive the radiative exchange factors is introduced in Section 1.3. As the GMM precedes the TMM in the traditional workflow, the lumped parameter and finite element methods for heat transfer analysis are then presented in Section 1.4 with a focus on conductive links computation. The inadequacy of generic FEM reduction methods is highlighted in Section 1.5. Finally, the conclusions of the present chapter are drawn in Section 1.6.

1.2 Review of radiative heat transfer

1.2.1 Thermal radiation quantities

Thermal radiation relies on three mechanisms: emission, absorption and scattering. Every medium continuously emits and absorbs electromagnetic radiation. It emits in all directions at a rate depending on the local temperature and properties of the material. The source of the radiated energy results from electronic, molecular and lattice vibration as well as transitions in the emitting medium. Each wave or photon carries an amount of energy, ϵ, defined as

$$\epsilon = h\nu$$

where $h = 6.626 \times 10^{-34}\,\mathrm{J\,s}$ is *Planck*'s constant, $\nu = c/\lambda$ the photon frequency, c the speed of light and λ the wavelength. $c = c_0/n$ is the speed of light in the considered medium with n the refractive index of that medium. While conduction and convection both require the presence of a medium for the transfer of energy, radiation does not. Absorption arises when the emitted wave interacts with another medium. It partially loses energy to generate electronic, molecular or lattice oscillations or transitions. The third radiation phenomenon consists in scattering. It describes the way the wave can be redirected without being converted to thermal energy. Scattering encompasses reflection, diffraction, refraction and re-scattering of energy.

Thermal radiation does not only depend on the wavelength but also on the direction in space. Four distinct types of physical radiation quantities are defined:

- *Directional spectral* quantities describe the directional and wavelength distribution of the radiative energy in details but they are very difficult to determine experimentally. This explains why radiation quantities that only include one effect - either the dependence on the wavelength or the direction - are usually used.

- *Hemispherical spectral* quantities average the radiation into all directions of the hemisphere over a surface element. They are only dependent on the wavelength.
- *Directional total* quantities average the radiation over the whole electro-magnetic spectrum and keeping the dependence on the directions within the hemisphere.
- *Hemispherical total* quantities average the radiation over all wavelengths and all directions. They are the most often used quantities in radiative heat transfer. Considering a constant value over the spectrum leads to the grey approximation. In spacecraft thermal analysis, the spectrum is divided in two bands and two values are derived. This is called the semi-grey approximation that is detailed in Section 1.2.4.

Regarding directionality, the concept of solid angle must be defined. It is the ratio of the area dA_n on the sphere to the sphere's radius squared.

$$d\Omega = \frac{dA_n}{r^2}$$

If θ is the zenith (polar) angle measured outwards from the surface normal and ϕ is the circumferential (azimuthal) angle, the dimension of dA_n is $rd\theta \times r\sin\theta d\phi$ and the solid angle can be rewritten as shown in Figure 1.3:

$$d\Omega = \sin\theta d\theta d\phi$$

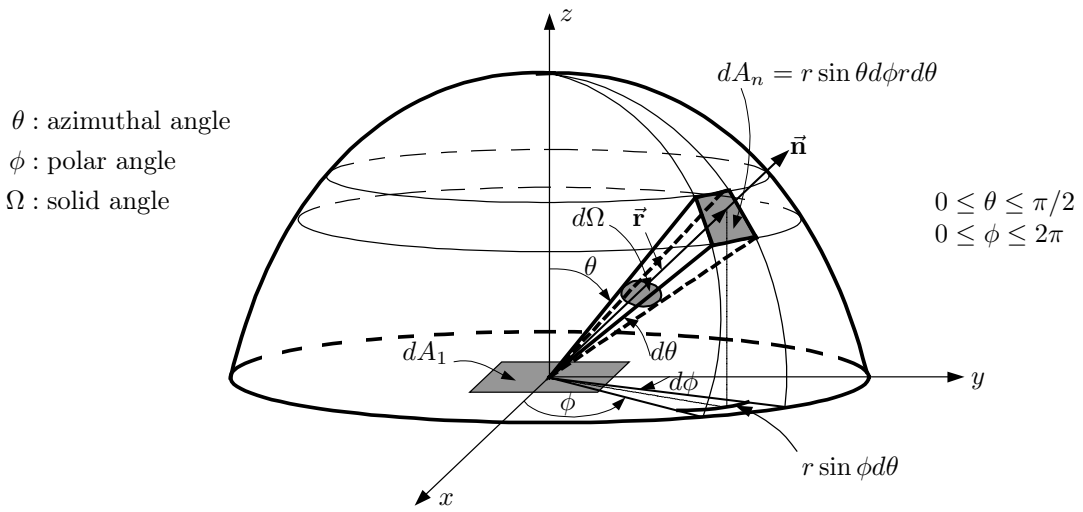

Figure 1.3 – Solid angle and projected area definition.

The radiative heat power emitted from a surface dA_1 in the θ, ϕ direction (through $dA_n = dA_1\cos\theta$) at the wavelength λ, per unit area of the emitting surface normal to this direction, per unit solid angle about this direction and per unit wavelength interval $d\lambda$ about λ is called the *spectral intensity* of radiation (often called spectral radiance in other domains):

$$L'_{\lambda,e}(T,\lambda,\theta,\phi) \equiv \frac{dQ}{dA_1\cos\theta d\Omega d\lambda} \quad \left[\mathrm{W\,m^{-2}\,m^{-1}\,sr^{-1}}\right] \tag{1.1}$$

The quantity

$$\frac{dQ}{d\lambda} \equiv dQ_\lambda \ \left[\mathrm{W\,m^{-1}}\right]$$

is the rate at which radiation of wavelength λ is emitted from dA_1 and passes through dA_n. The subscript e means an emission property, λ a spectral quantity and the superscript $'$ a directional quantity. The $\cos\theta$ term that appears in Equation 1.1 is a particularity of the definition of $L'_{\lambda,e}(T,\lambda,\theta,\phi)$: the spectral intensity is not relative to the size dA_1 of the surface element like in the emissive power $E(T)$ that will be later defined, but instead to its projection $dA_n = \cos\theta dA_1$ perpendicular to the radiation direction. It complies with the geometric fact that the emission of radiation for $\theta = \pi/2$ is zero and is usually maximum in the direction of the normal to the surface $\theta = 0$. An area that appears equally 'bright' from all directions is characterized by the simple condition that $L'_{\lambda,e}(T,\lambda,\theta,\phi)$ does not depend on θ and ϕ. This type of surface with $L'_{\lambda,e}(T,\lambda,\theta,\phi) = L_{\lambda,e}(T,\lambda)$ is known as a diffuse radiating surface as defined in Section 1.2.3.

Dividing dQ_λ by the unit area and integrating over the hemisphere defines the *spectral (hemispherical) emissive power* $E_\lambda(T,\lambda)$ $[\mathrm{W\,m^{-2}\,m^{-1}}]$ associated with dA_1:

$$E_\lambda(T,\lambda) \equiv \int_\Omega \frac{dQ_\lambda}{dA_1} = \int_0^{2\pi}\int_0^{\pi/2} L'_{\lambda,e}(T,\lambda,\theta,\phi)\cos\theta\sin\theta d\theta d\phi \tag{1.2}$$

The *(total hemispherical) emissive power* $E(T)$ $[\mathrm{W\,m^{-2}}]$ is

$$E(T) \equiv \int_0^\infty E_\lambda(T,\lambda)d\lambda \tag{1.3}$$

It is also useful to define the spectral and total directional emissive power:

$$E'_\lambda(T,\lambda,\theta,\phi) \equiv L'_{\lambda,e}(T,\lambda,\theta,\phi)\cos\theta \ \left[\mathrm{W\,m^{-2}\,m^{-1}\,sr^{-1}}\right] \tag{1.4}$$

$$E'(T,\theta,\phi) \equiv \int_0^\infty E'_\lambda(T,\lambda,\theta,\phi)d\lambda \ \left[\mathrm{W\,m^{-2}\,sr^{-1}}\right] \tag{1.5}$$

The quantities related to emitted radiation being defined, similar concepts can be introduced regarding incident radiation. Integrating the *spectral directional irradiance* $L'_{\lambda,i}(\lambda,\theta,\phi)$ $[\mathrm{W\,m^{-2}\,m^{-1}\,sr^{-1}}]$ over the hemisphere gives the *spectral irradiance* $G_\lambda(\lambda)$ $[\mathrm{W\,m^{-2}\,m^{-1}}]$:

$$G_\lambda(\lambda) = \int_0^{2\pi}\int_0^{\pi/2} L'_{\lambda,i}(\lambda,\theta,\phi)\cos\theta\sin\theta d\theta d\phi \tag{1.6}$$

and the *(total hemispherical) irradiance* G $[\mathrm{W\,m^{-2}}]$ is

$$G = \int_0^\infty G_\lambda(\lambda)d\lambda \tag{1.7}$$

Figure 1.4 summarises the relations between the different directional, total, spectral and hemispherical quantities.

The radiant power coming from a surface A has two components: the part effectively emitted by the surface (emissive power) and the part coming from surrounding surfaces

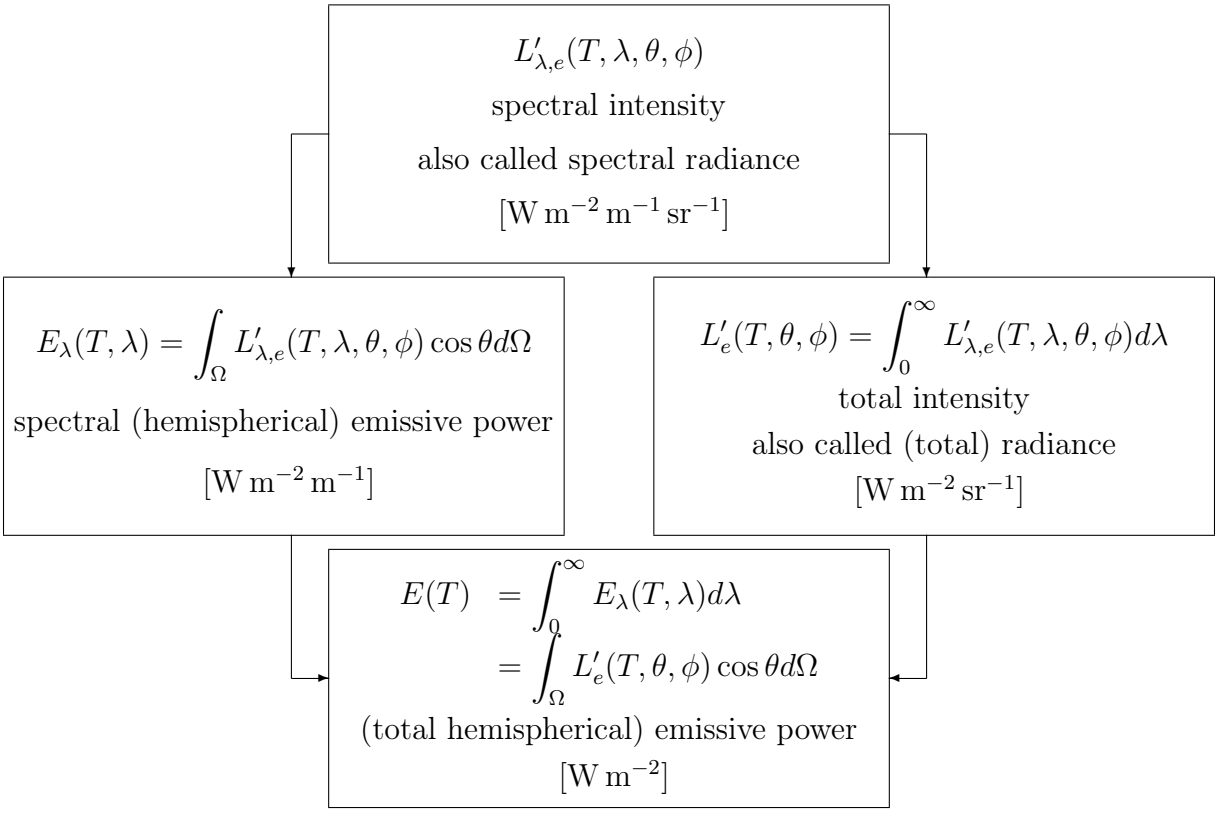

Figure 1.4 – From spectral directional quantities to total hemispherical quantities. The incident radiation $L'_{\lambda,i}(\lambda,\theta,\phi)$ can be treated similarly.

and reflected by A. The radiosity J $[\mathrm{W\,m^{-2}}]$ takes into account all radiant power leaving the surface and therefore includes the reflected portion of the irradiance in addition to the inherent emissive power.

$$J = \int_0^\infty J_\lambda(\lambda)d\lambda \tag{1.8}$$

with

$$J_\lambda(\lambda) = \int_0^{2\pi}\int_0^{\pi/2} L'_{\lambda,e+r}(T,\lambda,\theta,\phi)\cos\theta\sin\theta d\theta d\phi \tag{1.9}$$

1.2.2 Black body radiation

A black body is an opaque surface that does not reflect any radiation and therefore absorbs the maximum possible amount of radiative energy, independently of the wavelength and direction of the incident radiation. Through an energy balance at thermodynamic equilibrium, Gustav Kirchhoff [135] demonstrated that a black surface is also a perfect emitter.

Combining experimental data together with thermodynamic arguments, Wilhelm Wien proposed in 1896 [136] a spectral distribution for the black body emissive power that was very accurate over large parts of the spectrum. But it is in 1901 with his work on

quantum statistics that Max Planck [137] found the spectral black body emissive power distribution, now commonly known as Planck's law, for a black surface bounded by a transparent medium with refractive index n:

$$E_{b\nu}(T,\nu) = \frac{2\pi h\nu^3 n^2}{c_0^2(e^{\frac{h\nu}{kT}}-1)} \tag{1.10}$$

where $k = 1.380\,648\,8 \times 10^{-23}\,\mathrm{J\,K^{-1}}$ is *Boltzmann*'s constant. While frequency ν appears to be the most logical spectral variable (since it does not change when light travels from one medium into another), the wavelength λ is also commonly employed. If the refractive index n is independent of frequency:

$$E_{b,\lambda}(T,\lambda) = \frac{2\pi h c_0^2}{n^2\lambda^5(e^{\frac{hc_0}{n\lambda kT}}-1)} = \frac{C_1}{n^2\lambda^5(e^{\frac{C_2}{n\lambda T}}-1)} \tag{1.11}$$

with the custom abbreviations $C_1 = 2\pi h c_0^2$ and $C_2 = hc_0/k$. Figure 1.5 shows the black body emissive power distribution and the narrow visible part of the spectrum compared to the much wider infrared and ultraviolet ranges. It also illustrates the similarity between the solar extraterrestrial spectral irradiance and a black body at 5777 K.

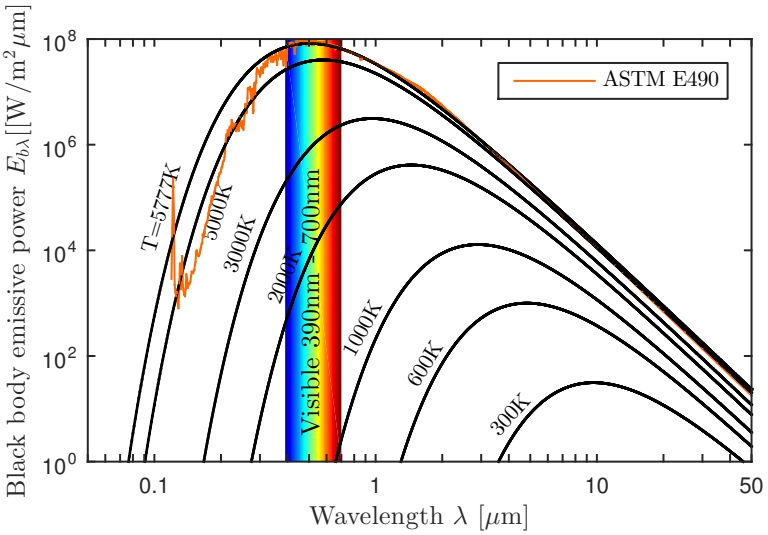

Figure 1.5 – Planck's Law - black body emissive power with the Sun's effective temperature of 5777 K compared to the ASTM-E490 AM0 [138] extraterrestrial solar reference emissive power (in orange).

After integration over λ, the total emissive power of a black body becomes only dependent on the fourth power of the temperature:

$$E_b(T) = n^2\sigma T^4 \tag{1.12}$$

where

$$\sigma = \frac{\pi^4 C_1}{15C_2^4} = \frac{2\pi^5 k^4}{15h^3c_0^2} = 5.6704 \times 10^{-8}\,\mathrm{W/m^2/K^4}$$

is *Stefan-Boltzmann*'s constant [139, 140]. This work is restricted to non-participating media and the refractive index n appearing in Equation 1.12 will be omitted for the rest of the manuscript since it is equal to 1 in vacuum.

1.2.3 The case of diffuse emitter/absorber

A surface may not be a black body but it may still exhibit properties independent of the incident/emitting direction. A perfectly diffuse emitter is such that its spectral (or total) intensity L' is independent of the angles θ, ϕ.

$$L_{\lambda,e}(T,\lambda) = L'_{\lambda,e}(T,\lambda,\theta,\phi) \tag{1.13}$$

From Equation 1.2, the spectral emissive power of a diffuse surface becomes

$$E_\lambda(T,\lambda) = L'_{\lambda,e}(T,\lambda,\theta,\phi)\int_0^{2\pi}\int_0^{\pi/2}\cos\theta\sin\theta\ d\theta d\phi = \pi L_{\lambda,e}(T,\lambda) \tag{1.14}$$

since $\int_0^{2\pi}\int_0^{\pi/2}\cos\theta\sin\theta\ d\theta d\phi = 2\pi[-\frac{1}{2}\cos^2\theta]_0^{\pi/2} = \pi$. Similarly, from Equation 1.5, the spectral directional emissive power of a perfectly diffuse surface is

$$E'_\lambda(T,\lambda,\theta,\phi) = L_{\lambda,e}(T,\lambda)\cos\theta = E'_{\lambda,n}(T)\cos\theta \tag{1.15}$$

where $E'_{\lambda,n}$ is the spectral directional emissive power in the direction of the normal to the surface. This concept was introduced by Johann Heinrich Lambert in 1760 and is known as the *Lambert's cosine law* [141]. Figure 1.6 schematically shows the relation between $L_{\lambda,e}(T,\lambda)$, $E_{\lambda,n}(T)$ and $E'_\lambda(T,\lambda,\theta,\phi)$.

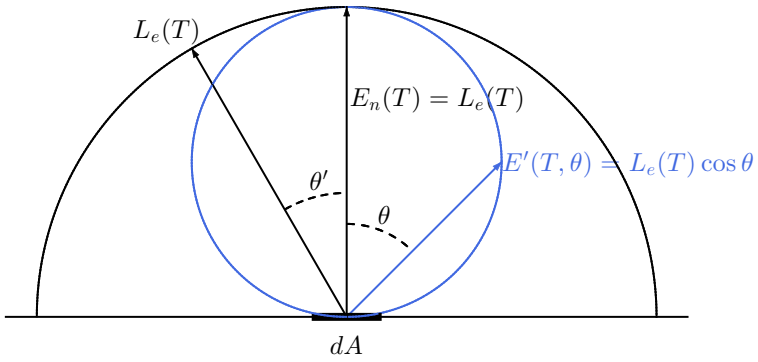

Figure 1.6 – Relation between directional emissive power and intensity for a Lambertian (diffuse) surface.

1.2.4 Surface properties

The way electromagnetic waves interact with the surface through absorption or scattering is characterised by the following quantities (referred to as thermo-optical properties in radiative heat transfer engineering):

- reflectance[1] $\rho \equiv \dfrac{\text{reflected part of incoming radiation}}{\text{total incoming radiation}}$
- absorptance $\alpha \equiv \dfrac{\text{absorbed part of incoming radiation}}{\text{total incoming radiation}}$
- transmittance $\tau \equiv \dfrac{\text{transmitted part of incoming radiation}}{\text{total incoming radiation}}$
- emittance $\varepsilon \equiv \dfrac{\text{energy emitted from a surface}}{\text{energy emitted by an ideal black surface at the same temperature}}$

The same spectral/total directional/hemispherical distinctions is performed for the thermo-optical properties: $\rho'_\lambda(T,\lambda,\theta,\phi)$, $\alpha'_\lambda(T,\lambda,\theta,\phi)$, $\tau'_\lambda(T,\lambda,\theta,\phi)$, $\varepsilon'_\lambda(T,\lambda,\theta,\phi)$. The directional spectral emittance is thus defined as

$$\varepsilon'_\lambda(T,\lambda,\theta,\phi) = \frac{E'_\lambda(T,\lambda,\theta,\phi)}{E_{b,\lambda}(T,\lambda)} \tag{1.16}$$

while the spectral hemispherical emittance is the ratio of the spectral emissive power to that of a black-body:

$$\begin{aligned}\varepsilon_\lambda(T,\lambda) = \frac{E_\lambda(T,\lambda)}{E_{b,\lambda}(T,\lambda)} &= \frac{\displaystyle\int_0^{2\pi}\int_0^{\pi/2} \varepsilon'_\lambda L_{b,\lambda}\cos\theta\sin\theta d\theta d\phi}{\pi L_{b,\lambda}} \\ &= \frac{1}{\pi}\int_0^{2\pi}\int_0^{\pi/2} \varepsilon'_\lambda \cos\theta\sin\theta d\theta d\phi\end{aligned} \tag{1.17}$$

Similarly, the total hemispherical emittance is the black body emissive power weighted average of the spectral hemispherical emittance:

$$\varepsilon(T) = \frac{E(T)}{E_b(T)} = \frac{\displaystyle\int_0^\infty E_\lambda(T,\lambda)d\lambda}{E_b(T)} = \frac{1}{\sigma T^4}\int_0^\infty \varepsilon_\lambda(T,\lambda)E_{b,\lambda}(T,\lambda)d\lambda \tag{1.18}$$

By conservation of energy, the radiant energy incident to a surface must either be absorbed, reflected or transmitted. This gives the following relation between the reflectance, absorptance and transmittance (spectral/total and directional/hemispherical):

$$\alpha'_\lambda(T,\lambda,\theta,\phi) + \rho'_\lambda(T,\lambda,\theta,\phi) + \tau'_\lambda(T,\lambda,\theta,\phi) = 1 \tag{1.19}$$

For an opaque surface, this simplifies into

$$\alpha'_\lambda(T,\lambda,\theta,\phi) + \rho'_\lambda(T,\lambda,\theta,\phi) = 1 \tag{1.20}$$

Distinguishing the incident and reflected angle, it is also useful to define the spectral (or total) bidirectional reflectance distribution function (BRDF) $\rho''_\lambda(T,\lambda,\theta_i,\phi_i,\theta_r,\phi_r)$ [2]. Similarly, one also defines the bidirectional transmittance distribution function (BTDF).

[1] The U.S. National Institute for Standards and Technology (NIST) has recommended to reserve the ending "-ivity" for radiative properties of ideal surfaces and ending "-ance" for real surface properties

[2] Unlike the other thermo-optical properties $\rho'_\lambda(T,\lambda,\theta,\phi)$, $\alpha'_\lambda(T,\lambda,\theta,\phi)$, $\tau'_\lambda(T,\lambda,\theta,\phi)$, $\varepsilon'_\lambda(T,\lambda,\theta,\phi)$, the BRDF $\rho''_\lambda(T,\lambda,\theta_i,\phi_i,\theta_r,\phi_r)$ can be greater than 1.

The BTDF or BRDF concepts are critical features of calibration mechanisms diffusers such as the ones developed at the Centre Spatial de Liège (CSL) for the UVN instrument described in Section 3.4. Measuring the BRDF or BTDF of large diffusers is a complex process that is usually performed on motorised optical benches such as the one developed at CSL.

Again, Kirchhoff showed [135] that the directional-spectral emittance is always equal to the directional-spectral absorptance of a surface:

$$\alpha'_\lambda(T, \lambda, \theta, \phi) = \varepsilon'_\lambda(T, \lambda, \theta, \phi) \tag{1.21}$$

Nevertheless, due to the wide wavelength range separating the solar spectral irradiance and the infrared emission of media at near-ambient temperature (temperature below 500 K), it is common in the spacecraft thermal design community to split up the spectrum into two parts, namely the visible and infrared parts. Even though Kirchhoff's law states that absorptance and emittance are equal for a given wavelength, spacecraft thermal engineers use the following (quite confusing) convention, called the semi-grey approximation. They redefine [142, 143]:

- the absorptance as the absorptance in the visible part of the spectrum. The total hemispherical absorptance is the weighted average with the solar spectral irradiance

$$\alpha = \frac{\int_{250\text{nm}}^{2800\text{nm}} \alpha_\lambda(\lambda) G_{\lambda,S}(\lambda) d\lambda}{\int_{250\text{nm}}^{2800\text{nm}} G_{\lambda,S}(\lambda) d\lambda} \tag{1.22}$$

  with $G_{\lambda,S}(\lambda)$ $[\mathrm{W\,m^{-2}\,nm^{-1}}]$ the extraterrestrial solar spectral irradiance given by the ASTM E-490 standard.

- the emittance as the emittance in the infrared part of the spectrum, the total emittance being usually weighted with the spectral emissive power of a black body 300 K (or any similar temperature) as defined in Equation 1.18.

This convention will be used throughout this manuscript. In spacecraft thermal modelling, it is common practice to further simplify and split the reflectance and transmittance into a diffuse component and a specular component for both infrared and visible ranges. Table 1.1 summarises the two sets of thermo-optical properties commonly used in spacecraft design.

Name	visible $(250 - 2800\,\mathrm{nm})$	infrared $(3 - 40\,\mu\mathrm{m}^1)$
Hemispherical emittance (absorptance)	α	ε
Diffuse reflectance	$\rho_{d,\mathrm{VIS}}$	$\rho_{d,\mathrm{IR}}$
Specular reflectance	$\rho_{s,\mathrm{VIS}}$	$\rho_{s,\mathrm{IR}}$
Diffuse transmittance	$\tau_{d,\mathrm{VIS}}$	$\tau_{d,\mathrm{IR}}$
Specular transmittance	$\tau_{s,\mathrm{VIS}}$	$\tau_{s,\mathrm{IR}}$

Table 1.1 – Definition of common thermo-optical properties used in spacecraft thermal modelling.

[1]The spectral range used in Equation 1.18 is obviously function of the expected temperature of the surface.

1.2.5 Exchange factors

Radiative heat exchanges involve long range interaction since, in non-participating media, the photons travel from surface to surface unimpeded. All surfaces that can exchange energy (either directly or by any type of reflection and/or transmission) must therefore be considered simultaneously, making the calculations quite complex.

The way two surfaces exchange energy can be described through an exchange factor between those two surfaces. It obviously depends on the distance, orientation and size of both surfaces. This geometric configuration leads to the definition of the view factor (also referred to as configuration factor, angle factor or shape factor). If surfaces are not black, multiple reflections and/or transmissions arise, specularly and/or diffusely. The concept of view factor between two surfaces must be extended to take this effect into account. In particular, surfaces that did not have a direct line of sight (view factor equals 0) can now "see" each other through reflections/transmissions with other surfaces. This leads to the definition of the radiative exchange factor. The definition of the view and radiative exchange factors is summarised below:

- **View factor** $F_{ij} \equiv$ fraction of the diffuse energy leaving surface i that is directly intercepted by surface j.
- **Radiative exchange factor (REF)** (or radiation interchange factor) $\mathcal{F}_{ij} \equiv$ fraction of the total energy emitted by surface i that is absorbed by surface j either directly or after any number or type of reflections and/or transmission.

The infinitesimal view factor between the two differential surfaces dA_i and dA_j is defined as

$$F_{dA_i,dA_j} \equiv \frac{dQ_{ij}}{dQ_i}$$

where dQ_i is the diffuse thermal energy leaving the infinitesimal surface dA_i per unit time and dQ_{ij} is the diffuse thermal energy leaving dA_i that is directly intercepted by the infinitesimal surface dA_j per unit time. Equation 1.14 leads to:

$$dQ_i = \pi L_{e+r}(T) dA_i$$
$$dQ_{ij} = L_{e+r}(T) dA_i \cos\theta_i d\Omega_{ij} \chi_{ij} = L_{e+r}(T) dA_i \cos\theta_i \frac{\cos\theta_j dA_j}{r_{ij}^2} \chi_{ij}$$

where χ_{ij} is the line-of-sight factor (1 if the two surfaces are mutually visible and 0 otherwise), $d\Omega_{ij}$ is the solid angle subtended by dA_j and r_{ij} the distance between dA_i and dA_j. The expressions of the infinitesimal, point wise and finite to finite surface view factors are therefore:

$$F_{dA_i,dA_j} = \frac{\cos\theta_i \cos\theta_j}{\pi r_{ij}^2} \chi_{ij} dA_j \tag{1.23}$$

$$F_{dA_i,A_j} = \int_{A_j} \frac{\cos\theta_i \cos\theta_j}{\pi r_{ij}^2} \chi_{ij} dA_j \tag{1.24}$$

$$F_{A_i,A_j} = \frac{1}{A_i} \int_{A_i} \int_{A_j} \frac{\cos\theta_i \cos\theta_j}{\pi r_{ij}^2} \chi_{ij} dA_j dA_i \tag{1.25}$$

For clarity, the view factor between A_i and A_j will be denoted F_{ij}. It is important to stress that while the view factors only depend on the geometry, the REFs depend on the surface thermo-optical properties which can be temperature dependent.

The law of reciprocity is straightforward for infinitesimal view factors and is given by Equation 1.23. The reciprocity law for the finite view factor expressed by Equation 1.26 is subject to the constraint that the radiation leaving the surfaces must not only be diffuse but also uniform over both surfaces (as it is usually the case in thermal modelling when considering many small faces of uniform properties and temperatures).

$$A_j F_{ji} = A_i F_{ij} \tag{1.26}$$

Again, assuming uniform thermo-optical properties over the surfaces, the reciprocity rule can be applied to the REFs:

$$\varepsilon_i A_i \mathcal{F}_{ij} = \varepsilon_j A_j \mathcal{F}_{ji} \tag{1.27}$$

Following directly from the definition of the view factor, the summation (or closure) rule states that the sum of all view factors between the N surfaces of an enclosure must add up to unity:

$$\sum_{j=1}^{N} F_{ij} = 1 \tag{1.28}$$

The sum includes the i^{th} surface since F_{ii} is not necessarily zero ($F_{ii} > 0$ for a concave surface). Similarly, the $\mathcal{F}_{ij}$'s also obey the summation rule:

$$\sum_{j=1}^{N} \mathcal{F}_{ij} = 1 \tag{1.29}$$

Different methods exist for computing view factors and/or radiative exchange factors. They can be divided into two categories: analytical and numerical methods. Analytical formulas exist to derive the view factor in some particular geometric configurations, but they are very limited and their expressions can be quite complex. The numerical methods are much more versatile, in particular the Monte Carlo method that will be detailed in the following sections. A comprehensive review of the numerical methods is available in [53]. Originally, there were three equivalent methods for computing radiant heat exchanges from the view factors [144]: Hottel's method [145], Eckert's method [146] and Gebhart's method [147, 148] to which can be added the electrical network analogy developed by Oppenheim [149], similar to Eckert's radiosity method. They are all similar, give the same results and all rely on the same common set of assumptions:

- Faces must be opaque.
- Faces must be isothermal. In practice, if non-uniform temperatures are expected, the faces are subdivided to approximate more closely the isothermality.
- Faces must be grey, meaning that they absorb or emit energy at different wavelengths in the same manner. Again, very few material exhibit this property over the whole spectral range. The range can be split into several bands and the calculation carried

out separately. The most common assumption is the semi-grey, splitting the range into the visible and infrared part of the spectrum, as presented in Section 1.2.4.

- Thermal radiation emission and reflection must be diffuse. The distinction between the emitted and reflected radiant fluxes cannot be made and therefore can be combined.
- Faces must radiate uniformly and be uniformly irradiated. The first part of the sentence implies that the surface properties must be uniform. The second part is more restrictive as demonstrated hereafter.

Following Gebhart's approach, the energy balance at location $\mathbf{s}$ is the difference between the incoming and outgoing radiation and provides the relation [36]:

$$q_r(\mathbf{s}) = \varepsilon(\mathbf{s})\sigma T^4(\mathbf{s}) - \int_A \varepsilon(\mathbf{s}')\sigma T^4(\mathbf{s}')\frac{d\mathcal{F}_{dA'\to dA}}{dA}dA' \tag{1.30}$$

where A is the total area of the enclosure and $\mathcal{F}_{dA'\to dA}$ is the differential radiative exchange factor from surface element dA' to dA defined above. If the enclosure is divided into n nodal surfaces A_j, the net radiative heat flow rate $Q_{r,j}$ of the j^{th} surface becomes

$$Q_{r,j} = A_j\varepsilon_j\sigma T_j^4 - \sum_{i=1}^{n}\varepsilon_i A_i\sigma T_i^4\mathcal{F}_{A_i\to A_j}$$

where ε_j and T_j are the average emittance and temperature of the j^{th} surface: $\varepsilon_j T_j^4 = 1/A_j\int_{A_j}\varepsilon T^4 dA$. The reciprocity and closure rules described in Equations 1.27 and 1.29 eventually give the well known fourth power temperature difference equation:

$$Q_{r,j} = A_j\varepsilon_j\sigma\sum_{i=1}^{n}\mathcal{F}_{A_i\to A_j}\left(T_j^4 - T_i^4\right) \tag{1.31}$$

As a by-product of the method, it is possible to derive the radiative exchange factors $\mathcal{F}_{ij}$'s from the view factors F_{ij}'s under the same assumptions. This method is often referred to as the *matrix method*:

$$\mathcal{F}_{ij} = F_{ij}\varepsilon_j + \sum_{k=1}^{N}F_{ik}(1-\varepsilon_k)\mathcal{F}_{kj} \tag{1.32}$$

Rearranging the above equation and using matrix notation allows to write

$$\boldsymbol{\mathcal{F}} = \left(\mathbf{I} - \mathbf{F}\boldsymbol{\rho}\right)^{-1}\mathbf{F}\boldsymbol{\varepsilon} \tag{1.33}$$

where $\boldsymbol{\varepsilon}$ and $\boldsymbol{\rho}$ are diagonal matrices with the surface emittance and reflectance, respectively. This leads to the famous relation describing the radiative heat exchange between two diffuse grey surfaces

$$Q_{12} = GR_{12}\sigma(T_1^4 - T_2^4) \tag{1.34}$$

where GR_{12} [m^2] is the radiative link between surface 1 and 2 given by:

$$GR_{12} = GR_{21} = A_1\varepsilon_1\mathcal{F}_{12} = \frac{1}{\dfrac{1-\varepsilon_1}{\varepsilon_1 A_1} + \dfrac{1}{A_1 F_{12}} + \dfrac{1-\varepsilon_2}{\varepsilon_2 A_2}}$$

This method is very convenient since REFs between perfectly diffuse grey surfaces can be obtained from the geometric view factors through a simple matrix inversion. The underlying assumptions however become rapidly restrictive as explained in [150]. Even with perfectly diffuse surfaces, analytical solutions are very limited. For example, in the particular case of two surfaces relatively close to each other such as two rectangles of width w_1 and w_2 in perpendicular planes and sharing a common edge of length l, the matrix method can lead to non-negligible errors. The exact, analytical view factor is expressed by [35]:

$$\begin{aligned} F_{12} = \frac{1}{\pi W_1}\Bigg(& W_1 \arctan\frac{1}{W_1} + W_2 \arctan\frac{1}{W_2} - W \arctan\frac{1}{W} \\ & + \frac{1}{4}\ln\left\{\frac{(1+W_1^2)(1+W_2^2)}{1+W^2}\left[\frac{W_1^2(1+W^2)}{(1+W_1^2)W^2}\right]^{W_1^2}\left[\frac{W_2^2(1+W^2)}{(1+W_2^2)W^2}\right]^{W_2^2}\right\}\Bigg) \end{aligned} \tag{1.35}$$

with $W_1 = w_1/l$, $W_2 = w_2/l$, $W = \sqrt{W_1^2 + W_2^2}$. In the case of two perpendicular squares, $W_1 = W_2 = 1$ and the view factor is $F_{12} = F_{21} = 0.200\,044$. The radiative exchange factors can be derived using the matrix method described above. They are compared to the results obtained with the MCRT method implemented in ESARAD, the ray tracing engine of ESATAN-TMS. Figure 1.7 shows that the relative error on $\mathcal{F}_{11}$ is over 25% and the one on $\mathcal{F}_{12}$ approaches 5% as the emittance (total, hemispherical) decreases. $\mathcal{F}_{12}$ and $\mathcal{F}_{11}$ are underestimated by the analytical method because the radiation is not uniform: it is higher close to the common edge. It therefore violates one of Gebhart's approach assumptions. The limitations of the analytical methods will be taken into account in the benchmarking processes, and the reference solution of the test cases will be obtained with ESARAD by tracing a sufficiently high number of rays.

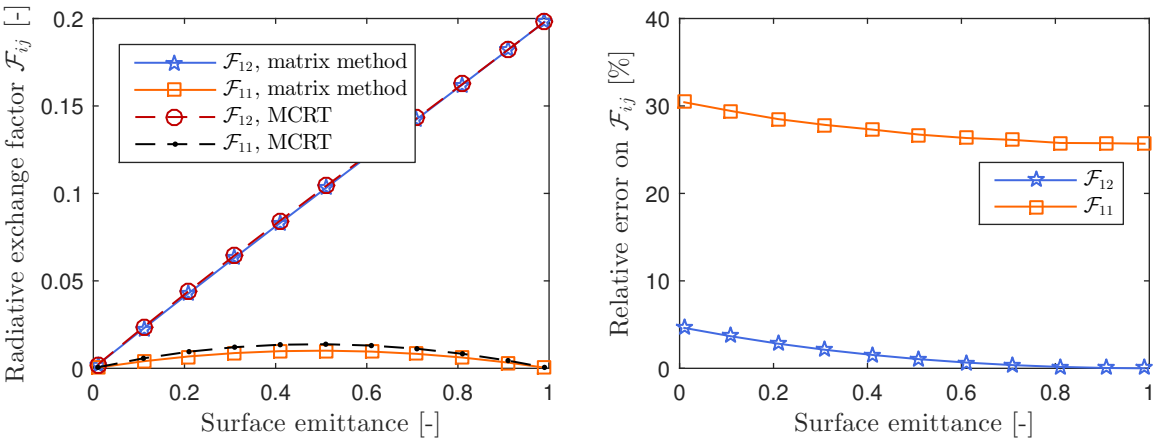

(a) (b)

Figure 1.7 – Benchmarking Gebhart's matrix method.

1.3 Monte Carlo ray tracing

As introduced in the previous section, computing the view factor is not an easy task since Equation 1.25 involves double integration taking into account shadowing effects. It becomes even more difficult for the radiative exchange factors where surfaces properties and multi-reflection/transmission come into play. A comprehensive review of the available methods is available in [53, 116] among which we find the hemicube method developed in [151] and implemented in I-deas TMG or NASTRAN, the hierarchical method developed by Hanrahan *et al.* [152] or the classical Gauss point double integration, for instance implemented in SAMCEF. These numerical methods however become quite computationally expensive as the problem grows in complexity. Conversely, the computational costs of Monte Carlo methods increase linearly with the size and complexity of the problem where the computational effort of conventional methods is usually increasing much more rapidly [36, 116], as schematically illustrated in Figure 1.8. Monte Carlo methods are therefore well suited to solve thermal radiation problems. As mentioned in the introduction of this chapter, Monte Carlo techniques were introduced in the 1940s in nuclear engineering to assess the diffusion of neutrons in fissile material by Metropolis, Ulam, von Neumann and Fermi [153–155] although Lord Kelvin already employed some Monte Carlo technique more than forty years earlier [155, 156]. It is only in the early 1960s that Monte Carlo method was applied to radiative heat transfer problems by Fleck and Howell [75–77].

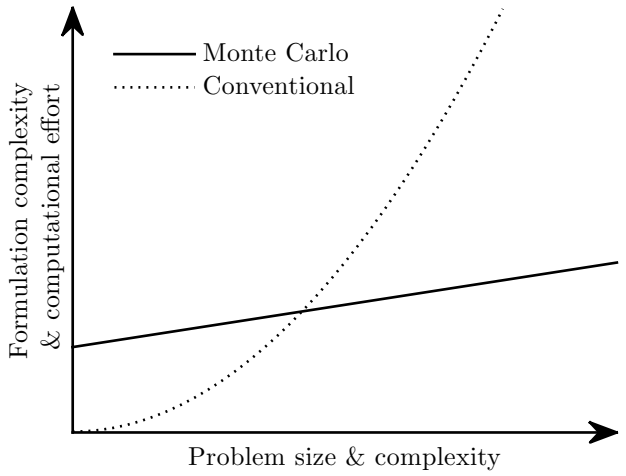

Figure 1.8 – Evolution of computational effort in function of the size and complexity of the problem for Monte Carlo and conventional techniques [36].

In the context of REFs (or view factors) computation, the Monte Carlo method is applied to ray tracing and consists in tracking the history of statistically meaningful samples of photons (or photon bundles) from their point of emission to their final absorption. MCRT can be applicable to the computation of the view factors but it also offers the advantage to enable the direct computation of the REFs, taking into account multiple reflections and/or transmissions with more realistic surface properties, without adding much complexity. MCRT avoids branching along the ray tracing process: the energy is not

reflected partially specularly, partially diffusely and/or transmitted partially specularly and partially diffusely at the same time. Instead, it is either reflected specularly or diffusely or transmitted specularly or diffusely and one ray is traced until extinction without generating children rays. The choice between specular/diffuse transmission/reflection is determined by comparing a random number ξ to ratios of thermo-optical properties:

- if $\xi \leq \frac{\rho_{s,\mathrm{IR}}}{1-\varepsilon}$, the ray is specularly reflected,
- if $\frac{\rho_{s,\mathrm{IR}}}{1-\varepsilon} < \xi \leq \frac{\rho_{s,\mathrm{IR}} + \tau_{s,\mathrm{IR}}}{1-\varepsilon}$, the ray is specularly transmitted,
- if $\frac{\rho_{s,\mathrm{IR}} + \tau_{s,\mathrm{IR}}}{1-\varepsilon} < \xi \leq \frac{\rho_{s,\mathrm{IR}} + \tau_{s,\mathrm{IR}} + \tau_{d,\mathrm{IR}}}{1-\varepsilon}$, the ray is diffusely transmitted,
- else the ray is diffusely reflected $\left(\frac{\rho_s + \tau_s + \tau_d}{1-\varepsilon} < \xi\right)$.

Similar ratios are used for computations in the visible part of the spectrum.

The cornerstone of Monte Carlo ray tracing is that if $n_{r,i}$ rays (or photon bundles) are emitted from the surface A_i among which $n_{r,ij}$ rays are absorbed by surface A_j either directly or after any type/number of reflections/transmissions, according to the Law of Large Numbers first proved by Bernoulli in 1713 [157] the REF between the surfaces i and j can be written:

$$\mathcal{F}_{ij} = \lim_{n_{r,i}\to\infty} \frac{n_{r,ij}}{n_{r,i}} \cong \left.\frac{n_{r,ij}}{n_{r,i}}\right|_{n_{r,i}>>1} \tag{1.36}$$

The view factor is obtained similarly by considering only direct absorption without any reflection or transmission. The basic concept behind MCRT is that the number of rays must be large enough to be statistically meaningful so that the REFs tend towards the correct solution. As any stochastic method, the results vary randomly around the correct answer and the amplitude of the fluctuation decreases as the number of samples increases. Typical Monte Carlo convergence process is shown in Figure 1.9.

The random samples determining the ray are generated with pseudo-random generators, whose sequences are usually initialized with a seed. One given seed generates a determined sequence of pseudo-random numbers.

Even though it does not depend on the dimension of the problem, the inconvenient of crude Monte Carlo techniques is their relatively low rate of convergence. The error is inversely proportional to the square root of the number of rays [48, 150, 158, 159]. Increasing the accuracy by one order of magnitude means multiplying the number of rays by two orders of magnitude.

$$\text{error} \propto \frac{1}{\sqrt{n_r}} = n_r^{-0.5} \tag{1.37}$$

To compute the exchange factors between one surface and the surrounding surfaces, the rays originating from the first surface must be distributed over the surface area and over the directions, in the same way that the view factor between two finite surfaces involves the double integration shown by Equation 1.25. Two separate samplings need to be performed:

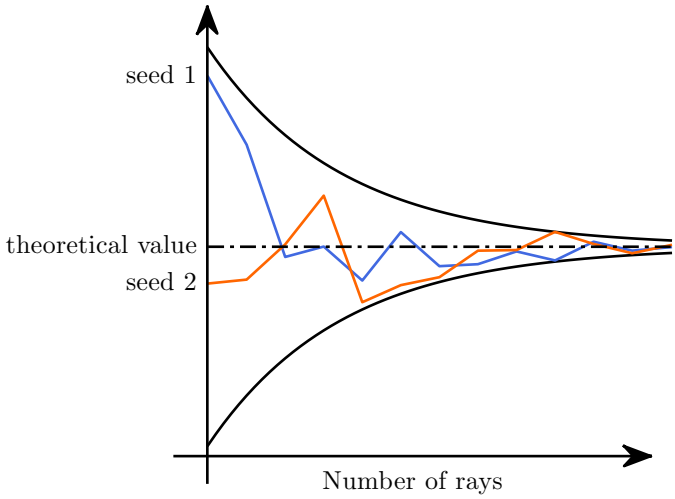

Figure 1.9 – Typical MCRT process convergence.

- direction sampling of the unit hemisphere,
- surface sampling of the emitting surface.

Direction sampling of the unit hemisphere leads to the point wise view factor which is then to be integrated over the emitting surface with surface sampling. It is interesting to note that the starting coordinates (spatial sampling) describe the near field properties of the radiation source, and that the direction sampling represents its far field properties.

1.3.1 Random samples generation

The ray direction cosines and starting coordinates are generated with pseudo-random numbers. As most pseudo random number generators give uniformly distributed samples ξ_i over $[0,1]$, the unit square $[0,1]^2$ (or cube, hypercube) is easily sampled by sampling each direction independently. The desired space to be sampled is however usually not the unit square and a transformation needs to be applied to map the random samples (ξ_{1_i}, ξ_{2_i}) to the desired space with the desired density. In case of ray direction sampling, the desired space is the unit hemisphere with the polar angle θ and azimuthal angle ϕ varying in $[0, \pi/2]$ and $[0, 2\pi]$, respectively. The naive transformation

$$\theta_i = \frac{\pi}{2}\xi_{\theta_i}$$
$$\phi_i = 2\pi\xi_{\phi_i}$$

does cover the whole hemisphere but does not cover it uniformly. An area-preserving transformation is therefore sought along with a way to apply the desired density. The probability density function (PDF) p describes the probability that a continuous random variable x takes a value in some interval $[a, b]$ through the following integral

$$\text{Probability}(x \in [a,b]) = \int_a^b p(x)dx \tag{1.38}$$

One technique, called the inversion technique, to generate random samples x_i following a PDF $p(x)$ from a set of random numbers ξ_i uniformly distributed in $[0, 1]$ is to use the cumulative probability distribution function $P(x)$ which gives the probability that the random variable x_i is less or equal to x:

$$\text{Probability}(x_i < x) = P(x) = \int_{-\infty}^{x} p(x)dx \tag{1.39}$$

Knowing $P(x)$, the x_i can be derived from the ξ_i by inverting $P(x)$:

$$x_i = P^{-1}(\xi_i) \tag{1.40}$$

In the case of a multivariate problem of dimension k with a probability density function $p(x_1, x_2, ..., x_k)$, the sample vectors $(x_1, x_2, ..., x_k)_i$ can be generated successively by the nested conditioning approach [46, 160]. The marginal cumulative distribution $P_{x_1}(x)$ is inverted to generate x_{1_i} from ξ_{1_i}

$$P_{x_1}(x) = \int_{-\infty}^{x} \int_{-\infty}^{\infty} ... \int_{-\infty}^{\infty} p(x_1, x_2, ..., x_k)dx_k...dx_2dx_1$$

x_{2_i} is then generated conditionally to x_{1_i} from the conditional distribution function

$$P_{x_2|x_{1_i}}(x|x_{1_i}) = \int_{-\infty}^{x} \int_{-\infty}^{\infty} ... \int_{-\infty}^{\infty} \frac{p(x_{1_i}, x_2, ..., x_k)}{p_{x_1}(x_{1_i}, x_2, ..., x_k)}dx_k...dx_3dx_2$$

where $p_{x_1}(x_1, x_2, ..., x_k)$ is the marginal PDF of x_1:

$$p_{x_1}(x_1, x_2, ..., x_k) = \int_{-\infty}^{\infty} \int_{-\infty}^{\infty} ... \int_{-\infty}^{\infty} p(x_1, x_2, ..., x_k)dx_k...dx_3dx_2$$

1.3.2 The cosine distribution law

For practical cases, most surfaces can be considered as Lambertian/diffuse emitting surface. In that case, the PDF is the cosine law [160, 161]:

$$p_{\theta,\phi}(\theta, \phi) = \frac{1}{\pi} \cos\theta \sin\theta \tag{1.41}$$

and the cumulative distribution function over the hemisphere is expressed by

$$P(\theta, \phi) = \int_0^{\theta} \int_0^{\phi} p(\theta', \phi')d\theta'd\phi' = \int_0^{\theta} \int_0^{\phi} \frac{\cos\theta'}{\pi} \sin\theta'd\theta'd\phi' = \frac{\phi \sin^2\theta}{2\pi}$$

The random polar angle sample θ_i is determined by taking the inverse of the marginal cumulative distribution function $P_\theta(\theta) = \sin^2\theta$:

$$\theta_i = \arcsin\sqrt{\xi_{\theta_i}} \tag{1.42}$$

Once the polar angle sample is determined, the azimuthal angle sample ϕ_i is derived from the conditional marginal cumulative distribution function $P_{\phi|\theta}(\phi|\theta_i)$ involving the marginal probability distribution function $p_\theta(\theta) = \int_0^{2\pi} p(\theta, \phi)d\phi = 2\cos\theta$:

$$P_{\phi|\theta}(\phi|\theta_i) = \int_0^{\phi} \frac{\cos\theta_i}{\pi p_\theta(\theta_i)} d\phi' = \int_0^{\phi} \frac{\cos\theta_i}{2\pi\cos\theta_i} d\phi' = \frac{\phi}{2\pi}$$

and

$$\phi_i = 2\pi\xi_{\phi_i} \tag{1.43}$$

In this case, the two random variables ϕ_i and θ_i are independent from each other. This is a consequence of the separability of the PDF $p(\theta, \phi)$ of a diffuse emitter. From two given sets of pseudo-random numbers $(\xi_{\theta_i}, \xi_{\phi_i})$, the polar and azimuthal sample angles are derived and the components of the i^{th} sample ray $\mathbf{r}_i$ in Cartesian coordinates is given by:

$$\mathbf{r}_i(\xi_{\theta_i}, \xi_{\phi_i}) = \begin{bmatrix} \sin\theta_i\cos\phi_i & \sin\theta_i\sin\phi_i & \cos\theta_i \end{bmatrix} \tag{1.44}$$

$$= \begin{bmatrix} \sqrt{\xi_{\theta_i}}\cos(2\pi\xi_{\phi_i}) & \sqrt{\xi_{\theta_i}}\sin(2\pi\xi_{\phi_i}) & \sqrt{1-\xi_{\theta_i}} \end{bmatrix} \tag{1.45}$$

1.3.3 Accuracy control

The MCRT technique offers the possibility to integrate accuracy control to balance the non-deterministic behaviour of the method. The number of rays required to achieved a given accuracy δ with a given confidence level C_I can be calculated from Equation 1.46 implemented in ESARAD [150, 162, 163] and THERMICA [164]:

$$n_r = 2\left(\frac{\text{erf}^{-1}(C_I)}{\delta}\right)^2 \frac{1-F}{F} \tag{1.46}$$

If an estimate of the view factor F is computed with an initial number of rays, Equation 1.46 gives the number of rays required to achieve the target accuracy and given confidence interval. This formula results from the central limit theorem and explains the crude Monte Carlo convergence rate of 0.5 given in Equation 1.37. Equation 1.46 is plotted in Figure 1.10 for different accuracies (δ =1, 5 and 20%) and confidence intervals (90 to 99.7%). As the view factor decreases, the number of rays rapidly increases to achieve the required accuracy. It also shows that the number of rays is less affected by the confidence interval that appears through the inverse error function, than by the accuracy that is squared in Equation 1.46.

This accuracy control scheme is implemented in several ray tracing software but in a slightly modified version. The error is measured through the *line sum error* (LSE) which is derived from the closure rule. The closure is inherently obeyed since all rays are eventually absorbed. Some variance reduction method however breaks it by enforcing the reciprocity. More details on REFs smoothing and variance reduction techniques will be given in Section 2.5.1. The LSE of node i is simply given by inverting Equation 1.29:

$$\text{LSE}_i = 1 - \sum_{j=1}^{n_f+1} \mathcal{F}_{ij} \tag{1.47}$$

with n_f the number of faces in the model. The additional face in the summation corresponds to the cavity or deep space node. This is the metric implemented in ESARAD: the user gives a target LSE value to achieve within a target confidence interval and an initial

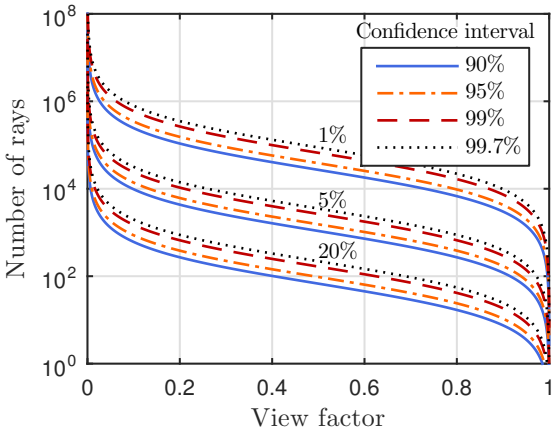

Figure 1.10 – Crude Monte Carlo accuracy control behaviour in function of the view factor.

number of rays to be traced. Based on the LSE obtained with the initial number of rays, the number of rays required to achieve the target LSE is computed with Equation 1.46.

1.4 Lumped parameter method and finite element method for heat transfer

As the GMM involving more the radiative heat exchanges precedes the TMM, this section presents the two major thermal modelling techniques, the FEM and LPM, in which the REFs and orbital heat fluxes are included as surface boundary conditions.

1.4.1 Energy conservation

The problem of heat transfer in a three-dimensional anisotropic medium bounded by the surface Γ is governed by the differential heat transfer equation derived from the conservation of energy [165]:

$$\rho c \frac{\partial T}{\partial t} = \boldsymbol{\nabla} \cdot (\mathbf{k} \cdot \nabla T) + Q \tag{1.48}$$

where $\mathbf{k}$ [$\mathrm{W\,m^{-1}\,K^{-1}}$] is the thermal conductivity tensor of the medium, T [K] its temperature, c [$\mathrm{J\,kg^{-1}\,K^{-1}}$] its specific heat, ρ [$\mathrm{kg\,m^{-3}}$] its density, Q [$\mathrm{W\,m^{-3}}$] is the rate of energy generation per unit volume and t is the time. Solving Equation 1.48 requires the temperature (Dirichlet or essential condition) or the heat flux (Neumann or natural condition) to be defined on all the boundaries of the region under study:

$$T = f^T(\mathbf{s}, t) \text{ on } \Gamma_T \tag{1.49}$$

$$-(\mathbf{k} \cdot \nabla T) \cdot \mathbf{n} \equiv \mathbf{q}(\mathbf{s}, t) \cdot \mathbf{n} = q_c(\mathbf{s}, t) + q_r(\mathbf{s}, t) + q_a(\mathbf{s}, t) \text{ on } \Gamma_q \tag{1.50}$$

where $\mathbf{s}$ contains the coordinates along the total boundary of the heat transfer region $\Gamma = \Gamma_q \cup \Gamma_T$, $\mathbf{n}$ is the outward unit normal to the boundary surface Γ and q_c, q_r, q_a are the convective, radiative and applied heat fluxes on the boundary, respectively. The radiative heat flux q_r is derived from Equation 1.30.

1.4.2 Lumped parameter method

For complex geometries and problems involving radiation, very few analytical solutions of Equation 1.48 exist [166, 167] and numerical techniques must therefore be employed. The basis of the lumped parameter (or resistor-capacitor R-C) method is a Taylor series expansion of Equation 1.48 as derived in [168, 169] to solve partial differential equations on analogue computer. In the LPM, the medium is divided into subvolumes called nodes to which are associated the total capacitance of the subvolume and its capacitance-averaged temperature. Since the temperature and capacitance are lumped to a single point (traditionally the centre of the node) the temperature through the subvolume can be linearly interpolated between the nodes [33, 57]. The discretised formula expresses the conservation of energy for each thermal node i [57, 69]:

$$C_i \frac{\partial T_i}{\partial t} = Q_i + \sum_{j=1}^{N} GL_{ij} \left(T_j - T_i\right) + \sigma \sum_{j=1}^{N} GR_{ij} \left(T_j^4 - T_i^4\right) \tag{1.51}$$

where C_i [$\mathrm{J\,K^{-1}}$] is the capacitance of node i, Q_i [W] is the applied heat rate (*e.g.* internal dissipation or environmental heat flux) integrated over node i, GL_{ij} [$\mathrm{W\,K^{-1}}$] and GR_{ij} [$\mathrm{m^2}$] are the conductive (linear conductance) and radiative links between nodes i and j, respectively. σ is Stefan-Boltzmann's constant introduced in Section 1.2.2. There exist three types of nodes: the diffusion node (finite capacitance), arithmetic node (zero capacitance, usually used to model surfaces adjacent to a diffusion node) and boundary node (infinite capacitance). Typically, the conductive link can be expressed as a thermal conductivity multiplying a shape factor. In one dimension, the shape factor becomes the cross section area to length ratio and gives the classical formula thoroughly used by the thermal engineer and derived from Fourier's law [170]:

$$GL_{ij} = k \frac{S}{L}$$

where S is the cross section area and L is the length separating the two nodes i and j.

The problem with LPM arises when conductive links in complex 3D geometries need to be computed with relatively large nodes to avoid too many REFs [171]. Lately, several specific methods were developed to generate the conductive links. In the REBECA (REliable Boundary Element Conductive Analyzer) software, an iterative method based on the boundary elements method was developed in the late 1990s for Alcatel Space [172, 173]. In parallel, developed by Aerospatiale Cannes (later becoming Alcatel Space then Thales Alenia Space), the CORATHERM thermal software discretised the nodes by an extremely fine orthogonal TLP mesh whose conductances are given by standard expressions and then reduce it by defining average nodes [31, 62, 174, 175]. This software was also used to provide thermo-elastic input [63] to FE tools.

Now integrated into ESATAN-TMS, the Far-Field Method (FFM) [176–178] relies on a fine FE submesh of the two nodes to be linked together. The FFM consists in three steps: first, for each LP node, identify the far-field edge by imposing a temperature on the common edge (surface for 3D nodes) with a uniform heat flux on the node surface (volume). The far-field edge (or surface) is defined as the zone whose temperature is close the the maximum temperature (with a given threshold). Second, the two FE meshed LP nodes are considered together and a given positive Q and equally negative $-Q$ heat flow

rates are imposed on the far-field edge (surface) of the first and second node, respectively. The problem is solved and the temperature distribution is computed over the two LP nodes. Third, the average temperature of the two LP nodes $T_{1,av}$ and $T_{2,av}$ are computed and the conductive link GL_{12} is deduced from Equation 1.51 simplified to linear steady-sate:

$$Q = GL_{12}(T_{1,av} - T_{2,av})$$

This method computes the conductive link between two nodes discarding all other surrounding nodes. This ensures that no negative link is generated as recommended by [14] since they could be considered as absurd from physical point of view (yet not from a mathematical point of view). Thermica determines the conductive links based on the Reduced Conductive Network (RCN) [102, 179]. This method also relies on a reduction of a submesh of the LP nodes. It introduces edge nodes and generates links inside a LP node between the average surface (volume) node and the edge (surface) node.

1.4.3 Finite element method

This section does not intend to give a thorough view of the FEM but rather gives the nuts and bolts necessary for spacecraft thermal analysis. More details about the FEM applied in heat transfer is given in [165]. If the LPM can be classified as a discrete method, the FEM could be considered as semi-discrete. With the FEM, the temperature within each element $T^{(e)}(x, y, z, t)$ is interpolated from the nodal temperatures of the element $\mathbf{T}^{(e)}$ through shape functions $\mathbf{\Psi}^{(e)}$. The FE nodes correspond to vertices and control points of the element. Adjacent elements therefore share the nodes located on their common boundary. Temperature continuity is enforced across element boundaries by a careful choice of the shape functions.

$$T^{(e)}(x, y, z, t) = \left(\mathbf{\Psi}^{(e)}\right)^{\mathsf{T}} \mathbf{T}^{(e)} \tag{1.52}$$

where $\mathbf{\Psi}^{(e)}$ and $\mathbf{T}^{(e)}$ are a $(n_n^{(e)} \times 1)$ vectors containing the element shape functions and the nodal temperatures, respectively and $n_n^{(e)}$ is the number of nodes of the element. Galerkin's method of weighted residuals consists in multiplying Equation 1.48 by the shape function and integrating it over the element domain $V^{(e)}$ [165]. Gauss's theorem that introduces surface integrals of the heat fluxes across element boundary $\Gamma^{(e)}$ and Equation 1.50 successively give:

$$\begin{aligned}
\int_{V^{(e)}} \Psi_i^{(e)} \rho c \frac{\partial T}{\partial t} dV &= \int_{V^{(e)}} \Psi_i^{(e)} \boldsymbol{\nabla} \cdot \left(\mathbf{k}^{(e)} \cdot \nabla T\right) dV + \int_{V^{(e)}} \Psi_i^{(e)} Q dV, \quad i = 1, 2..., n_e \\
&= \int_{\Gamma^{(e)}} \Psi_i^{(e)} \left(\mathbf{k}^{(e)} \cdot \nabla T\right) \cdot \mathbf{n} d\Gamma - \int_{V^{(e)}} \nabla \Psi_i^{(e)} \cdot \left(\mathbf{k}^{(e)} \cdot \nabla T\right) dV + \int_{V^{(e)}} \Psi_i^{(e)} Q dV \\
&= -\int_{\Gamma^{(e)}} \Psi_i^{(e)} \mathbf{q}(\mathbf{s}, t) \cdot \mathbf{n} d\Gamma - \int_{V^{(e)}} \nabla \Psi_i^{(e)} \cdot \left(\mathbf{k}^{(e)} \cdot \nabla T\right) dV + \int_{V^{(e)}} \Psi_i^{(e)} Q dV
\end{aligned}$$

The element matrices are then derived introducing Equation 1.52:

$$\mathbf{C}^{(e)}\frac{\partial \mathbf{T}^{(e)}}{\partial t} + \mathbf{K}_L^{(e)}\mathbf{T}^{(e)} = \mathbf{Q}^{(e)} \tag{1.53}$$

with $\mathbf{C}^{(e)}$, $\mathbf{K}_L^{(e)}$ being the nodal capacitance and conduction ($n_n^{(e)} \times n_n^{(e)}$) matrices, respectively and $\mathbf{Q}^{(e)}$ a ($n_n^{(e)} \times 1$) vector containing the nodal heat flow rates coming from the heat generation integrated over the volume and the boundary conditions heat fluxes integrated over the boundary surface. All matrices can be temperature dependent if *e.g.* the material properties vary with the temperature.

$$\begin{aligned}
\mathbf{C}^{(e)} &= \int_{V^{(e)}} \rho c \mathbf{\Psi}^{(e)} \left(\mathbf{\Psi}^{(e)}\right)^{\mathsf{T}} dV \\
\mathbf{K}_L^{(e)} &= \int_{V^{(e)}} \mathbf{B}^{(e)}\mathbf{k}^{(e)} \left(\mathbf{B}^{(e)}\right)^{\mathsf{T}} dV \\
\mathbf{Q}^{(e)} &= \int_{V^{(e)}} \mathbf{\Psi}^{(e)} Q dV - \int_{\Gamma^{(e)}} \mathbf{\Psi}^{(e)}(q_c + q_r + q_a) d\mathbf{s}
\end{aligned}$$

where the ($n_n^{(e)} \times 3$) matrix $\mathbf{B}^{(e)}$ is the gradient of the shape functions:

$$\mathbf{B}^{(e)} = \nabla \mathbf{\Psi}^{(e)} = \left[\frac{\partial \mathbf{\Psi}^{(e)}}{\partial x} \quad \frac{\partial \mathbf{\Psi}^{(e)}}{\partial y} \quad \frac{\partial \mathbf{\Psi}^{(e)}}{\partial z}\right]$$

Element matrices are usually computed by Gauss integration with the introduction of the element Jacobian matrix. After all element matrices are evaluated, they are assembled to form the global system of equations:

$$\mathbf{C}\frac{\partial \mathbf{T}}{\partial t} + \mathbf{K}_L\mathbf{T} = \mathbf{Q} \tag{1.54}$$

If the convective heat flux q_c is written in the form $q_c = h_c(T - T_f)$ where T_f is the fluid temperature and h_c the convective heat transfer coefficient, the convective term of $\mathbf{Q}^{(e)}$ can be developed into

$$\begin{aligned}
\int_{\Gamma^{(e)}} \mathbf{\Psi}^{(e)} q_c d\mathbf{s} &= \int_{\Gamma^{(e)}} \mathbf{\Psi}^{(e)} h_c (T - T_f) d\mathbf{s} \\
&= \left(\int_{\Gamma^{(e)}} h_c \mathbf{\Psi}^{(e)} \left(\mathbf{\Psi}^{(e)}\right)^{\mathsf{T}} d\mathbf{s}\right) \mathbf{T}^{(e)} - \int_{\Gamma^{(e)}} h_c \mathbf{\Psi}^{(e)} T_f d\mathbf{s} \\
&= \mathbf{K}_C^{(e)}\mathbf{T}^{(e)} - \mathbf{Q}_C^{(e)}
\end{aligned}$$

Even though isothermal surface assumption is inconsistent with finite-element formulation since the temperature over the element varies according to its shape functions, determining the radiation heat transfer flux q_r traditionally assumes that surfaces are small enough to be considered as isothermal and that the incident radiant heat fluxes on them are uniform. In enclosure radiation, q_r can be expressed as a matrix multiplying the difference of the fourth power of the temperature through the net radiation method [35] or the Gebhart's method [147, 148] presented in Section 1.2.5. Equation 1.31 can be rewritten under matrix form to give

$$\mathbf{Q}_r = \mathbf{K}_R \mathbf{T}^4 = \mathbf{A}\boldsymbol{\varepsilon}\left(\mathbf{I} - \boldsymbol{\mathcal{F}}\right)\sigma \mathbf{T}^4$$

where the diagonal matrices $\mathbf{A}$ and $\boldsymbol{\varepsilon}$ contain the nodal area and emittance, respectively and the REFs matrix $\boldsymbol{\mathcal{F}}$ is defined by Equation 1.33. For clarity, the notation $\mathbf{T}^4$ expresses the element-wise fourth power of the nodal temperatures. The element $K_{R,i,j}$ of the square matrix $\mathbf{K}_R$ is the radiative link between node i and node j. $\mathbf{K}_R$ is symmetric and the diagonal terms are the sum of all other elements on the same row/column such that the row/column sum is zero.

Finally, the surface heat fluxes are integrated in Equation 1.54 and the finite element formulation can be summarised in the form

$$\mathbf{C}\frac{\partial \mathbf{T}}{\partial t} + \left(\mathbf{K}_L + \mathbf{K}_C\right)\mathbf{T} + \mathbf{K}_R\mathbf{T}^4 = \mathbf{Q}_v + \mathbf{Q}_c - \mathbf{Q}_a \tag{1.55}$$

where $\mathbf{Q}_v$, $\mathbf{Q}_c$ and $\mathbf{Q}_a$ are the volume, convective and applied nodal heat flow rates. Convective heat exchanges are not considered in this work and $\mathbf{K}_C$ and $\mathbf{Q}_c$ will be discarded.

Some FEM based thermal analysis software include MAYA TMG and Thermal Desktop. FEM is used for the conductive link generation and the FE mesh serves as GMM [31]. The size of the mesh is again limited by the number of REFs, preventing the use of the structural analysis mesh.

1.4.4 Comparison

The problem of the ESATAN far-field or Thermica RCN methods is that it restricts the heat flow paths: they do not consider the effect of the adjacent nodes. The case of the rectangle divided into four nodes described in Figure 1.11 gives a good example of the problem. The far-field method as implemented in ESTAN-TMS gives the following conductive links:

$$GL_{12} = GL_{13} = GL_{24} = GL_{34} = \frac{1}{\frac{1}{1.69} + \frac{1}{2}} = 0.916$$

$$GL_{23} = \frac{1}{\frac{1}{2} + \frac{1}{2}} = 1$$

The global conductive heat transfer between nodes 1 and 4 is $0.916\,\mathrm{W\,K^{-1}}$ instead of $1\,\mathrm{W\,K^{-1}}$. It is underestimated by 8.4% because the FFM neglects the effect of the presence of node 3 when computing the conductive ling between 1 and 2, and vice-versa.

Another striking example is the *T-shape* configuration. Taking for instance three unit squares sharing a common edge in the form of a T as illustrated in Figure 1.12. All three squares will be connected to each other with the same conductive link computed independently by the far-field method: $GL_{12} = GL_{13} = GL_{23} = 1$. This incorrectly implies that the heat can flow from node 1 to node 3 through node 2 in addition to the direct path $1 \rightarrow 3$. In this case, this results in a 50% error. Adding a fourth square to form a cross shape will further increase the error to 100% since the heat can flow from node 1 to node 3 either directly or through node 2 or 4, thus incorrectly doubling the conductive link. This type of error can be easily corrected by considering only the link to the shared edge and the famous star-delta (Y-Δ) transformation used in electrical circuits invented

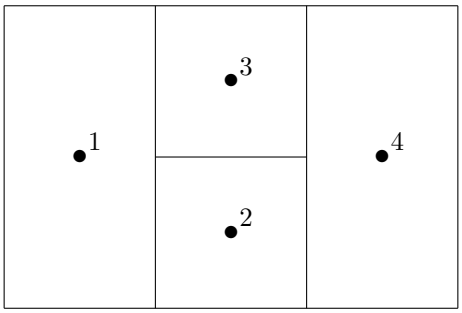

Figure 1.11 – Simple geometry consisting of a 2 m × 3 m rectangle divided into 4 LP nodes. Nodes 1 and 4 are 2 m wide × 1 m long and nodes 2 and 3 are 1 m × 1 m squares. The thickness is unitary as well as the thermal conductivity.

by Kennely in 1899 [180]. The RCN method implemented in Thermica does not generate this type of error because it inherently uses edges nodes. These two simple examples show the limitation of LP conductive link generation methods considering node pairs separately. It highlights the need for a global approach considering the nodes altogether.

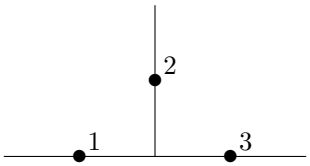

Figure 1.12 – *T-shape* configuration of three LP nodes sharing a common edge (side view). All three nodes are unit squares with unit thickness and unit thermal conductivity.

As mentioned in [31], another non-intuitive behaviour can occur with the LPM and the far-field conductive links computation method. Considering the L-shape configuration sketched in Figure 1.13 and imposing a 10 K temperature gradient between both extremities, the global heat flow rate is computed. The problem is analysed with both the LPM and FEM and two cases are studied: a regular mesh made of square elements or nodes and a trapezoidal mesh, as depicted in Figure 1.13. The reference solution was computed with SAMCEF and 270000 quadratic square elements (812401 nodes) and led to a heat flow rate of 3.908 544 W. The conductive links of the LP trapezoidal nodes are generated by the far-field method of ESATAN-TMS. Figures 1.13(a) and (c) show that with the FEM, the mesh geometry does not affect significantly the results. Comparing Figures 1.13(a) and (b) also shows that LPM and FEM gives similar results when the LP mesh is regular. However, the temperature profile obtained with trapezoidal nodes as given in Figure 1.13(d) clearly diverges from the other three results.

The convergence of the results when refining the FE or LP meshes is analysed in Figure 1.14.

The relative heat flow rate error with respect to the reference solution is plotted against the number of nodes (either LP nodes or FE nodes, not elements). The regular and trapezoidal FE meshes give the best results, better than the regular LPM mesh. The awkward behaviour is the one of the trapezoidal LPM mesh which does not converge.

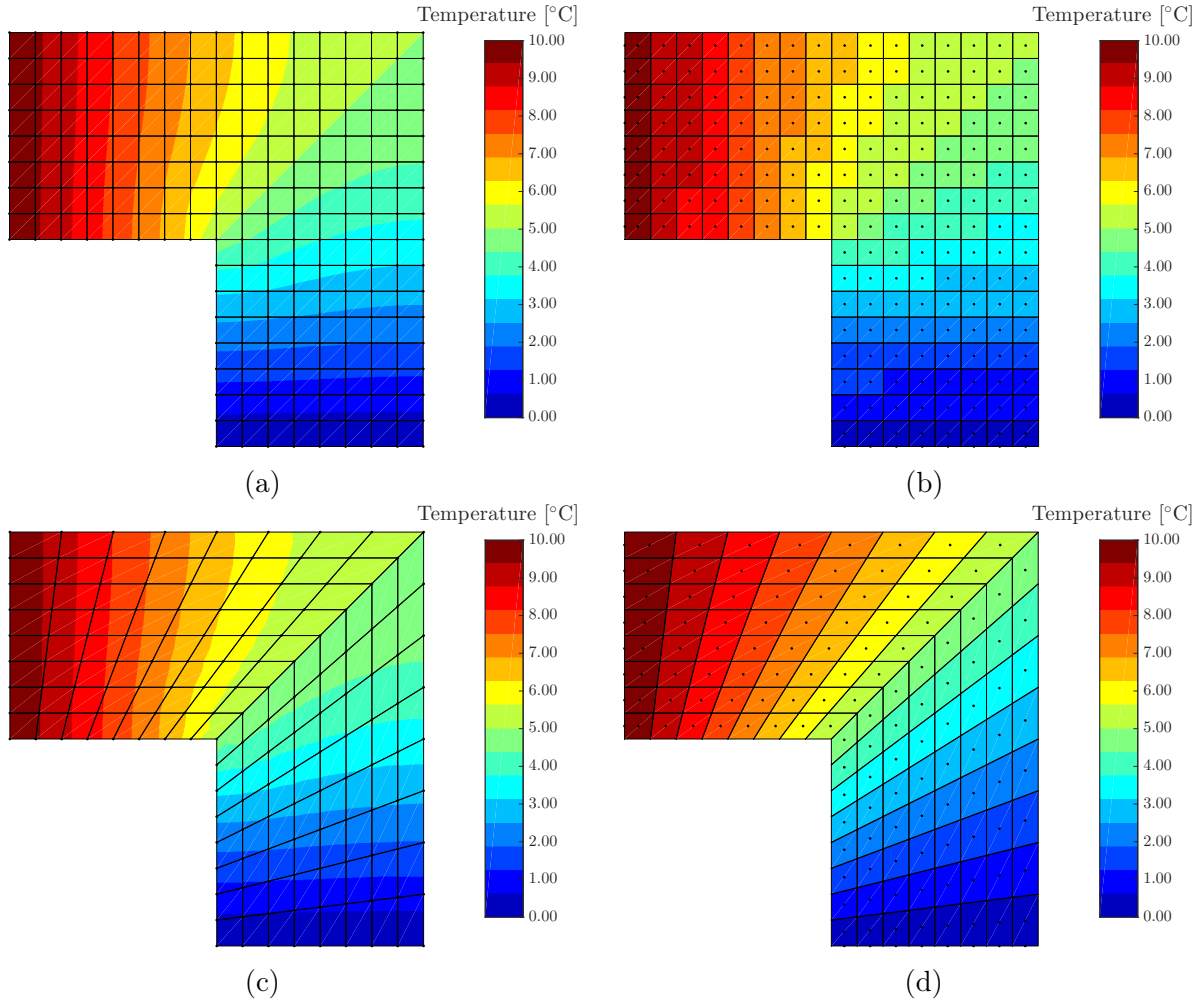

Figure 1.13 – L-shape modelling with square FE (a), square LP nodes (b), trapezoidal FE (c), trapezoidal LP nodes (d). A 10 K temperature gradient is imposed between the bottom right and top left edges.

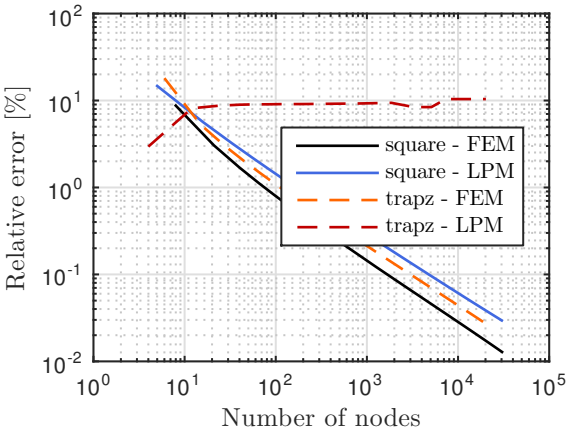

Figure 1.14 – Convergence of the heat flow rate error as a function of the mesh refinement for the problem described in Figure 1.13.

The trapezoidal LP mesh nevertheless gives better results with very few number of nodes. This is a consequence of the far field method that already relies on a fine FE mesh to generate the conductive link.

1.5 Thermal model reduction

The previous sections highlighted the fact that the FE structural mesh is not suitable for thermal analysis because it implies too many radiative links. Model reduction techniques may come to mind to overcome the problem. Over the years, in spite of the advances in computational techniques and numerical analysis, the increasing complexity of scientific and engineering problems gave rise to many reduction techniques to overcome the curse of dimensionality. One of the most influential model reduction technique initially developed for structural analysis is the sub-structuring or *Component Mode Synthesis* (CMS) technique introduced by Hurty [181, 182] in the 1960s. Most famous versions of CMS are that of Guyan [183] that includes only static response, Craig-Bampton [184] which consists in the extension of Guyan's method by including internal vibration modes with fixed interfaces or MacNeal [185] that is similar to Craig-Bampton's but uses free-vibration modes. These methods are still widely used today for linear systems. In [186], CMS is applied to the linear transient thermal analysis of a turbine disc and their method was improved in [187] and [188] to compute on-line thermal stresses taking into account non-linear effects caused by convection. They however relied on the off-line computation of the step response using the full model. In [189, 190], the linear reduced basis is enriched with, e.g., modal derivatives, but several iterations are required to converge to an adequate basis. There exist other modal bases including nodal temperature derivatives [191] or trajectory piecewise linearisation [192].

The *Modal Identification Method* (MIM) introduced in linear heat conduction [193, 194] relies on an optimisation problem to match the parameters of the reduced model to the full model, the reduced model being expressed following the same structure of equation as the full model written in its modal base. This modal superposition technique was applied to several problem in heat transfer [195, 196]. This technique was also applied to non-linear heat conduction in [197] and to heat conduction with radiative heat transfer boundary conditions in [198] but also requires the computation of the full model in the optimisation step.

Alternative projection methods were proposed in the literature. The *Proper Orthogonal Decomposition* (POD also known as the Karhunen-Loève decomposition (KLD) [199]) relies on the separation of the physical space and exploits snapshots of the detailed solution to derive an optimal basis corresponding to a specific load case. The POD was applied in numerous cases [200–206] including thermo-mechanical reduction with radiative boundary conditions [207]. POD was also applied to Monte Carlo simulation of radiation in [208] but only considers small variation of the input. In [209], the MIM and POD methods are compared on a non-linear diffusive system and give similar performances. In [210], POD is combined to the CMS method by replacing the component modes are by the proper orthogonal modes to generate a reduced model of a microelectromechanical system. This method however proved inaccurate when the input differs from the one used for the snapshot generation. To increase the accuracy of the reduced model response to

different inputs of a transient non-linear heat conduction model, Binion and Chen [211] use Krylov subspaces to enhance the POD.

Recently, *Branch Eigenmodes Reduction Method* (BERM) which relies on particular modes called branch modes [212–214] was developed. The particularity of the branch modes is that they do not depend on the boundary conditions. In [215], BERM is combined with CMS to overcome the difficulty of obtaining the branch basis with large models. While POD can be considered as an *a posteriori* model reduction technique, the *Proper Generalized Decomposition* (PGD) is viewed as an *a priori* model reduction technique[216–219] avoiding any knowledge on the detailed solution in contrast to the vast majority of POD based model reduction techniques. PGD was introduced in computational solid mechanics by Ladevèze *et al* in the mid 1980s [220–222] and also relies on the separated representation of the problem, like POD. In [223], PGD is applied to thermal model reduction in the frequency domain for real-time thermal process monitoring.

Other approaches were proposed such as Latin Hypercube sampling with Gaussian process regression of the detailed model [224] or the grey-box reduction method for non-linear systems [225].

All these techniques, either rely on the computation of the detailed solution or at least on the availability of the detailed model matrices, in particular the radiation matrix which is exactly what we want to reduce.

In the context of space instrument thermal design, thermal models are often exchanged to be integrated into higher level thermal models. Integrating detailed models would imply too large system models. Therefore, engineers build separate reduced models, manually fitting the reduced model to the detailed one with empiric parameter adjustments. Automatic LPM thermal model reduction is thus a key subject of research [226, 227]. Tools like TMRT (Themal Model Reduction Tool) were developed under supervision of ESA [228–232]. Again, these techniques are not suited to the present problem since they rely on the correlation with the detailed model.

1.6 Concluding remarks

After a brief introduction on space thermal modelling and radiative heat transfer, this chapter introduced the Monte Carlo ray tracing method. The main strengths of MCRT are its versatility and scalability. However, it requires a lot of rays to provide statistically meaningful REFs due to its low convergence rate. Increasing the accuracy by an order of magnitude implies multiplying the number of rays by two order of magnitudes. Chapter 2 proposes modifications to MCRT to improve the convergence rate and decrease the error.

Next, the basic concepts of the finite element and lumped parameter methods were reviewed in the context of space thermal analysis. LPM allows for a higher level of abstraction than FEM since it does not necessarily require an associated geometry (GMM). It is therefore well suited for system level preliminary and trade-off studies. However, the main weakness of the LPM lies in the computation of accurate conductive links which is exactly the strength of the finite element method thanks to its automatic meshing schemes and derivation of conduction matrices. LPM becomes less convenient for detailed design of subsystems that involve stringent requirements combined with complicated geometries calling for more detailed models and thermo-mechcanical analyses. A FEM reduction method associating the strengths of both methods is developed in Chapter 4.

Quasi Monte Carlo ray tracing for radiative heat transfer

2

Abstract

This chapter focuses on the development of a new sampling strategy to speed up the computation of radiative heat exchanges factors with ray tracing. Several quasi-Monte Carlo techniques are presented for direction sampling, namely isocell and hemisphere stratified sampling and Halton low discrepancy sequences. The combination with surface sampling is studied to achieve a global, robust 4-dimensional (surface + direction) sampling. The method is then applied to orbital heat fluxes computation. In particular, the planet focused sampling strategy is developed for planetary heat fluxes computation. This method avoids wasting rays by only tracing rays towards the useful part of the Earth.

2.1 Introduction

As described in Chapter 1, the backbone of MCRT is pseudo-random sampling of the unit hemisphere to derive ray directions and of the unit square to derive ray origins on the emitting surface. Chapter 1 also highlighted the low convergence rate κ of crude Monte Carlo. Even though it is independent of the dimensionality of the problem, the stochastic error is inversely proportional to the square root of the number of rays *i.e.* error $\delta \propto n_r^{-\kappa}$ with the convergence rate $\kappa = 0.5$ [150, 158, 159, 162].

Two types of techniques were introduced to overcome this drawback: variance reduction and quasi Monte-Carlo. For a comprehensive review of these techniques, we refer to the books of Niederreiter [47], Fishman [233] and Lemieux [46]. The main type of variance reduction method relies on auxiliary information in order to improve the naive Monte Carlo estimator. In the context of REFs computation, the closure rule is inherently obeyed (all rays are eventually absorbed) but the reciprocity rule is not. Since both $\mathcal{F}_{ij}$ and $\mathcal{F}_{ji}$ are computed independently, a-posteriori enforcing reciprocity with Equation 1.27 may help to reduce the error resulting from the crude Monte Carlo method. This REFs smoothing technique is detailed in Section 2.5.1.

The second major type of variance reduction technique, called stratified sampling, partitions the domain into strata, each stratum being sampled independently. This technique was introduced by Cochran in 1953 [234] and is largely used in the computer graphics community [48, 235]. Taking one sample per stratum is known as jittering in the computer graphics community [236–238]. To reduce clumping (when two or more samples are close to each other), half jittering was implemented in [239] as a simpler version of Cook's algorithm [236] and consists in sampling the point uniformly from the stratum but in half the stratum. In [240], adaptative stratified sampling is performed to generate more samples where the integrand exhibits more fluctuations. The generalisation of stratified sampling to higher dimensions is called Latin hypercube sampling, invented by McKay *et al.* [241]. Instead of dividing the unit hypercube $[0, 1)^d$ into n subvolumes with each dimension divided into $n^{1/d}$, Latin hypercube sampling provides simultaneous stratification in all dimensions, *i.e.* each dimension is divided into n strata. In thermal radiative heat transfer, Vueghs applied stratified sampling to the hemisphere to generate more uniform ray directions [53]. Each stratum in the method corresponds to the same view factor share of the hemisphere, but the strata do not exhibit the same shape, which can deteriorate the performances in particular configurations as it will be demonstrated in Section 2.2.5.

Besides variance reduction methods, quasi Monte-Carlo methods rely on samples more uniformly spread over the integration domain and generated from the so-called low-discrepancy sequences. Quasi Monte-Carlo is almost as old as Monte Carlo itself and the first article in which the expression *quasi-Monte Carlo method* appeared dates back to 1951 [242]. Compared to exactly uniformly spread samples (periodic lattice), low discrepancy sequences are less likely to produce unwanted aliasing artefacts. The most famous include Sobol [243] and Halton [244] sequences. Sobol is for instance used in the optical design software Zemax [245] or Synopsys'[1] LightTools. In the frame of radiative heat transfer, low discrepancy sequences were scarcely used. Halton sequence was used for directional sampling in [50] and for the computation of the view factor between two

[1]Synopsys is also the developer of the famous optical design software Code V.

squares (same as in Section 1.2.5) in [246]. Sobol sequence was also applied to directional sampling in reverse Monte Carlo [49]. In relatively low dimension problems such as the REF computation, Halton and Sobol sequences give similar results but Halton is usually preferred to Sobol due to its easier implementation [247].

The afore-mentioned methods focused more on the stochastic behaviour of MCRT, independently of the ray tracing technique. From the ray tracing perspective, many acceleration techniques were introduced in the other fields applying MCRT such as computer graphics. This includes hardware acceleration using, e.g., graphics processing units. In [248], a broad classification of software-oriented acceleration techniques is given, namely

- computing faster ray-face intersections by either
  - reducing the number of intersections to compute or
  - improving the intersection algorithm,
- firing fewer rays (stochastic behaviour of Monte Carlo method already presented above),
- firing generalized rays.

As mentioned in [53], generalized rays have a finite cross section and are not suited for the computation of radiative exchanges factors since their cross section becomes rapidly complex as they partially intersect surfaces. The two major techniques to reduce the number of intersections to compute are space subdivision and bounding volumes hierarchy. They both consist in creating a data structure and assigning each face of the model to a volume [161]. Propagating the rays from volume to volume avoids checking for intersection with all faces of the model by only considering the faces in the current volume.

This chapter focusses first on variance reduction and is organised as follows. In Section 2.2, the stratified and low-discrepancy methods are applied to the ray-direction sampling. In particular, the isocell stratification and Halton sequence are presented. At the end of the section, the methods are compared to classic random sampling and to Vueghs' stratified hemisphere method in the context of differential (point-wise) view factor computation. Extending the sampling to finite to finite exchange factors computation is tackled in Section 2.3. The combination of surface sampling with the direction sampling strategies is analysed. Orbital heat fluxes computation and planet sampling strategies are discussed in Section 2.4. Finally, Section 2.5 discusses the implemented ray tracing acceleration techniques: the ray-face intersection algorithm is presented as well as space subdivision. Conclusions of the present chapter are eventually drawn in Section 2.6.

2.2 Direction sampling strategies

As the view factor involves the integration over the unit hemisphere and over the emitting surface, this section first focuses on the stratified and low-discrepancy sampling of the unit hemisphere. Generating random[1] directions from a set of random points was introduced in Section 1.3.2 and the ray directions were given by directly sampling the polar and azimuthal angles as in Equation 1.45. An indirect but equivalent way

[1]From this point on, we imply by random numbers computer generated pseudo-random numbers.

to sample the unit hemisphere is based on sampling the underlying unit disc. It relies on Nusselt's analogy combined to Malley's method. The stratified and low-discrepancy sequence sampling strategies presented hereafter are based on this method.

2.2.1 Nusselt's analogy and Malley's method

Nusselt's analogy [249] states that the point-wise view factor between a point $\mathbf{p}$ on surface i and a surface j is equal to the area of its orthographic projection[1] divided by π (ratio of the projected area to the area of the unit disc). Based on Nusselt's analogy, Malley [161, 250] proposed a method to generate the ray directions by sampling the unit disc with uniformly distributed random numbers. After sampling the unit disc with uniformly distributed pseudo-random numbers, each point on the unit disc defines a direction by projecting it back to the unit hemisphere. Figure 2.1 depicts Nusselt's analogy and Malley's method.

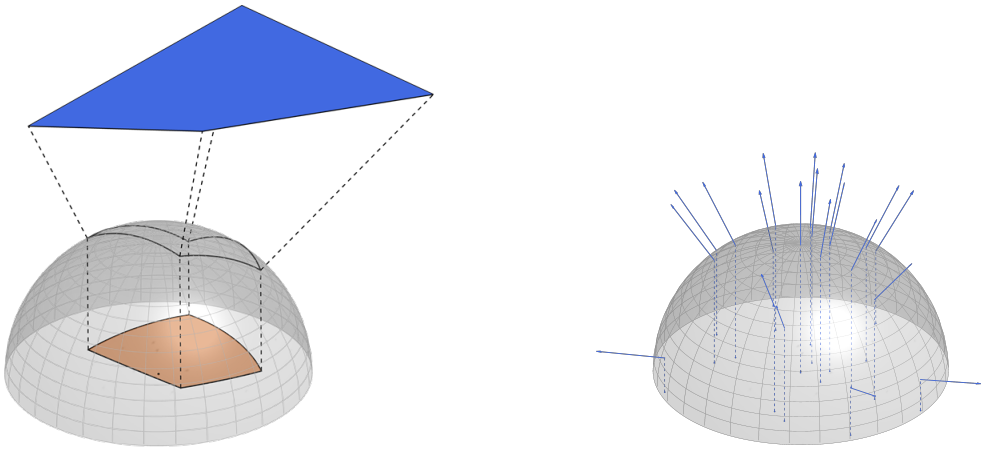

(a) (b)

Figure 2.1 – Nusselt's analogy with the orange surface being the orthographic projection of the blue surface (a) and Malley's method generating ray directions from the unit disc sample points (b).

2.2.2 Hemisphere stratified sampling

As introduced above, stratified sampling consists in dividing the integration domain into strata that are randomly sampled independently. Instead of generating strata directly over the unit hemisphere, the technique is applied to the unit disc thanks to Nusselt's analogy. The stratified hemisphere method developed in [53, 251] divides the hemisphere along its parallels and meridians by dividing the unit disc into concentric annuli of equal area then divided in equal sectors. Jittering is applied to avoid aliasing by picking one sample in each stratum.

The i^{th} annulus is defined by its inner and outer radii $\sqrt{(i-1)/n_{rad}}$ and $\sqrt{i/n_{rad}}$, respectively and the i^{th} sector defined by its minimum and maximum longitudes

[1] The orthographic projection is composed of a projection on the unit sphere centered on point $\mathbf{p}$ and an orthogonal projection onto the plane of tangent to the surface i and point $\mathbf{p}$

$(i-1)2\pi/n_{circ}$ and $i2\pi/n_{circ}$. n_{rad} and n_{circ} are the number of radial and circumferential divisions, respectively and the total number of rays is equal to $n_{rad}n_{circ}$.

The naive positioning of the sample within the stratum

$$\sqrt{(i-1)/n_{rad}} + \xi\Delta r \tag{2.1}$$

with $\Delta r = \sqrt{i/n_{rad}} - \sqrt{(i-1)/n_{rad}}$ and the uniformly distributed random number ξ is not correct since the radial position has to follow the cosine law also inside the stratum. The correct position of the i^{th} sample in the unit disc, corresponding to the j^{th} annulus and k^{th} sector is given by

$$\begin{pmatrix} r_i \cos\phi_i & r_i \sin\phi_i \end{pmatrix} \tag{2.2}$$

with

$$\begin{aligned} r_i &= \sqrt{\frac{j-\xi_{r_i}}{n_{rad}}} \\ \phi_i &= \frac{2\pi(k-\xi_{\phi_i})}{n_{circ}}, \quad j = 1,\ldots,n_{rad} \text{ and } k = 1,\ldots,n_{circ} \end{aligned}$$

and the uniformly distributed random variables ξ_r and ξ_ϕ. The i^{th} ray direction is then deduced by projecting the point back onto the hemisphere:

$$\mathbf{r}_i(\xi_{r_i},\xi_{\phi_i}) = \begin{bmatrix} r_i\cos\phi_i & r_i\sin\phi_i & \sqrt{1-r_i^2} \end{bmatrix} \tag{2.3}$$

$$= \begin{bmatrix} \sqrt{\frac{j-\xi_{r_i}}{n_{rad}}}\cos\left(\frac{2\pi(k-\xi_{\phi_i})}{n_{circ}}\right) & \sqrt{\frac{j-\xi_{r_i}}{n_{rad}}}\sin\left(\frac{2\pi(k-\xi_{\phi_i})}{n_{circ}}\right) & \sqrt{1-\frac{j-\xi_{r_i}}{n_{rad}}} \end{bmatrix} \tag{2.4}$$

Equations 2.4 and 1.45 are equivalent. Figure 2.2(a) illustrates the stratified hemisphere direction sampling process from the unit disc. Similarly to [53], the disc is divided equally along radial and circumferential directions and $n_{rad} = n_{circ}$.

This technique leads to a better convergence rate κ of the view factor (no multiple reflection) computation than crude MCRT: 0.75 instead of 0.5 [53]. However, Masset *et al.* showed in [252] that because the cells of the unit disc in the stratified hemisphere method have very different shapes and aspect ratios (although they have the same area), the method behaves poorly in some particular configurations as it will be presented in Section 2.2.5. This is the origin for the development of the isocell method to generate *strata* with more uniform shapes and aspect ratios.

Another minor drawback of the method is that the number of samples can not be chosen freely since n_{rad} and n_{circ} are integers. If $n_{rad} = n_{circ}$, the actual number of rays n_r might differ from the desired number of rays $n_{r,sh}$:

$$n_r = \left\lceil \sqrt{n_{r,sh}} \right\rceil^2 \tag{2.5}$$

2.2.3 Isocell stratified sampling

The need for a division of the unit disc into cells having both similar area and shape (aspect ratio) led to the development of the isocell method [52]. The method and properties of the cells are described in details in [252] and recalled here. As opposed to the

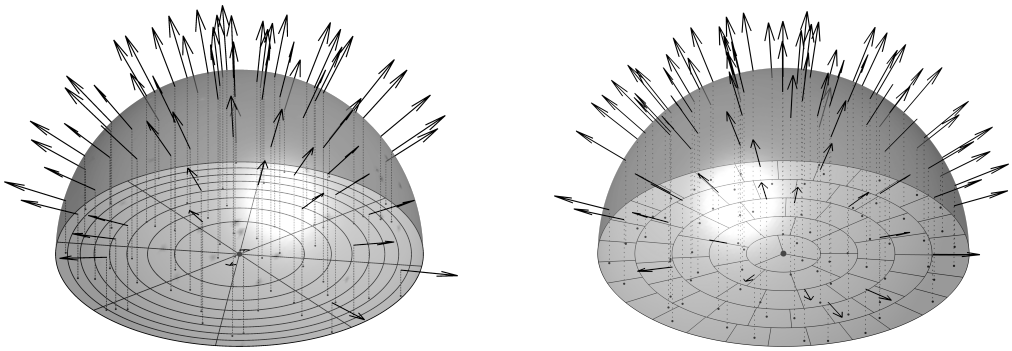

(a) (b)

Figure 2.2 – The stratified direction sampling generates one random sample in each cell that is projected back onto the unit hemisphere to determine the ray direction. Stratified hemisphere direction sampling strategy is shown in (a) with parallel and meridians divisions. The isocell method is illustrated in (b) with equally spaced annuli and increasing number of cells as the annulus radius increases.

stratified hemisphere where each annuli had the same area and was further divided in the same number of cells, the isocell method relies on equally spaced ring but the number of circumferential division increases linearly with the ring radius:

$$n_r = n_1 \sum_{i=1}^{n_a} (2i-1) = n_1 n_{rad}^2 \tag{2.6}$$

where n_{rad} is the number of annuli and n_1 the number of cells dividing the initial central annulus (actually a disc). Again, due to the discreteness of Equation 2.6, the required number of cells can not necessarily be achieved exactly. Provided a target number of rays $n_{r,is}$, the actual number of rays is given by injecting the actual number of annuli obtained by inverting Equation 2.6:

$$n_{rad} = \left\lceil \sqrt{\frac{n_{r,is}}{n_1}} \right\rceil \tag{2.7}$$

Figure 2.3 shows the oscillations of the relative error between the target number of rays and the actual one. Above 10^4 rays, the difference is always lower than 3%.

Like the stratified hemisphere method, one random sample is taken from each cell (jittering) and projected back to the unit hemisphere. The i^{th} sample, corresponding to the j^{th} annulus and k^{th} sector (now depending on j) is again given by Equation 2.2 where r_i and ϕ_i are now defined by

$$r_i = \frac{1}{n_{rad}} \sqrt{\xi_{r_i}(2j-1) + (j-1)^2}$$
$$\phi_i = \frac{2\pi(k - \xi_{\phi_i})}{n_1(2j-1)}, \quad j = 1, \ldots, n_{rad} \text{ and } k = 1, \ldots, n_1(2-j)$$

and the uniformly distributed random variables ξ_r and ξ_ϕ. The ray direction is then

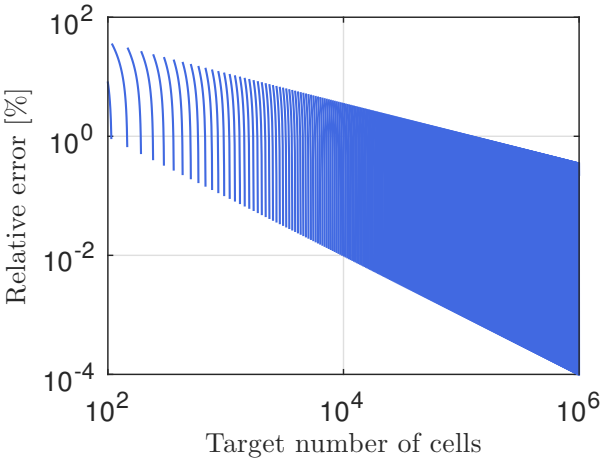

Figure 2.3 – Relative error between the actual number of rays and the target one with the isocell stratified sampling method.

deduced by projecting the point back onto the hemisphere with Equation 2.3 exactly as in the stratified hemisphere method.

It was shown that the cell shape factor β defined as the ratio between the square of the cell perimeter and its area was minimum for $n_1 = 3$ [252] ($\beta_{n_1=3} = 16.01$ while it is equal to 16 for a square and 4π for a disc). Figure 2.2 compares the two stratified sampling schemes with their respective unit disc partitioning.

2.2.4 Low-discrepancy sequence

Besides stratified sampling, replacing random numbers used in Equation 1.45 by low-discrepancy sequences also offers an improvement in the accuracy and convergence rate. The discrepancy measures the non-uniformity of a sequence of points distributed in the unit hypercube. A low-discrepancy sequence is such that the fraction of points lying in any subset of the unit hypercube is as close as possible to the volume of this subset. Halton sequence [244] is a natural generalization of the one-dimensional van der Corput sequence [253] developed in 1935, well before the advent of Monte Carlo techniques. Halton proposed to take the j^{th} prime number as base for the j^{th} coordinate. The i^{th} point $\mathbf{p}_i$ of the Halton sequence of dimension d is then given by:

$$\mathbf{p}_i = \left[\psi_{b_1}(i), \psi_{b_2}(i), \ldots, \psi_{b_j}(i), \ldots, \psi_{b_d}(i)\right]^\mathsf{T}, \; i \geq 1$$

where $\psi_{b_j}(i)$ is the j^{th} radical inverse function which defines the van der Corput sequence in base b_j:

$$\psi_{b_j}(i) = \sum_{k=0}^{l(j)} \frac{a_k(j,i)}{b_j^{k+1}}$$

The $a_k(j,i)$ coefficients come from the expansion of the integer i in base b_j:

$$i = \sum_{k=0}^{l(j)} a_k(j,i) b_j^k$$

with $l(j) = \left\lfloor \log_{b_j}(i) \right\rfloor$.

In very high dimensions, the Halton sequence requires large bases and leads to poor uniformity. To solve this problem, instead of using different bases for each dimension, Sobol [243] proposed to use the same base for all dimensions and apply a linear transformation (different for each coordinate) to the $a_k(j,i)$ coefficients before they are input into the radical-inverse function $\phi_{b_j}(i)$. In this context, the number of dimensions is limited to two for direction sampling and the faster Halton option is preferred. The Halton sequence generation algorithm is derived from [254, 255]. As suggested in [247, 255], a different portion of the sequence is extracted by discarding the first n_{skipped} points in the sequence that exhibit correlation among different dimensions. Leaping over and omitting n_{leap} points for every point selected also improve the quality of the point set. To generate multiple sequences and reduce their deterministic behaviour, n_{skipped} and n_{leap} are changed randomly for each run (or face).

If d is the dimension of the problem, low-discrepancy sequences offer a convergence in $\mathcal{O}\big((\log n_r)^d/n_r\big)$ which is asymptotically better than the $\mathcal{O}\big(1/\sqrt{n_r}\big)$ convergence of Monte Carlo method. As mentioned in [50], in practical applications, the convergence rate of quasi Monte Carlo methods generally lies between 0.5 and 1.

2.2.5 Comparison and application to point-wise view factors

Based on Nusselt's analogy, Figure 2.4 qualitatively compares the different sampling schemes of the unit disc. Stratified hemisphere and isocell and low discrepancy sequences visually give better results than crude random sampling. Clumping is observed in the stratified sampling based on meridians and parallels, *i.e.* it shows some concentration of the points near the centre of the unit disc. The stratified hemisphere also contains more samples than the specified target ($n_r = 300$).

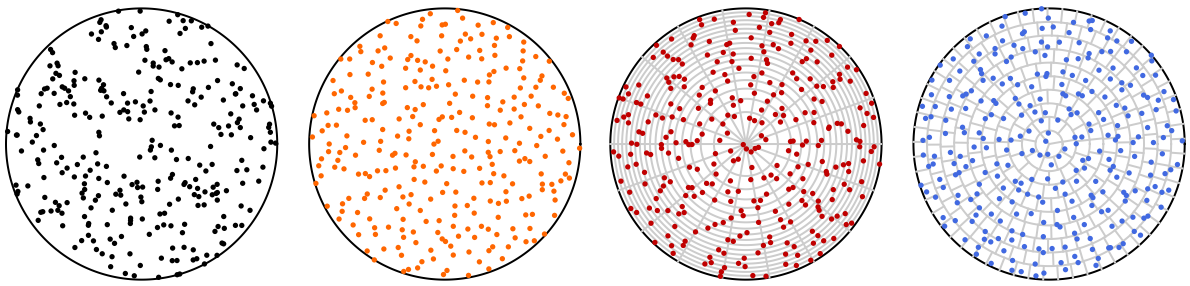

(a) (b) (c) (d)

Figure 2.4 – Unit disc sampling. (a) Random ($n_r = 300$); (b) Halton sequence ($n_r = 300$); (c) stratified hemisphere ($n_r = 324$), and (d) isocell ($n_r = 300$).

As mentioned in Section 2.2.2, the samples from the two stratified sampling methods presented above also have to follow the cosine law within each strata. To check that the samples follow the expected PDF and obtain more intuitive results, the change of variable $r = \sin\theta$ is performed to express the cosine law given by Equation 1.41 as a function of the radial position r of the samples within the unit disc:

$$p_{r,\phi}(r,\phi) = p_{\theta,\phi}(\arcsin r, \phi) \left| \begin{matrix} \frac{\partial\theta}{\partial r} & \frac{\partial\theta}{\partial\phi} \\ \frac{\partial\phi}{\partial r} & \frac{\partial\phi}{\partial\phi} \end{matrix} \right| = \frac{1}{\pi} \cos(\arcsin r) \sin(\arcsin r) \left| \begin{matrix} \frac{\partial\theta}{\partial r} & \frac{\partial\theta}{\partial\phi} \\ \frac{\partial\phi}{\partial r} & \frac{\partial\phi}{\partial\phi} \end{matrix} \right| = \frac{r}{\pi}$$

The marginal radial PDF becomes

$$p_r(r) = \int_0^{2\pi} p_{r,\phi}(r,\phi')d\phi' = \int_0^{2\pi} \frac{r}{\pi} d\phi' = 2r \tag{2.8}$$

and represents the density of the sample along the radius of the unit disc. Equation 2.8 shows that the marginal radial PDF exhibits the expected linear behaviour since a uniform sampling of the disc is sought and the differential area of a disc increases with the radius. Figures 2.5(a) shows the obtained marginal radial PDF with the naive sampling given by Equation 2.1 and Figure 2.5(b) shows the one obtained with the correct distribution in each cell. The naive stratified distributions exhibit a staircase behaviour, each step corresponding to the constant distribution within each cell. In Figure 2.5(b), all curves superimpose and follow the marginal radial PDF defined in Equation 2.8. The width of the steps in Figure 2.5(a) highlights the equally-spaced annuli of the isocell method compared to the decreasing width of the rings in the stratified hemisphere.

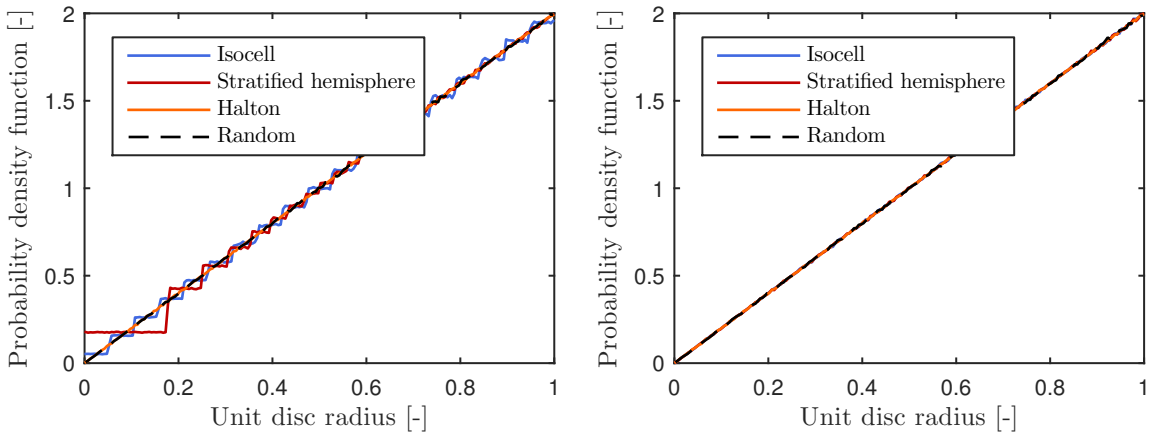

Figure 2.5 – Unit disc samples radial probability density function with $n_{\mathrm{r,is}} = n_{\mathrm{r,sh}} = 1000$: (a) without correction and (b) with correction. Randomness is smoothed by averaging over 10^4 runs.

A more quantitative assessment of the uniformity of the different sampling strategies is obtained by computing the Voronoi tessellation corresponding to the sample points on the unit disc. Based on a set of n points $\mathbf{p}_i$, the Voronoi tessellation consists in the partitioning of the plane into n regions or cells such that every point in region i is closer to $\mathbf{p}_i$ than any other point $\mathbf{p}_k$ [256]. The area of each Voronoi cell inside the unit disc is computed to assess the uniformity of the samples. The Voronoi cell area is normalized by dividing it by the theoretical cell area (unit disc area, π, divided by the number of samples). Figure 2.6(a) illustrates the Voronoi tessellation in the unit disc sampling and Figure 2.6(b) shows the distribution of normalized Voronoi cell areas. 10^4 disc sample

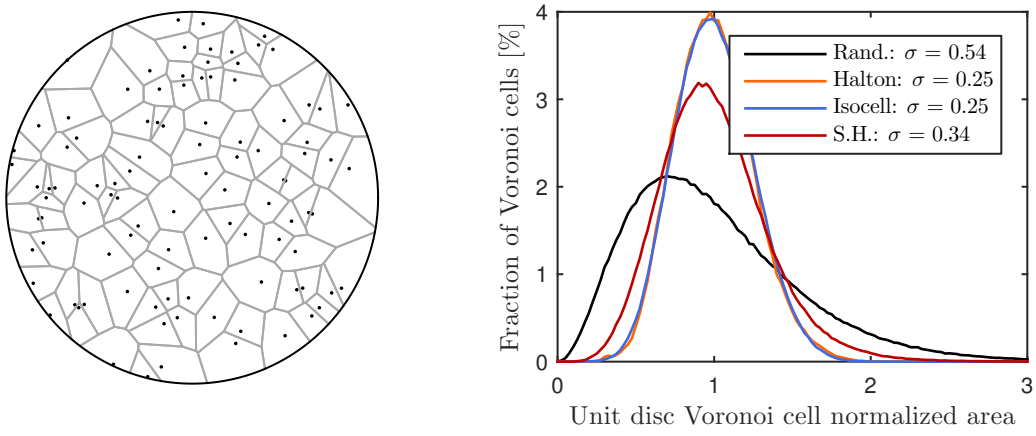

(a) (b)

Figure 2.6 – (a) Unit disc Voronoi cells for 100 random samples. (b) Voronoi normalized cell area distribution for 1000 samples and 10^4 runs.

points were generated and results averaged over 100 runs to smooth out the randomness of the process.

Random sampling leads to a standard deviation of the relative Voronoi cell area of 0.53 which is twice as much as those of isocell (0.25) and Halton (0.25) distributions. The stratified hemisphere lies in between with a standard deviation of 0.33. The results further attest of the better uniformity of the isocell and Halton schemes.

Computing the differential (point-wise) view factor between the infinitesimal surface dA_i and the finite surface A_j is probably the more representative way to assess the direction sampling schemes. Since there is no surface sampling, all rays are traced from the same emitting point corresponding to dA_i. The unit hemisphere and unit disc are simply centred on dA_i whose normal is aligned with the zenith axis of the hemisphere. Equation 1.36 gives the estimate of the view factor as the ratio between the number of rays intercepting A_j and the total number of rays traced (covering the whole hemisphere).

The first example considers A_j as a rectangle parallel to dA_i with the following coordinates of its four vertices $\mathbf{p}_i,\ i = 1 \dots 4$

$$\begin{bmatrix} \mathbf{p}_1 \\ \mathbf{p}_2 \\ \mathbf{p}_3 \\ \mathbf{p}_4 \end{bmatrix}^\intercal = \begin{bmatrix} 2 & 3 & 5 \\ -3 & 3 & 5 \\ -3 & -4 & 5 \\ 2 & -4 & 5 \end{bmatrix}^\intercal$$

The analytical value of the differential view factor is obtained by adding the contributions of each quadrant given separately by [36]:

$$F_{dA_i,A_j} = \frac{1}{2\pi}\left(\frac{X}{\sqrt{1+X^2}}\arctan\frac{Y}{\sqrt{1+X^2}} + \frac{Y}{\sqrt{1+Y^2}}\arctan\frac{X}{\sqrt{1+Y^2}}\right)$$

where X and Y are the ratio of the width and length of the rectangle to its normal distance from the differential area, respectively. In this case, $F_{dA_i,A_j} = 0.295578$.

Figure 2.7 shows the convergence of the error with the number of rays where each data point corresponds to the average of 1000 runs with the associated standard deviation. In practice and as introduced in Section 2.2.4, to reduce the deterministic behaviour of the low-discrepancy sequence, a different portion of the sequence is extracted by discarding the first $n_{skipped}$ points of the sequence and then picking only one point every n_{leap} points, $n_{skipped}$ and n_{leap} being changed randomly for each run (or face).

As expected, the convergence rate κ of crude Monte Carlo method tends to 0.5. All three alternative methods namely stratified hemisphere, isocell and Halton techniques present almost identical results. They all give lower mean error with similar standard deviations and a convergence rate approaching 0.75. A convergence rate of 0.75 means that each time the number of rays is multiplied by 2, the mean error is divided by 1.7 as opposed to 1.4 for $\kappa = 0.5$.

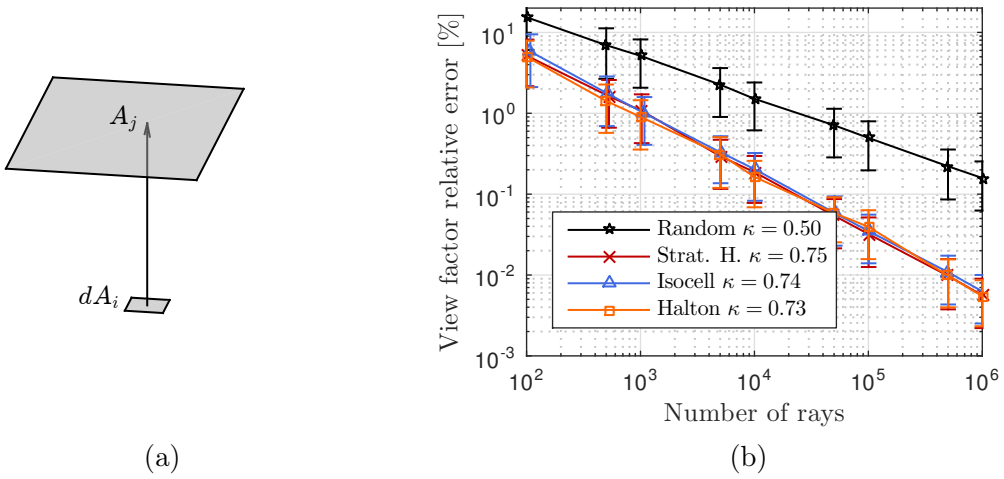

(a) (b)

Figure 2.7 – Convergence of the relative error on the point-wise view factor computed with the rectangle depicted in (a). The rectangle is parallel to the differential surface dA_i, located abovec. Results are averaged over 1000 runs. Error bars show the RMS value and standard deviation.

Even if all three methods exhibit a similar behaviour in this particular case, Figure 2.8 illustrates the weakness of the stratified hemisphere method developed in [53] and already identified in [252]. The far from exceptional geometrical configuration is described in Figure 2.8(a) where a small rectangle is located close to zenith. The coordinates of the rectangle vertices are

$$\begin{bmatrix} \mathbf{p}_1 \\ \mathbf{p}_2 \\ \mathbf{p}_3 \\ \mathbf{p}_4 \end{bmatrix}^{\intercal} = \begin{bmatrix} 0.5 & 0.6 & 5 \\ 0.1 & 0.6 & 5 \\ 0.1 & -0.6 & 5 \\ 0.5 & -0.6 & 5 \end{bmatrix}^{\intercal}$$

and the analytical view factor is $F_{dA_i,A_j} = 0.006004$. Figure 2.8(b) plots the average error and its standard deviation over 1000 runs as function of the number of traced rays. For the same number of rays, it is higher than in Figure 2.7(b) since the view factor is smaller, as predicted by Equation 1.46. Halton and isocell schemes again give almost identical results but even though its convergence rate is similar, the stratified hemisphere exhibits a higher error. This behaviour is explained by the large aspect ratio of the central strata,

providing good angular but poor radial stratification. A similar behaviour is observed when the surface is located far away from zenith because external strata are involved with poor angular and good radial stratification.

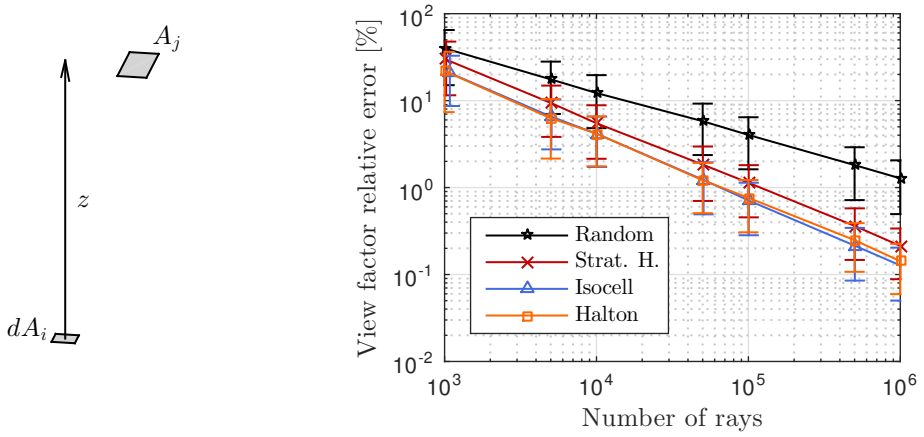

(a) (b)

Figure 2.8 – Convergence of the relative error on the point-wise view factor computed with a small eccentric rectangle parallel to the differential surface dA_i depicted in (a). Results are averaged over 1000 runs. Error bars show the RMS value and standard deviation.

The radial stratification of both stratified hemisphere and isocell methods also leads to unexpected behaviour in some particular configurations. Figure 2.9(a) describes the case of a disc A_j of radius $r = 1$ centred above the differential area dA_i at an altitude $z = 1.5$. Figure 2.9(b) presents the convergence results and Halton now proves to be superior to stratified strategies.

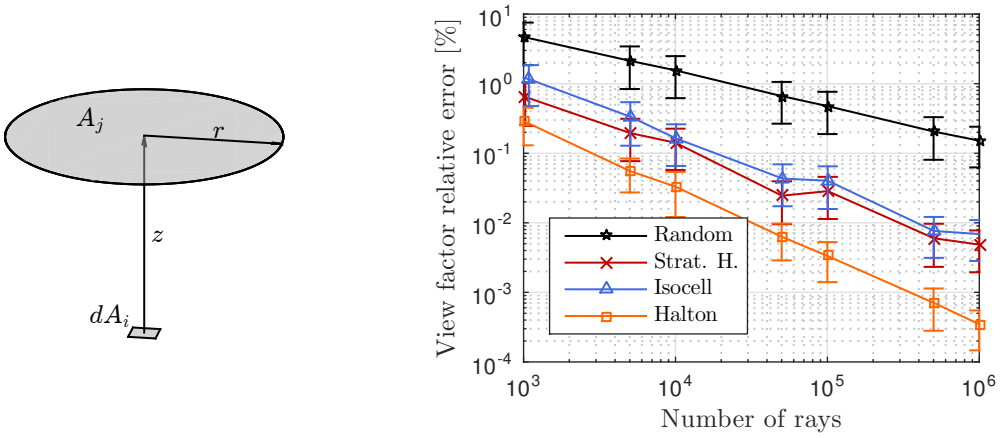

(a) (b)

Figure 2.9 – Convergence of the relative error on the point-wise view factor computed with a disc located right above the differential surface dA_i as depicted in (a). Results are averaged over 1000 runs. Error bars show the RMS value and standard deviation.

The poorer performance of the stratified schemes is explained by the radial stratification. Since A_j is circular, only one ring of the stratified unit disc affects the error. All rays

originating from rings with a lower radius automatically hit A_j and all rays originating from rings with a larger radius fall outside A_j. Inside the only effective radial stratum, the samples follow the same random distribution as the crude Monte Carlo therefore leading to poorer results. The irregular convergence behaviour is explained by the fact that some number of radial strata are more adequate than other, in particular if they match the solid angle subtended by A_j.

To assess the latter effect, Figure 2.10 finally presents the effect of the solid angle subtended by the disc. Halton low discrepancy sampling clearly gives better results except for very low apex angle for which the isocell exhibits a slightly lower error thanks to its first three pie-shaped strata ensuring at least three rays in the very small polar angle directions.

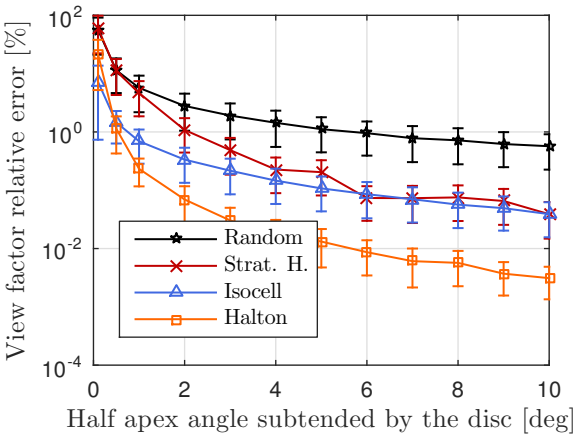

Figure 2.10 – Relative error on the point-wise view factor computed with a disc located above to the emission point as depicted in Figure 2.9(a). The radius of the disc is varied and expressed as the half apex angle of the solid angle subtended by the disc. Results are obtained with 10^6 rays and are averaged over 1000 runs. Error bars show the RMS value and standard deviation.

2.2.6 Conclusions

Different hemisphere sampling strategies were investigated to generate more uniformly distributed ray directions. Relying on Nusselt's analogy, two stratification techniques were applied to the unit disc, namely the stratified hemisphere developed in [53] and the isocell method introduced in [52]. A third alternative involving Halton low-discrepancy sequence was considered to replace directly the pseudo-random numbers of the crude MCRT. The performances of all three techniques were assessed through the computation of differential (point-wise) view factor with various geometries. The techniques presented similar performances in general cases but stratification schemes exhibited reduced performances in some particular geometrical configurations. Halton sequence proved to be the most robust strategy and gave higher accuracy and convergence rate than crude MCRT in all cases considered.

2.3 Surface sampling strategies

Section 2.2 focused on the hemisphere sampling and analysed three alternatives to crude Monte Carlo approach namely the stratified hemisphere, isocell and Halton low discrepancy sampling strategies. Halton sampling proved to be the most robust and effective technique and will be considered from this point on. In order to compute REFs between finite surfaces, the integration over the emitting surface needs to be carried out. Once again the integration is performed by sampling the emitting surface. At this stage, we face two options to couple the direction sampling to the surface sampling:

- either fire multiple rays with different directions per emission point (called origins),
- or assign each direction to a different surface sample and therefore have as many directions as origins.

The first approach offers in its turn two possibilities: either perform a different direction sampling for each origin, referred to as local direction sampling, or perform a global direction sampling to be distributed among the surface emission points. In this approach, another choice is needed to select the number of origins n_o from which is deduced the number of rays per origin for a given total number of rays n_r to be traced from the surface. The second approach is implemented in ESARAD where each ray has a random direction and a random emission point, leading to crude Monte Carlo.

Different surface sampling schemes are considered in this section namely

- random (Monte Carlo),
- Halton low-discrepancy sequence,
- uniform (lattice),
- Gauss-Legendre quadrature.

They all share the common property that they usually generate samples either in $[0, 1]$ or $[-1, 1]$. Like the hemisphere sampling, surface sampling thus requires a mapping step to project the samples from the square $[0, 1]^2$ or $[-1, 1]^2$ to the global cartesian coordinates of the model.

2.3.1 Random sampling and area preserving mapping

Natural coordinates usually range from 0 to 1 or from -1 to 1. The natural coordinates have the particularity to each take their extreme values (-1 or 0 and 1) at one vertex of the face and they vary linearly in between. Their range is particularly adapted to standard random number generation algorithms and quadrature rules were specifically derived in these ranges. Through a given set of interpolation functions ψ_i, two-dimensional natural coordinates (ζ, η) express the position of any point $\mathbf{p}$ in terms of the Cartesian coordinates of the vertices $\mathbf{p}_i$ $(i = 1 \dots n_v)$ of the considered surface:

$$\mathbf{p} = \sum_{i=1}^{n_v} \psi_i(\zeta, \eta)\mathbf{p}_i \tag{2.9}$$

Triangle

Choosing the correct set of interpolation functions to generate appropriate samples in triangles and quadrangles is not straightforward. For instance, Equation 2.10 defines a particular set of coordinates traditionally exploited to compute the ray-triangle intersection. For sample generation, this set is not suitable because they do not map the triangle from the unit square with two independent variables. Approximately half of the generated samples would need to be discarded to satisfy the condition $\zeta + \eta \leq 1$ and getting exactly n_r samples would require several iterations. This trial and error scheme is however the one used in ESARAD [159].

$$\mathbf{p} = (1 - \zeta - \eta)\mathbf{p}_1 + \zeta\mathbf{p}_2 + \eta\mathbf{p}_3 \tag{2.10}$$

The simple idea of folding the discarded samples back into the triangle can alleviate this problem but may produce clumping and undesirable effects thwarting the stratified or low discrepancy sampling objectives [161].

Instead, Arvo [257, 258] describes a general method to generate area-preserving mapping from the unit square $[0, 1]^2$ to any two-dimensional manifold. Area-preserving mapping is such that uniformly distributed samples over the unit square are uniformly distributed over the 2D-manifold and ensure that stratification (if any) is also preserved. A parametrisation mapping the surface from the unit square to the global Cartesian coordinate system $\psi_i(\zeta, \eta) : [0, 1]^2 \to \mathbb{R}^3$ is first selected, here in the case of a triangle:

$$\boldsymbol{\psi}(\zeta, \eta) = \begin{bmatrix} 1 - \zeta \\ \zeta(1 - \eta) \\ \zeta\eta \end{bmatrix} \tag{2.11}$$

An area-preserving parametrization $\psi_i'(\zeta', \eta')$ is then derived following Arvo's method by performing the change of coordinate:

$$\psi_i'(\zeta', \eta') = \psi_i(f^{-1}(\zeta'), g^{-1}(\zeta', \eta')) \tag{2.12}$$

where f and g are the cumulative distribution functions:

$$f(\zeta) \equiv \frac{\int_0^1 \int_0^\zeta J(u, v)dudv}{\int_0^1 \int_0^1 J(u, v)dudv} \tag{2.13}$$

$$g(\zeta, \eta) \equiv \frac{\int_0^\eta J(\zeta, v)dv}{\int_0^1 J(\zeta, v)dv} \tag{2.14}$$

$$\tag{2.15}$$

with J the pseudo-jacobian of the transformation from $(\zeta, \eta) \in \mathbb{R}^2$ to $\mathbb{R}^3$:

$$J(\zeta, \eta) = \left\| \frac{\partial \boldsymbol{\psi}}{\partial \zeta} \times \frac{\partial \boldsymbol{\psi}}{\partial \eta} \right\| \tag{2.16}$$

By definition, integrating J over the surface gives the area of that surface:

$$\int_0^1 \int_0^1 J(\zeta, \eta) d\zeta d\eta = A \tag{2.17}$$

In the case of the triangle with the interpolation functions of Equation 2.11, $J(\zeta, \eta) = 2\zeta A$ with A the area of the triangle. The inverse of the cumulative distribution functions $f(\zeta) = \zeta^2$ and $g(\zeta, \eta) = \eta$ have a closed-form expression and lead to the area-preserving parametrization:

$$\boldsymbol{\psi}(\zeta', \eta') = \begin{bmatrix} 1 - \sqrt{\zeta'} \\ \sqrt{\zeta'}(1 - \eta') \\ \sqrt{\zeta'}\eta' \end{bmatrix} \tag{2.18}$$

Figure 2.11 shows that this new set of interpolation functions allows the generation of uniformly distributed pseudo-random samples in the triangle through the uniform independent pseudo-random variables (ζ', η') in $[0, 1]^2$. The initial interpolation functions (Equation 2.11) lead to a denser distribution where the magnitude of J is lower.

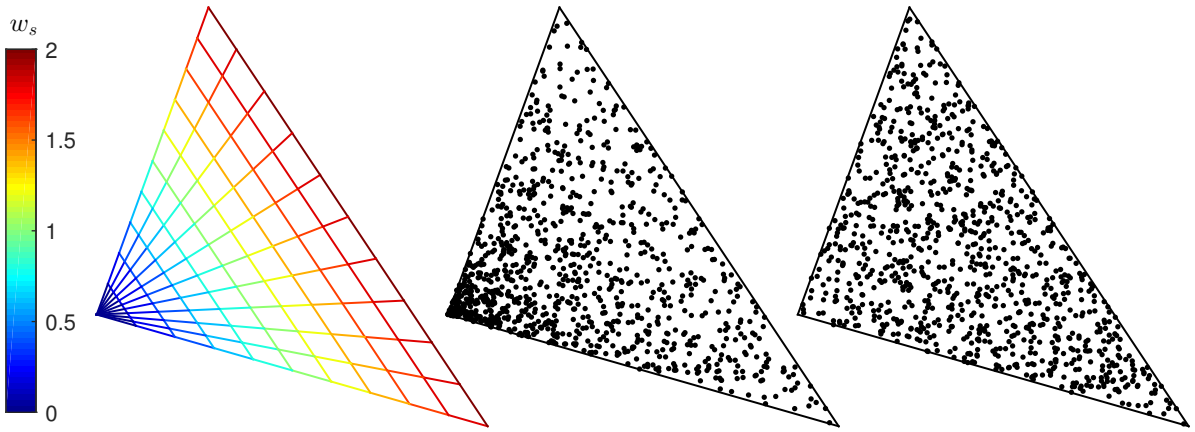

(a) (b) (c)

Figure 2.11 – (a) Magnitude of J/A. (b) Distribution of 1000 random samples in a triangle using the initial interpolation functions of Equation 2.11 and (c) using the area-preserving interpolation functions of Equation 2.18.

Quadrangle

In the case of a general quadrangle, the following interpolation functions are used

$$\boldsymbol{\psi}(\zeta,\eta) = \begin{bmatrix} \frac{1}{4}(1-\zeta)(1-\eta) \\ \frac{1}{4}(1+\zeta)(1-\eta) \\ \frac{1}{4}(1+\zeta)(1+\eta) \\ \frac{1}{4}(1-\zeta)(1+\eta) \end{bmatrix} \tag{2.19}$$

with the coordinates (ζ, η) varying from -1 to +1 and equal to zero at the quadrangle barycenter. This particular variation range (instead of 0 to 1) was chosen historically to facilitate the use of the standard Gauss integration formulas. The expression of J becomes more complex:

$$J(\zeta,\eta) = \frac{1}{8}\left\|\mathbf{p}_{31}\times\mathbf{p}_{42} + \zeta(\mathbf{p}_{43}\times\mathbf{p}_{21}) + \eta(\mathbf{p}_{32}\times\mathbf{p}_{41})\right\| \tag{2.20}$$

where $\mathbf{p}_{ij} \equiv \mathbf{p}_j - \mathbf{p}_i$. There is no closed-form expression of the inverse of the cumulative distribution functions f and g as defined in Equations 2.13 and 2.14. There is thus no simple area-preserving interpolation functions to directly generate uniformly distributed random samples over a general quadrangle. The alternative is to integrate $J(\zeta, \eta)$ in a weighting function w_s for each ray emitted from the i^{th} origin. Since $\int_{-1}^{1}\int_{-1}^{1} J d\zeta d\eta = A/4$ with A the area of the quadrangle, the weights of the i^{th} origin is defined as

$$w_s(\zeta_i,\eta_i) = \frac{4}{A}J(\zeta_i,\eta_i) \tag{2.21}$$

so that the average of the weighting function is 1:

$$\frac{1}{n_o}\sum_{i=1}^{n_o} w_s(\zeta_i,\eta_i) = 1$$

Figure 2.12 shows the magnitude of the weighting function in a typical quadrangle: it is linear in the natural coordinates but non-linear in the Cartesian coordinates. Similar to the triangle, the samples are more densely populated in the regions where J is small and inversely. This time, the non area-preserving mapping is balanced by weighting the rays with the value of J corresponding to their emission point, as performed in THERMICA [102].

In the case of a parallelogram $J(\zeta, \eta)$ simplifies to $A/4$ since both $\mathbf{p}_{43}\times\mathbf{p}_{21}$ and $\mathbf{p}_{32}\times\mathbf{p}_{41}$ are equal to zero. The mapping defined by Equation 2.19 becomes area preserving: $f(\zeta) = \zeta$ and $g(\zeta, \eta) = \eta$ and the weighting coefficients $w_s(\zeta_i, \eta_i)$ become all equal to 1.

ESARAD generates random samples inside quadrangles as it does for triangles: sampling is performed on the parallelogram enclosing the quadrangle and the points falling outside the quadrangle are removed. New points are added iteratively until the desired number is achieved [159].

To avoid weighting to correct the sampling non-uniformity, quadrangles can also be considered as two triangles and sampled separately with a number of samples proportional to their area. This final alternative is the one preferred.

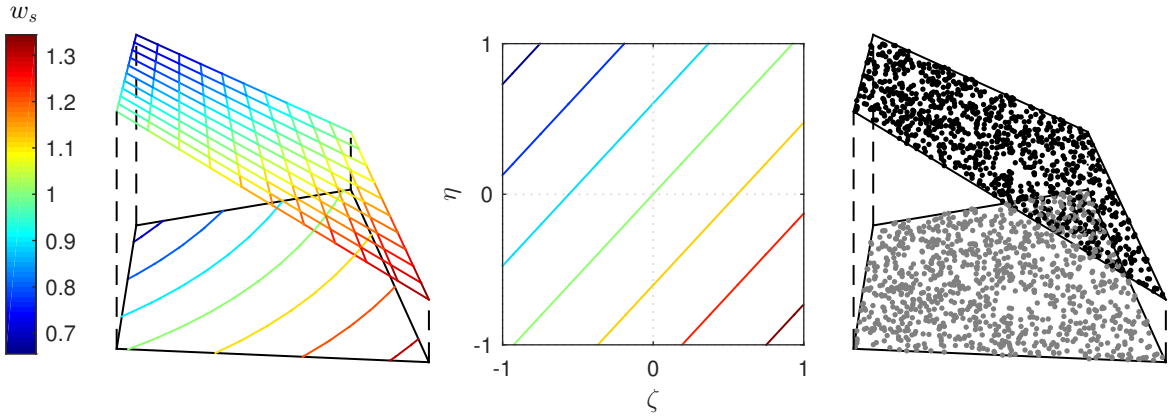

(a) (b) (c)

Figure 2.12 – (a) Magnitude of the weighting function w_s defined in Equation 2.21 in Cartesian coordinates, (b) in natural coordinates, (c) distribution of 1000 random samples.

2.3.2 Coupled and segregated low-discrepancy sequence

In the exact same manner as it was realised for direction sampling, quasi-random numbers like the Halton sequence can conveniently replace pseudo-random numbers to sample the surface. The first alternative consists in naively generating the surface samples independently from the directions and two separate two-dimensional samplings are carried out. The second alternative considers the four-dimensional integration involved in the view factor equation as a whole. The hemisphere and emitting surface are therefore sampled concurrently by a four-dimensional Halton sequence, two of which are used for the direction and the other two for the origin.

2.3.3 Uniform sampling

For random and Halton surface sampling, any number of origins can be used since both coordinates are sampled concurrently with the same, desired number of origins. Uniform spatial sampling relies on a grid and each direction needs to be divided into an integer number of samples. The aspect ratio of the face is taken into account so that the number of samples in each direction is proportional to its length. The aspect ratio a_r of the face is defined here as the ratio between its medians. The definition of the aspect ratio usually involves the ratio between its longer and shorter edges, but the medians are preferred in this case to avoid too much disparity in the density of samples. It is given by:

$$a_r = \frac{|\mathbf{p}_2 - \mathbf{p}_1| + |\mathbf{p}_4 - \mathbf{p}_3|}{|\mathbf{p}_3 - \mathbf{p}_2| + |\mathbf{p}_1 - \mathbf{p}_4|}$$

if the points $\mathbf{p}_i$ are ordered circularly. The actual total number of origins n_o is given by the product of the number of origins in each direction $n_{o,1} = \lceil \sqrt{n_{o,t} a_r} \rceil$ and $n_{o,2} = \lceil n_{o,1}/a_r \rceil$ with $n_{o,t}$ is the target number of origins. This explains why the actual number of origins $n_o = n_{o,1} n_{o,2}$ may be larger than the target number of origins $n_{o,t}$.

2.3.4 Gauss sampling

Gauss method for quadrature states that the integral of the function f weighted by w can be approximated by the weighted sum of the function value evaluated at n suitably chosen nodes x_i:

$$\int_a^b w(x)f(x)dx = \sum_{i=1}^{n} w_i f(x_i)$$

It even gives the exact solution if $f(x)$ is a $(2n-1)^{\text{th}}$ order polynomial. The optimal abscissae of the n-point Gaussian quadrature formula are the roots of the orthogonal polynomial for the same interval and weighting function. If the weight function $w(x)$ is 1 and the interval is $[-1, 1]$ then the x_i are the roots of the Legendre polynomials $P_n(x)$. They were first introduced in 1782 in the computation of the attraction of solids of revolution [259] and present n distinct roots between -1 and +1, arranged symmetrically about $x = 0$. In his original paper published in 1814 [260] and republished in [261], Gauss gave the weights and abscissae up to the seventh order with 16 decimals in the $[0, 1]$ interval. This was adapted to the $[-1, 1]$ range in [262] and [263] with errors for $n = 4$ [264, 265]. Gauss-Legendre integration points are given in natural coordinates conventionally varying from -1 to 1 for quadrilaterals and from 0 to 1 for triangles. Gaussian quadrature rules are extensively used in FEM to derive the element matrices presented in Section 1.4.3.

For quadrangles, a grid is formed in the unit square with Gauss-Legendre integration points and weights that are applied to each dimension. Like the uniform sampling, the grid is obtained by dividing each direction into a different number of points according to the quadrangle aspect ratio. Linear shape functions described in Equation 2.19 are then used to map the Gauss points from the natural coordinates to the model coordinates. Since the mapping from $[0, 1]^2$ to 3D is non area-preserving, the sample points further need to be weighted by the Jacobian associated to the mapping defined in Equation 2.20. For triangles, many specific quadrature rules were developed [266–268] and expressed in the natural coordinates (area or barycentric coordinates) of the triangle to respect its symmetry:

$$\boldsymbol{\psi}(\xi_1, \xi_2, \xi_3) = \begin{bmatrix} \xi_1 \\ \xi_2 \\ \xi_3 \end{bmatrix} \tag{2.22}$$

with $\xi_1 + \xi_2 + \xi_3 = 1$. The integration points in these coordinates and associated weights are based on the extensive compilation of quadrature rules made by Cools *et al.* [269, 270] as a continuation of the work of Stroud [271].

2.3.5 Comparison and application to surface-to-surface exchange factors

Figure 2.13 gives a visual representation of the four surface sampling strategies. Figures 2.13(a-d) and Figures 2.13(e-h) depict the quadrangle and triangle, respectively. For Gauss and uniform sampling strategies applied to the quadrangle, Figures 2.13(a) and (b) show the concentration occurring close to the bottom edge of the quadrangle, where the

mapping squeezes the samples together while it stretches the samples in the upper part. This effect is balanced by the Jacobian weighting of the samples. The number of samples in each direction is different through the effect of the aspect ratio. Halton and random sampling do not need this compensation since the quadrangle is split in two triangle to apply the area-preserving mapping defined by Equation 2.18. Uniform triangle sampling, Figure 2.13(f), clearly reveals the underlying sampling of the quadrangle from which the points falling outside the triangle are discarded.

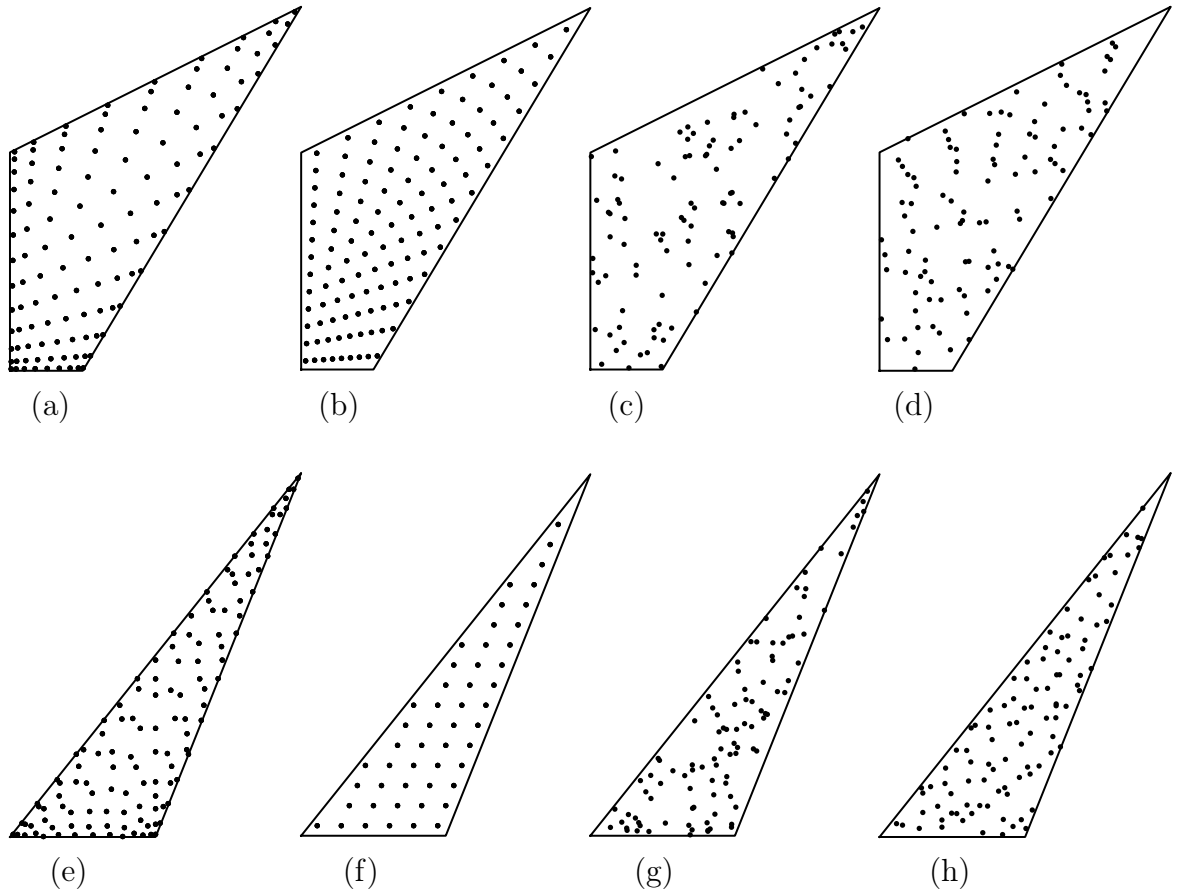

Figure 2.13 – Top: different sampling strategies for the quadrangle: Gauss (a), uniform (b), random (c) and Halton (d). Bottom: the same sampling strategies are applied to a triangle: Gauss (e), uniform (f), random (g) and Halton (h).

Now the coupling between the surface sampling and the direction sampling is analysed. To this aim, the computation of the REF between two quadrangles is considered. They are defined by their four vertices:

$$\begin{bmatrix}\mathbf{p}_{1,1}\\ \mathbf{p}_{1,2}\\ \mathbf{p}_{1,3}\\ \mathbf{p}_{1,4}\end{bmatrix}^{\mathsf{T}} = \begin{bmatrix}1 & 0 & 0\\ 6 & -1 & 0\\ 6 & 5.5 & 0\\ 1 & 5 & 0\end{bmatrix}^{\mathsf{T}} \quad \text{and} \quad \begin{bmatrix}\mathbf{p}_{2,1}\\ \mathbf{p}_{2,2}\\ \mathbf{p}_{2,3}\\ \mathbf{p}_{2,4}\end{bmatrix}^{\mathsf{T}} = \begin{bmatrix}0 & 0 & 0.5\\ 0 & 4 & 0.5\\ 0 & 5 & 4.5\\ 0 & -1 & 4.5\end{bmatrix}^{\mathsf{T}}$$

and are represented in Figure 2.14. The emittance of both faces is set to 0.8 with a

diffuse reflectance of 0.2 (no specular component). The reference solution, obtained with ESARAD by tracing 10^9 rays gives $\mathcal{F}_{12} = 0.0868$.

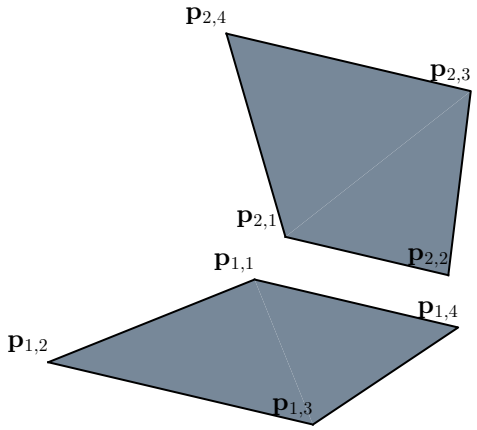

Figure 2.14 – Geometrical configuration of the two quadrangles.

Table 2.1 summarises the different combinations between direction and surface sampling strategies that are investigated. For random and Halton surface sampling, three alternatives are studied: two for which the number of origins is lower that the number of rays, the directions being generated locally for each origin or globally and distributed among the origins. The third alternative consists in assigning one direction to each origin ($n_o = n_r$). For uniform and Gauss surface sampling strategies, only the first two alternatives are studied because it becomes impractical to generate very high number of origins to match the number of rays.

Surface sampling	$n_o \stackrel{?}{=} n_r$	**Direction sampling**	Figure
Random	$n_o \neq n_r$	local	2.15(a)
	$n_o \neq n_r$	global	2.15(b)
	$n_o = n_r$	n.a.	2.16
Halton	$n_o \neq n_r$	local	2.17(a)
	$n_o \neq n_r$	global	2.17(b)
	$n_o = n_r$	segregated	2.18(a)
	$n_o = n_r$	coupled	2.18(b)
Uniform	$n_o \neq n_r$	local	2.19(a)
	$n_o \neq n_r$	global	2.19(b)
Gauss	$n_o \neq n_r$	local	2.20(a)
	$n_o \neq n_r$	global	2.20(b)

Table 2.1 – Surface and direction sampling schemes combinations.

Figure 2.15(a) gives the convergence results for the random surface sampling strategy combined with a local direction sampling. The number of origins plays a crucial role. There is a threshold below which the number of surface samples is too small to achieve a given accuracy. As the number of origins increases, the error saturation level decreases. From 10^3 to 10^6 rays, sampling the surface with 5 origins always produces higher error than

crude MCRT like ESARAD. For 1000 origins, the saturation level is about 0.7%. Compared to Figure 2.15(b) where the directions are sampled globally before being distributed among the origins, the results are almost identical and lead to the same conclusions.

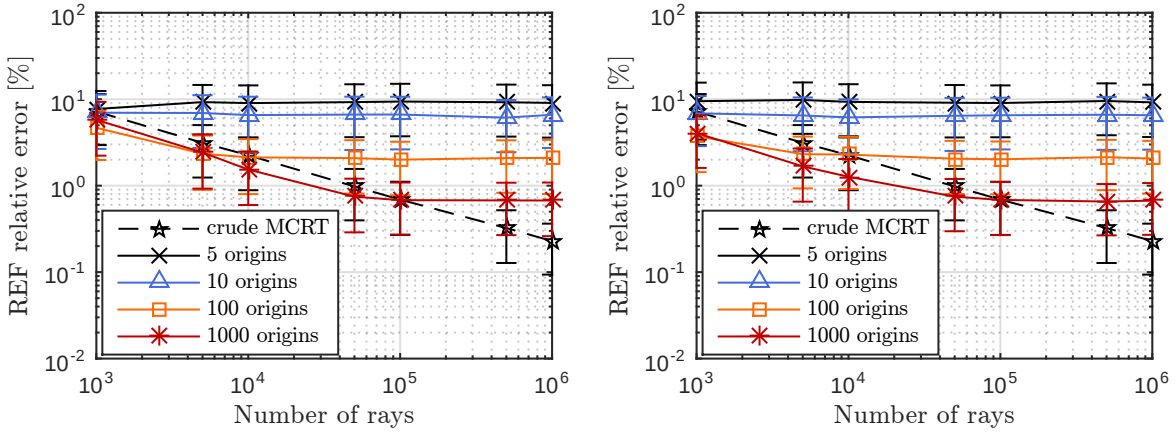

Figure 2.15 – Convergence of the relative error on the REF as a function of the number of rays for random surface sampling combined with local (a) and global (b) direction samplings. Results are averaged over 1000 runs and error bars give the RMS error and associated standard deviation.

As increasing the number of origins decreases the error saturation level, extending the philosophy to have one ray fired per origin leads to the results presented in Figure 2.16. The convergence curve is this time parallel to the one obtained with crude MCRT and almost a factor two below. This implies that to achieve a given accuracy, three times as less rays need to be traced.

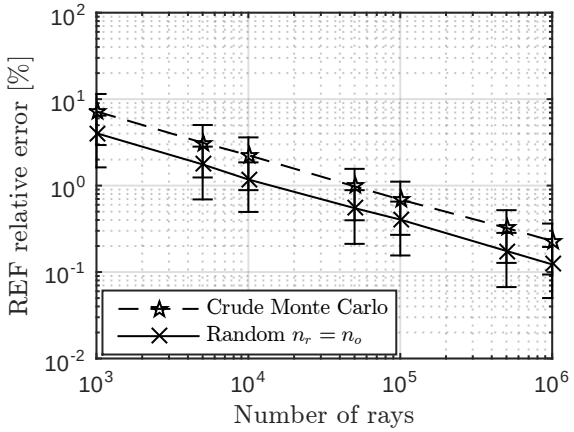

Figure 2.16 – Convergence of the relative error on the REF as a function of the number of rays for random surface sampling with one ray per origin. Results are averaged over 1000 runs and error bars give the RMS error and associated standard deviation.

Replacing the pseudo-random generator by a Halton low-discrepancy sequence to sample the surface gives the results given in Figures 2.17(a) and (b). The same saturation

behaviour is observed but for the same number of origins, the error saturation levels are lower. With 1000 origins and local direction sampling, the results are always better than crude MCRT, giving almost one order of magnitude improvement to achieve 0.2%. For a large number of origins, the convergence curve is no longer parallel to crude MCRT and the expected improved convergence rate becomes visible. The global sampling procedure generates unexpected non-smooth convergence behaviour with 1000 origins. This behaviour can be explained by the potential interaction between the two Halton sequences generated separately for direction and surface sampling. Scrambling each sequence could probably mitigate this effect for a slight increase of the generation time which remains negligible in whole the ray tracing process.

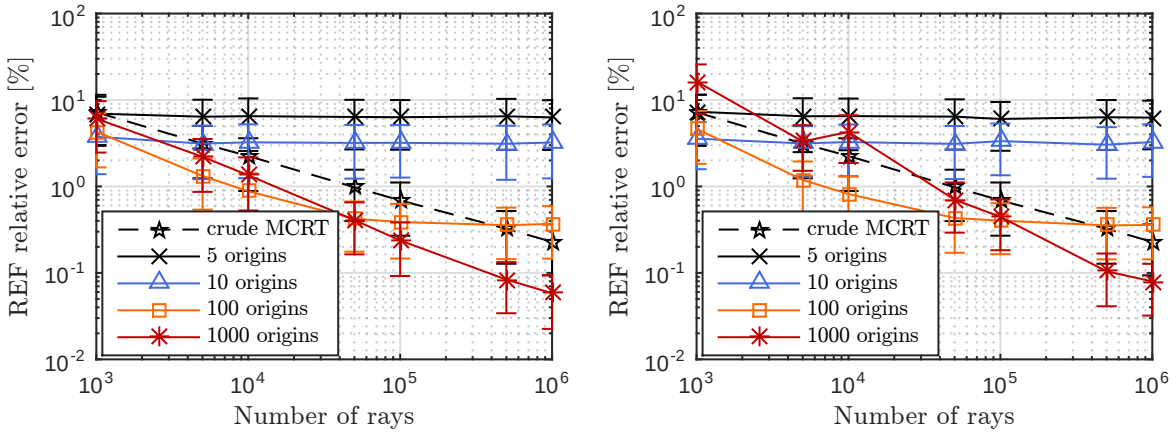

Figure 2.17 – Convergence of the relative error on the REF as a function of the number of rays for Halton surface sampling combined with local (a) and global (b) direction samplings. Results are averaged over 1000 runs and error bars give the RMS error and associated standard deviation.

Instead, the same philosophy associating one ray per origin is applied. First the two Halton sequences are generated independently, constituting the segregated method. The other alternative consists in generating the direction and surface samples through a unique 4-dimensional Halton sequence. This second approach is called the coupled Halton sampling. The resulting convergence curves are plotted in Figures 2.18(a) and (b), respectively. The segregated method gives results almost identical to those obtained with random sampling. Conversely, the coupled approach presents not only a lower error but also a better convergence rate as observed for the direction sampling alone. Achieving 1% accuracy requires 10 times as less rays as it does with crude MCRT. This gain further increases with the required accuracy because of the higher convergence rate.

In Figures 2.19(a) and (b), the quasi-random sampling of the surface is substituted by a uniform grid of equally spaced samples. Again, the same saturation behaviour is observed. Nevertheless, from random then Halton and this time uniform sampling, the saturation levels are progressively lowered with the local direction sampling scheme. Similar to Halton sampling, increasing the number of origins reveals the higher convergence rate observed in the direction sampling. With the global direction sampling approach, the convergence curves tend to superimpose for small number of rays and become parallel

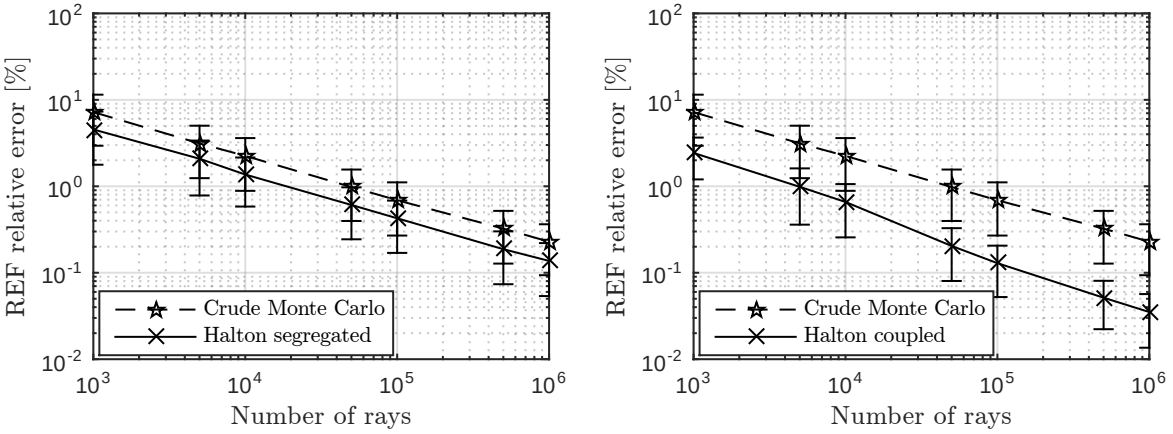

Figure 2.18 – Convergence of the relative error on the REF as a function of the number of rays for Halton surface sampling with one rays per origin. Results are averaged over 1000 runs and error bars give the RMS error and associated standard deviation.

to crude MCRT without any gain in the convergence rate when the number of origins increases.

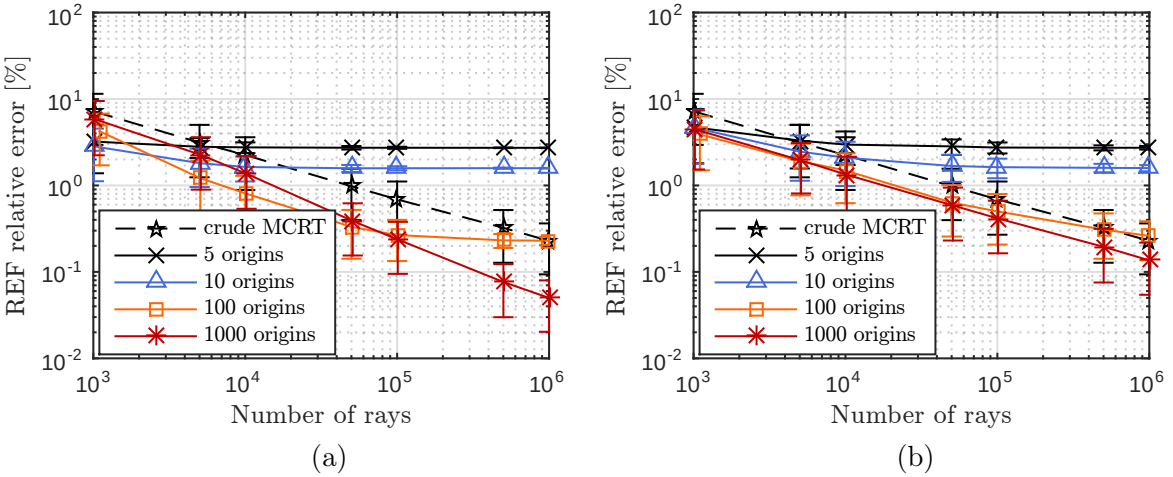

Figure 2.19 – Convergence of the relative error on the REF as a function of the number of rays for uniform surface sampling combined with local (a) and global (b) direction samplings. Results are averaged over 1000 runs and error bars give the RMS error and associated standard deviation.

Gauss surface sampling is the last option studied and the corresponding results are given in Figures 2.20(a) and (b). The saturation effect disappears almost completely except for very low number of origins ($n_o = 5$). With 10 origins, the method provides outstanding results: the required number of rays to achieve 0.2% accuracy (accuracy obtained with crude MCRT and 10^6 rays) is reduced by almost a factor 30. The drawback of this method is that increasing the number of surface samples generally shifts the convergence curves up since for a given number of rays, the number of directions decreases as the number of origins increases. Again, the global direction sampling approach gives

poorer results with all curves tending to superimpose and become slightly lower than and parallel to the crude MCRT convergence curve.

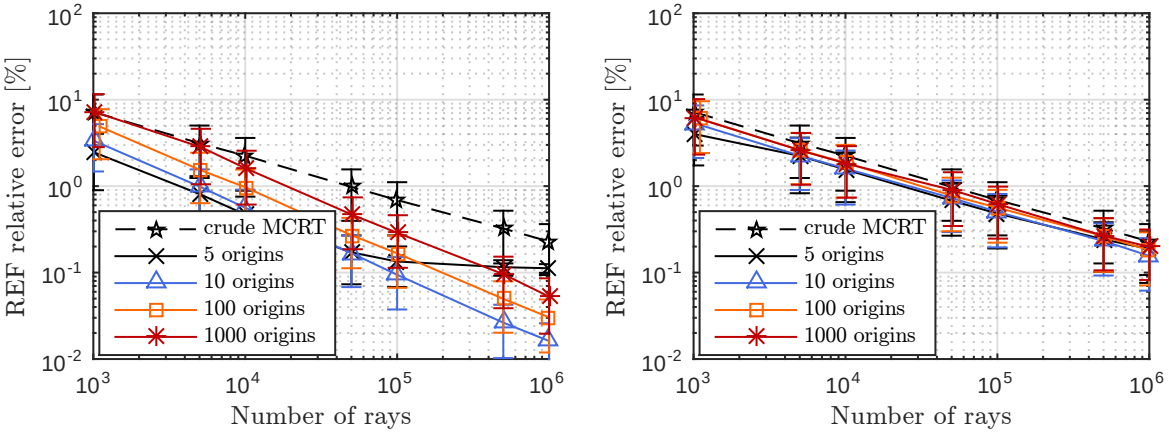

Figure 2.20 – Convergence of the relative error on the REF as a function of the number of rays for Gauss surface sampling combined with local (a) and global (b) direction samplings. Results are averaged over 1000 runs and error bars give the RMS error and associated standard deviation.

2.3.6 Influence of thermo-optical properties

In the previous example, the effects of multiple reflections are not investigated. To this aim, another geometrical configuration is considered to better highlight those effects. A third face is added to enable a non-zero REF between the first two quadrangles. Figure 2.21 presents the considered geometry with the following vertices:

$$\begin{bmatrix}\mathbf{p}_{1,1}\\ \mathbf{p}_{1,2}\\ \mathbf{p}_{1,3}\\ \mathbf{p}_{1,4}\end{bmatrix}^{\mathsf{T}} = \begin{bmatrix} 5 & -5 & 1.8\\ 4 & -1 & 0\\ -1 & -1 & 0\\ 0 & -5 & 1.8\end{bmatrix}^{\mathsf{T}} \text{ and } \begin{bmatrix}\mathbf{p}_{2,1}\\ \mathbf{p}_{2,2}\\ \mathbf{p}_{2,3}\\ \mathbf{p}_{2,4}\end{bmatrix}^{\mathsf{T}} = \begin{bmatrix} 4 & 0 & 0\\ 5 & 5 & 0\\ -1 & 4 & 0\\ 0 & 0 & 0\end{bmatrix}^{\mathsf{T}} \text{ and } \begin{bmatrix}\mathbf{p}_{3,1}\\ \mathbf{p}_{3,2}\\ \mathbf{p}_{3,3}\\ \mathbf{p}_{3,4}\end{bmatrix}^{\mathsf{T}} = \begin{bmatrix} 4 & -4 & 2\\ -1 & -3 & 2\\ -2 & 3 & 2\\ 5 & 4 & 2\end{bmatrix}^{\mathsf{T}}$$

In view of the previous results, only the coupled Halton and Gauss surface sampling (with $n_o = 10$ and $n_o = 50$) schemes are considered for the comparison. All quadrangles have the same thermo-optical properties with the infrared reflectance varying from 0.1 to 0.9, either diffuse or specular. In total, six cases are studied and compared in Figure 2.22. On the left, Figures 2.22(a), (c) and (e) show the convergence curves obtained with 0.9, 0.5 and 0.1 diffuse reflectance, respectively. The reference solution $\mathcal{F}_{12}$ is maximum for 0.5 reflectance ($\mathcal{F}_{12} = 0.0228$) and smaller for 0.1 ($\mathcal{F}_{12} = 0.0108$) and 0.9 ($\mathcal{F}_{12} = 0.0132$). A higher reflectance increases the number of multiple reflections. Because MCRT avoids branching and generates only one ray after a reflection or transmission, the direction of the diffusely reflected (or transmitted) ray is chosen randomly from Lambert's cosine law.

The benefit of the Halton direction sampling is thus weakened as it affects only emission. This phenomenon is observed as the Gauss and coupled Halton convergence curves

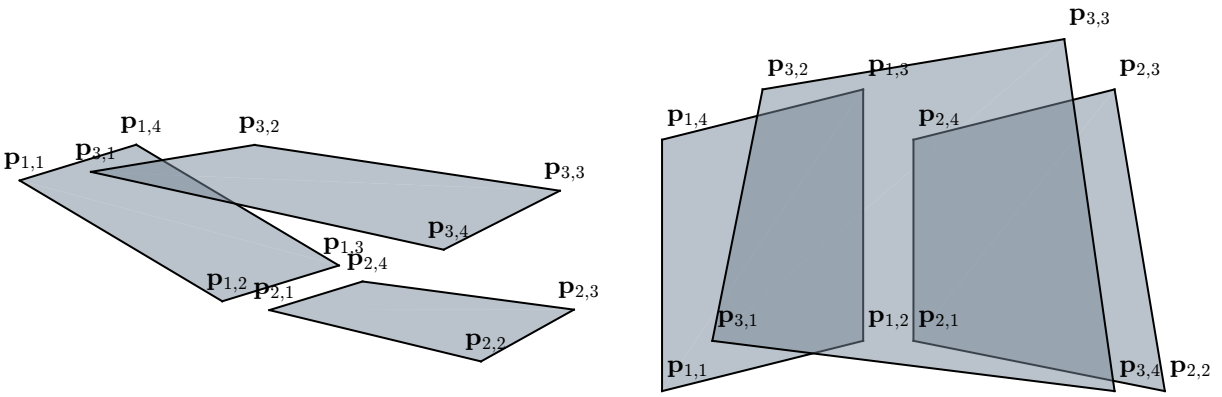

(a) (b)

Figure 2.21 – Geometrical configuration considered to assess the effect the thermo-optical properties. Three quadrangles are considered: two at the bottom and one on top to achieve a REF between the first two quadrangles through reflection on the third one. 3D view (a) and top view (b).

are almost parallel and closer to crude MCRT in Figures 2.22(a) and (c) than in Figure 2.22(e). Nevertheless, the coupled Halton strategy presents better results in all cases. The saturation effect of the Gauss surface sampling for small number of origins is only slightly visible below an error of 0.3% and with 10 origins in the 0.1 reflectance case shown in Figure 2.22(e). Figures 2.22(b), (d) and (f) located on the right present the results obtained in the specular case. Coupled Halton and Gauss sampling strategies are much more efficient in the specular case. The saturation of the convergence is however more present, again with 10 origins but this time more at high reflectance than low reflectance. While 50 origins give good results at lower error, sampling the surface with 10 origins offers better performances to achieve low to modest accuracy levels. In all six cases, the four-dimensional Halton sampling scheme exhibits better and more robust performances than the two-dimensional Halton direction sampling combined with Gauss surface sampling.

2.3.7 Conclusions

The effects of combining the Halton direction sampling to four different surface sampling strategies namely random, Halton, uniform and Gauss were investigated. In addition, three ways of distributing the directions among the surface sample points were analysed: local direction sampling for each origin with n_r/n_o directions per origin, global direction sampling with n_r directions distributed randomly among the n_o origins and finally the global strategy extended to one direction per origin with $n_r = n_o$. Their performances were compared to crude MCRT (random directions and origins) by computing the REF between two quadrangles. Two strategies emerged from this benchmark: Gauss spatial with local direction sampling and coupled directional-surface sampling with a 4-dimensional Halton sequence. While the former may present better performances for a suitably chosen number of origins, the latter brings robustness and better performances

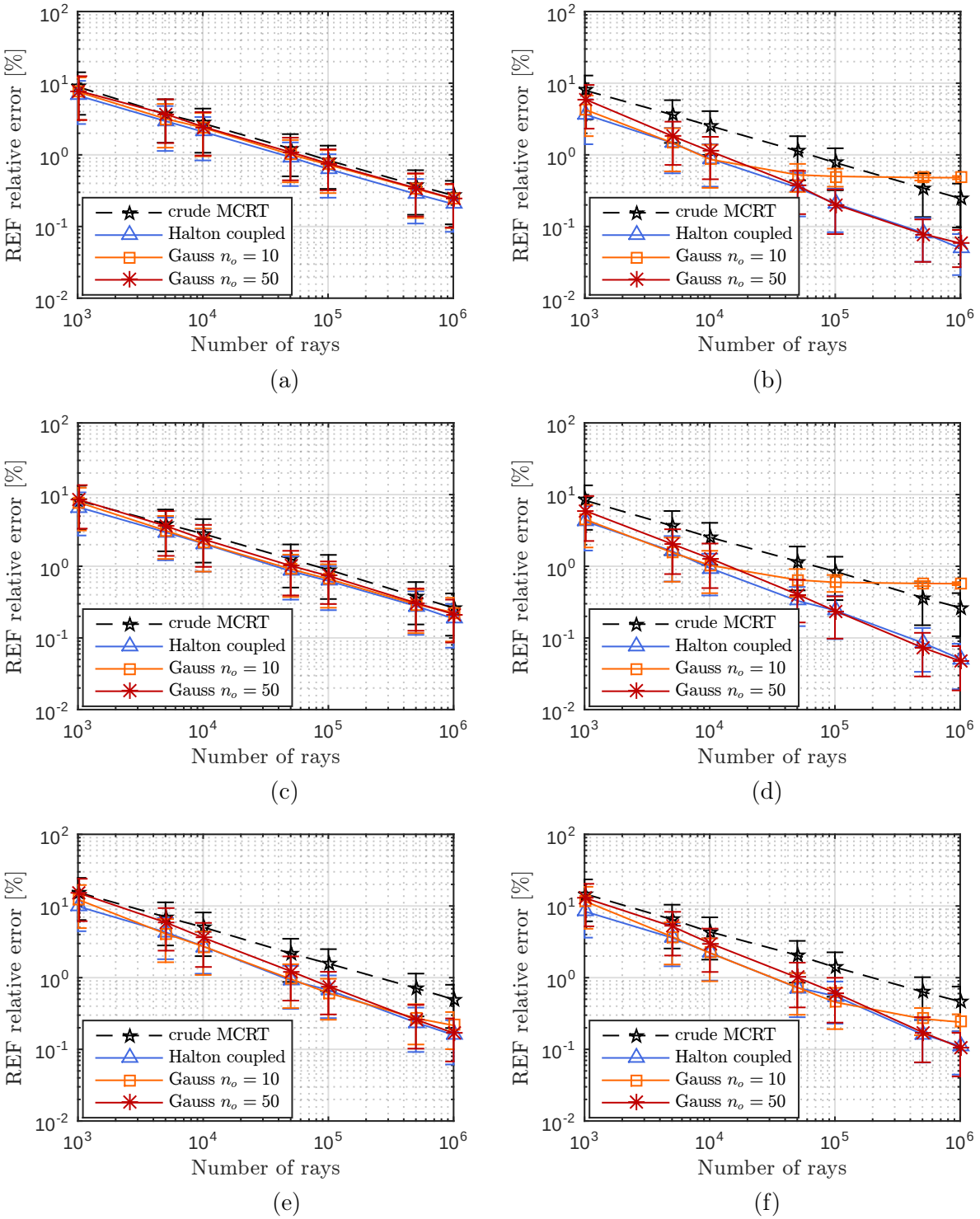

Figure 2.22 – The plots on the left (a,c,e) shows the convergence curves with 0.9, 0.5 and 0,1 diffuse reflectance, respectively. The plots on the right (b,d,f) shows the convergence curves with 0.9, 0.5 and 0,1 specular reflectance, respectively.

than crude MCRT in all cases. It was demonstrated that the number of origins is a strong driver of the achievable accuracy. It is configuration dependent as a low number of origins means a better sampling of the hemisphere which is more important for computing the REF between distant faces. For faces close to each other, spatial sampling is more important and having more origins is necessary to avoid saturation.

The effect of thermo-optical properties considering both diffuse and specular behaviour was also assessed and further demonstrated the robustness of the coupled Halton strategy.

2.4 Sampling strategies for orbital heat fluxes

2.4.1 Introduction

Ray tracing cannot only be applied to the computation the REFs but may also be useful to compute the orbital heat fluxes: the solar irradiation, the longwave radiation (mostly infrared) coming from the orbited body and the shortwave radiation coming from solar fluxes reflected onto the body (albedo). Figure 2.23 depicts the three orbital heat fluxes. Other planetary heat fluxes may need to be evaluated and specific algorithms were also implemented in the TSS[1] ray tracing engine to compute the infrared and albedo radiation coming from Saturn's rings for Cassini mission [272].

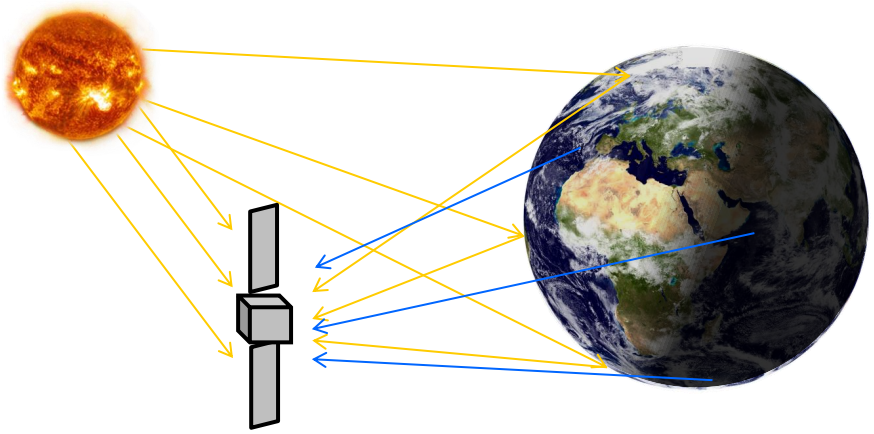

Figure 2.23 – Classical orbital heat fluxes comprising the direct solar heat flux (yellow rays), the planetary albedo (yellow rays) and IR (blue rays) heat fluxes.

To compute the solar heat flux, *shadow* rays are first traced from the considered face in the direction of the Sun. The rays are either parallel or uniformly distributed over the solar disc (about 32 arcmin angular diameter at 1 astronomical unit). If a ray hits another face in the model, its emission point is in the shadow of the hit face. Hence, the ray does not contribute to the illumination of the current face. If the ray does not intersect any other surface in the model, the emission point is irradiated with an energy

$$dQ_s = C_\odot \cos\theta dA$$

[1]Thermal Software System developed by Spacedesign Corp.

with θ the angle between the face normal and the Sun direction and $C_\odot$ the solar constant and dA the surface sample point area which is equal to A/n_r if origins are uniformly distributed over the face. The American Society for Testing and Materials (ASTM) developed in 2000 the ASTM-E490 standard to define the solar constant and spectral irradiance at 1 astronomical unit based on data from satellites, high-altitude aircraft, rocket sounding and ground-based telescopes [138]. The corresponding spectral irradiance was presented in Figure 1.5. The ASTM-E490 standard solar constant is $C_\odot = 1366.1\,\mathrm{W\,m^{-2}}$ and varies from $1412.5\,\mathrm{W\,m^{-2}}$ at perihelion (occurring during northern hemisphere winter) to $1321.7\,\mathrm{W\,m^{-2}}$ at aphelion (occurring during northern hemisphere summer).

If the irradiated face absorptance is not equal to one, the shadow ray is reverted and considered as coming from the Sun towards its initial surface sample point. It is then reflected or transmitted and propagated through the model to undergo absorptions, reflections and transmissions until extinction (based on a user-input relative energy threshold).

Computing planetary heat fluxes is much more complex for various reasons:

- the source solid angle is much wider,
- large variations of infrared and albedo may appear over the surface of the planet,
- emitted and reflected radiation may be anisotropic,
- longwave (infrared) and shortwave (albedo) radiation spectra may differ from the black-body and solar spectra, respectively.

Each planetary body exhibits different characteristics in its way it emits longwave radiation or reflects sunlight according to its surface and atmospheric properties, its distance to the Sun and its spinning rate. From the S/C point of view the albedo value mainly depends on the sunlit part of the body seen by the S/C. A common approximation assumes the albedo spectrum to be equal to Sun spectrum.

The reflectance of the Earth is known to be anisotropic. However, Knocke *et al.* [273] reason that since the Earth reflection is essentially diffuse at small solar zenith angles and more anisotropic at larger solar zenith angles as shown in [274], and since Earth elements at large solar zenith angles do not contribute much to the radiation pressure, Earth radiation pressure may be calculated to acceptable accuracy using a diffuse reflection model. European Space Standards [275] give values for the Earth: the average albedo coefficient $a_\oplus$ (surface reflectance) is 0.3 but can strongly vary between 0.05 over the ocean (without clouds) and 0.6 over high clouds and icecaps. The infrared radiation usually varies less over the surface of the body than the albedo. The diurnal variations of rapidly rotating bodies are often neglected and the body is sometimes assumed to be uniform in temperature and properties. The Earth is for instance often modelled as a black body at 288[K] [275]. Albedo and infrared do not only affect the thermal behaviour of the S/C but also affect the orbit of the spacecraft. Infrared and albedo models taking into account the latitude and seasonal dependence were thus developed for high-accuracy orbit predictions [273, 275]. In their model, solar reflectance (albedo coefficient $a_\oplus$) and infrared emittance of the Earth's surface are approximated by

$$a_\oplus = a_0 + a_1 P_1(\sin\phi) + a_2 P_2(\sin\phi)$$
$$\varepsilon_\oplus = e_0 + e_1 P_1(\sin\phi) + e_2 P_2(\sin\phi)$$

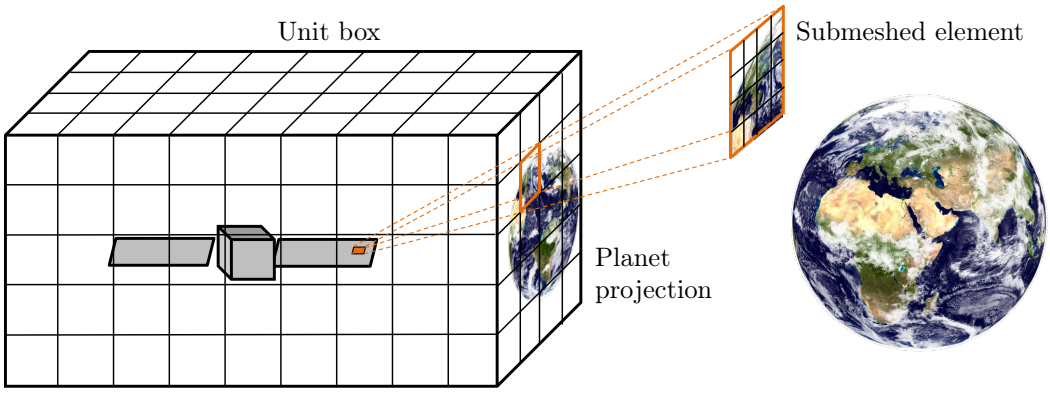

Figure 2.24 – Unit box surrounding the S/C used for albedo and infrared flux computation in ESARAD and Thermica. At each orbital position, the planet is projected onto the unit box and the intercepted elements are submeshed to compute the individual contribution of each submeshed area.

where $a_0 = 0.34$, $a_2 = 0.29$, $a_1 = c_{a,0} + c_{a,1}\cos(\omega(J_D - t_0)) + c_{a,2}\sin(\omega(J_D - t_0))$ with the date t_0, the orbital pulsation $\omega = 2\pi/365.25$, the equatorial latitude ϕ, the epoch Julian date J_D, the i^{th} Legendre polynomial P_i and the constants $c_{a,0} = c_{a,2} = 0$ and $c_{a,1} = 0.1$. The parameters for the emittance are similar: $e_0 = 0.68$, $e_2 = -0.18$ and $e_1 = c_{e,0} + c_{e,1}\cos(\omega(J_D - t_0)) + c_{e,2}\sin(\omega(J_D - t_0))$ with $c_{e,0} = c_{e,2} = 0$, $c_{e,1} = -0.07$.

In ESARAD [159, 276] and Thermica [102], the procedure to compute planetary heat fluxes is totally different from the one used to compute the solar heat fluxes described above. The method implemented in ESARAD and Thermica requires to compute the REFs in the visible part of the spectrum and introduces an artificial unit box surrounding the model and located at infinity. The box is regularly meshed and the visible and IR REFs are computed not only between the faces of the model but also with the faces of the unit box. Since the box is located at infinity, the S/C can be considered as a point and the direction of the ray exiting the S/C envelope is sufficient to determine which face of the unit box the rays fall into. Then, for each orbital position, the unit box element receives an albedo and infrared heat flux originating from a certain part of the planet that can be transferred to the appropriate model faces through the corresponding REFs. Figure 2.24 illustrates the method and shows the box surrounding the S/C that is meshed and onto which the planet is projected. Further details about the method are available in [159].

For the albedo, this method requires to compute and store the REFs in the visible spectrum but may take advantage of the already computed infrared REFs for infrared planetary fluxes. If the planet temperature is too far from the expected S/C temperature (very hot or very cold planets), the grey assumption may not be valid anymore as the infrared absorptance used in IR REFs may differ from the one corresponding to the planet temperature spectral range. If this is the case, REFs in the correct spectral range need to be re-computed anyway. If there is no articulated component onboard the S/C, the visible (and potentially IR) REFs need only to be computed once. If there is a relative movement between parts of the model, REFs anyway need also to be computed and stored for each orbital position. The drawback of the method is that many rays are wasted because

REFs computation involves sampling the whole hemisphere while planetary heat fluxes rays originate only from specific directions within the planet field of view.

Instead, we propose to apply the method used for solar heat fluxes. To this aim, the equations involved in the computation of planetary heat fluxes are recalled. They will serve to define the amount of energy carried by each ray as a function of its origin on the planet surface. The link between the origin on the directional sampling unit disc and the origin on the planet surface will be derived.

Even for a spatially-uniform, diffuse-grey model, very few closed-form solutions for the incident albedo and infrared heat fluxes incident to an arbitrary oriented satellite surface exist. In his papers from 1960s [277, 278], Levin considers a symmetric model corresponding to the case where the satellite's orbital plane contains the Sun vector. Another limitation in that model is that only the radiation reflected specularly is considered without any diffusely reflected radiation. Some closed-form solutions for the albedo heat flux but for a spherical satellite whose field of view does not intersect the terminator are available in [279] and [280].

Considering one face of the satellite instead of a spherical S/C complicates even further the analytical developments. The geometry of the problem is depicted in Figure 2.25. The chosen reference frame is such that the z axis points towards the centre of the satellite face under study, the y axis is defined as the cross product between the z axis and the surface normal and x axis completes the right handed coordinate system. Hence, the face normal $\mathbf{n}$ lies in the xz plane. The angle between the face normal and the nadir axis $(-z)$ is defined as γ (which also lies in xz plane). The Sun orientation is given by the vector $\mathbf{r}_{\oplus\to\odot}$ defined with the angles $\theta_\odot$ and $\phi_\odot$ which also define the terminator[1]. The portion of the planetary body seen by the spacecraft is a function of the altitude of the spacecraft and is defined by a cone of apex angle $\theta_{n,\max}$ centred on the satellite and directed towards the planet centre. Its limit is represented by the black small circle in Figure 2.25. From the plant point of view, this cone is defined by the angle $\theta_{z,\max}$. The intersection between the plane containing the face of the satellite and the planet is represented by the red small circle. In the reference frame, the two intersections between the footprint of the S/C field of view and face plane, if any, are located symmetrically on each side of the xz plane.

For infrared, the terminator equation is not needed and the problem consists in integrating over the portion of the Earth visible by the face, *i.e.* inside the black small circle and above the red one. For albedo, the terminator must further be taken into account to get the limits of integration. In [281, 282], the integral equations describing the albedo and infrared heat fluxes assume a planar surface but are solved numerically. In [283], the problem is simplified and the face normal is assumed to be coplanar with the Earth-Sun vector. In [284] the acceleration due to albedo and infrared radiation impinging the satellite is also computed numerically considering planar faces with non-uniform albedo and infrared heat fluxes that are expanded in spherical harmonics. More recently, numerical models integrating satellites measurement data were developed for CubeSats attitude determination with miniaturised sun sensors [285].

[1]The terminator or twilight zone is the line separating the sunlit area of a planet from its night side.

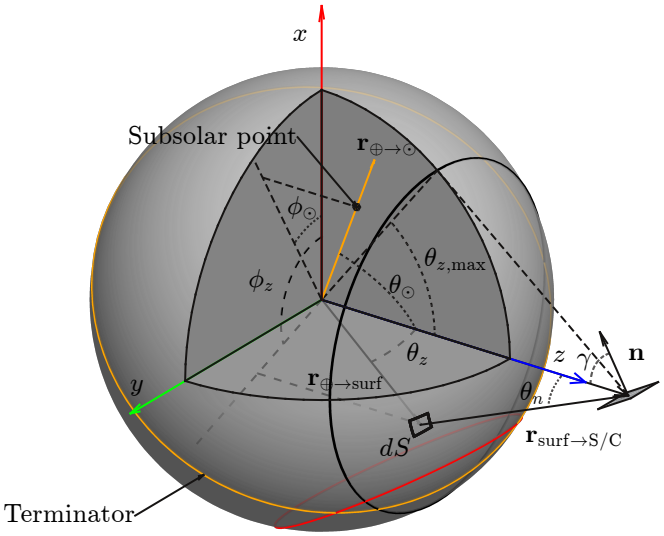

Figure 2.25 – Geometrical framework for the computation of albedo and infrared orbital heat fluxes. The yellow vector and great circle define the position of the Sun and terminator, respectively. The red small circle represents the intersection between the plane of the face and the Earth. The black small circle represents the limit of the portion of the Earth seen by the satellite.

2.4.2 Orbital heat fluxes key equations

Using the notation introduced in Figure 2.25, the solar power $dQ_\oplus$ [W] incident to the differential Earth surface dS is given by the extraterrestrial solar constant C_S multiplied by dS and by the cosine of the angle between the Sun direction vector $\mathbf{r}_{\text{surf}\to\odot}$ and the local vertical at dS location $\mathbf{r}_{\oplus\to\text{surf}}$.

$$dQ_\oplus = \hat{\mathbf{r}}_{\oplus\to\text{surf}} \cdot \hat{\mathbf{r}}_{\text{surf}\to\odot} C_\odot dS$$

where $\hat{\mathbf{r}} = \mathbf{r}/\|\mathbf{r}\|$. If $\hat{\mathbf{r}}_{\oplus\to\text{surf}} \cdot \hat{\mathbf{r}}_{\text{surf}\to\odot}$ is negative, dS is on the dark side of the Earth and $dQ_\oplus = 0$. $dQ_\oplus$ is then reflected by the Earth according to the albedo parameter $a_\oplus$ at the location of dS. As mentioned above, it is assumed here that the sunlight is reflected diffusely over 2π sr. Some portion goes into the S/C direction $\mathbf{r}_{\text{surf}\to\text{S/C}}$ and the heat flux incident to S/C surface defined by its normal $\mathbf{n}$ and coming from dS is given by:

$$dq_a = a_\oplus dQ_\oplus \frac{\hat{\mathbf{r}}_{\oplus\to\text{surf}} \cdot \hat{\mathbf{r}}_{\text{surf}\to\text{S/C}}}{\pi \left\|\mathbf{r}_{\text{surf}\to\text{S/C}}\right\|^2} \left(\mathbf{n} \cdot \hat{\mathbf{r}}_{\text{S/C}\to\text{surf}}\right)$$

The total albedo heat flux q_a [W/m^2] is obtained by integrating over the domain $\mathcal{S}_a$ corresponding to the sunlit Earth area within the field of view of the surface A:

$$q_a = \int_{\mathcal{S}_a} a_\oplus C_\odot \left(\hat{\mathbf{r}}_{\oplus\to\text{surf}} \cdot \hat{\mathbf{r}}_{\text{surf}\to\odot}\right) \frac{\hat{\mathbf{r}}_{\oplus\to\text{surf}} \cdot \hat{\mathbf{r}}_{\text{surf}\to\text{S/C}}}{\pi \left\|\mathbf{r}_{\text{surf}\to\text{S/C}}\right\|^2} \left(\mathbf{n} \cdot \hat{\mathbf{r}}_{\text{S/C}\to\text{surf}}\right) dS \tag{2.23}$$

The infrared heat flux q_e [W/m^2] is obtained by replacing the diffusely reflected part $a_\oplus C_\odot \hat{\mathbf{r}}_{\oplus\to\text{surf}} \cdot \hat{\mathbf{r}}_{\text{surf}\to\odot}$ by the planet infrared emissive power $\sigma\varepsilon_\oplus T_\oplus^4$:

$$q_e = \int_{\mathcal{S}_e} \sigma \varepsilon_\oplus T_\oplus^4 \frac{\hat{\mathbf{r}}_{\oplus\to\text{surf}} \cdot \hat{\mathbf{r}}_{\text{surf}\to\text{S/C}}}{\pi \left\|\mathbf{r}_{\text{surf}\to\text{S/C}}\right\|^2} \left(\mathbf{n} \cdot \hat{\mathbf{r}}_{\text{S/C}\to\text{surf}}\right) dS \tag{2.24}$$

Equations 2.23 and 2.24 integration domains $\mathcal{S}_e$ and $\mathcal{S}_a$ are defined as the intersection of the following subdomains:

- the spacecraft field of view $\mathcal{S}_1$ limited by the S/C FoV footprint $\mathcal{C}_1$ (black small circle in Figure 2.25),
- the surface of the planet $\mathcal{S}_2$ located above the face plane footprint $\mathcal{C}_2$ (red small circle in Figure 2.25),
- the sunlit side of the planet $\mathcal{S}_3$ limited by the terminator $\mathcal{C}_3$ (yellow great circle in Figure 2.25).

$$\mathcal{S}_a = \mathcal{S}_1 \cap \mathcal{S}_2 \cap \mathcal{S}_3 \tag{2.25}$$
$$\mathcal{S}_e = \mathcal{S}_1 \cap \mathcal{S}_2 \tag{2.26}$$

$\mathcal{S}_a$ and $\mathcal{S}_e$ both involve the integration limits $\mathcal{C}_1$, $\mathcal{C}_2$ and $\mathcal{C}_3$ that are developed in Appendix A, hence making the computation of q_e and q_a quite complex.

All vectors appearing in Equations 2.23 and 2.24 can be expressed through the angles $\theta_\odot \in [0, \pi]$ and $\phi_\odot \in [0, 2\pi[$ defining the Sun position, $\theta_z \in [0, \theta_{z,\max}]$ and $\phi_z \in [0, 2\pi[$ defining the position of dS from the planet point of view (zenith direction), $\theta_n \in [0, \theta_{n,\max}]$ and $\phi_n \in [0, 2\pi[$ from the S/C point of view (nadir direction), and the angle $\gamma \in [0, \pi]$ defining the face normal orientation away from the nadir direction. Expressed in function of the angles, the vector become

$$\begin{aligned}
\mathbf{n} &= \begin{bmatrix}\sin\gamma & 0 & -\cos\gamma\end{bmatrix} \\
\hat{\mathbf{r}}_{\text{surf}\to\odot} &\approx \hat{\mathbf{r}}_{\oplus\to\odot} = \begin{bmatrix}\cos\phi_\odot \sin\theta_\odot & \sin\phi_\odot \sin\theta_\odot & \cos\theta_\odot\end{bmatrix} \\
\hat{\mathbf{r}}_{\oplus\to\text{surf}} &= \begin{bmatrix}\cos\phi_z \sin\theta_z & \sin\phi_z \sin\theta_z & \cos\theta_z\end{bmatrix} \\
\mathbf{r}_{\text{surf}\to\text{S/C}} &= r_\oplus \begin{bmatrix}-\cos\phi_z \sin\theta_z & -\sin\phi_z \sin\theta_z & h_r - \cos\theta_z\end{bmatrix}
\end{aligned}$$

with h_r the ratio between the S/C distance to planet centre $r_\oplus + h$, h being the S/C altitude, and $r_\oplus$ the planet radius:

$$h_r = 1 + h/r_\oplus$$

Hence, the scalar products appearing in Equations 2.23 and 2.24 become

$$\begin{aligned}
\hat{\mathbf{r}}_{\oplus\to\text{surf}} \cdot \hat{\mathbf{r}}_{\text{surf}\to\odot} &= \sin\theta_\odot \sin\theta_z \cos(\phi_z - \phi_\odot) + \cos\theta_\odot \cos\theta_z \\
\hat{\mathbf{r}}_{\oplus\to\text{surf}} \cdot \hat{\mathbf{r}}_{\text{surf}\to\text{S/C}} &= \frac{h_r \cos\theta_z - 1}{\sqrt{1 + h_r^2 - 2h_r \cos\theta_z}} \\
\mathbf{n} \cdot \hat{\mathbf{r}}_{\text{S/C}\to\text{surf}} &= \frac{\cos\gamma(h_r - \cos\theta_z) + \sin\gamma \sin\theta_z \cos\phi_z}{\sqrt{1 + h_r^2 - 2h_r \cos\theta_z}}
\end{aligned}$$

Using the differential planet surface area definition

$$dS = r_{\oplus}^2 \sin\theta_z d\theta_z d\phi_z \tag{2.27}$$

Equations 2.23 and 2.24 are recast in terms of the angles:

$$q_a = \int_{\mathcal{S}_a} \frac{a_{\oplus} C_{\odot}}{\pi} dq_a(\theta_z, \phi_z) \tag{2.28}$$

$$q_e = \sigma \int_{\mathcal{S}_e} \frac{\varepsilon_{\oplus} T_{\oplus}^4}{\pi} dq_e(\theta_z, \phi_z) \tag{2.29}$$

where the planet parameters $a_{\oplus}$, $\varepsilon_{\oplus}$ and $T_{\oplus}$ may also vary over the planet surface and where the integrands are:

$$dq_a(\theta_z, \phi_z) = \frac{\cos\theta_{\odot}\cos\theta_z + \sin\theta_{\odot}\sin\theta_z\cos(\phi_z - \phi_{\odot})}{\big(1 + h_r^2 - 2h_r\cos\theta_z\big)^2}\big(h_r\cos\theta_z - 1\big) \\ \Big(\cos\gamma\big(h_r - \cos\theta_z\big) + \sin\gamma\sin\theta_z\cos\phi_z\Big)\sin\theta_z d\theta_z d\phi_z \tag{2.30}$$

$$dq_e(\theta_z, \phi_z) = \frac{\big(h_r\cos\theta_z - 1\big)\Big(\cos\gamma\big(h_r - \cos\theta_z\big) + \sin\gamma\sin\theta_z\cos\phi_z\Big)\sin\theta_z}{\big(1 + h_r^2 - 2h_r\cos\theta_z\big)^2} d\theta_z d\phi_z \tag{2.31}$$

With constant properties, and assuming the face plane does not intersect the Earth field of view ($\gamma < \theta_{z,\max}$) and all the visible portion of the planet is illuminated ($\theta_{\odot} < \pi/2 - \theta_{z,\max}$), the limits of integration are simply from 0 to $\theta_{z,\max}$ for θ_z and from 0 to 2π for ϕ_z. In that case, it becomes possible to integrate analytically Equations 2.30 and 2.31 to obtain simple closed-form expressions:

$$q_{a,\text{full}} = \frac{a_{\oplus} C_{\odot}}{16 h_r^3}\Bigg(2c_2\cos\gamma\cos\theta_{\odot}\big(4 + 2h_r c_1 - c_1^2 c_2\log(c_2/c_1)\big) + \\ \sin\gamma\cos\phi_{\odot}\sin\theta_{\odot}\big(4 + 2h_r - 6h_r^3 - c_3\log(c_2/c_1)\big)\Bigg) \tag{2.32}$$

with $c_1 = h_r - 1$, $c_2 = h_r + 1$ and $c_3 = 1 + 2h_r^2 - 3h_r^4$. The infrared heat flux reduces to the even more simple expression

$$q_{e,\text{full}} = \frac{\sigma\varepsilon_{\oplus} T_{\oplus}^4 \cos\gamma}{h_r^2} \tag{2.33}$$

If the spacecraft is located above the subsolar point ($\theta_{\odot} = 0$ and $\phi_{\odot} = 0$) and the face normal is pointing nadir ($\gamma = 0$), the albedo heat flux expression further reduces to:

$$q_{a,\text{full,sub,nad}} = \frac{a_{\oplus} C_{\odot} c_2}{8 h_r^3}\big(4 + 2h_r c_1 - c_1^2 c_2\log(c_2/c_1)\big) \tag{2.34}$$

2.4.3 Planet-focused sampling and derivation of ray energy

Like the finite-to-finite REF, 4-dimensional integration needs to be performed. Integration over the hemisphere generates ray directions originating from different regions of the planet, each direction corresponding to a different irradiance magnitude given by the integrand of Equations 2.23 and 2.24. Sampling the irradiated surface A attributes an origin to each direction associated with a differential area dA. Each ray thus carries an amount of energy equal to

$$dQ_a = a_{\oplus} C_{\odot} \left(\hat{\mathbf{r}}_{\oplus\to\text{surf}} \cdot \hat{\mathbf{r}}_{\text{surf}\to\odot}\right) \frac{\hat{\mathbf{r}}_{\oplus\to\text{surf}} \cdot \hat{\mathbf{r}}_{\text{surf}\to\text{S/C}}}{\pi \left\|\mathbf{r}_{\text{surf}\to\text{S/C}}\right\|^2} \left(\mathbf{n} \cdot \hat{\mathbf{r}}_{\text{S/C}\to\text{surf}}\right) dSdA \tag{2.35}$$

for an albedo ray and

$$dQ_e = \sigma \varepsilon_{\oplus} T_{\oplus}^4 \frac{\hat{\mathbf{r}}_{\oplus\to\text{surf}} \cdot \hat{\mathbf{r}}_{\text{surf}\to\text{S/C}}}{\pi \left\|\mathbf{r}_{\text{surf}\to\text{S/C}}\right\|^2} \left(\mathbf{n} \cdot \hat{\mathbf{r}}_{\text{S/C}\to\text{surf}}\right) dSdA \tag{2.36}$$

for an infrared ray. Both equations involve the planet differential surface dS defined in Equation 2.27 and involving the angle θ_z. Direction sampling is however performed from the S/C to the planet with the angle θ_n. The angle θ_z must be expressed in function of θ_n which itself depends on the random (or quasi-random) variable ξ_{θ_n}. The angles ϕ_z and ϕ_n are equal. Equation 2.27 is recast:

$$dS = r_{\oplus}^2 \sin\theta_z \frac{d\theta_z}{d\theta_n} \frac{d\theta_n}{d\xi_{\theta_n}} d\xi_{\theta_n} \frac{d\phi_z}{d\xi_{\phi_z}} d\xi_{\phi_z} \tag{2.37}$$

To avoid wasting rays falling outside the planet field of view, direction sampling is performed on the useful portion of the unit hemisphere centred on the S/C and directed towards the planet. Figure 2.26 shows in red the portion of the hemisphere corresponding to the solid angle subtended by the planet with an half apex angle $\theta_{n,\max}$.

Equation 1.42 describing how to obtain the polar angle samples from its corresponding uniformly distributed random variable is thus slightly modified to take into account the fact that the only part of the hemisphere is sampled, up to $\theta_{n,\max}$.

$$\theta_n = \arcsin\left(\sqrt{\xi_{\theta_n}} \sin\theta_{n,\max}\right) = \arcsin\left(\frac{\sqrt{\xi_{\theta_n}}}{h_r}\right) \tag{2.38}$$

since $\sin\theta_{n,\max} = \cos\theta_{z,\max} = 1/h_r$. The derivatives $\frac{d\theta_n}{d\xi_\theta}$ and $\frac{d\phi_z}{d\xi_\phi}$ are derived from Equations 2.38 and 1.43, respectively

$$\frac{d\phi_z}{d\xi_{\phi_z}} = 2\pi \quad \text{and} \quad \frac{d\theta_n}{d\xi_{\theta_n}} = \frac{1}{2\sqrt{\xi_{\theta_n}(h_r^2 - \xi_{\theta_n})}} \tag{2.39}$$

To derive $\frac{d\theta_z}{d\theta_n}$ and $\sin\theta_z$ in terms of θ_n, the intersection between the ray and the Earth's surface is computed. The local coordinate system z, x' corresponding to the $x-z$ plane rotated by the angle ϕ_z around z and containing the vectors $\hat{\mathbf{r}}_{\oplus\to\text{S/C}}$ and $\hat{\mathbf{r}}_{\oplus\to\text{surf}}$ is defined. In this coordinate system, the origin of the ray coming from the surface of the Earth $z_{\text{surf}}, x'_{\text{surf}}$ is determined by equating equations of the ray and the Earth surface:

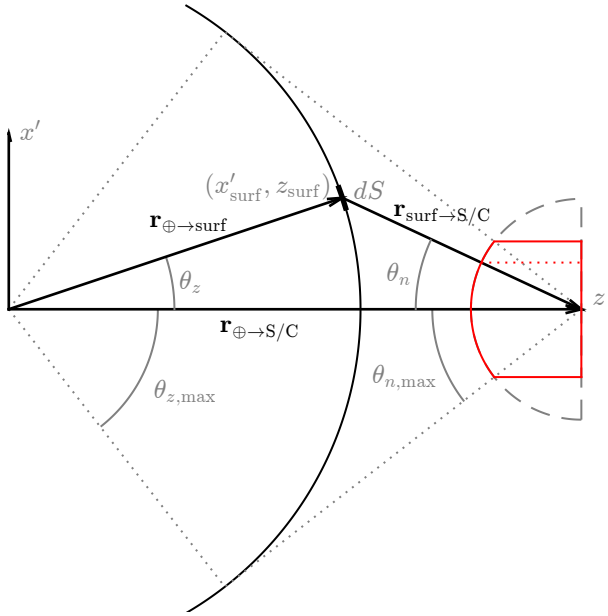

Figure 2.26 – To sample planetary heat fluxes ray directions, the hemisphere is limited to the red spherical cap. The point $(z_{\text{surf}}, x'_{\text{surf}})$ defines the origin the ray $\mathbf{r}_{\text{surf}\to\text{S/C}}$ and is expressed in the plane containing both $\hat{\mathbf{r}}_{\oplus\to\text{S/C}}$ and $\hat{\mathbf{r}}_{\oplus\to\text{surf}}$ which corresponds to the xz plane rotated by ϕ_z around z.

$$\begin{cases} z_{\text{surf}}^2 + x_{\text{surf}}'^2 = r_\oplus^2 \\ x'_{\text{surf}} = \tan\theta_n (r_\oplus h_r - z_{\text{surf}}) \end{cases} \tag{2.40}$$

Solving Equations 2.40 for x'_{surf} and z_{surf} gives

$$x'_{\text{surf}} = r_\oplus \tan(\theta_n) \frac{h_r - c_2}{1 + c_1}$$
$$z_{\text{surf}} = \sqrt{r_\oplus^2 - x_{\text{surf}}'^2} = \frac{r_\oplus c_3}{1 + c_1}$$

with $c_1 = \tan^2\theta_n$ and $c_2 = \sqrt{1 + c_1(1 - h_r^2)}$ and $c_3 = \sqrt{(1+c_1)^2 - c_1(h_r - c_2)^2}$ from which $\sin(\theta_z)$ and $\frac{d\theta_z}{d\theta_n}$ are finally expressed in function of θ_n.

$$\sin(\theta_z) = \frac{x'_{\text{surf}}}{r_\oplus} = \tan\theta_n \frac{h_r - c_2}{1 + c_1}$$
$$\frac{d\theta_z}{d\theta_n} = \frac{h_r(1+c_1)(h_r c1 + c_2) - c_3^2}{c_2 c_3}$$

In view of the performances exhibited by the coupled Halton strategy presented in Section 2.3, the same method is applied here the combination of both methods leads to the planet-focused Halton sampling strategy (PFHS). Since the four quasi-random variables used for the direction sampling and for surface sampling are uniformly distributed over the unit hypersquare, it leads to $d\xi_{\theta_n} d\xi_{\phi_z} dA = A/n_r$.

The term $\cos\theta_z$ present in $\left\|\mathbf{r}_{\text{surf}\to\text{S/C}}\right\|^2$ and in $\hat{\mathbf{r}}_{\oplus\to\text{surf}}\cdot\hat{\mathbf{r}}_{\text{surf}\to\text{S/C}}$ can also be replaced since $\cos\theta_z = z_{\text{surf}}/r_\oplus$. Introducing the results obtained above in the ray energy Equations 2.35 and 2.36 finally gives

$$dQ_a = a_\oplus C_\odot \frac{A}{n_r} f\left(\hat{\mathbf{r}}_{\oplus\to\text{surf}}\cdot\hat{\mathbf{r}}_{\text{surf}\to\odot}\right)\left(\mathbf{n}\cdot\hat{\mathbf{r}}_{\text{S/C}\to\text{surf}}\right) \tag{2.41}$$

for albedo and

$$dQ_e = \sigma\varepsilon_\oplus T_\oplus^4 \frac{A}{n_r} f\left(\mathbf{n}\cdot\hat{\mathbf{r}}_{\text{S/C}\to\text{surf}}\right) \tag{2.42}$$

with the dimensionless factor f depending only on ξ_{θ_n} and h_r and defined as

$$f = \frac{(c_1-1)\left(1-2\xi_{\theta_n}+c_1(2\xi_{\theta_n}-h_r^2)\right)(c_2-1)}{c_1c_2h_r(1+h_r^2-2c_2)^{3/2}} \tag{2.43}$$

since $\tan\theta_n = \sqrt{\xi_{\theta_n}/(h_r^2-\xi_{\theta_n})}$ and by redefining the constants c_1 and c_2:

$$c_1 = \sqrt{\frac{1-\xi_{\theta_n}}{h_r^2-\xi_{\theta_n}}}$$

and

$$c_2 = \sqrt{h_r^2(1-\xi_{\theta_n}) - \xi_{\theta_n}\left(1-2\xi_{\theta_n}-2\sqrt{(1-\xi_{\theta_n})(h_r^2-\xi_{\theta_n})}\right)}$$

Figure 2.27 presents how the factor f evolves with the altitude of the S/C and angular sampling variable ξ_{θ_n}. As h_r increases, f tends towards zero and if $\xi_{\theta_n}=0$ (the surface is pointing nadir), f reduces to $1/h_r^2$ and logically tends to 1 as the S/C gets closer to the surface. f increases with θ_n to represent the growth of dS.

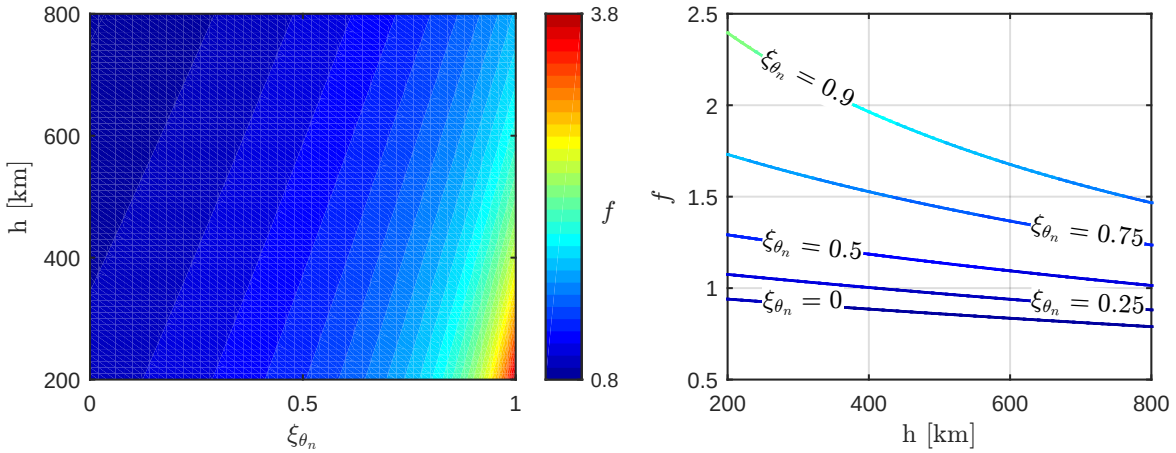

Figure 2.27 – Evolution of planetary heat fluxes sampling factor f with orbit altitude h and quasi-random variable ξ_{θ_n}.

Sampling the red portion of hemisphere shown in Figure 2.26 may still waste a lot of rays if the S/C face under study intersects the Earth field of view. Figure 2.28 shows how

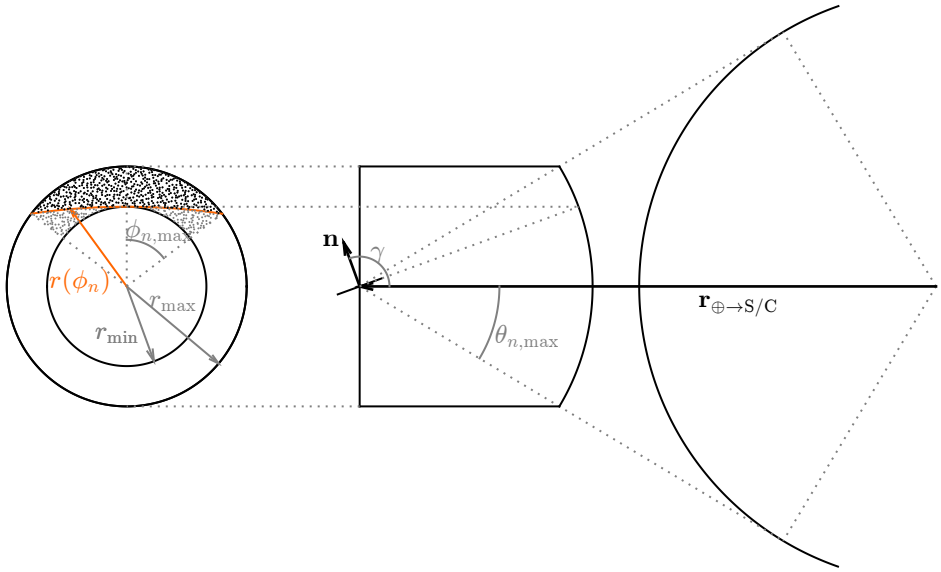

Figure 2.28 – The S/C face further limits the useful portion of the unit hemisphere to be sampled. On the left, the direction samples are projected onto the unit disc and only the black samples above the orange curve are useful.

the S/C face limits the useful portion of the unit hemisphere to be sampled. Only the black samples shown on the unit disc are useful.

To define the useful portion of the unit disc, the intersection between the unit hemisphere and the face plane is computed and forms a great circle. The equation of the great circle is found by equating the unit sphere and the plane equation. The unit hemisphere coordinate system (x_h, y_h, z_h) is defined as a rotation of 180° around x of the coordinate system defined in Figure 2.25 to have z_h pointing nadir: $(x_h, y_h, z_h) = (x, -y, -z)$. In this coordinate system, the face normal becomes

$$\mathbf{n} = \begin{bmatrix} \sin\gamma & 0 & \cos\gamma \end{bmatrix}$$

and the great circle equation is defined by:

$$\sin\gamma\cos\phi_n\sin\theta_n + \cos\gamma\cos\theta_n = 0$$

from which the angle θ_n is extracted

$$\tan\theta_n = \frac{-1}{\cos\phi_n\tan\gamma}$$

The useful portion of the unit disc to be sampled is bounded externally by the radius $r_{\max} = \sin\theta_{n,\max}$ and internally by the projection of the great circle onto the unit disc defined in polar coordinates $r_i(\phi_n)$.

$$r_i(\phi_n) = \sin\theta_n = \sin\left(\arctan\frac{-1}{\cos\phi_n\tan\gamma}\right)$$

The minimum radius $r_{\min}$ occurs when $\phi_n = 0$ and is equal to $\cos\gamma$ and the maximum angle $\phi_{n,\max}$ is given by

$$\phi_{n,\max} = \arccos \frac{-1}{\tan\gamma \tan\theta_{n,\max}}$$

To sample the useful portion of the unit disc with n samples, the subtended annulus sector is over-sampled by a factor f_o and samples not falling in the useful area are then discarded. The over-sampling factor f_o is equal to the ratio between the useful area to the annulus sector area.

$$f_o = \frac{\phi_{n,\max}(r_{\max}^2 - r_{\min}^2)}{A_u}$$

where A_u is the useful sampling disc surface area:

$$A_u = 2\int_0^{\phi_{n,\max}} \int_{r_i(\phi_n)}^{r_{\max}} r dr d\phi_n = \phi_{n,\max} r_{\max}^2 - \cos\gamma \arctan\left(\cos\gamma \tan\phi_{n,\max}\right)$$

Sampling the annulus sector avoids over-sampling the whole disc of radius $r_{\max}$ by a factor $f_0^* = \frac{\pi r_{\max}^2}{A_u}$ that is much larger than f_o. Figure 2.29 gives the evolution of f_o and f_0^* in function of γ for an altitude of 800 km. The configuration being symmetric with respect to yz plane, γ is varied between 90° and $\theta_{n,\max}$. For $\gamma = 90°$, $f_o = 1$ since the face plane cuts the hemisphere in two equal parts and exactly half the annulus is sampled and $f_0^* = 2$. As γ increases, the useful sampling area decreases and f_o reaches a maximum before tending towards 1.5 for any $\theta_{n,\max}$.

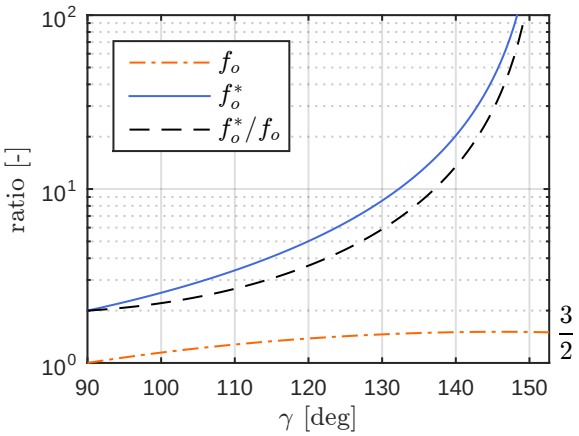

Figure 2.29 – In blue, the ratio between the limited unit disc area πr_{max}^2 and its useful area A_u in function of the S/C face angle γ. In orange, the ratio between the sampled annulus sector and A_u. The altitude is fixed to 800 km which corresponds to $\theta_{n,\max} = 62.7°$.

The above strategy did not take into account the presence of the terminator which further reduces the useful sampling area. For albedo computation, the samples in A_u are further tested for illumination and discarded if the condition $\hat{\mathbf{r}}_{\oplus\to\text{surf}} \cdot \hat{\mathbf{r}}_{\text{surf}\to\odot} > 0$ is not verified.

2.4.4 Application to albedo heat flux over a flat plate

First, all parameters being equal (Earth equatorial radius $r_\oplus = 6378.136\,\text{km}$ defined in the EGM2008 [286, 287], solar constant $C_\odot = 1366.1\,\text{W}\,\text{m}^{-2}$, uniform diffuse albedo coefficient $a_\oplus = 0.3$, altitude and attitude) the method implemented in ESARAD leads to a systematic bias with respect to the analytical solution. Considering for instance a unit square at 800 km altitude whose normal is pointing nadir right above subsolar point, the closed form solution given by Equation 2.34 leads to an albedo heat flux of $319.9\,\text{W}\,\text{m}^{-2}$ while ESARAD converges to the value of $319.6\,\text{W}\,\text{m}^{-2}$. This 0.1% error remains however negligible compared to the variations due to Earth surface inhomogeneity that are also usually neglected.

Only albedo is computed in this example since the method to compute infrared is very similar. The orbit considered for this analysis is a 800 km circular equatorial orbit. The epoch corresponds to the vernal equinox and is such that the subsolar point lies exactly on the equator. Eclipse entry and exit points are computed following the method described in [288] and the Sun position from [289]. The attitude of the unit square is constant with respect to the Sun. It is such that the normal to the flat plate, *i.e.* the z axis, is constantly oriented 130 degrees away from the Sun direction and such that the angle with the orbital plane is 50 degrees. At subsolar point, the angle γ between the face normal and the nadir axis is thus 50 degrees. The orbit and attitude are represented in Figures 2.30(a) and (b).

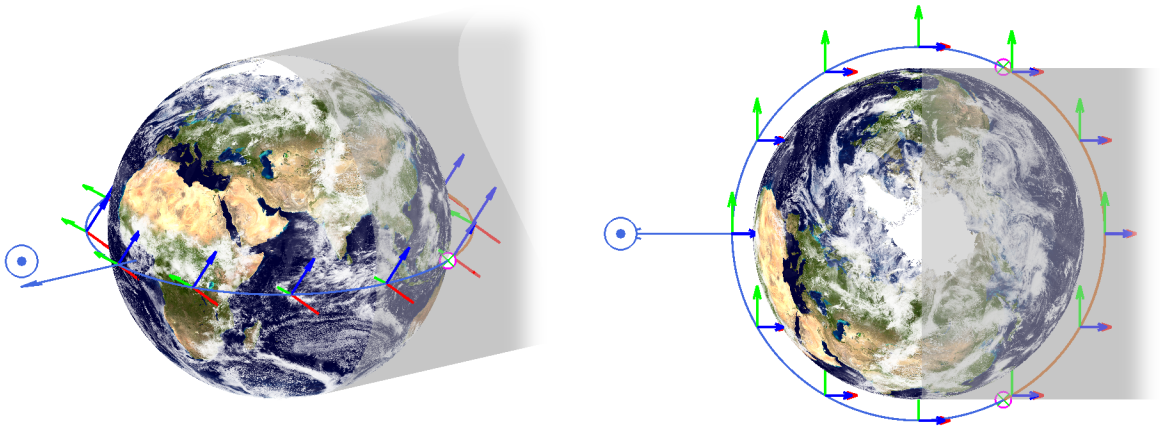

(a) (b)

Figure 2.30 – Equatorial 800 km circular orbit with 3D view (a) and top view (b). The Sun direction is given by the blue $\odot$ vector and the Earth shadow is represented by the grey cylinder with eclipse entry and exit points. The attitude is displayed by plotting the local coordinate system axes (x, y, z) at several true anomalies with red, green and blue arrows, respectively.

Because there are multiple positions along the orbit, multiple faces in the model and since the computation is repeated several times with different seeds to assess the statistical variations of the results, the global error indicator δ is defined as the rms error over the faces, orbital positions and computational runs:

$$\delta = \sqrt{\frac{1}{n_{\text{orbit pos.}} n_{\text{runs}} n_{\text{faces}}} \sum_{i=1}^{n_{\text{faces}}} \sum_{j=1}^{n_{\text{orbit pos.}}} \sum_{k=1}^{n_{\text{runs}}} (Q_{a,i,j,k} - Q_{a,\infty,i,j})^2} \tag{2.44}$$

with $n_{\text{orbit pos.}}$ the number of orbital positions, n_{runs} the number of times the computation is carried out, n_{faces} the number of faces in the model and $Q_{a,\infty,i,j}$ the analytical solution of the i^{th} face and j^{th} orbital position.

Figure 2.31(a) shows the reference solution obtained by integrating Equation 2.23. For both faces, it is symmetrical with respect to the Sun direction, with a maximum above the subsolar point corresponding to a true anomaly of 0. Because the face is inclined, both sides are illuminated above the subsolar point, each side is exposed to a different part of the Earth. Both sides still receive energy after crossing the terminator (90 degrees true anomaly) with a higher value for the back (Sun) side. The new planetary sampling scheme is compared to the planetary heat flux computation algorithm implemented in ESATAN-TMS r2016 sp2. Figure 2.31(b) presents the convergence of the error indicator δ with the number of rays. With 100 rays, the error is about 7.5 W while it is only 1.0 W with the new method. Halton low discrepancy sequences also provide a higher convergence rate. Combined with the Earth focused sampling, 2 to 3 orders of magnitude improvement over ESARAD (ESATAN-TMS ray tracing engine) is achieved.

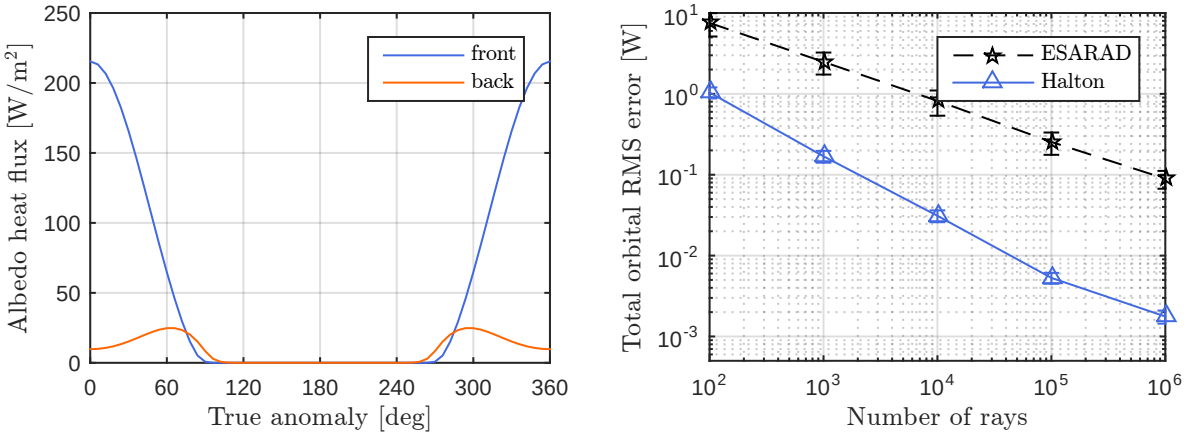

Figure 2.31 – Analytical solution of albedo heat flux incident to both sides of a unit square in the xy plane and orbiting the Earth as described in Figure 2.30. Convergence of the total RMS error δ on the albedo heat flux, averaged over the orbit and over 100 runs (b).

A second orbital case is considered to verify the method. This time, the orbit is no longer equatorial but is inclined by 98 degrees and the right ascension of the ascending node is set to 60 degrees. The attitude is now such that the normal to the face is always pointing away from the Sun and the x axis is in the orbital plane. Figure 2.32 shows the second orbit and the attitude.

Figure 2.33(a) shows the reference solution obtained through the integration of Equation 2.23 over the correct field of view. The evolution of the albedo heat flux is no longer symmetric with respect to the direction of the Sun. The maximum heat flux of the $+z$ and $-z$ faces are 81 W m^{-2} and 21 W m^{-2}, respectively. The back face is again exposed for a longer period than the front face. Figure 2.33(b) gives the convergence of the error indicator δ. Even though the orbit is largely different from the first case, the same conclusions are drawn: more than 100 times as less rays than ESARAD are required to achieve 0.1 W accuracy.

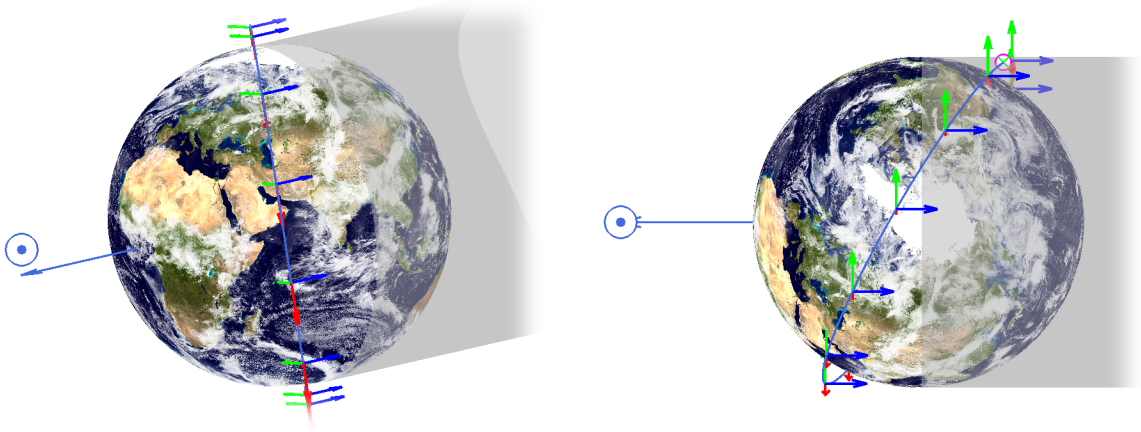

(a) (b)

Figure 2.32 – Equatorial 800 km circular orbit with 3D view (a) and top view (b). The Sun direction is given by the blue $\odot$ vector and the Earth shadow is represented by the grey cylinder with eclipse entry and exit points. The attitude is displayed by plotting the local coordinate system axes (x, y, z) at several true anomalies in red, green and blue, respectively.

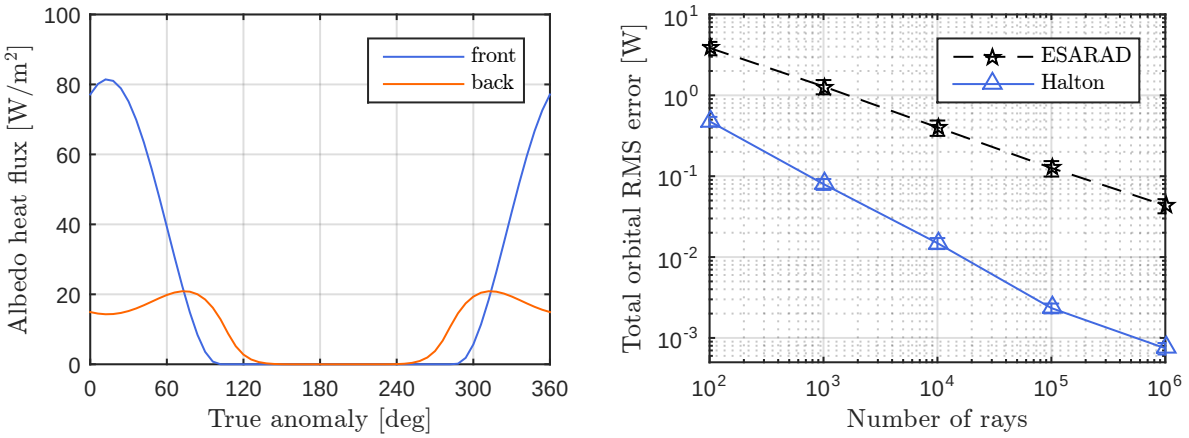

(a) (b)

Figure 2.33 – Analytical solution of albedo heat flux incident to both sides of a unit square in the xy plane and orbiting the Earth as described in Figure 2.32. Convergence of the total RMS error δ on the albedo heat flux, averaged over the orbit and over 100 runs (b).

2.5 Additional variance reduction and MCRT acceleration techniques

As mentioned in the introduction of this chapter, two complementary approaches may reduce the REFs computation: either reduce the number of rays to be traced or reduce the ray-face intersection computation time itself. Previous sections focused on the first approach and presented how more uniform direction and surface sampling strategies could improve the accuracy of MCRT. Within this framework, stratified sampling and low discrepancy sequences can be considered as *a priori* variance reduction techniques. This section first presents *a posteriori* variance reduction techniques relying on the enforcement of reciprocity and closure rules. In particular, the one already implemented in our algorithm and in ESARAD is discussed.

Besides variance reduction methods that are inherently related to the stochastic behaviour of the Monte Carlo process, this section also describes classical ray tracing acceleration techniques implemented to reduce either the number of ray-face intersections to compute or their computation time with efficient intersection algorithms. Reducing the number of intersections to compute is achieved by space partitioning.

2.5.1 Reciprocity and closure enforcement

While the closure rule expressed by Equation 1.29 presented in Section 1.2.5 is inherently enforced, the raw REFs computed by ray tracing do not necessarily obey the reciprocity expressed by Equation 1.27. The reciprocity rule may then be exploited as an a posteriori variance reduction method. Reciprocity also allows a factor 2 reduction of the REF matrix to be stored. However, the naive enforcement of reciprocity generally results in a violation of closure. Different smoothing schemes were proposed in the literature and can be classified in two main categories:

- simple procedures that do not limit the size of the corrections to be applied to the initial set of REFs (and therefore do not guarantee that the corrected set is more accurate than the initial REFs) [290–293];
- and more elaborated algorithms that find the smallest corrections to be added to satisfy both reciprocity and closure and ensure non-negativity (constrained least-squares minimization [294–296] or constrained maximum likelihood [297] techniques).

Taylor *et al.* [298] reviewed and compared the different REFs smoothing schemes and concluded that least-squares smoothing presented the best results, as well as maximum likelihood applied in [297].

The least squares and maximum likelihood algorithms were developed for closed models (enclosures), having a square REF matrix. It is usually not the case in space applications. In particular when analysing the exterior of a spacecraft or any model having exchange factors with deep space. The REF matrix is therefore a $n \times n+1$ matrix with the $n+1^{\text{th}}$ node representing the deep space node and these algorithms cannot directly be applied. To generate a square matrix, an additional surface surrounding the model and representing the environment is required. A large number of additional rays would

be required to compute the exchange factor from the surrounding box to the faces of the model.

Nevertheless, it was shown in [53, 299, 300] that enforcing reciprocity is more important than closure, especially to the accuracy of the final results than the accuracy of the radiative exchange factors themselves. In ESARAD and Thermica, only the reciprocity is enforced by linear averaging [102, 159] following the empirical technique demonstrated in [301]. After reciprocity enforcement, the closure is left broken. The method takes advantage of the fact that both the REF from face i to j and from j to i are computed. The corrected $\mathcal{F}_{ij}$ is obtained through the suitable weighting of the ray tracing raw output $\tilde{\mathcal{F}}_{ij}$ and $\tilde{\mathcal{F}}_{ji}$

$$A_i\epsilon_i\mathcal{F}_{ij} = wA_i\varepsilon_i\tilde{\mathcal{F}}_{ij} + (1-w)A_j\varepsilon_j\tilde{\mathcal{F}}_{ji} \tag{2.45}$$

where the weight w is defined as

$$w = \frac{1}{2}(1 + \text{sign}(X)\,|X|^n) \tag{2.46}$$

As already mentioned in [116] and later demonstrated in [300], every effort should be made to compute the larger of the two REFs between the two surfaces. The uncertainty on $\mathcal{F}_{ij}$ is lower than on $\mathcal{F}_{ji}$ if $\varepsilon_i A_i/n_{r,i}$ is smaller than $\varepsilon_j A_j/n_{r,j}$. The X factor appearing in the expression of the weight w includes this conclusion and is such that w is higher for larger REFs obtained with a larger number of rays:

$$X = \frac{\dfrac{A_j\varepsilon_j}{n_{r,j}} - \dfrac{A_i\varepsilon_i}{n_{r,i}}}{\dfrac{A_j\varepsilon_j}{n_{r,j}} + \dfrac{A_i\varepsilon_i}{n_{r,i}}}$$

where $n_{r,i}$, $n_{r,j}$ are the number of rays fired from the faces i and j, respectively. The best value of the exponent n is empirically found to be 0.4 [159]. This technique was already applied to the results presented in the previous sections to allow a fair comparison with ESARAD.

Another linear averaging technique discussed in [53] and [300] is the fractional variance. In their work, the weights w appearing in Equation 2.45 are based on the variance $\sigma^2_{\tilde{\mathcal{F}}_{ij}}$ of the REFs:

$$w = \frac{\sigma^2_{\tilde{\mathcal{F}}_{ji}}}{\sigma^2_{\tilde{\mathcal{F}}_{ij}} + \sigma^2_{\tilde{\mathcal{F}}_{ji}}}$$

with the variance approximated by:

$$\sigma^2_{\tilde{\mathcal{F}}_{ij}} = (A_i\varepsilon_i)^2\frac{\tilde{\mathcal{F}}_{ij}(1-\tilde{\mathcal{F}}_{ij})}{n_{r,i}}$$

since the $\tilde{\mathcal{F}}_{ij}$ follow a binomial distribution [300].

Figure 2.34 compares the error convergence resulting from the computation of the REF between the two quadrangles presented in Figure 2.14 for the different methods described above. Crude Monte Carlo results with linear averaging smoothing correspond to ESARAD output and served as reference in previous sections. ESARAD raw unenforced

results are also given. They are compared with the Halton coupled sampling strategy combined with the two smoothing techniques described above. The red curve is identical to the one already presented in Figure 2.18. There is a significant improvement between raw and smoothed data: the two curves are parallel and the linear averaging technique reduces the error of the crude Monte Carlo from 10.8 ± 6.4 % to 7.1 ± 4.3 % for $n_r = 10^3$. The effect when it is applied to Halton coupled sampling is almost identical. Compared to the linear averaging technique, the fractional variance technique gives very similar results.

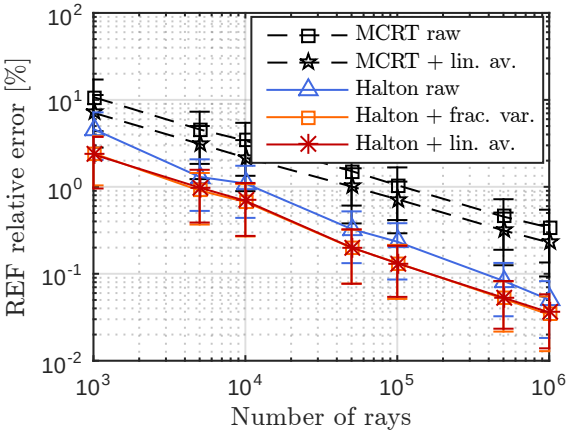

Figure 2.34 – Relative error on the REF between the two quadrangles of Figure 2.14 for different reciprocity enforcement strategies.

For open models ($n \times n + 1$ REFs matrix), once reciprocity is enforced for the $n \times n$ REFs, the REF with the environment node ($n + 1^{\text{th}}$ column) is adapted to meet the closure requirement. Before adapting the REFs to environment value, the line sum error (LSE) is calculated with Equation 1.47, representing the error on the closure rule due to reciprocity enforcement. The LSE can then be viewed as an error indicator and used with accuracy control methods such as the one presented in Section 1.3.3.

Since the convergence rate κ of the coupled Halton sampling is above 0.5 but depends on the thermo-optical properties present in the model, the classic Monte Carlo accuracy control strategy may overestimate the number of rays required for a target accuracy and confidence level since $\kappa = 0.5$ is assumed. Instead it is proposed to perform two ray tracing runs with two different but small number of rays to assess the actual convergence rate based on the LSE obtained for each run. The required number of rays for a target LSE is then computed by linear extrapolation (in log log scale) from the two previous runs. The model should however be sufficiently large such that the i^{th} node LSE encompasses REFs with several other faces to smooth the statistical variations in the convergence.

2.5.2 Space partitioning

As the size of the model and the number of faces increases, checking for each ray the intersection with all faces becomes rapidly prohibitive. More popular than the bounding volumes techniques, space subdivision techniques were developed to reduce the computational effort associated with ray/face intersection checks [248, 300]. The main idea

behind this type of techniques is to divide the volume containing the model into sub-volumes called voxels. Each voxel is then associated with the faces it contains (totally or partially). The rays are then propagated from one voxel to the adjacent voxel and so on, checking intersection only with the faces contained in the current voxel.

Different space subdivision techniques were proposed and studied since the 1980s. The two main techniques are the uniform space subdivision (USD) [302, 303] and non-uniform space subdivision (NUSD) such as the octree or k-d tree subdivision [304]. In USD, the bounding volume is uniformly divided and all voxels have the same size. The octree and k-d-tree methods divide the bounding volume in such a way that there are more voxels in regions more densely populated with faces and inversely. Both the USD [159, 305] and NUSD [37] methods were implemented in radiative heat transfer ray tracing codes because they store the geometry information more efficiently. When the model is not too empty, USD is usually preferred over NUSD algorithms because moving from one voxel to the next one with NUSD is more computationally expensive [305]. Figure 2.35 gives an example of the ray propagation across uniformly-spaced voxels.

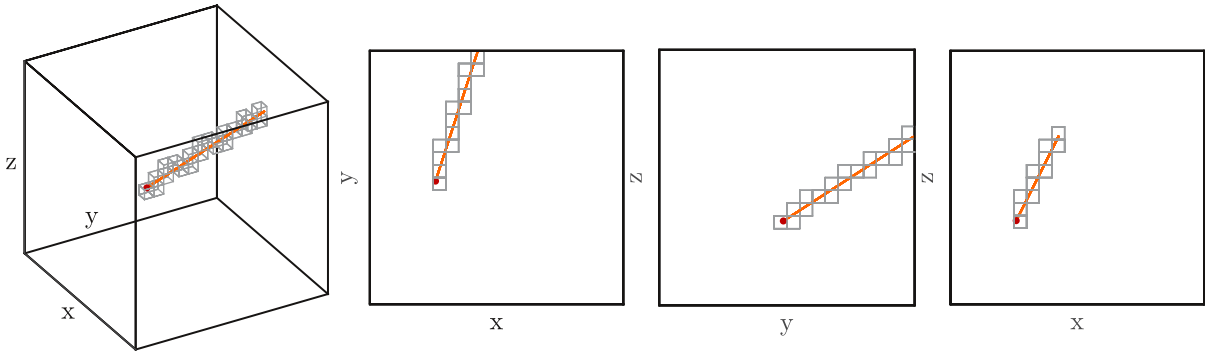

Figure 2.35 – Ray propagation across uniformly distributed voxels. The ray origin is represented by the red dot and only the intercepted voxels are shown.

Choosing the right number of voxels is not straightforward. Yet, the computation of the next voxel is cheaper than the computation of an intersection and the optimal number of voxel therefore favours fewer surfaces per voxel over fewer empty voxels. This empirical result will be confirmed in Section 3.5 where complex structures involving many faces are studied.

To achieve a target number of faces per voxel, the space subdivision is done iteratively by increasing the number of voxels until the number of shells per voxel is below the target.

As a face may be part of different voxels, the same intersection may be computed repeatedly [304]. To alleviate this problem, *mailboxing* is an additional acceleration technique mentioned in [300, 303, 306] and introduced by Arnaldi *et al.* [307]. The technique consists in attaching a mailbox to each face, storing the results of the intersection check with a ray counter that is incremented each time a ray is reflected or a new ray is emitted. When an intersection must be computed, it first checks the ray counter: if it is the same as the current ray, the computation is skipped and the value in the mailbox is used. Though interesting, Zeeb [300] showed that this technique was not effective for simple surface intersections as it is the case here, and because the number of faces spanning several voxels is inherently kept low due to USD.

2.5.3 Intersections computation

Besides ray propagation across voxels, most of the ray tracing process time is spent for computing intersections. For each voxel crossed by a given ray, all shells belonging to that voxel must be checked. This step is optimized to reduce the number of operations to be performed by observing several rules of thumb applied in image rendering and described in [308]:

- perform simple operations and comparisons early on that might trivially accept or reject the intersection,
- postpone expensive calculations until they are needed,
- try to reduce the dimension of the problem,
- take advantage of potential off-line pre-computed values,
- if an intersection is expensive, envisage a first level of quick rejection using a simpler shape,
- take care of floating-point operation errors.

In our case, the plane containing each shell is first computed during the pre-processing phase. Each plane is defined through its parameters a, b, c and d appearing in Equation 2.47.

$$ax + by + cz + d = 0 \tag{2.47}$$

with the plane unit normal $\mathbf{n} = [a, b, c]$. Given three distinct non-collinear points $\mathbf{p}_i = [x_i, y_i, z_i], i = 1..3$, the plane coefficients are obtained from the relations:

$$\begin{aligned}
a &= \frac{a'}{\sqrt{a'^2 + b'^2 + c'^2}} \text{ with } a' = (y_2 - y_1)(z_3 - z_1) - (z_2 - z_1)(y_3 - y_1) \\
b &= \frac{b'}{\sqrt{a'^2 + b'^2 + c'^2}} \text{ with } b' = (z_2 - z_1)(x_3 - x_1) - (x_2 - x_1)(z_3 - z_1) \\
c &= \frac{c'}{\sqrt{a'^2 + b'^2 + c'^2}} \text{ with } c' = (x_2 - x_1)(y_3 - y_1) - (y_2 - y_1)(x_3 - x_1) \\
d &= -ax_1 - by_1 - cz_1
\end{aligned}$$

The intersection check is carried out by progressing through the following successive steps:

1. Starting from the ray equation:

$$\mathbf{r}(t) = \mathbf{p}_0 + t\mathbf{r}_0 \tag{2.48}$$

with $\mathbf{p}_0$ the ray origin, $\mathbf{r}_0$ the ray direction and t a positive variable describing the position along the ray from the origin, the distance t_i to the intersection with the plane containing the i^{th} shell is computed with Equation 2.49.

$$t_i = -\frac{\mathbf{p}_0 \cdot \mathbf{n}_i + d_i}{\mathbf{r}_0 \cdot \mathbf{n}_i} \tag{2.49}$$

The denominator and numerator in Equation 2.49 are computed sequentially.

2. If the denominator is 0 the ray is parallel to the plane and no further calculation for this shell is needed.

3. If not, the numerator and t_i are computed. If t_i is negative, the plane is behind the ray origin and no further calculation is needed.

4. Floating-point errors can lead to incorrect self-intersections (since flat surfaces are considered here) when rays are traced starting from a previously computed ray-surface intersection point. To avoid this problem, there is a threshold below which the intersection is considered as a self-intersection.

5. The minimum valid intersection distance encountered so far in the current voxel is denoted $t_{\min}$. If $t_i > t_{\min}$, it means that the current shell is farther than the shell corresponding to $t_{\min}$. In that case, no further calculation is needed.

6. If $t_i < t_{\min}$, the intersection point $\mathbf{p_i} = \mathbf{p}_0 + t_i\mathbf{r}_0$ is computed. If it is outside the current voxel, no further calculation is required.

7. During the pre-processing phase, the square of the maximum distance $d_{i,\max}$ between the shell barycenter $\mathbf{p}_{\text{cog},i}$ and all its vertices is pre-computed. If the squared distance d_i between $\mathbf{p}_i$ and $\mathbf{p}_{cog,i}$ is larger than $d_{i,\max}$, then the intersection is automatically ruled out without detailed check if the intersection is inside the face.

8. If the intersection is closer to the barycenter than $d_{i,\max}$, then the detailed intersection check is carried out and the triangles and quadrangles are treated separately.

Triangle

Based on the triangle coordinates introduced in Equation 2.10, any point $\mathbf{p}_P$ can be expressed by means of the three triangle vertices $\mathbf{p}_A$, $\mathbf{p}_B$ and $\mathbf{p}_C$:

$$\mathbf{p}_P(\zeta, \eta) = (1 - \zeta - \eta)\mathbf{p_A} + \zeta\mathbf{p_B} + \eta\mathbf{p_C}$$

The conditions for a point to lie inside the triangle are expressed by

$$\begin{cases} \zeta & \geq & 0 \\ \eta & \geq & 0 \\ \zeta + \eta & \leq & 1 \end{cases} \tag{2.50}$$

Different methods to compute efficiently the barycentric coordinates were developed in the past decades. A review of ray triangle intersection computation techniques is available in [309] and include results from [310–313]. The intersection-in-face check is carried out using Wald's method [310] because of its simplicity of implementation and efficiency. Wald's method is simply based

on solving the barycentric coordinates equations and grouping as much coefficients that can be precomputed as possible. Since only two equations of the barycentric coordinates are linearly independent, the computation can be done in 2 dimensions. To avoid any shape degeneration, the triangle and point to be tested are projected on one of the Cartesian plane by discarding the coordinate corresponding to the largest component of the triangle normal. The remaining two coordinates are denoted x' and y'. The barycentric coordinates equations can be rewritten in matrix form:

$$\begin{bmatrix} x'_{AP} \\ y'_{AP} \end{bmatrix} = \begin{bmatrix} x'_{AB} & x'_{AC} \\ y'_{AB} & y'_{AC} \end{bmatrix} \begin{bmatrix} \zeta_P \\ \eta_P \end{bmatrix} \tag{2.51}$$

where $x'_{ij} = x'_j - x'_i$ and similarly for y'. Inverting the relation gives the intersection coordinates:

$$\begin{bmatrix} \zeta_P \\ \eta_P \end{bmatrix} = \frac{1}{x'_{AB}y'_{AC} - x'_{AC}y'_{AB}} \begin{bmatrix} y'_{AC} & -x'_{AC} \\ -y'_{AB} & x'_{AB} \end{bmatrix} \begin{bmatrix} x'_{AP} \\ y'_{AP} \end{bmatrix}$$

which is further simplified by grouping the coefficients that can be precomputed:

$$\begin{bmatrix} \zeta_P \\ \eta_P \end{bmatrix} = \begin{bmatrix} x'_P c_{\zeta,1} + y'_P c_{\zeta,2} + c_{\zeta,3} \\ x'_P c_{\eta,1} + y'_P c_{\eta,2} + c_{\eta,3} \end{bmatrix} \tag{2.52}$$

where the coefficients $c_{\zeta,i}$ and $c_{\eta,i}$, $i = 1..3$ are precomputed for each triangle.

$$\begin{array}{lcllcl} c_{\zeta,1} & = & c_4 y'_{AC} & c_{\eta,1} & = & -c_4 y'_{AB} \\ c_{\zeta,2} & = & -c_4 x'_{AC} & c_{\eta,2} & = & c_4 x'_{AB} \\ c_{\zeta,3} & = & c_4(y'_A x'_{AC} - x'_A y'_{AC}) & c_{\eta,3} & = & c_4(x'_A y'_{AB} - y'_A x'_{AB}) \end{array}$$

with

$$c_4 = \frac{1}{x'_{AB}y'_{AC} - x'_{AC}y'_{AB}}$$

The computation of the ζ and η each requires 2 multiplications and 2 additions. ζ_P and η_P are computed sequentially to avoid computing η_P if ζ_P does not meet the condition given by Equation 2.50.

Quadrangle

Any point $\mathbf{p}_P$ in a quadrangle can be expressed in terms of the quadrangle natural coordinates ζ, η (which differs from the one presented in Equation 2.19 that varies between -1 and 1 for Gauss-Legendre integration):

$$\mathbf{p}_P = (1-\zeta_P)(1-\eta_P)\mathbf{p}_A + \zeta_P(1-\eta_P)\mathbf{p}_B + \zeta_P\mathbf{p}_C + \eta_P(1-\zeta_P)\mathbf{p}_D$$

that can be rewritten

$$\mathbf{p}_P - \mathbf{p}_A = \zeta_P(\mathbf{p}_B - \mathbf{p}_A) + \eta_P(\mathbf{p}_D - \mathbf{p}_A) + \zeta_P\eta_P(\mathbf{p}_A - \mathbf{p}_B + \mathbf{p}_C - \mathbf{p}_D) \tag{2.53}$$

The intersection computation is again performed in two dimensions. As opposed to the triangle, the computation of ζ_P and η_P now requires to solve a second degree equation (due to the term $\zeta_P \eta_P$ present in Equation 2.53) involving more mathematical operations including one square root:

$$\left\{ \begin{array}{rcl} x'_{AP} & = & \zeta_P x'_{AB} + \eta_P x'_{AD} + \zeta_P \eta x'_{ABCD} \\ y'_{AP} & = & \zeta_P y'_{AB} + \eta_P y'_{AD} + \zeta_P \eta y'_{ABCD} \end{array} \right. \tag{2.54}$$

Equation 2.54 can be solved analytically to find the value of ζ_P and η_P:

$$\left\{ \begin{array}{rcl} \zeta_P & = & \dfrac{-(c_2 + c_3) \pm \sqrt{(c_2 + c_3)^2 - 4 c_1 c_4}}{2 c_1} \\ \eta_P & = & \dfrac{y'_{AP} - \zeta_P y'_{AB}}{y'_{AD} + \zeta_P y'_{ABCD}} \end{array} \right. \tag{2.55}$$

with the constants

$$\begin{array}{rcl} c_1 & = & x'_{AB}\, y'_{ABCD} - x'_{ABCD}\, y'_{AB} = x'_{CD} y'_{AB} - x'_{AB} y'_{CD} \\ c_2 & = & x'_{AB}\, y'_{AD} - x'_{AD}\, y'_{AB} \\ c_3 & = & x'_{ABCD}\, y'_{AP} - x'_{AP}\, y'_{ABCD} \\ c_4 & = & x'_{AD}\, y'_{AP} - x'_{AP}\, y'_{AD} \end{array}$$

c_1 and c_2 can be pre-computed and stored while c_3 and c_4 must be computed on the fly. This method is very similar to the one presented in [314].

Another way to carry out the intersection-in-quadrangle check is to divide the quadrangle into two triangles and perform twice the method presented above. Both approaches were compared and conclusions similar to the ones found in [314] are drawn: the direct quadrangle check does not give better results than the two triangles approach which is preferred here.

Another acceleration strategy implemented proposes to skip all faces that only see the deep space node. During the pre-processing phase, the relative position of all faces is computed. Faces that have no shell in the half hemisphere in front of them are labelled to be skipped during ray tracing and a unit view factor (or REF) to the environment is assigned to these faces. This check is relatively inexpensive since only flat faces are considered.

2.6 Concluding remarks

This chapter focused on reducing the time required to compute the REFs by ray tracing through more uniform sampling of the unit hemisphere and emitting surface. Several direction sampling strategies were studied. Stratified hemisphere, isocell and Halton low-discrepancy sequences exhibited similar performances in general cases. However, the

Halton strategy proved to be more robust against variations in the geometrical configuration of the REF to compute than the other two sampling schemes. It was kept as baseline to be combined with surface sampling.

Several surface sampling alternatives were studied namely random, quasi-random (Halton), uniform and Gauss integration points. Stratified sampling of the surface was not studied. For the quadrangle, stratification of the unit square would have required to take into account the aspect ratio of the face in a similar way to the uniform and Gauss surface sampling schemes and origins would have needed to be weighted by the Jacobian of the mapping.

Local direction sampling performed at each origin was also compared to *a priori* global sampling distributed among the origins. The best performances were obtained with the local direction sampling coupled with Gauss integration points. The performance was however highly dependent on the selected number of origins and geometrical configuration. Giving almost identical performances but providing more robustness, the 4-dimensional Halton sequence sampling both ray directions and origins at the same time was thus preferred. This technique outperforms classical MCRT by almost one order of magnitude. The gain depends on the required accuracy since the convergence rate is higher: the higher the required accuracy, the higher the gain.

An alternative sampling scheme was also proposed to compute the planetary heat fluxes. By sampling only the useful field of view between the S/C face and the planet and exploiting again the 4-dimensional Halton sampling scheme, the PFHS method offers two orders of magnitude improvement. Compared to ESARAD, this method requires a ray tracing step at each orbital position, step anyway required if a moving geometry is involved, but does not require to store solar REFs.

Finally, a posteriori variance reduction strategies were reviewed along with ray tracing acceleration techniques. Already implemented in ESARAD, USD and linear averaging REFs smoothing schemes were selected. Efficient ray-intersection algorithms were also presented.

Benchmarking quasi-Monte Carlo ray tracing

3

Abstract

This chapter applies the REFs and OHFs computation strategies developed in Chapter 2 to more complex geometries. Three cases are considered among which two are actual space structures. The performances observed with two or three faces are validated. As the REFs are only intermediate results, the convergence of the temperatures is also assessed. Finally, the ray tracing acceleration provided by the USD technique is discussed.

3.1 Introduction

The purpose of this chapter is to apply the developments and confirm the results presented in the previous chapter. So far, models containing only two or three faces with limited multiple reflection possibilities were considered. This chapter assesses the performances of the method with more complicated geometries and multiple reflections.

The concept of face and shell is now distinguished. We define a shell as a two-sided surface while a face refers to one of its sides. As opposed to mechanical analyses, the two sides of one shell may have different thermo-optical properties and one side of a shell may even be inactive if for instance it represents the skin of an opaque volume. In that case, no ray is emitted from that side. Different thermo-optical properties on each side is very common in thermal analysis as S/C and instrument panels may have a different surface finish. In some cases, the mechanical engineer may model thick walls with shells while the thermal analyst may require different nodes on each side to represent thermal gradient across the thickness of the shell. In that case, the mechanical mesh may need to be slightly adapted for the thermal analysis and/or the thermal engineer involved in the creation of the structural mesh. One specific example is the multi-layer insulation (MLI) that is usually not modelled in the mechanical mesh and modelled as one shell with two faces in the thermal model. The two faces of the MLI are coupled through the thickness of the shell conductively and radiatively.

This chapter is organised as follows. Section 3.2 focusses on the more academic case of two perpendicular cylinders. Next, two actual space structures developed at the Centre Spatial de Liège are studied namely one reflective entrance baffle of the Extreme UV imager on board Solar Orbiter mission and the sun baffle of the CAA mechanism on board the Sentinel-4 UVN mission. Conclusions of the benchmarking are eventually drawn in Section 3.6.

3.2 Perpendicular cylinders

The first structure to be analysed consists of two 500 mm long identical cylinders with a diameter of 100 mm and perpendicular to each other. Both are composed of 240 identical shells and the internal side of each cylinder is set inactive. Figure 3.1(a) represents the perpendicular cylinders mesh and the shell numbering. The infrared emittance and solar absorptance are set to 50% with 50% specular reflectance in both visible and infrared bands.

3.2.1 Radiative exchanges factors

The REFs are computed with ESARAD and compared to the coupled Halton sampling strategy. Figure 3.1(b) gives the convergence of the RMS LSE in function of the number of rays. The RMS LSE takes into account all faces in the model and is defined as

$$\mathrm{LSE}_{\mathrm{RMS}} = \sqrt{\frac{1}{n_{\mathrm{faces}}} \sum_{i=1}^{n_{\mathrm{faces}}} \mathrm{LSE}_i^2}$$

The gain is less significant than in the previous chapter since most of the faces have a unit REF with the environment and only few of them see the other cylinder and can contribute to the improvement. A factor 3 reduction is achieved if the target LSE is 0.1% and increases to ten if the target is 0.01%.

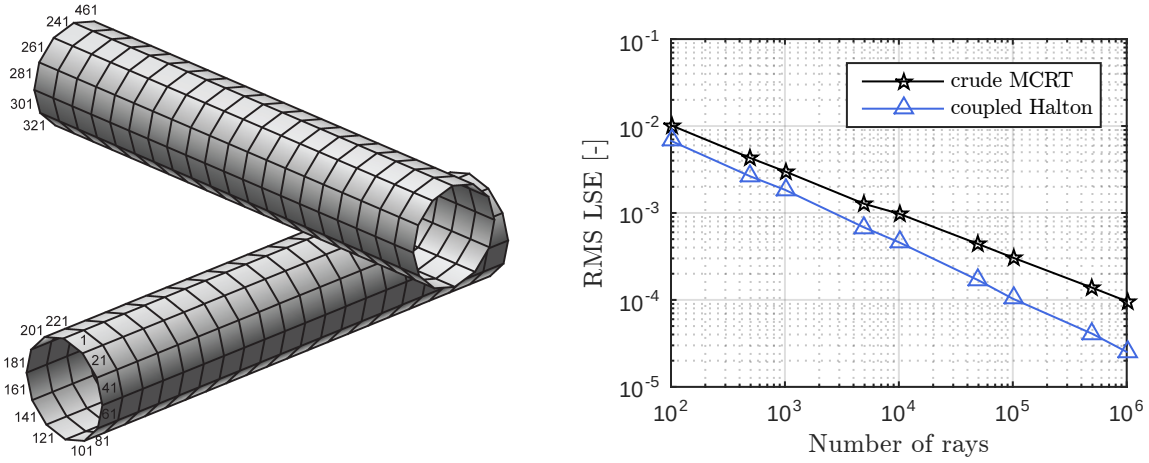

(a) (b)

Figure 3.1 – Perpendicular cylinders mesh and shell numbering (a). Convergence of the LSE (b).

3.2.2 Orbital heat fluxes

To assess the performances of the PFHS method for OHFs computation, the two cylinders are placed in orbit around the Earth at an altitude of 400 km with an inclination of 51.6 degrees, similar to the one of the International Space Station. Figure 3.2(a) shows the circular orbit and its orientation with respect to the Sun and the Earth with the right ascension of the ascending node fixed at 60 degrees. The attitude is such that the x axis depicted by the red arrows always points towards the Sun and that the z axis depicted by the blue arrows lies within the orbital plane. Figure 3.2(b) represents the distribution of the average albedo heat flux absorbed by the cylinders all over the orbit. The top cylinder shows a circular distribution with a maximum around 34 W m^{-2} and casts a shadow over the second one. Figure 3.3(a) gives the evolution of the total absorbed albedo heat rate of each cylinder. Starting from around 5 W at the ascending node for both front and back cylinders, it drops to zero in eclipse before rising again to 8.5 W and 6.5 W for the $-x$ and $+x$ cylinder, respectively.

Figure 3.3(b) shows the convergence of the error on albedo heat fluxes. It is measured as the RMS error over the faces and orbital positions as defined in Equation 2.44. The PFHS method exhibits a large performance increase and requires more than 10 times fewer rays for the same accuracy even though the convergence rate is only slightly higher than the one obtained with ESARAD.

3.2.3 Radiative equilibrium temperatures

The REFs and OHFs are usually not the ultimate variables of interest and are only auxiliary data used to derive the temperatures. To assess the end-to-end performances of

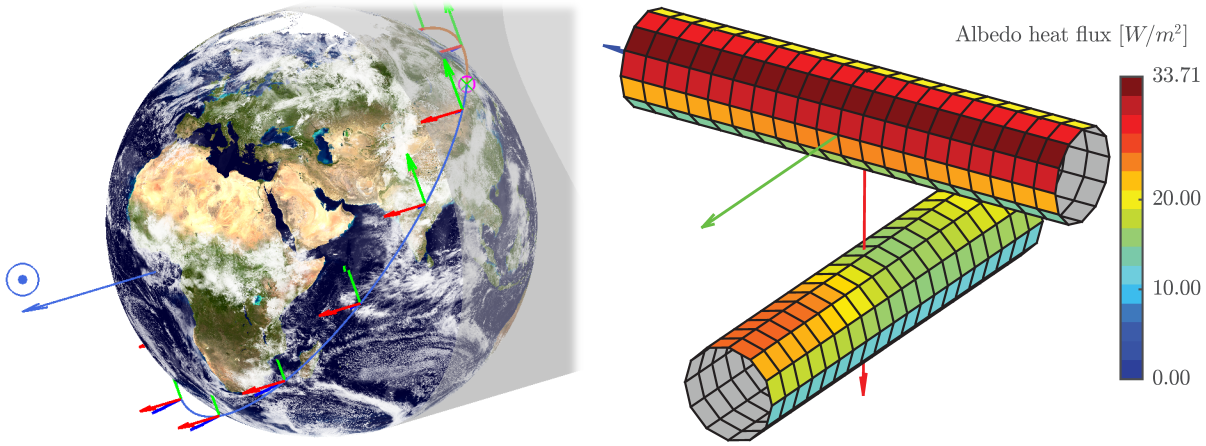

(a) (b)

Figure 3.2 – 400 km high, 51.6 degrees inclination circular orbit with the x axis (in red) Sun pointing and the z axis (in blue) in the orbital plane (a). Average albedo heat flux absorbed by the cylinders. The internal faces are greyed since they are inactive (b).

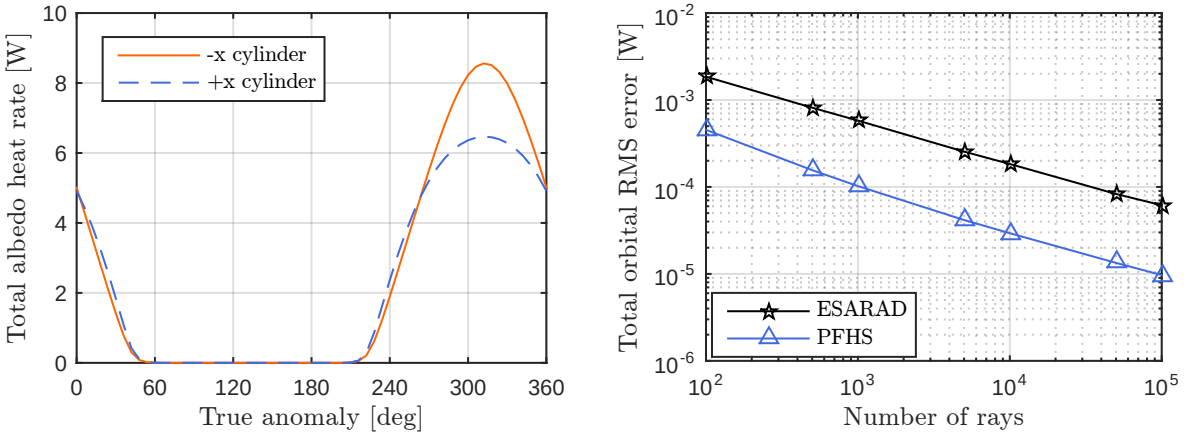

(a) (b)

Figure 3.3 – Evolution of the total albedo heat rate absorbed by each cylinder over the orbit (a). Convergence of the error on the albedo heat fluxes with the number of rays. The planet focused Halton sampling (PFHS) method gives more than one order of magnitude improvement over ESARAD (b).

the method, the temperatures are computed based on a pure steady state radiative equilibrium. The system then becomes linear in terms of the fourth power of the temperature or emissive power. To compute the nodal temperatures, the REFs and OHFs computed between faces are evenly distributed on the nodes as described in [31]. The model is thus composed of 504 nodes in addition to the 3 K deep space node. The linear system is solved by splitting the system into the known and unknown variables $\mathbf{E}_\mathrm{B}$ and $\mathbf{E}_\mathrm{U}$, respectively.

$$\begin{bmatrix} \mathbf{K}_{R\mathrm{UU}} & \mathbf{K}_{R\mathrm{UB}} \\ \mathbf{K}_{R\mathrm{UB}}^\intercal & \mathbf{K}_{R\mathrm{BB}} \end{bmatrix} \begin{bmatrix} \mathbf{E}_\mathrm{U} \\ \mathbf{E}_\mathrm{B} \end{bmatrix} = \begin{bmatrix} \mathbf{Q}_\mathrm{U} \\ \mathbf{Q}_\mathrm{B} \end{bmatrix}$$

The unknown nodal emissive powers $\mathbf{E}_\mathrm{U} = \sigma \mathbf{T}_\mathrm{U}^4$ are obtained with

$$\mathbf{E}_\mathrm{U} = \mathbf{K}_{R\mathrm{UU}}^{-1} \left(\mathbf{Q}_\mathrm{U} - \mathbf{K}_{R\mathrm{UB}} \mathbf{E}_\mathrm{B} \right)$$

Figure 3.4(a) presents the reference temperature solution corresponding to the albedo heat fluxes at the initial true anomaly. Radiative equilibrium temperatures vary between 66 K and 229 K and the back side of the $+x$ cylinder presents lower temperatures as it is directly facing deep space. As expected, the $+x$ cylinder influences the $-x$ cylinder by radiatively heating its back side. Figure 3.4(b) gives the convergence of the RMS temperature error as a function of the number of rays traced for REFs and OHFs computations. To achieve 1 K error, the PFHS method requires ten times fewer rays than ESARAD. Because the convergence rate is higher the gain further increases with the required accuracy level.

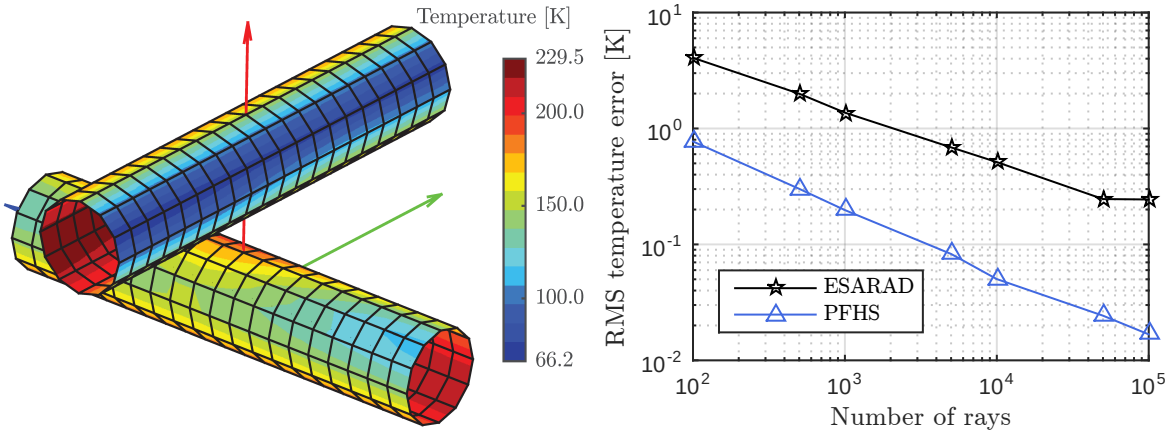

(a) (b)

Figure 3.4 – Temperature distribution of the reference solution. The $+x$ (red axis) cylinder is colder than the other cylinder (a). Convergence of the temperature results with the number of rays traced for the computation of the REFs and OHFs (b).

3.3 Solar Orbiter EUI entrance baffle

The previous example did not involve many internal exchanges between the surfaces of the model but had many surfaces exposed to albedo with shadowing effects. One entrance

baffle of the EUI (Extreme UV Imager) instrument was chosen as second benchmarking geometry because of its more complex shape generating more internal heat exchanges.

3.3.1 EUI and the Solar Orbiter Mission

EUI is a remote sensing space instrument currently in its development phase D at the Centre Spatial de Liège (CSL) [24, 315, 316]. It was selected to fly on board the Solar Orbiter Mission, the first European Space Agency medium-class mission (from ESA's Cosmic Vision 2015-2025 Programme), dedicated to study the solar and heliospheric physics. The S/C will be launched in 2019 in a 0.28 A.U. perihelion Sun-centred orbit. The spacecraft will be in Venus resonant orbit to increase its inclination and providing a unique out-of-ecliptic co-rotating vantage point at perihelion.

The solar heat flux increasing quadratically as the distance decreases, it will reach 13 solar constants, *i.e.* $17.4\,\mathrm{kW\,m^{-2}}$ at perihelion. The thermal design of the instrument is highly critical and its temperature ranges from $-70\,^{\circ}\mathrm{C}$ to $200\,^{\circ}\mathrm{C}$. Figure 3.5 gives a picture of the qualification model of the instrument in CSL ISO 5[1] cleanroom. EUI comprises three telescopes: two high resolution imagers (HRI), one observing at the Lyman-α line (121.6 nm) and one in the extreme-UV (EUV) at the 17.4 nm line, achieving both a resolution of 100 km per pixel and one full-Sun imager presenting a resolution of 900 km per pixel and observing alternatively at 17.4 nm and 30.4 nm. Highly critical filters are located close to each pupil of the instrument to reject the unwanted visible and infrared part of the solar spectrum. The extreme-UV entrance filter is particularly sensitive because it is made of a 150 nm thick Aluminium foil. Each filter is protected by reclosable doors on top of which are mounted entrance baffles. To avoid overheating, the heat absorbed by the entrance filter, door and baffle assemblies is evacuated through heat pipes towards a thermal interface with the S/C. An Aluminium coating developed at CSL is deposited on the internal side of the HRI entrance baffles to provide low solar absorptance and higher specular reflectance. Their conical shape is designed to reflect the unwanted solar flux and to protect the entrance filters.

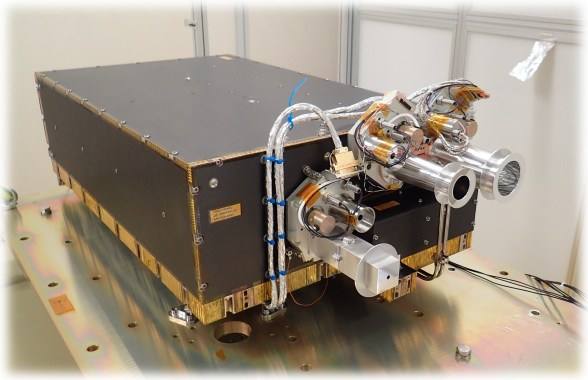

Figure 3.5 – EUI instrument qualification model in CSL ISO 5 cleanroom, with doors and entrance baffles in the foreground.

[1] ISO 5 standard cleanroom is equivalent to previously named class 100. The class number corresponds to the maximum number of particles of size 0.5 µm or larger allowed per cubic foot of air.

3.3.2 Radiative exchanges factors

Figure 3.6(a) presents a preliminary GMM mesh of the HRI EUV entrance baffle where the back of the baffle is artificially closed for the purpose of this study. It is composed of 363 vertices, 360 shells (720 faces). The average face area is 62.8 mm^2 (ranging from 19 mm^2 to 151 mm^2). For the purpose of this validation, both sides are assumed to have the same thermo-optical properties: 0.1 IR emittance with 0.9 IR specular reflectance and 0.2 solar absorptance (end-of-life property which include potential degradation of the coating) with 0.8 specular reflectance.

Figure 3.6(b) gives the convergence of the RMS LSE as a function of the number of rays and compares the coupled Halton sampling to ESARAD. This time, the performance gain is slight higher than for the two cylinders case with a factor 5 improvement for a target LSE of 0.1% and still gives a factor 10 improvement for 0.01%.

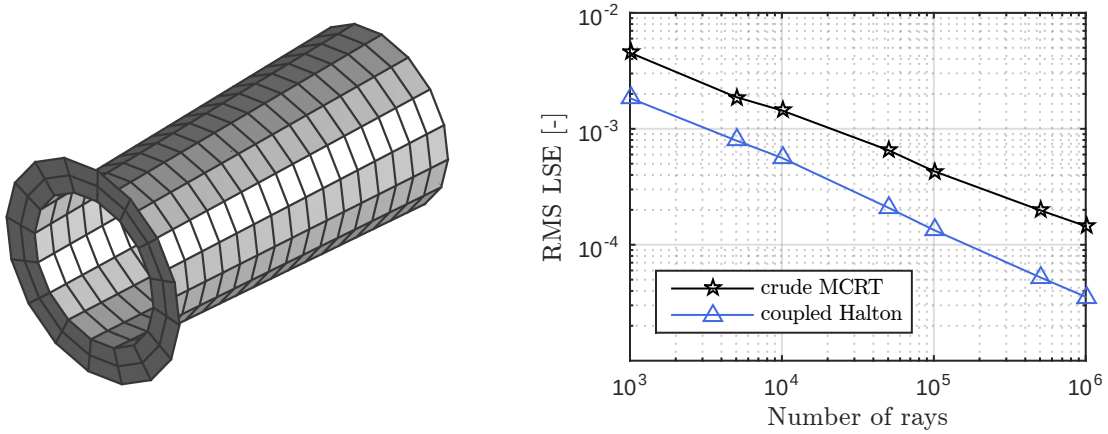

(a) (b)

Figure 3.6 – Early EUI entrance baffle GMM (a). Convergence of the RMS LSE with the number of rays (b).

Figure 3.7(a) and (b) show the distribution of the LSE over the model obtained with ESARAD and coupled Halton sampling, respectively. Both methods show qualitatively similar results with high LSE appearing only for a few faces inside the baffle. For a same number of rays, the level of the LSE is however three times lower with the coupled Halton sampling.

3.3.3 Orbital heat fluxes

Except during Earth and Venus fly-bys, Solar Orbiter is not exposed to planetary heat fluxes. This benchmark thus focuses on the solar heat fluxes computed at perihelion. The baffle is tilted by 10 degrees from the Sun axis to simulate off-pointing[1]. Figure 3.8(a) shows the resulting absorbed solar heat fluxes. Due to the reflection on the side of the baffle, the flux is concentrated at the back of the baffle. Even though the absorptance

[1]In reality, feedthrough inside the 400 mm thick S/C heat-shield block any sunlight from entering the aperture of the instrument at such high off-pointing angle. This simulation case is thus purely academic.

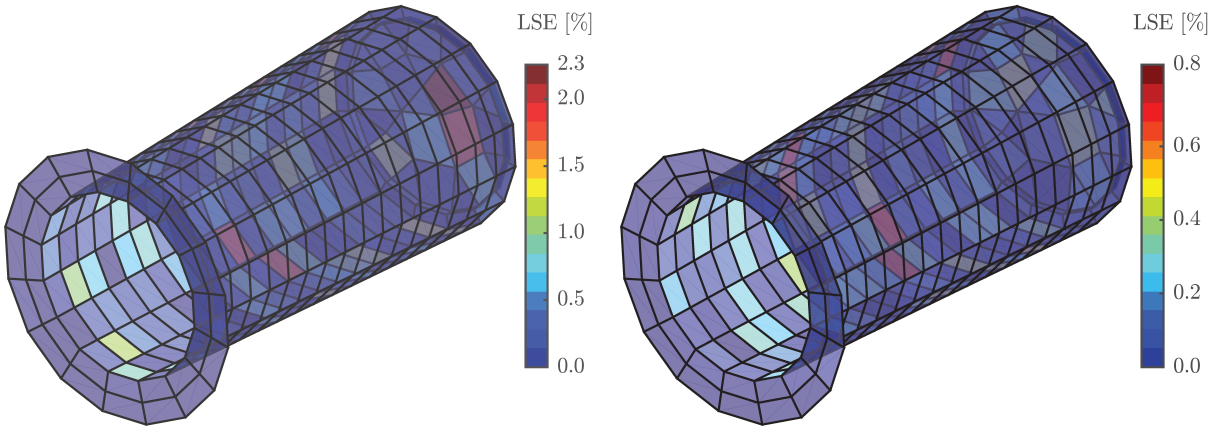

(a) (b)

Figure 3.7 – EUI entrance baffle LSE obtained with the crude MCRT from ESARAD (a) and coupled Halton sampling (b) and 1000 rays. The mesh is made transparent to better view internal faces. Both methods produce similar results in terms of distribution with only a few faces exhibiting high values.

is 0.2 and leads to an absorbed heat flux of $3485\,\mathrm{W\,m^{-2}}$ for a normal incidence, it is concentrated up to $10.4\,\mathrm{kW\,m^{-2}}$.

The convergence of the RMS error on the solar absorbed heat fluxes is presented in Figure 3.8(b). Solar rays are considered parallel so that the only difference consists in the surface sampling that is performed with the Halton low-discrepancy sequence. The new strategy offers two orders of magnitude improvement with an RMS error already ten times lower with 1000 rays. As described in Section 2.3.6 where the effect of thermo-optical properties was assessed, specular reflections tend to produce better results than diffuse reflections since the uniformity of the sampling is not modified after being reflected. Diffuse reflections are expected to reduce the performances of the method. This reduction is assessed with the next study case.

3.3.4 Radiative equilibrium temperatures

Again, temperatures resulting from a pure radiative equilibrium are computed. The mechanical interface of the baffle, located at the back along the circumference, is maintained at 20 °C and the radiative environment is fixed at 50 °C. The converged temperature distribution is presented in Figure 3.9(a). The off-pointing and the concentration at the end of the baffle give rise to an asymmetrical temperature profile and very high temperatures are observed because conduction is neglected in this analysis. The front of the baffle also exhibits very high temperatures because the sunlight is almost normal to the surface. Figure 3.9(b) shows the convergence of the error in function of the number of rays traced to compute the REFs and the OHFs. The performances are similar to the one observed in the cylinder case: the Halton sampling requires ten times as less rays as ESARAD to achieve the same accuracy on the temperature.

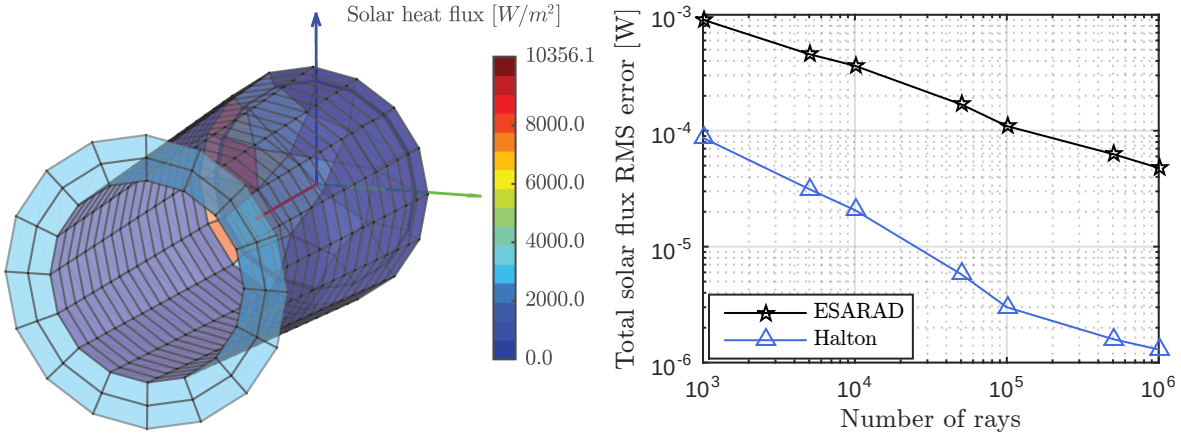

(a) (b)

Figure 3.8 – EUI entrance baffle absorbed solar heat fluxes (a). Convergence of the solar heat fluxes computed with ESARAD and Halton method (b).

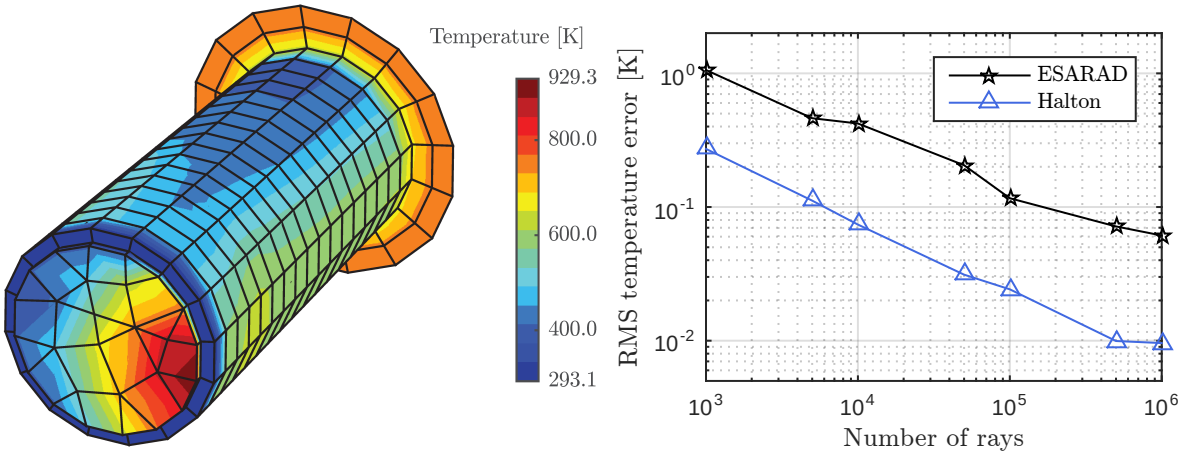

(a) (b)

Figure 3.9 – Temperature distribution resulting from the application of heat fluxes presented in Figure 3.8(a) with a boundary condition applied at the back of the baffle (a). Convergence of the error in function of the number of traced rays (b).

3.4 Sentinel 4 UVN baffle LPM model

3.4.1 The Sentinel 4 mission, UVN instrument and CAA mechanism

SENTINEL 4 is an imaging UVN (Ultraviolet 305-400nm/Visible 400-500nm/Near-infrared 750-775nm) spectrometer, developed by Airbus Defence and Space under an ESA contract in the frame of the joint European Union/ESA COPERNICUS program [317]. The mission objective is the monitoring of air quality through trace gas concentrations [318]. Sentinel-4 will share the Meteosat Third Generation (MTG) platform with the IRS (infrared sounder) instrument as depicted in Figure 3.10(a). It will fly on a geostationary orbit to provide air quality measurements over Europe at spatial and temporal frequencies corresponding to typical tropospheric pollutants variability (temporal frequency less than 1h and spatial scales less than 10 km). The UVN instrument features a calibration assembly (CAA) mechanism currently under development at the Centre Spatial de Liège. Its qualification model is shown in Figure 3.10(b). This mechanism provides two means of calibration: one with a white light source and one with diffused sunlight entering the mechanism through a Sun baffle located on the left of Figure 3.10(b). The CAA is located outside the S/C and the Sun baffle is thus painted in white to avoid too high temperature when exposed to the Sun. To limit straylight coming from the Earth entering the instrument, the Sun baffle is also equipped with vanes and is black anodized to absorb unwanted light. The name Sun baffle is therefore misleading since the baffle is designed to let only the Sun rays in and to trap photons coming from the Earth.

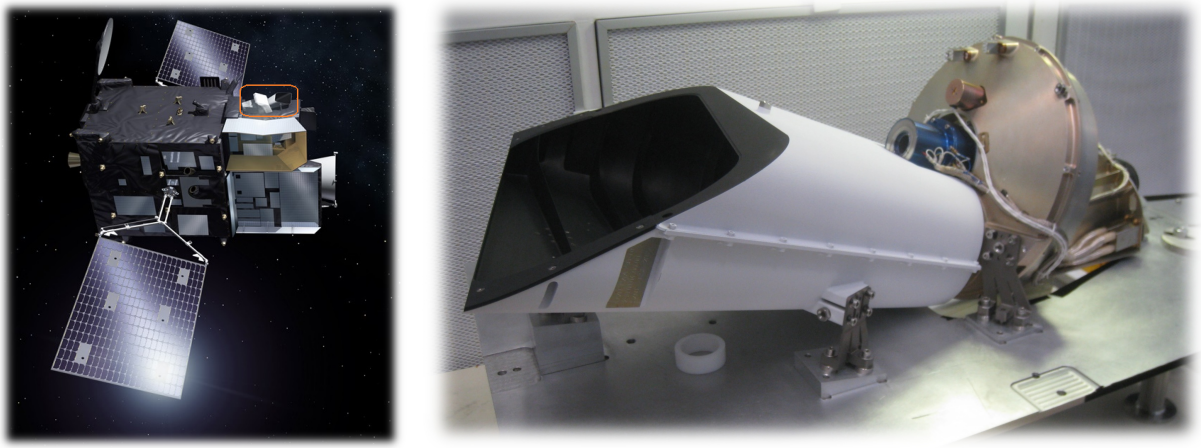

(a) (b)

Figure 3.10 – MTG platform with the IRS instrument on the bottom right, the UVN instrument above it and the CAA encircled in orange (a). UVN CAA qualification model with the Sun baffle mounted in front of the wheel mechanism in CSL ISO 5 cleanroom (b).

3.4.2 Radiative exchanges factors

The thermo-optical properties of the CAA Sun baffle are summarised in Table 3.1. End-of-life properties are assumed. In particular, the solar absorptance of the MAP

PCBE white paint is high due to the space environment degradation (UV exposure, contamination). In both parts of the spectrum, the reflectance is diffuse. Figure 3.11(a) shows the location of the thermo-optical properties on the GMM. This GMM is the actual one used in ESATAN for all thermal analyses in the project. The irregular geometry of the Sun baffle required to model it as flat faces since no ESATAN-TMS primitive shape was able to match the CAD model.

	ε	$\rho_{d,\mathrm{IR}}$	α	$\rho_{d,\mathrm{VIS}}$
MAP PCBE	0.88	0.12	0.50	0.50
Black anodization	0.90	0.10	0.93	0.07

Table 3.1 – CAA Sun baffle thermo-optical properties.

The coupled Halton sampling method was applied to compute the REFs. Figure 3.11(b) gives the convergence of the error with only diffuse reflections compared to specular reflections occurring in the EUI entrance baffle. With 1000 rays, the gain in terms of number of rays is slightly reduced from 5 to 3 compared to Figure 3.6(b). Because of the higher convergence rate, the gain increases to almost 10 to achieve 3 10^{-4} RMS LSE.

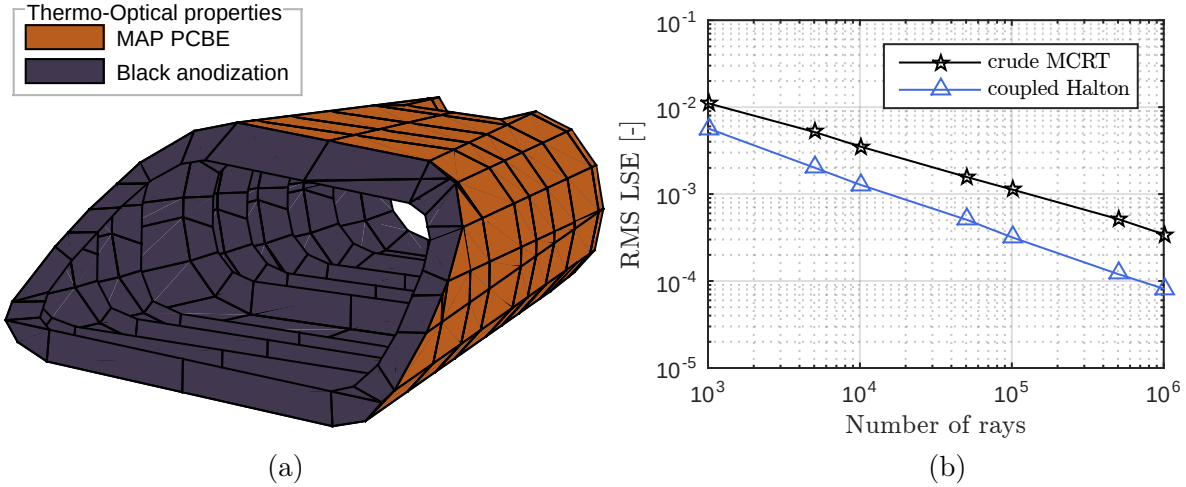

(a) (b)

Figure 3.11 – Sun Baffle GMM with thermo-optical properties location (a). Convergence of the RMS line sum error with the number of rays (b).

3.4.3 Orbital heat fluxes

Being on a geostationary orbit, infrared and albedo planetary heat fluxes are neglected and only solar heat fluxes are computed. The CAA Sun baffle is oriented such that the vector $\begin{bmatrix}-1 & 1 & -1\end{bmatrix}$ is pointing to the Sun. The axes are represented in Figure 3.12(a) along with the absorbed heat fluxes. Because it is black anodized, the front face and internal sides of the baffle absorb more sunlight than the external lateral sides with a maximum occurring on the internal vanes.

Figure 3.12(b) presents the convergence of the solar heat fluxes computation. Because of the diffuse reflectance, the performances are reduced compared to a specular case. Nevertheless, for the same RMS error, the Halton sampling requires at least 50 times as less rays as the crude Monte Carlo method implemented in ESARAD.

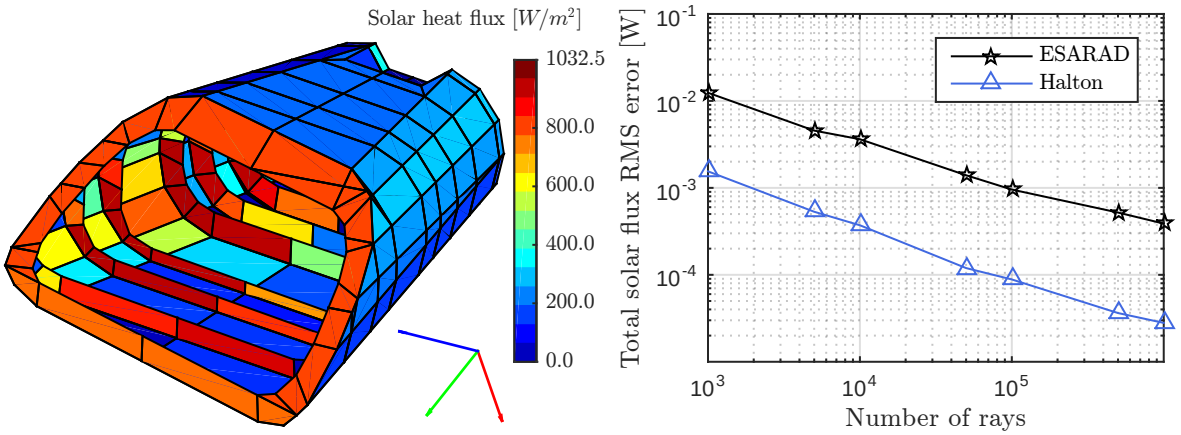

(a) (b)

Figure 3.12 – Solar heat fluxes absorbed when the vector $[-1\ 1\ -1]$ is pointing to the Sun. The x, y and z axes are represented by the red, green and blue arrows, respectively (a). Convergence solar heat flux RMS error in function of the number of rays (b).

3.4.4 Radiative equilibrium temperatures

For the computation of the temperatures, the Sun baffle is left free to reach its radiative equilibrium with the deep space environment. Again, conduction is neglected and only one position is analysed.

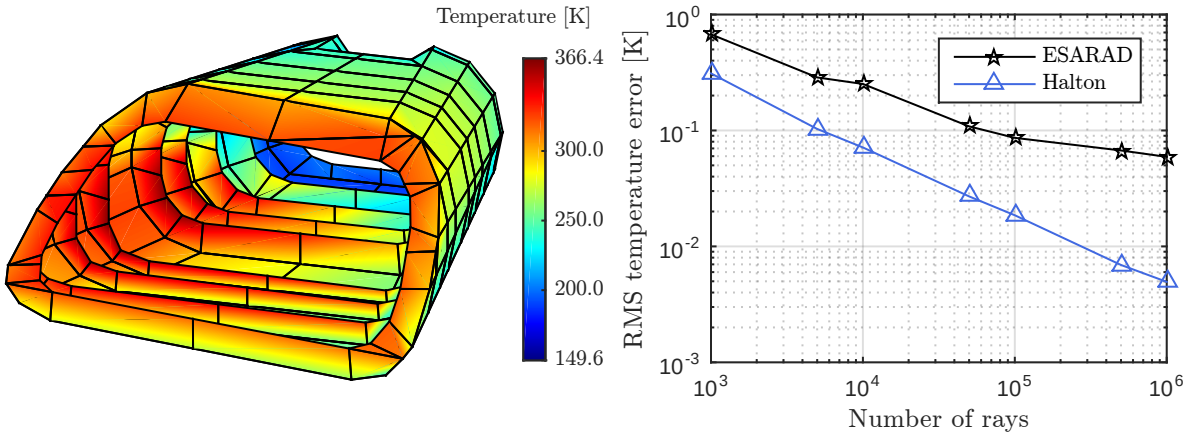

(a) (b)

Figure 3.13 – Temperature distribution of the UVN CAA Sun baffle submitted to the solar heat flux depicted in Figure 3.12(a), in radiative equilibrium with the deep space node at 3 K without conduction (a). Convergence of the RMS temperature error (b).

The resulting temperature profile is given in Figure 3.13. Temperatures vary between 150 K and 366 K with the maximum temperature located along the internal vane edges. The minimum temperature is located in the shaded region at end of the baffle. For the convergence, results similar to the ones obtained with EUI entrance baffle are observed. A factor 5 reduction is achieved with 1000 rays. The small saturation effect visible in the ESARAD convergence curve is explained by numeric inaccuracies in the large quadrangle intersection computation. Control parameters implemented in our ray tracing algorithm might not be the same than the one implemented in ESARAD.

3.5 Space subdivision

In all previous study cases, the USD technique described in Section 2.5.2 was employed as a means of ray tracing acceleration. Table 3.2 summarises the key geometrical figures of the three configurations. A wide range of active faces density is covered to validate the philosophy. The faces density is the number of active faces divided by the total volume of the box surrounding the model. The EUI entrance baffle is more compact and the number of faces per unit volume is higher than for the other two geometries.

	# of active faces n_f	Surrounding box volume [m^3]	n_f density [m^{-3}]	Face area [m^2]		
				Min	Mean	Max
Cylinders	480	$7.7\ 10^{-2}$	$6.2\ 10^{3}$	$6.5\ 10^{-4}$	$6.5\ 10^{-4}$	$6.5\ 10^{-4}$
EUI baffle	720	$5.6\ 10^{-4}$	$1.3\ 10^{6}$	$1.9\ 10^{-5}$	$6.3\ 10^{-5}$	$1.5\ 10^{-4}$
UVN baffle	648	$5.9\ 10^{-2}$	$1.1\ 10^{4}$	$5.6\ 10^{-7}$	$1.6\ 10^{-3}$	$1.3\ 10^{-2}$

Table 3.2 – Comparison between the FEM and the LPM.

Figure 3.14 gives the relative time (actual time divided by the minimum achieved) spent for the REFs computation with 1000 rays. For each case, the number of voxels was varied and the computation time measured. As the computation time may slightly fluctuate from one run to another, it is averaged over 10 runs. All three curves show that USD offers a significant reduction of the computation time if the volume is divided in the optimum number of voxels.

ed The right end of each curve corresponds to one voxel, *i.e.* the space is not divided and all shells are checked for intersection for each ray. As the number of voxels increases, the computation time decreases until an minimum is reached. Further increasing the number of voxels involves more time wasted in the voxel traversal computation and voxel data processing. Comparing all three curves seems to indicate that the optimum number of voxel does strongly depend on the geometrical configuration of the model and that a value around two shells per voxel always requires a computation time close to the minimum. This value was used in the previous sections and the optimal number of voxels to achieve two shells per voxel is obtained iteratively.

3.6 Concluding remarks

The purpose of this chapter was to assess the performances of the method developed in Chapter 2 on real space structures. The 4-dimensional Halton sampling and planet-

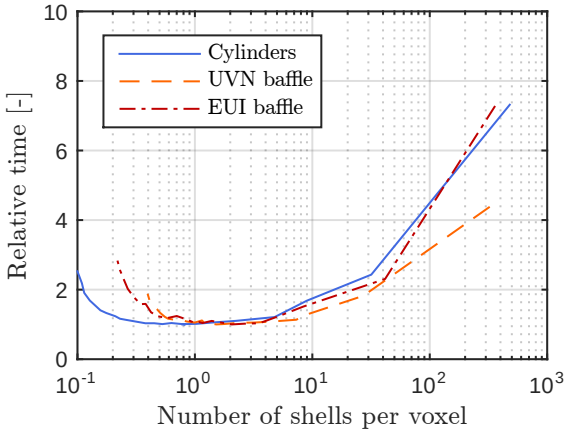

Figure 3.14 – Total relative computation time in function of the total number of voxels for all three configurations studied in this chapter.

focused Halton sampling strategies were applied to models with several hundreds of faces. Performances similar to the two or three faces cases were observed: between two and ten times as less rays as crude MCRT are required to achieve the same REFs accuracy and between 10 and 100 times as less rays are required for orbital heat fluxes computation for both albedo and solar heat fluxes. Diffuse and specular reflectances were considered. Based on heat fluxes and REFs, the convergence of the temperature was also studied. The improvements observed for REFS and OHFs were transposed to the temperatures. Conduction was neglected to highlight radiative effects. If conductive links are included and if the solution is primarily driven by conductive effects, temperature differences are reduced and the curves in Figures 3.4(b), 3.9(b) and 3.13(b) are closer to each other.

Finite element mesh clustering and super nodes

4

Abstract

Reducing the number of faces is another key to decrease the REFs computation time. To this aim, this chapter first discusses the clustering of a detailed FE mesh. The process includes initialisation through k-means clustering followed by greedy region growing and boundary smoothing. In addition to the radiative reduction, the generated clusters also drive the conductive reduction and the concept of super node is defined. From this definition, the algorithm to efficiently derive the reduced conduction matrix is developed. The procedure also allows recovering the detailed temperatures from the reduced ones. The reduction process and detailed temperature recovery are then validated with two simple structures.

4.1 Introduction

Improving the MCRT was the first step to alleviate the radiative couplings computation issue. As mentioned in the introduction, reducing the number of faces is the second natural approach to decrease the REFs computation time.

The idea of creating patches for radiative heat transfer analyses with FEM has been around for quite some time [45, 319]. The method described in [319] relies on Oppenheim's radiosity method [149] and needs corrective terms to cancel false diffusion effects due to the redistribution of the reduced radiation couplings to the underlying mesh since the model is solved on the detailed mesh. The radiation super element method introduced in [45] also redistributes back the reduced REFs onto the detailed FE mesh. In the computational fluid dynamics (CFD) tool ANSYS Fluent, face clustering is also exploited to compute radiation heat exchanges but they are again re-distributed to the underlying detailed mesh faces. These methods reduce the radiative model without the conductive model and redistribute the REFs onto the conductive mesh, therefore limiting the use of detailed structural meshes.

As the temperature field is usually much smoother than the deformation field, the thermal model requires a much coarser mesh than a mechanical model. Finite element mesh clustering therefore seems the proper path to follow to reduce the number of REFs to compute and the size of the associated non-sparse matrix. However, the accuracy of the conductive links still relies on the detailed FE mesh. We therefore propose to take advantage of the clusters to reduce both the conductive and radiative models. This is the second step and keystone towards the re-unification of LPM and FEM through global reduction.

Each cluster will be associated to one or several super nodes representing its average temperature. The proposed scheme exploits all the conductive information of the underlying detailed FE mesh to generate accurate reduced conductive links. In parallel, the ray tracing will be applied to the super node external surfaces, called super faces, to generate the reduced radiative couplings between the super nodes. The reduced conductive radiative model can then be solved to determine the temperature of the super nodes. The conductive reduction further provides a method to recover back an approximation of the detailed mesh temperatures from the reduced ones. Figure 4.1 illustrates the proposed global reduction process.

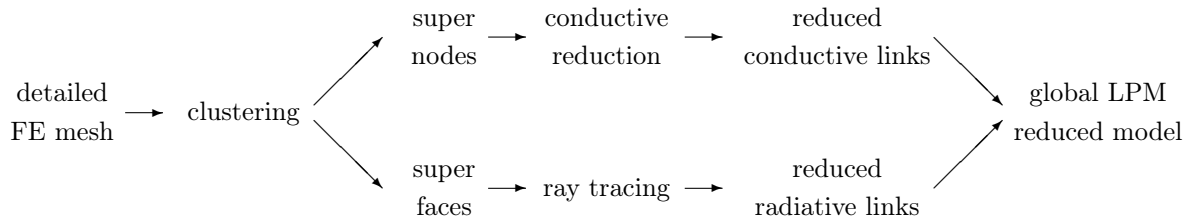

Figure 4.1 – The FE mesh clustering drives the conductive and radiative reduction process to generate a global LPM reduced model.

This chapter first focusses on the clustering algorithm in Section 4.2. In Section 4.3,

the super node concept is mathematically defined and the reduced conduction matrix is derived. The reduction method is then validated in one and two dimensions in Section 4.4. Section 4.5 eventually provides some concluding remarks. Chapter 5 will be devoted to the adaptation of the ray tracing to the super faces.

4.2 The clustering process

This section presents the clustering process, starting point towards the reduction of the number external faces and REF matrix size. Mesh clustering is already used in a variety of mesh-based scientific simulations to reduce computation time by taking advantage of parallel computing [320–323]. Clustering is also widely applied to image processing [324, 325] and reverse engineering to retrieve surface properties from scanned data [326]. While there exist many standard clustering algorithms like METIS [320] and others [322, 323] developed in different fields, we chose to develop our own partitioning algorithm to keep it simple, versatile and adapted to our needs.

The clustering of the detailed FE mesh is performed in several steps and each independent part of the model is processed separately. The desired number of clusters is set for each part by the thermal engineer, like when creating a separate dedicated thermal model and mesh. As introduced later in Section 4.3, the concept of super node relies on the unique assumption which is being uniformly subjected to external heat fluxes. 2D parts are therefore first divided into regions to avoid clusters from crossing sharp edges or junctions (edges sharing more than 2 elements) because these features inherently involve non-uniformity in the REFs and environmental heat fluxes. Each 2D region as defined above is then partitioned independently. Thermo-optical properties can also be taken into account in the clustering process to avoid again clusters from being composed of too non-uniform radiative properties.

3D parts are not divided into regions since volume elements have external faces crossing sharp edges by definition. They are partitioned as a whole in volume clusters. However, should the material have low thermal conductivity or a large gradient be expected between the centre of the 3D clusters and the external faces of those clusters, one may add dedicated 2D super nodes to represent the external faces temperature to better capture radiative heat exchanges. Figure 4.2 describes the 2D and 3D clustering schemes.

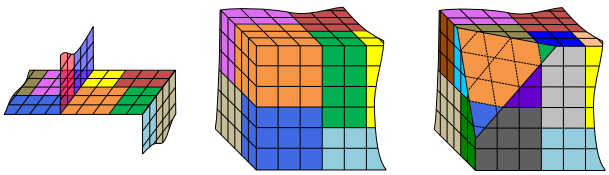

(a) (b) (c)

Figure 4.2 – Different clustering strategies for 2D and 3D: clusters do not cross sharp edges for 2D parts (a) while 3D clusters may contain faces on different sides (b) or have dedicated surface super nodes associated with each 3D cluster (c).

After separating the 2D and 3D parts into the different regions, the clustering scheme is applied to each of them independently. It is based on a multiple source greedy region growing algorithm [323] and is divided into three steps:

- the k-means clustering initialisation of a user-defined number of seed elements,
- the greedy region growing itself, starting from those seed elements
- and finally boundary smoothing with max-flow/min-cut algorithm.

4.2.1 K-means clustering seeding

This region growing algorithm strongly depends on the seeds that initiate the process. To create uniform clusters, the seed elements are selected by applying the k-means clustering algorithm to the centre of gravity of all elements. K-means was developed in the mid-1950s independently in several scientific fields [327, 328], the most famous being Lloyd [329] (k-means algorithm is also known as Lloyd's algorithm). It provides a partition of a set of points $\mathbf{p}$ that minimises the distance between the cluster average and all its assigned points:

$$\min \sum_{k=1}^{n_c} \sum_{\mathbf{p}_i \in c_k} \|\mathbf{p}_i - \boldsymbol{\mu}_k\|^2$$

where n_c is the requested number of clusters and $\boldsymbol{\mu}_k$ is the centre of the k^{th} cluster c_k defined as

$$\boldsymbol{\mu}_k = \frac{1}{n_k} \sum_{\mathbf{p}_i \in c_k} \mathbf{p}_i$$

with n_k the number of points in the cluster c_k. K-means is an iterative algorithm that requires cluster centre initialisation and therefore only converges to a local minimum, different initial cluster centres resulting in different partitions.

In structural analysis, the mesh is often refined in location where large stresses are expected. To avoid the k-means clustering algorithm from producing more clusters in the refined mesh area, a weighted version of the algorithm is used. The cluster centre is re-defined as the weighted average of its constituents:

$$\boldsymbol{\mu}_k = \frac{\sum_{\mathbf{p}_i \in c_k} w_i \mathbf{p}_i}{\sum_{\mathbf{p}_i \in c_k} w_i}$$

and the algorithm now minimises the sum of the weighted distance in all clusters

$$\min \sum_{k=1}^{n_c} \sum_{\mathbf{p}_i \in c_k} w_i \|\mathbf{p}_i - \boldsymbol{\mu}_k\|^2$$

Since the points $\mathbf{p}_i$ here correspond to the centre of gravity of the elements, the weights are simply defined as the area for 2D elements or their volume for 3D elements. Figure 4.3 gives an example of k-means clustering of 2000 points non-uniformly distributed over the unit square. In Figure 4.3(a), the unweighted version of the k-means clustering algorithm is applied and more populated regions therefore attract more clusters. Conversely, Figure 4.3(b) shows that the weighted k-means algorithm produces more uniformly spaced clusters even in non-uniform data point sets. Details about the implementation of the algorithm are given in [330, 331].

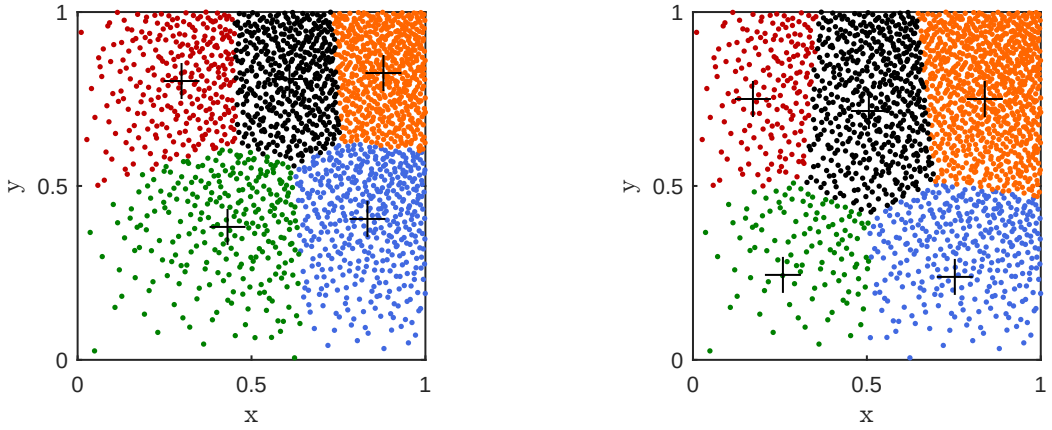

Figure 4.3 – Two-dimensional unweighted k-means clustering of 2000 non-uniformly spread points in the unit square (a). Weighted k-means clustering (b). The point set is partitioned in 5 clusters and the final cluster centres are depicted by the black crosses.

The k-means algorithm already provides clusters but does not ensure contiguous clusters. This is why it is only used for the generation of the seed elements of the greedy region growing. The seed element is thus defined as the closest element to each k-means cluster centre.

Because the region growing process is based on a distance criterion to some seeds that are initiated by a k-means clustering, the clustering strategy tends to generate Voronoi-like shapes, as illustrated in Figure 4.3. The boundaries between the clusters consist in the perpendicular bisector segments (or planes in 3D) of the line segment joining the cluster centres. The Voronoi-like nodal shapes agree with Dusinberre [14] recommendation to perform LPM nodal breakdown following a triangular heat flow pattern. The classical rectangular nodal breakdown is however preferred to Dusinberre's sound approach for practical reasons: as depicted in Figure 4.4, the triangular pattern results in Voronoi-like shapes whose volume and conductive link are less easy to compute compared to rectangular pattern.

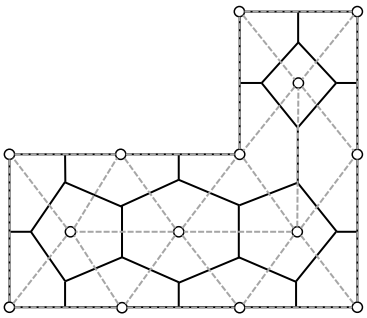

Figure 4.4 – Dusinberre's triangular heat flow nodal breakdown approach [14, 33]. The grey dotted lines represent the heat flows and the black lines the nodes boundaries.

4.2.2 Greedy region growing clustering

For a given set of seed elements, the algorithm iteratively adds the adjacent elements to build each cluster in parallel, therefore enforcing contiguous clusters. To determine the next element to be added to a given cluster, the distance between the centre of gravity of the element and the one of the seed element of the cluster is computed. All candidates (next adjacent elements of all existing clusters) are pushed in a queue that is sorted with respect to the distance to the seed of their potential cluster affiliation. The candidate with the smallest distance is pulled out from the queue, attributed to the corresponding cluster and its adjacent elements are added to the queue. Figures 4.5(a-e) depict the region growing process. The elements in the queue are represented by the light-shaded colour and correspond to the adjacent elements of the already assigned ones represented by bright colours. Starting from the orange, blue and red seed elements, the queue is initialised with the three neighbours of each seed (Figure 4.5(b)). In Figure 4.5(c), one of the orange neighbour is pulled out from the queue and its two unassigned adjacent elements added. The next element to be assigned is the blue one as depicted in Figure 4.5(d). At some point, elements will appear multiple times in the queue when they are adjacent to several clusters. Since they are sorted according to their distance to the cluster seed, only the closest will be assigned. The algorithm loops until all elements are assigned to one cluster. Finally the boundary smoothing step is performed.

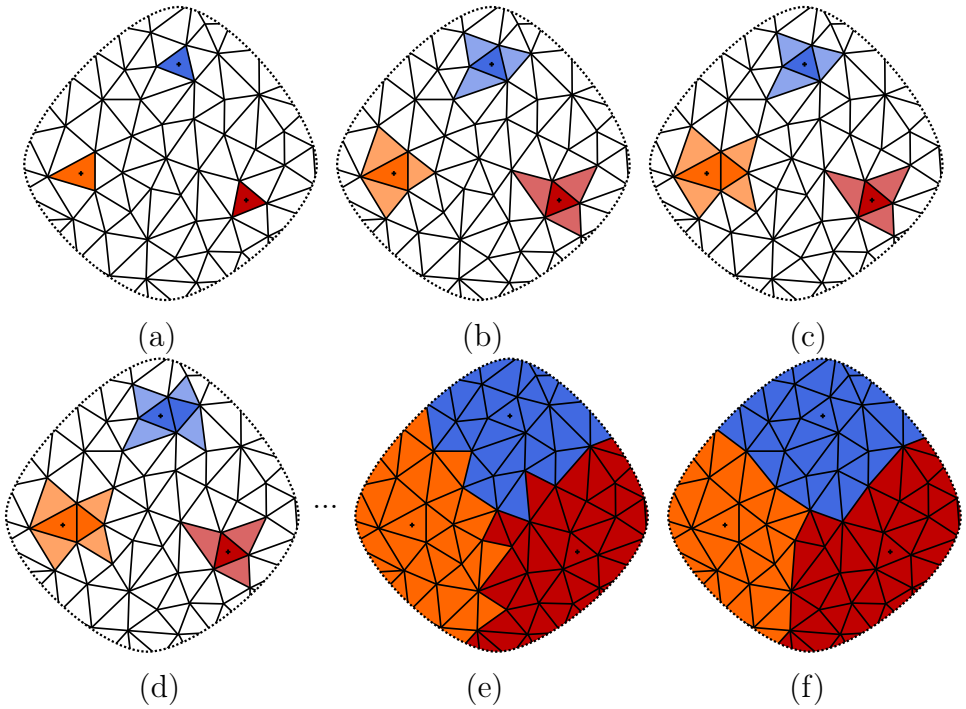

Figure 4.5 – The different mesh clustering steps: k-means clustering selection of seeds (a), initialisation of the queue with adjacent elements of seeds (b), iterative extraction from the queue (represented by the light shaded elements) and assignment of candidate with smallest distance to its cluster seed with addition of its adjacent elements to the queue (c,d) until all elements are assigned to one cluster (e), boundary smoothing (f).

4.2.3 Cluster boundary smoothing

As introduced in the previous sections, once the greedy region growing is completed, a post-processing phase to smooth the cluster boundaries is performed as in [326]. Smoothing the boundaries is not mandatory but having straight edges instead of zigzag boundary curves can be exploited in the subsequent ray tracing step to reduce the computation time.

Smoothing the boundary is equivalent to minimising the total length of the boundary between two clusters by re-assigning the elements of the fuzzy region to either one of the two clusters, knowing that each element is attracted to both clusters according to its distance to the cluster centre. First, the dual undirected graph of the fuzzy region to smooth is considered: each external face becomes a vertex in the dual graph and two vertices are linked if their corresponding faces are adjacent to each other. The set of dual vertices v_i belonging to the fuzzy region to smooth and the set of edges e_i linking the vertices of the dual graph are denoted $\mathcal{V}$ and $\mathcal{E}$, respectively. The function to minimise is expressed by

$$E(\mathbf{x}) = \sum_{v_i \in \mathcal{V}} E_1(x_i) + \sum_{e_i \in \mathcal{E}} E_2(e_i) \tag{4.1}$$

where $\mathbf{x}$ is a binary vector representing the affiliation of the dual vertices v_i to either one of the two clusters ($x_i = 0$ if v_i belongs to the first cluster and $x_i = 1$ if v_i belongs to the second). The term $E_1(x_i)$ represents a penalty function based on the attraction of the vertex v_i to either the first cluster A or the second cluster B:

$$E_1(x_i = 0) = \frac{d_i^A}{d_i^A + d_i^B} \quad \text{and} \quad E_1(x_i = 1) = \frac{d_i^B}{d_i^A + d_i^B}$$

The second energy term $E_2(e_i)$ is the cost of the dual edge e_i connecting too linked vertices x_j and x_k:

$$E_2(e_i) = \frac{l_{ij}}{l_{ij} + \bar{l}}$$

where l_{ij} is the length of the primal shared edge between the two faces corresponding to x_j and x_k and $\bar{l}$ is the average edge length over the whole boundary.

Greig *et al.* discovered in the end of the 1980s [332] that max-flow/min-cut algorithms are suitable to minimise energy functions of binary variables as Equation 4.1 and the implementation of Greig's algorithm by Boykov and Kolmogorov [333], thoroughly used in image processing and computer vision, is exploited.

Figure 4.6 shows the result of the boundary smoothing procedure applied after partitioning a circular mesh in two clusters. The initial k-means cluster centres are drawn with the white crosses and the corresponding region growing seed elements are filled with red. Figure 4.6(a) shows the dual graph with the dual vertices $v_i \in \mathcal{V}$ (light green dots) and edges $e_i \in \mathcal{E}$ (light green dotted line) of the boundary elements and their first neighbours (on each side of the boundary). Figure 4.6(b) gives the results of the minimisation of Equation 4.1 through the max-flow/min-cut algorithm. In this example, the number of layers on each side of the boundary taken into account for the dual graph generation was two but it can be easily modified to include more elements and give more freedom to the smoothing process.

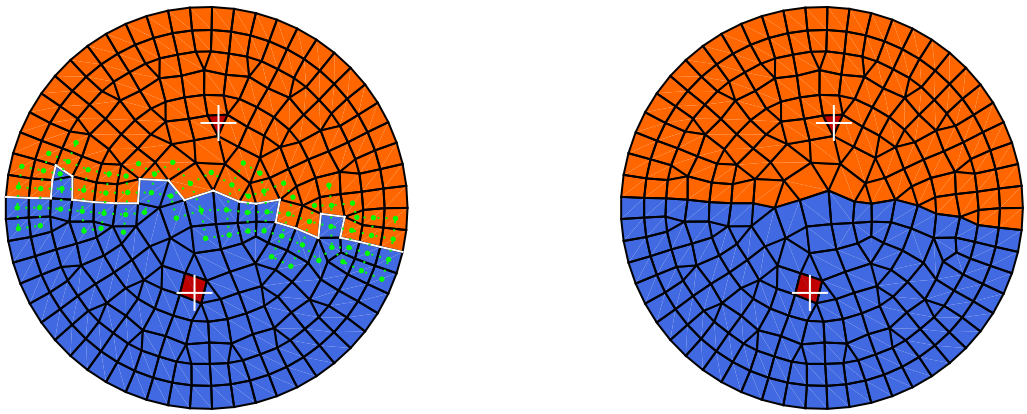

(a) (b)

Figure 4.6 – Raw output of the greedy region growing algorithm with the unsmoothed boundary between the two clusters is depicted in white and the dual graph in light green (a). Boundary smoothing resulting from the Boykov-Kolmogorov's max-flow/min-cut algorithm (b).

4.3 The conductive reduction process

4.3.1 Super node definition, reduction and recovery

Once the detailed mesh is partitioned, the conductive model needs to be mathematically reduced. The reduction procedure is inspired from the EQUIVALE method [105, 174] developed by Aerospatiale (now Thales Alenia Space), the RCN (reduced conductive network) method implemented in THERMICA [102], from the TLP-reduction method introduced in [176] and the LPM-FEM mapping tool SINAS [56, 60]. First the concept of super node is defined: it is a new mathematical node whose temperature represents the average temperature of a group of nodes of the underlying detailed finite element model:

$$T_{\mathrm{SN}_i} = \sum_{j=1}^{n_n} a_{ij} T_j$$

where T_{SN_i} is the temperature of the i^{th} super node, n_n is the number of nodes of the detailed model. a_{ij} is the relative weight of the detailed mesh node j contributing to super node i and is equal to 0 if it does not belong to super node i. The sum of all relative weights of a super node is equal to 1: $\sum_{j=1}^{n_n} a_{ij} = 1$. In matrix form this gives:

$$\mathbf{T}_{\mathrm{SN}} = \mathbf{A}\mathbf{T} \tag{4.2}$$

with the $n_{\mathrm{SN}} \times n_n$ matrix $\mathbf{A}$ containing the relative weights and n_{SN} the number of super nodes. Weights are given by the capacitance associated to the node divided by the total capacitance of the cluster:

$$a_{ij} = \frac{c_j}{\sum_{j \in \mathrm{SN}_i} c_j}$$

where c_j is the capacitance associated with a detailed node j. In steady state, the specific heat is not required and the weights can be based on the volume (area times thickness for 2D elements). As introduced in Section 4.2, surface super nodes can also be defined on the external boundary of 3D clusters if a strong gradient is expected between the surface and its centre. For those super nodes, the weight is defined as the area of the node divided by the total area of the super node. Dedicated super nodes are also defined similarly at the boundary conditions and at interfaces between connected parts (where contact conductance might be applied).

The foundation of the reduction procedure is the linear steady state heat equation obtained from Equation 1.55:

$$\mathbf{K}_L \mathbf{T} = \mathbf{q} \tag{4.3}$$

where $\mathbf{K}_L$ is the linear $n_n \times n_n$ conduction matrix, $\mathbf{T}$ is the $n_n \times 1$ vector of nodal temperatures and $\mathbf{q}$ the $n_n \times 1$ nodal thermal load vector. Combining the definition of the super nodes given by Equation 4.2 and the above equation gives:

$$\mathbf{M} \begin{bmatrix} \mathbf{T} \\ \mathbf{0}^{n_{\text{SN}} \times 1} \end{bmatrix} = \begin{bmatrix} \mathbf{q} \\ \mathbf{T}_{\text{SN}} \end{bmatrix} \tag{4.4}$$

with the $(n_n + n_{\text{SN}}) \times (n_n + n_{\text{SN}})$ matrix $\mathbf{M}$ defined as follows:

$$\mathbf{M} = \begin{bmatrix} \mathbf{K}_L & \mathbf{A}^\intercal \\ \mathbf{A} & \mathbf{0}^{n_{\text{SN}} \times n_{\text{SN}}} \end{bmatrix}$$

Solving Equation 4.4 for $\mathbf{T}$ and sub-structuring the inverse of $\mathbf{M}$ gives:

$$\begin{bmatrix} \mathbf{T} \\ \mathbf{0}^{n_{\text{SN}} \times 1} \end{bmatrix} = \mathbf{M}^{-1} \begin{bmatrix} \mathbf{q} \\ \mathbf{T}_{\text{SN}} \end{bmatrix} = \begin{bmatrix} \mathbf{X} & \mathbf{Y}^\intercal \\ \mathbf{Y} & \mathbf{Z} \end{bmatrix} \begin{bmatrix} \mathbf{q} \\ \mathbf{T}_{\text{SN}} \end{bmatrix} \tag{4.5}$$

If the load is uniform over each super node, *i.e.* uniform with respect to the super node definition given in Equation 4.2, the detailed thermal load vector $\mathbf{q}$ is related to the super nodes thermal load $\mathbf{q}_{\text{SN}}$ by the same matrix $\mathbf{A}$:

$$\mathbf{q} = \mathbf{A}^\intercal \mathbf{q}_{\text{SN}} \tag{4.6}$$

Since $\mathbf{Y}\mathbf{A}^\intercal = \mathbf{I} = \mathbf{A}\mathbf{Y}^\intercal$, the super nodes thermal load vector $\mathbf{q}_{\text{SN}}$ can be obtained from the detailed one $\mathbf{q}$:

$$\mathbf{q}_{\text{SN}} = \mathbf{Y}\mathbf{q}$$

Extracting the second row of Equation 4.5

$$-\mathbf{Z}\mathbf{T}_{\text{SN}} = \mathbf{Y}\mathbf{q} = \mathbf{q}_{\text{SN}}$$

leads to the identification of the matrix $-\mathbf{Z}$ as the linear conduction matrix of the reduced system $\mathbf{K}_{L\text{SN}}$:

$$\mathbf{K}_{L\text{SN}} \mathbf{T}_{\text{SN}} = \mathbf{q}_{\text{SN}} \tag{4.7}$$

The first row of Equation 4.5 is used to compute back the detailed mesh temperatures from the super nodes temperatures:

$$\mathbf{T} = \mathbf{X}\mathbf{q} + \mathbf{Y}^{\intercal}\mathbf{T}_{\text{SN}} \tag{4.8}$$

To proof that the reduced system is equivalent to the detailed system, the above equation and Equation 4.6 are inserted in the detailed system equation defined by Equation 4.3 and pre-multiplied by $\mathbf{Y}$:

$$\mathbf{K}_L(\mathbf{X}\mathbf{q} + \mathbf{Y}^{\intercal}\mathbf{T}_{\text{SN}}) = \mathbf{A}^{\intercal}\mathbf{q}_{\text{SN}}$$

$$\mathbf{Y}\mathbf{K}_L\mathbf{X}\mathbf{q} + \mathbf{Y}\mathbf{K}_L\mathbf{Y}^{\intercal}\mathbf{T}_{\text{SN}} = \mathbf{Y}\mathbf{A}^{\intercal}\mathbf{q}_{\text{SN}} = \mathbf{q}_{\text{SN}}$$

This equation is equivalent to the reduced system described by Equation 4.7 if:

- the first term $\mathbf{Y}\mathbf{K}_L\mathbf{X}$ is equal to zero,
- and $\mathbf{Y}\mathbf{K}_L\mathbf{Y}^{\intercal}$ is equal to the reduced conduction matrix $\mathbf{K}_{L\text{SN}}$

The first condition is demonstrated by inverting the matrix $\mathbf{M}$ block-wise:

$$\begin{aligned}\mathbf{M}^{-1} &= \begin{bmatrix}\mathbf{X} & \mathbf{Y}^{\intercal} \\ \mathbf{Y} & -\mathbf{K}_{L\text{SN}}\end{bmatrix} = \begin{bmatrix}\mathbf{K}_L & \mathbf{A}^{\intercal} \\ \mathbf{A} & \mathbf{0}^{n_{\text{SN}}\times n_{\text{SN}}}\end{bmatrix}^{-1} \\ &= \begin{bmatrix}\mathbf{K}_L^{-1} - \mathbf{K}^{-1}\mathbf{A}^{\intercal}\left(\mathbf{A}\mathbf{K}_L^{-1}\mathbf{A}^{\intercal}\right)^{-1}\mathbf{A}\mathbf{K}_L^{-1} & \mathbf{K}_L^{-1}\mathbf{A}^{\intercal}\left(\mathbf{A}\mathbf{K}_L^{-1}\mathbf{A}^{\intercal}\right)^{-1} \\ \left(\mathbf{A}\mathbf{K}_L^{-1}\mathbf{A}^{\intercal}\right)^{-1}\mathbf{A}\mathbf{K}_L^{-1} & -\left(\mathbf{A}\mathbf{K}_L^{-1}\mathbf{A}^{\intercal}\right)^{-1}\end{bmatrix}\end{aligned}$$

and expanding the term $\mathbf{Y}\mathbf{K}_L\mathbf{X}$:

$$\begin{aligned}\mathbf{Y}\mathbf{K}_L\mathbf{X} &= \left(\mathbf{A}\mathbf{K}_L^{-1}\mathbf{A}^{\intercal}\right)^{-1}\mathbf{A}\mathbf{K}_L^{-1}\mathbf{K}_L\left(\mathbf{K}_L^{-1} - \mathbf{K}_L^{-1}\mathbf{A}^{\intercal}\left(\mathbf{A}\mathbf{K}_L^{-1}\mathbf{A}^{\intercal}\right)^{-1}\mathbf{A}\mathbf{K}_L^{-1}\right) \\ &= \left(\mathbf{A}\mathbf{K}_L^{-1}\mathbf{A}^{\intercal}\right)^{-1}\mathbf{A}\mathbf{K}_L^{-1}\mathbf{K}_L\mathbf{K}_L^{-1} - \left(\mathbf{A}\mathbf{K}_L^{-1}\mathbf{A}^{\intercal}\right)^{-1}\mathbf{A}\mathbf{K}_L^{-1}\mathbf{K}_L\mathbf{K}_L^{-1}\mathbf{A}^{\intercal}\left(\mathbf{A}\mathbf{K}_L^{-1}\mathbf{A}^{\intercal}\right)^{-1}\mathbf{A}\mathbf{K}_L^{-1} \\ &= \left(\mathbf{A}\mathbf{K}_L^{-1}\mathbf{A}^{\intercal}\right)^{-1}\mathbf{A}\mathbf{K}_L^{-1} - \left(\mathbf{A}\mathbf{K}_L^{-1}\mathbf{A}^{\intercal}\right)^{-1}\mathbf{A}\mathbf{K}_L^{-1} = 0\end{aligned}$$

The second condition $\mathbf{Y}\mathbf{K}_L\mathbf{Y}^{\intercal} = \mathbf{K}_{L\text{SN}}$ is also validated:

$$\mathbf{Y}\mathbf{K}_L\mathbf{Y}^{\intercal} = \left(\mathbf{A}\mathbf{K}_L^{-1}\mathbf{A}^{\intercal}\right)^{-1}\mathbf{A}\mathbf{K}_L^{-1}\mathbf{K}_L\mathbf{K}_L^{-1}\mathbf{A}^{\intercal}\left(\mathbf{A}\mathbf{K}_L^{-1}\mathbf{A}^{\intercal}\right)^{-1} = \left(\mathbf{A}\mathbf{K}_L^{-1}\mathbf{A}^{\intercal}\right)^{-1}$$

since the term $\left(\mathbf{A}\mathbf{K}_L^{-1}\mathbf{A}^{\intercal}\right)^{-1}$ is precisely defined as the reduced conduction matrix $\mathbf{K}_{L\text{SN}}$.

4.3.2 Augmented conduction matrix local inversion

It is worth mentioning here that the super nodes must all be linearly independent for the matrix $\mathbf{M}$ to be invertible, meaning that the super node definition matrix $\mathbf{A}$ cannot contain linearly dependent rows, making it singular.

Inverting matrix $\mathbf{M}$ to derive the reduced conduction matrix can be computationally very intensive because it is even larger than the full conduction matrix $\mathbf{K}_L$ and memory demanding since even if $\mathbf{M}$ is relatively sparse, its inverse is not. Furthermore, only a small fraction of $\mathbf{M}^{-1}$ is required to obtain $\mathbf{K}_{L\text{SN}}$ and the matrices $\mathbf{X}$ and $\mathbf{Y}$ are only required to compute back the detailed temperatures. Algorithms were developed for selective

inversion of square matrices [334] that are helpful to generate the reduced conduction matrix but less effective if the $\mathbf{X}$ and $\mathbf{Y}$ matrices are required and need to be stored.

An equivalent alternative was therefore developed to avoid computing $\mathbf{M}^{-1}$. It consists of two steps: first construct and invert, for each super node i, a local version of $\mathbf{M}$ augmented by all interface nodes at the boundary with other super nodes to generate a local reduced conduction matrices of $\mathbf{K}^i_{L\text{SN}}$. These local reduced conduction matrices are then assembled in $\mathbf{K}^*_{L\text{SN}}$, a temporary version of the global reduced conduction matrix containing all interfaces nodes at the boundaries between the super nodes. The second step uses the classical Guyan static condensation [183] technique to remove the temporary kept interfaces nodes from $\mathbf{K}^*_{L\text{SN}}$ and obtain $\mathbf{K}_{L\text{SN}}$. Static condensation consists in splitting the $\mathbf{K}^*_{L\text{SN}}$ matrix into retained and condensed nodes, here denoted with the subscripts $_{\text{SN}}$ and $_{\text{IF}}$:

$$\begin{bmatrix} \mathbf{K}^*_{L\text{SN}_{\text{SN}-\text{SN}}} & \mathbf{K}^*_{L\text{SN}_{\text{SN}-\text{IF}}} \\ \mathbf{K}^*_{L\text{SN}_{\text{IF}-\text{SN}}} & \mathbf{K}^*_{L\text{SN}_{\text{IF}-\text{IF}}} \end{bmatrix} \begin{bmatrix} \mathbf{T}_{\text{SN}} \\ \mathbf{T}_{\text{IF}} \end{bmatrix} = \begin{bmatrix} \mathbf{q}_{\text{SN}} \\ \mathbf{q}_{\text{IF}} \end{bmatrix}$$

The interface nodes can be condensed as in Equation 4.9 to derive the reduced conduction matrix $\mathbf{K}_{L\text{SN}}$ that contains the super nodes.

$$\mathbf{K}_{L\text{SN}} = \mathbf{R}_G^{\intercal} \mathbf{K}^*_{L\text{SN}} \mathbf{R}_G \tag{4.9}$$

where the Guyan reduction matrix $\mathbf{R}_G$ is given by:

$$\mathbf{R}_G = \begin{bmatrix} -\mathbf{K}^*_{L\text{SN}_{\text{IF}-\text{IF}}}{}^{-1} \mathbf{K}^*_{L\text{SN}_{\text{IF}-\text{SN}}} \\ \mathbf{I}^{n_{\text{SN}} \times n_{\text{SN}}} \end{bmatrix}$$

This procedure gives the exact same results as the direct inversion of $\mathbf{M}$. To recover the temperature of the detailed mesh, the same strategy is applied backwards. First the interfaces temperatures are recovered through the Guyan reduction matrix $\mathbf{R}_G$ and then the local $\mathbf{X}^i$ and $\mathbf{Y}^i$ matrices are computed for each super node and the detailed temperature progressively recovered. This procedure avoids the direct inversion of $\mathbf{M}$ and enables to recover the detailed temperatures without storing the full $\mathbf{X}$ and $\mathbf{Y}$ matrices. Figure 4.7 gives a schematic overview of the local inversion procedure.

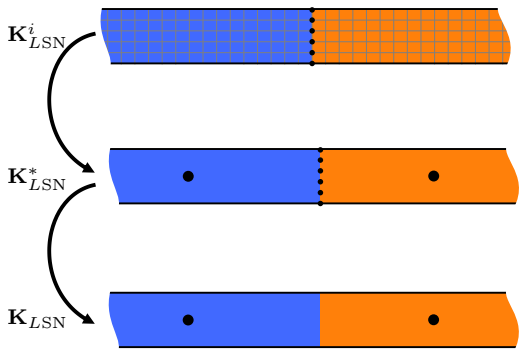

Figure 4.7 – Local inversion scheme to derive the reduced conduction matrix.

The only assumption required for the reduction/recovery process to be exact is that the thermal load on the super nodes is uniform *i.e.* follows the super node relation with its constitutive nodes as expressed by Equation 4.6.

4.4 Validation

4.4.1 The one-dimensional conductive beam

The first example aims at verifying the super node definition by comparison with the analytical solution and considers a beam of length L, cross section S and thermal conductivity k represented in Figure 4.8. The beam is meshed in n_e linear elements with $n_n = n_e + 1$ nodes. In this first example, the temperature of both extremities of the beam is fixed to T_1 and T_2, respectively and a linear heat rate $q(x)$ $\mathrm{W\,m^{-1}}$ is applied. The beam is divided into two super nodes and their temperature is compared to the analytical solution.

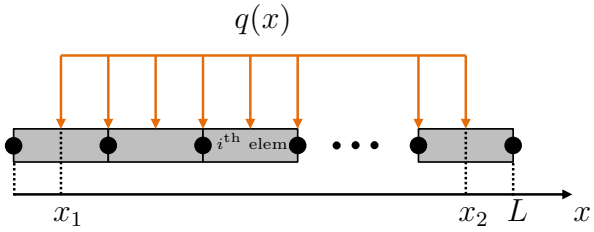

Figure 4.8 – One-dimensional beam of length L and uniform cross section S meshed with n_e elements.

The analytical steady-state temperature distribution of the beam is driven by the second order partial differential equation

$$\frac{d^2T}{dx^2} + \frac{q(x)}{kS} = 0 \tag{4.10}$$

with the boundary conditions $T(x = 0) = T_1$ and $T(x = L) = T_2$. The linear heat rate $q(x)$ is assumed constant over each half of the beam and thus each super node to meet the conductive reduction requirements:

$$q(x) = \begin{cases} q_a, & 0 < x < L/2 \\ q_b, & L/2 < x < L \end{cases}$$

The analytical solution is obtained by solving Equation 4.10 in each half of the domain and ensuring continuity of the solution. The temperature in the first and second halves of the beam are given by

$$T_a(x) = -\frac{q_a x^2}{2kS} + \frac{x}{L}(T2 - T1) + x\frac{L}{8kS}(3q_a + q_b) + T_1 \tag{4.11}$$

$$T_b(x) = -\frac{q_b x^2}{2kS} + \frac{x}{L}(T2 - T1) + x\frac{L}{8kS}(-q_a + 5q_b) + \frac{L^2}{8kS}(q_a - q_b) + T_1 \tag{4.12}$$

respectively. Integrating Equations 4.11 and 4.12 over each half and dividing by $L/2$ gives the analytical expression of the average temperature of each half $\bar{T_a}$ and $\bar{T_b}$:

$$\bar{T_a} = \frac{5L^2 q_a}{96kS} + \frac{L^2 q_b}{32kS} + \frac{3T_1}{4} + \frac{T_2}{4} \tag{4.13}$$

and

$$\bar{T_b} = \frac{L^2 q_a}{32kS} + \frac{5L^2 q_b}{96kS} + \frac{T_1}{4} + \frac{3T_2}{4} \tag{4.14}$$

Now considering the FE solution, the $n_n \times n_n$ conduction matrix $\mathbf{K}_L$ is built and given by

$$\mathbf{K}_L = \frac{n_e kS}{L} \begin{bmatrix} 1 & -1 & 0 & 0 & \dots & 0 & 0 & 0 \\ -1 & 2 & -1 & 0 & \dots & 0 & 0 & 0 \\ 0 & -1 & 2 & 0 & \dots & 0 & 0 & 0 \\ 0 & 0 & -1 & 2 & \dots & 0 & 0 & 0 \\ \vdots & \vdots & \vdots & \vdots & \ddots & \vdots & \vdots & \vdots \\ 0 & 0 & 0 & 0 & \dots & 2 & -1 & 0 \\ 0 & 0 & 0 & 0 & \dots & -1 & 2 & -1 \\ 0 & 0 & 0 & 0 & \dots & 0 & -1 & 1 \end{bmatrix}$$

In addition to the 2 super nodes representing the average temperature of each half of the beam, the 2 interface nodes are kept and the $4 \times n_n$ super node definition matrix $\mathbf{A}$ becomes

$$\mathbf{A} = \frac{1}{n_e} \begin{array}{c} \begin{matrix} 1 & 2 & 3 & \dots & \frac{n_e}{2} & \frac{n_e}{2}+1 & \frac{n_e}{2}+2 & \dots & n_e-1 & n_e & n_e+1 \end{matrix} \\ \begin{bmatrix} n_e & 0 & 0 & \dots & 0 & 0 & 0 & \dots & 0 & 0 & 0 \\ 1 & 2 & 2 & \dots & 2 & 1 & 0 & \dots & 0 & 0 & 0 \\ 0 & 0 & 0 & \dots & 0 & 1 & 2 & \dots & 2 & 2 & 1 \\ 0 & 0 & 0 & \dots & 0 & 0 & 0 & \dots & 0 & 0 & n_e \end{bmatrix} \end{array}$$

where the number of elements n_e is assumed even to have the $n_e/2 + 1^{\text{th}}$ node exactly at the centre of the beam and hence shared equally between the two super nodes. All super nodes are linearly independent and matrix $\mathbf{M}$ can be inverted to give the reduced conduction matrix. If the number of elements of the detailed mesh tends to infinity, the reduced conduction matrix converges to

$$\lim_{n_e \to \infty} \mathbf{K}_{L\text{SN}}(n_e) = \frac{kS}{L} \begin{bmatrix} 7 & -9 & 3 & -1 \\ & 15 & -9 & 3 \\ & \text{sym.} & 15 & -9 \\ & & & 7 \end{bmatrix} \tag{4.15}$$

Extracting rows 2 and 3 from the reduced system formed with reduced converged conduction matrix given in Equation 4.15 leads to

$$\begin{aligned} \frac{kS}{L}\left(-9T_{\text{SN}_1} + 15T_{\text{SN}_2} - 9T_{\text{SN}_3} + 3T_{\text{SN}_4}\right) &= q_{\text{SN}_2} = q_a \frac{L}{2} \\ \frac{kS}{L}\left(3T_{\text{SN}_1} - 9T_{\text{SN}_2} + 15T_{\text{SN}_3} - 9T_{\text{SN}_4}\right) &= q_{\text{SN}_3} = q_b \frac{L}{2} \end{aligned}$$

with T_{SN_1} and T_{SN_4} being equal to the boundary condition temperatures T_1 and T_2, respectively. Solving for T_{SN_2} and T_{SN_3} gives the exact same solution as the one given by Equations 4.13 and 4.14 and obtained from the analytical distribution, *i.e.* $\bar{T_a} = T_{\text{SN}_2}$ and $\bar{T_b} = T_{\text{SN}_3}$.

The performances of the local inversion process is also assessed. To this aim, the time to compute the reduced conduction matrix with the local strategy is compared to the one taken by the global inversion, for different levels of detailed mesh refinement ($10^2 \leq n_e \leq 10^4$) and for 4, 10 and 100 of super nodes. The time complexity of inverting a $n \times n$ matrix ranges between $\mathcal{O}(n^3)$ and $\mathcal{O}(n^{2.38})$ [335]. The observed performance in Matlab (actually using the LAPACK library [336]) is about $\mathcal{O}(n^{2.6})$. Assuming $n_n >> n_{\text{SN}}$, the local inversion strategy therefore reduces the computation time by a factor $n_{\text{SN}}^{1.6}$ which is observed in Figure 4.9. With 10^4 nodes in the detailed model, the gain is about $2^{1.6} \cong 3$ and $10^{1.6} \cong 40$ for $n_{\text{SN}} = 2$ and $n_{\text{SN}} = 10$, respectively.

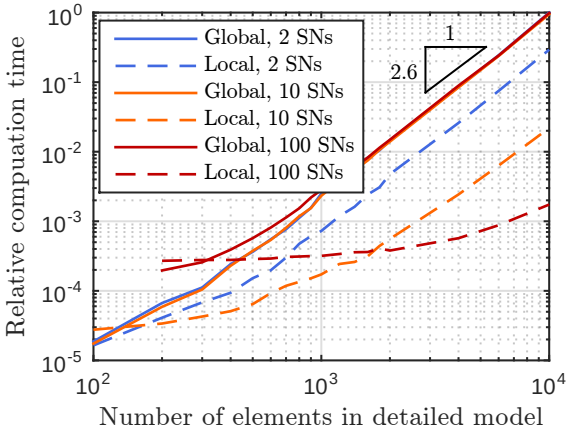

Figure 4.9 – Comparison of the relative computation time of the reduced conduction matrix with the global and local matrix inversion strategies. For $n_n >> n_{\text{SN}}$, the gain approaches $n_{\text{SN}}^{1.6}$.

4.4.2 The one-dimensional conductive-radiative beam

The same beam is considered but only the temperature of the left extremity is fixed. The beam is assumed to be made of Aluminium ($k = 170\,\text{W m}^{-1}\,\text{K}^{-1}$, $c = 900\,\text{J kg}^{-1}\,\text{K}^{-1}$ and $\rho = 2700\,\text{kg m}^{-3}$) and it is 1 m long with a 1 cm wide square cross section. The emissivity ε of its external surface is 1 and the radiative environment temperature T_{sink} is $-100\,°\text{C}$. The fixed temperature T_1 is 20 °C and a 1 W thermal load is spread uniformly along the beam ($q(x) = 1\,\text{W m}^{-1}$). The reference temperature profile along the beam $T(x)$ is given by solving numerically the non-linear second order partial differential equation:

$$\rho c \frac{\partial T}{\partial t} + \frac{\partial^2 T}{\partial x^2} + \frac{4\epsilon\sigma}{kw}(T_{sink}^4 - T^4) + \frac{q}{kw^2} = 0 \tag{4.16}$$

with w the width of the cross section and the following boundary and initial conditions

$$\begin{cases} T(t,0) = 20\,°\text{C} \;\forall\; t \geq 0 \\ \left.\dfrac{\partial T}{\partial x}\right|_{t,x=L} = 0 \;\forall\; t \geq 0 \\ T(0,x) = 20\,°\text{C} \;\forall\; x \end{cases}$$

Figures 4.10(a) and (b) give the steady-state temperature and gradient profiles obtained by numerical integration, respectively. They also show the solution obtained from

the detailed FEM mesh consisting of 1000 linear elements for which the temperature gradient is computed thanks to the super-convergent patch recovery technique described in [337] and introduced by [338]. Both solutions almost perfectly overlap. The solutions obtained after reducing the system to one and two super nodes are also presented with the value of the super nodes and the recovered detailed profiles. The two super nodes solution already give good results with an error of only 3.1 K at the tip of the beam. Figure 4.10(b) highlights that the reduction process assumes a uniform thermal load over the super node and therefore a linear gradient profile in each super node.

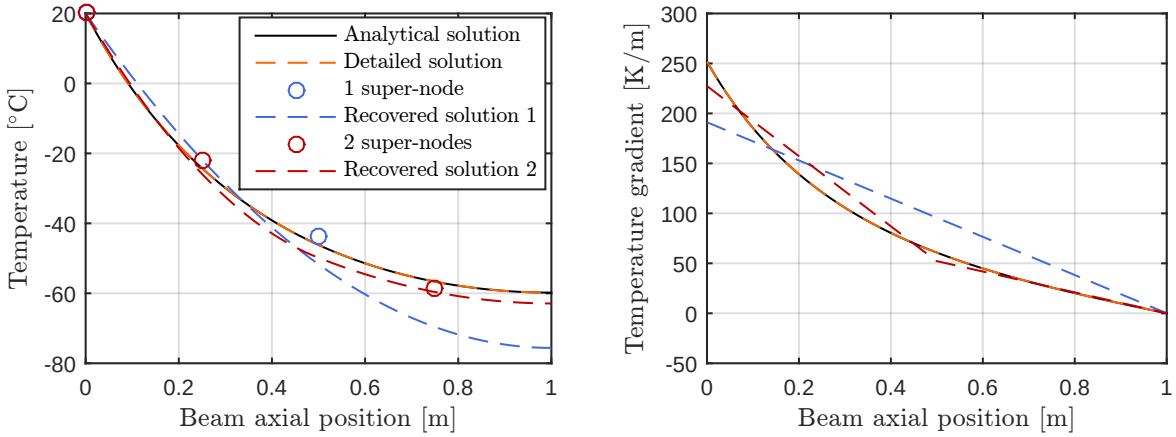

(a) (b)

Figure 4.10 – Temperature profiles along the beam obtained with the numerical integration, FEM detailed and reduced (1 and 2 super nodes) models (a). Corresponding temperature gradient (b).

To compare the recovered solution with the detailed solution, the RMS temperature error $\Delta_{T,\text{RMS}}$ is computed:

$$\Delta_{T,\text{RMS}} = \sqrt{\sum_{i=1}^{n_n} T_{i,d}^2 - T_{i,r}^2} \tag{4.17}$$

where $T_{i,d}$ is the i^{th} node temperature of the detailed solution and $T_{i,r}$ is the i^{th} node temperature recovered after solving the reduced system. In this particular one-dimensional case, the error can be computed with respect to the reference solution obtained from numerical integration of Equation 4.16 for both the detailed and the reduced model: $T_{i,d}$ is then the temperature given by the reference solution at the i^{th} node location and $T_{i,r}$ the temperature given by the finite element detailed or reduced model for the same node.

Using 1 super node leads to approximately 15 K error at the tip and 9.1 K RMS error with respect to the reference solution because the radiative flux is not uniform and violates the reduction assumption. Adding 1 super node already gives better results with only 3.0 K error and the tip for 2.8 K RMS error along the beam. Figure 4.11 shows the RMS error evolution as the number of super nodes is further increased (*i.e.* the reduction factor decreased). Almost quadratic convergence behaviour is observed for both reduced and detailed models and the reduced model gives almost exactly the same error as the FEM with the same number of elements.

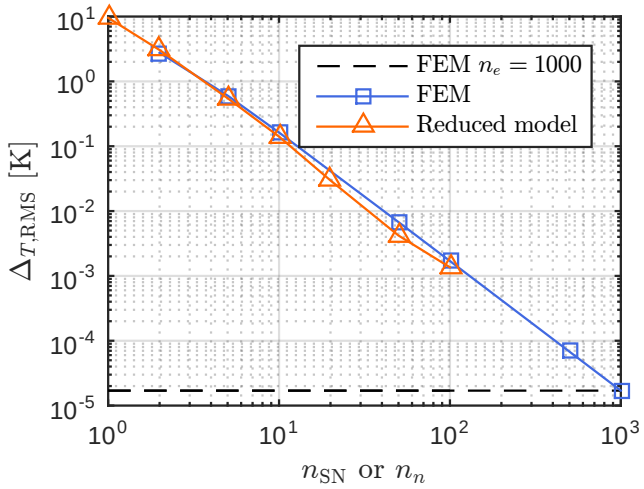

Figure 4.11 – Convergence of the RMS error as a function of the number of nodes or super nodes.

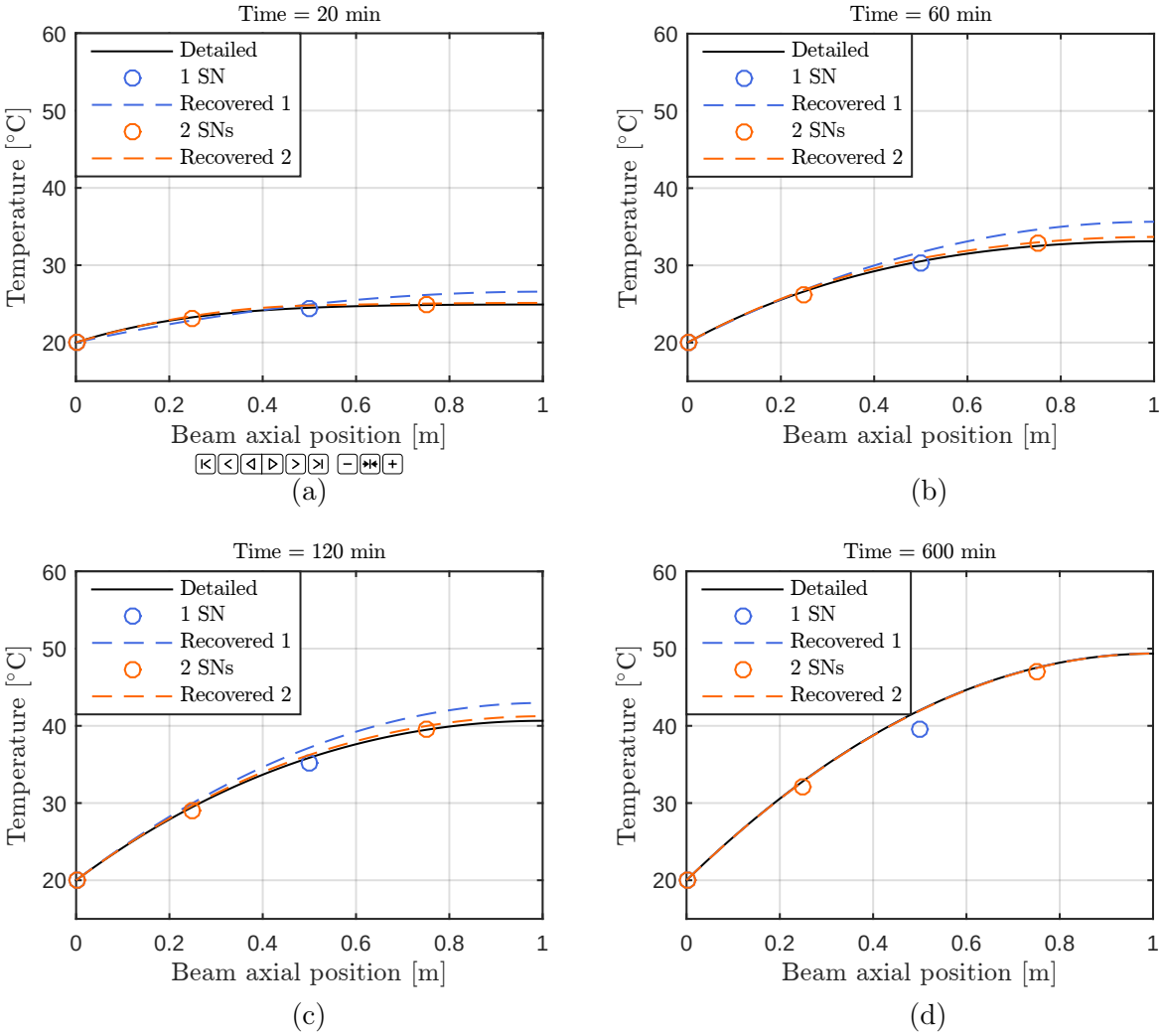

Figure 4.12 – Transient temperature profiles along the cantilever beam obtained with the detailed and reduced (1 and 2 super nodes) models after 20, 60, 120 and 600 minutes.

Radiation is not the only source of non-uniformity and transients also generate non-uniform heat fluxes inside the super nodes. Radiation is neglected to discriminate the effects and only assess the impact of transients, starting from 20 °C and applying the uniform thermal load defined above ($q(x) = 1\,\mathrm{W\,m^{-1}}$). Figures 4.12(a-d) present snapshots of the temperature profile at different times. As expected, transients induce internal energy changes that are not uniform over the super nodes and cannot be captured by the reduced solution. As for radiative heat fluxes, Figures 4.12(a-d) show that increasing the number of super nodes rapidly decreases the error. The solution recovered from the 1 super node reduced model leads to a maximum error with respect to the detailed solution over space and time of 2.6 K while adding one super node already decreases it down to 0.6 K. Once steady state is reached, both reduced models give back the same results as the detailed FEM since the uniform thermal load assumption is again satisfied.

4.4.3 The circular radiating fin

The validation of the methodology is now extended to two dimensions by studying a circular radiating fin. The problem is symmetric and is governed by the one-dimensional non-linear differential equation as described in [35, 339]:

$$\frac{\partial^2 T}{\partial r^2} + \frac{1}{r}\frac{\partial T}{\partial r} + \frac{2\epsilon\sigma}{kt}(T_{sink}^4 - T^4) = 0 \tag{4.18}$$

with the temperature fixed on the inner edge and an insulated outer edge:

$$\begin{cases} T(r_i) = 20\,^\circ\mathrm{C} \\ \left.\dfrac{\partial T}{\partial r}\right|_{r=r_e} = 0 \end{cases}$$

The thickness t of the fin is constant and equal to 1 mm with the internal and external radii being 50 mm and 150 mm, respectively. It is made of Aluminium as the beam in the previous example and is also exposed to a radiative environment whose temperature T_{sink} is at −100 °C. The reference solution is obtained by integrating Equation 4.18 numerically and presented in Figure 4.13(a). Starting from 20 °C on the inner edge, the temperature drops down to −2.87 °C at its outer edge where the temperature gradient becomes equal to zero.

Figure 4.13(b) gives the result of the clustering process obtained with 50 super nodes. It also depicts the underlying detailed FE mesh dividing the fin in 20 elements along the radius and in 120 elements along the circumference for a total of 2400 elements. While there is a constant number of FE over the fin circumference, the number of super nodes increases with the radius since all super nodes tend to have the same area. With 50 super nodes, this results in 10 super nodes at the inner edge and 21 at the outer edge. Figure 4.13(b) also shows that some cluster boundaries are less smoothed than others. This is a consequence of the cluster seed element that are not free to move during the boundary smoothing process and of the boundary smoothing that is operated pair-wise, *i.e.* without considering adjacent elements.

The error with respect to the reference solution is computed with Equation 4.17 and is 0.023 K RMS for the detailed FEM. Figure 4.14 presents the convergence of the reduced and detailed models. The detailed model converges linearly with the number of nodes.

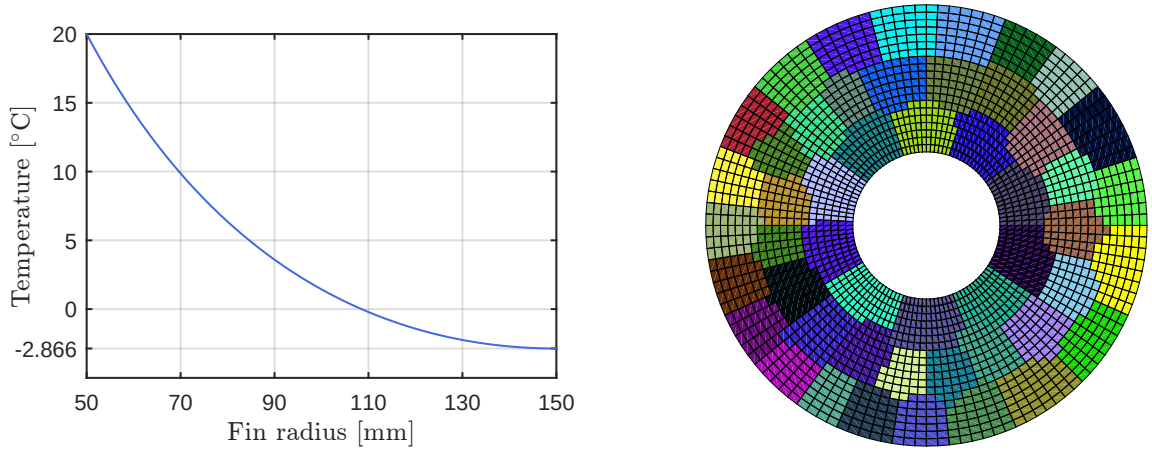

(a) (b)

Figure 4.13 – Radial temperature profile obtained by numerical integration (a) and detailed mesh divided into 50 clusters represented by different colours (b).

The reduced model convergence is affected by the location of the super nodes: the error is identical for 1 and 5 super nodes because the gradient is radial and both reduced models have one super node radially. From 10 super nodes, there are multiple super nodes along the radius and the error starts decreasing. The convergence of the reduced model even exceeds the linear convergence of the detailed FEM and results in a better accuracy than the underlying detailed FEM with 2400 elements for $n_{\mathrm{SN}} > 100$. This can be explained by the better distribution of the super nodes combined with the fact that they can be considered as second order elements since they assume a quadratic temperature profile with a linear gradient.

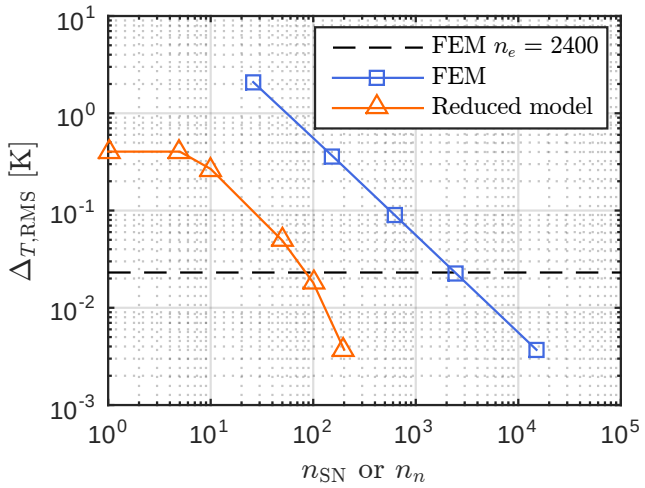

Figure 4.14 – Convergence of the RMS error with respect to the reference solution as a function of the number of nodes or super nodes. The linear detailed FEM convergence is also plotted and the dashed line corresponds to the error of the detailed FEM at the base of the reduced model convergence. The reduced model results in lower error than its underlying detailed FEM for $n_{\mathrm{SN}} > 100$.

4.5 Concluding remarks

This chapter covered the clustering of FE mesh and the associated conductive reduction. The mesh partitioning process consists in three steps: k-means initialisation of seed elements from which starts the greedy region growing ending up by a boundary smoothing step through max-flow/min-cut algorithm. To further improve the boundary smoothness, other algorithms might be applied such as the one proposed in [340] which tries to align the boundary with the straight line segment joining the extremities of the boundary. The seed elements could also be left free to change during the boundary smoothing step or the cluster boundary smoothness might be taken into account during the region growing step.

The reduced conduction matrix giving the conductive links between the clusters is then computed. The reduction process relies on the only assumption that the super node must be uniformly subjected to external heat fluxes. The sources of non-uniformity may arise from radiative heat fluxes on the surfaces, applied heat dissipation or environmental heat fluxes and heat fluxes produced by transients. Non-linear thermal properties such as temperature-dependent thermal conductivity could also lead to non-uniform heat fluxes. These would however be secondary effects since the reduced conductive links depend only on the geometry and can be expressed as shape factor multiplying the potentially temperature-dependent thermal conductivity that could depend on the super nodes it is linking.

Based on the divide and conquer strategy, an innovative local matrix inversion scheme was derived to avoid inverting the whole detailed mesh conductive matrix augmented with the super node definition.

The validation of the methodology was performed on two academic cases in one and two dimensions. The effects of non-uniformity generated by radiative heat fluxes or transients were assessed and the convergence of the method was demonstrated. In some particular cases, the reduced model was shown to exhibit higher accuracy and convergence rate than the underlying detailed FEM.

As a perspective, for steady-state analysis or arithmetic super nodes, the weights used in the super node definition could be updated by considering the fourth power of the recovered detailed temperature inside the super node. This simple iterative scheme avoids modifying the cluster definition and the corresponding radiative links. A more elaborated iterative process might refine or merge the clusters based on their recovered temperature non-uniformity.

Partitioned mesh ray tracing with quadrics fitting

5

Abstract

To complement the reduced conductive links and achieve a global reduced model, the ray tracing needs to be carried out on the partitioned mesh to derive the reduced radiative links and orbital heat fluxes. This chapter presents the modifications brought to the ray tracing algorithm presented in Chapters 2 and 3. In particular, quadrics are fitted to critical regions of the FE mesh to better capture potential concentration effects.

5.1 Introduction

Once the detailed mesh is partitioned and the conductive reduction is performed, the super nodes radiative links and orbital heat fluxes must be computed. To this aim, the ray tracing algorithm developed in Chapter 2 needs to be adapted to be applied to the external surfaces of the super nodes. As mentioned in the introduction, CAD surface information is lost during FE meshing step and FE faces may not be suitable when accurate surface normals are required. Tessellated surfaces need very large number of elements to correctly reproduce the original surface behaviour such as focusing effects. For instance, Figure 5.1(a) depicts a square parabolic surface meshed with triangles reflecting parallel incoming rays. The reflected rays are represented along with their intersection with the focal plane. Parallel rays reflected onto a parabola should converge towards its focal point represented in red. Instead, their intersections with the focal plane spread over a finite area whose size varies with the mesh refinement. Figure 5.1(b) shows how the spot size reduces as the number of triangles increases. Almost twenty thousands faces are required to capture a 1 cm radius spot size while exploiting the paraboloid surface equation makes the rays converge exactly to the focal point.

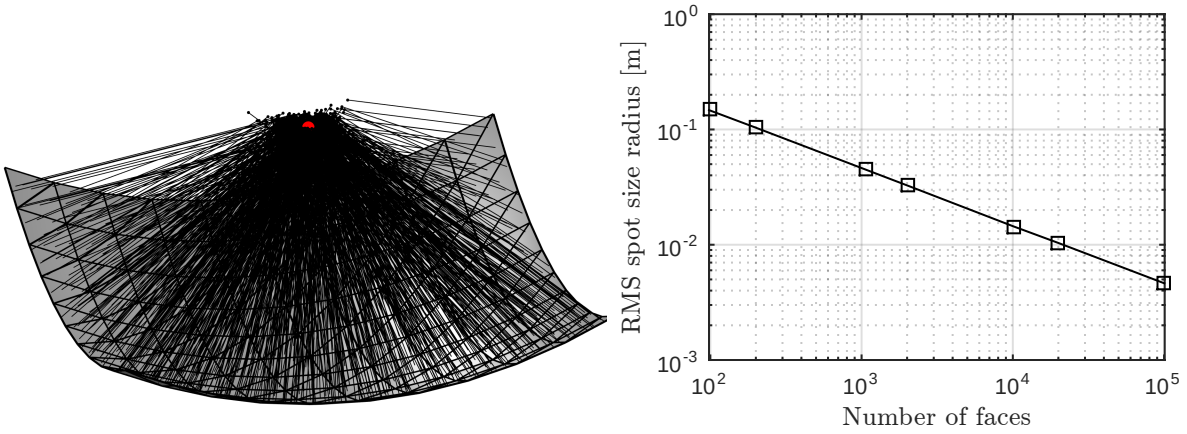

(a) (b)

Figure 5.1 – 2 m square shaped parabola ($z = (x^2 + y^2)/4f$ with $f = 1$) reflecting parallel incoming rays. Reflected rays and their intersection with the focal plane are plotted and the actual focal point is represented in red (a). Evolution of the RMS spot size radius as a function of the number of elements (b).

Most surfaces in S/C and instrument structures that require accurate representation for thermal purposes consist in relatively simple shapes such as cones, spheres, paraboloids that belong to the quadrics family. Fitting the FE mesh with a quadric may therefore provide accurate surface normals to be exploited in the ray tracing algorithm. In [326, 341], the quadric is an integral part of the partitioning algorithm. They iteratively add regions in such a way that all regions are eventually fitted by a quadric (planes being degenerate cases of the quadric). Although interesting, this approach cannot be applied blindly to classical detailed structural FE meshes that often contain details such as chamfers or fillets. Such details are sometimes represented with only one element along the width and

the algorithm is therefore not able to discriminate between chamfer and fillet. Screw holes would be fitted with quadric while they are not useful for the radiative heat transfer.

Because the true normal information is only required for a few specific surfaces in the model, we propose an approach more tailored to our need that only fits quadrics to user-tagged critical surfaces.

As explained in Section 4.2, super nodes can be composed of several external surfaces that will be called super faces. According to their shape, they are divided into three categories:

- super faces that correspond to part of the FE mesh that was fitted with a quadric,
- super faces that are composed of coplanar FE faces, therefore forming a polygon,
- super faces that only consist of a single FE face that was not part of quadrics-fitted regions and does not have coplanar neighbours.

Sampling and intersection computation are performed differently for each kind of super faces. The first section of this chapter focusses on the quadrics where the fitting, sampling and intersection strategies are developed. Then, Section 5.3 discusses planar polygons super faces together with single FE faces. Validation of ray tracing with quadrics is performed in Section 5.4 and performances are assessed by comparing detailed and reduced REFs computation times on various space structures. Conclusions of this chapter are finally drawn in Section 5.5.

5.2 Quadric super faces

5.2.1 Quadrics fitting

Shape recovery and in particular quadrics fitting problems occur in a wide variety of scientific and engineering applications [342] such as geometric reverse engineering [343], surface reconstruction [344] or mesh segmentation [323, 326, 341]. For our application, we seek the quadric equation coefficients that minimise the mean square distance between a given set of vertices and the quadric. As demonstrated in [345], the distance from a point $\mathbf{p}$ to an implicit curve f can be approximated by

$$\frac{f(\mathbf{p})}{\|\nabla f(\mathbf{p})\|} \tag{5.1}$$

where f is the implicit equation of the quadric:

$$f(\mathbf{p}) = f(x, y, z) = \mathbf{c}^\intercal \mathbf{f} = 0 \tag{5.2}$$

with the vector $\mathbf{c} = [c_0, c_1, \ldots, c_9]^\intercal$ containing the quadric coefficients and the vector $\mathbf{f}(x, y, z) = [1, x, y, z, x^2, xy, xz, y^2, yz, z^2]^\intercal$ the quadric monomials. Following the method described in [326, 341] and originally developed by Taubin [346], fitting the quadric f to a set of n_v vertices $\mathbf{p}_i$ consists in finding the coefficients $\mathbf{c}$ that minimise

$$\frac{1}{n_v} \sum_{i=1}^{n_v} \frac{f(\mathbf{p}_i)^2}{\|\nabla f(\mathbf{p}_i)\|^2} \tag{5.3}$$

Because $\|\nabla f(\mathbf{p})\|$ is constant over f, Equation 5.3 simplifies to

$$\frac{\mathbf{c}\mathbf{M}\mathbf{c}^\intercal}{\mathbf{c}\mathbf{N}\mathbf{c}^\intercal} \tag{5.4}$$

with the matrix $\mathbf{M}$ and $\mathbf{N}$ defined as

$$\mathbf{M} = \frac{1}{n_v}\sum_{i=1}^{n_v}\mathbf{f}(\mathbf{p}_i)\mathbf{f}(\mathbf{p}_i)^\intercal \quad \text{and} \quad \mathbf{N} = \frac{1}{n_v}\sum_{i=1}^{n_v}\nabla\mathbf{f}(\mathbf{p}_i)\nabla\mathbf{f}(\mathbf{p}_i)^\intercal$$

and the monomial vector gradient

$$\nabla\mathbf{f} = \begin{bmatrix} 0 & 1 & 0 & 0 & 2x & y & z & 0 & 0 & 0 \\ 0 & 0 & 1 & 0 & 0 & x & 0 & 2y & z & 0 \\ 0 & 0 & 0 & 1 & 0 & 0 & x & 0 & y & 2z \end{bmatrix}^\intercal$$

Finally, minimising Equation 5.4 is equivalent to computing the eigenvector corresponding to the minimum eigenvalue of

$$\mathbf{c}(\mathbf{M} - \lambda\mathbf{N}) = \mathbf{0} \tag{5.5}$$

The method is applied to the EUI entrance baffle presented in Section 3.3. This time, the mesh created for the structural analysis is considered. Figure 5.2(a) shows that two quadrics are fitted to the FE mesh: one for the main conical part and one for the area surrounding the aperture. The quadric is represented with a partially transparent surface whose limits are slightly expanded compared to the vertices. In the CAD model, both surfaces are cones and were designed to reflect sunlight efficiently taking into account off-pointing. Figure 5.2(b) presents the quadric fit error, *i.e.* the distance between the FE mesh vertices and the quadrics. The original shapes are almost perfectly captured with errors below 1 nm.

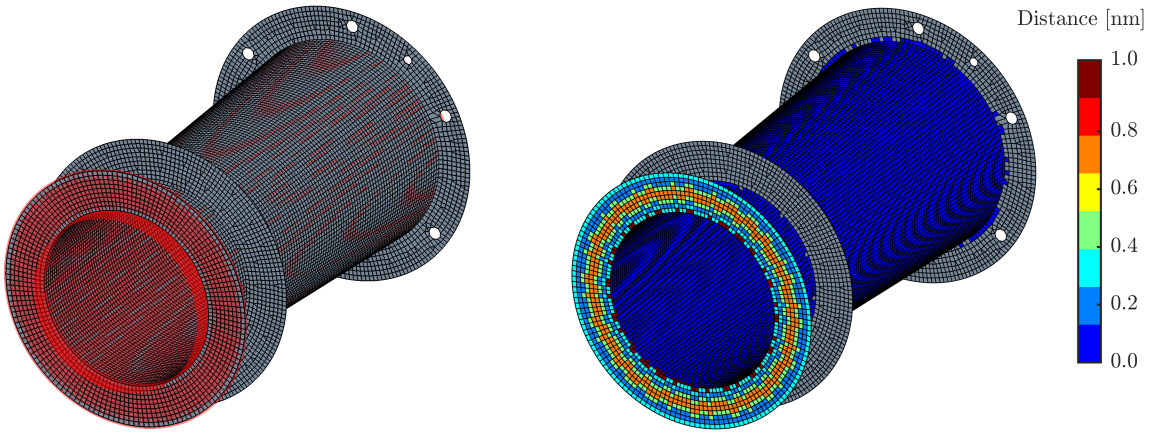

(a) (b)

Figure 5.2 – One quadric (in red) is fitted for the front conical annulus and another one is fitted to the main part of the body (a). The distance between the mesh vertices and the quadrics is less than 1 nm (b).

The UVN CAA Sun baffle presented in Section 3.4 exhibits a more complex shape that is not designed from a quadric. Again, the structural FE mesh is now considered. The difficulty lies in the correct determination of the region to fit. As opposed to the EUI entrance baffle, there is no sharp edge delimiting the curved surface. The planar regions adjacent to the curved surface to fit are first recovered and all FE faces belonging to the planes are removed. The limit between the adjacent planar regions and the curved region is fuzzy because of the discrete feature of the mesh itself and some tolerance on the FE face normal deviation must be given to determine if it belongs to the curved or the planar region. For practical purposes, only the top part of the Sun baffle is considered. Figure 5.3(a) shows the two quadrics on each side of the Sun baffle part and the quadrics limits are again expanded to better visualise them. Figure 5.3(b) gives the quadric fit error that goes up to 14 µm with an RMS value of 2 µm. As expected, larger error levels are observed close to the boundary with the planar regions.

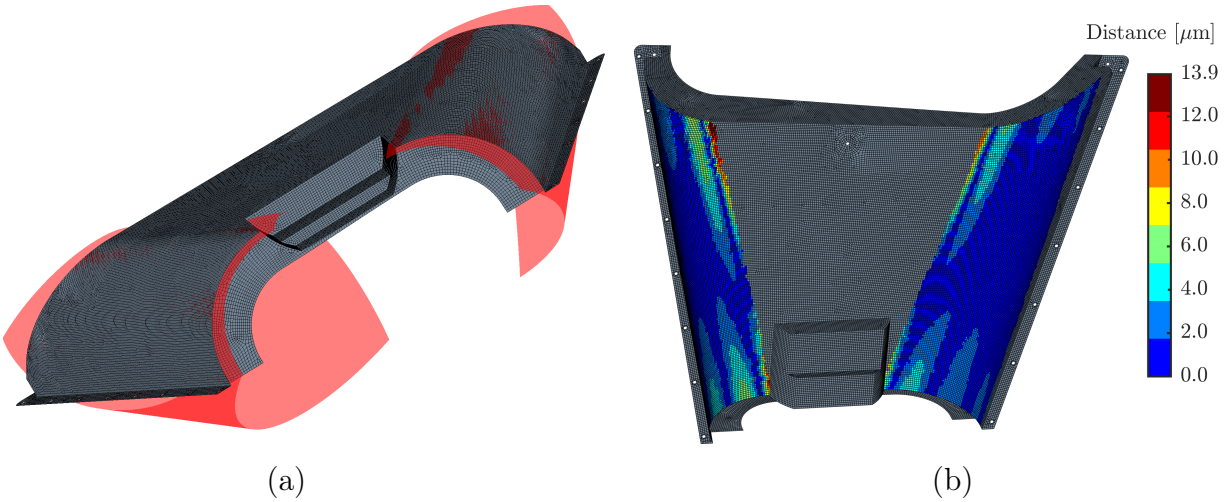

(a) (b)

Figure 5.3 – One quadric is fitted on each side of the UVN Sun baffle top part (a). The distance between the mesh vertices and the quadrics is only a few µm and is larger close to the boundaries of the fitted regions (b).

The $\mathbf{M}$ and $\mathbf{N}$ matrices are 10×10 and the computation of the eigenvalues and eigenvectors remains fast and takes only a few seconds even for such fine meshes.

5.2.2 Surface and direction sampling

Because the super faces exhibit large differences in area, a ray density leading to a number of rays proportional to the area is preferred to a constant number of rays per face regardless of its size. Nevertheless, as provided in ESATAN-TMS, the ray density can easily be increased in specific critical regions of the model for which more accurate results are desired.

Instead of sampling directly the quadric, the ray origins and directions are generated with the coupled Halton sampling strategy at FE face level and then projected back onto the quadric. This avoids the complicated determination of the super face boundary on the quadric. The origins are projected onto the quadric along the quadric normal instead of using the FE face normal. This procedure avoids the generation of gaps between the

origins of adjacent faces. It is also assumed that the maximum distance between the quadric and the underlying FE faces is small and such that the uniformity of the FE surface sampling is preserved. Structural FE meshes are usually sufficiently fine for that assumption to be valid.

The problem of projecting a point $\mathbf{p}_0 = \begin{bmatrix} x_0 & y_0 & z_0 \end{bmatrix}^\intercal$ onto the quadric consists in finding the footprint $\mathbf{p}$ of $\mathbf{p}_0$ such that $\mathbf{p}$ lies on the quadric and such that the segment $\mathbf{p} - \mathbf{p}_0$ is perpendicular to the quadric at $\mathbf{p}$. This is expressed by the non linear system of equations:

$$\begin{cases} f(\mathbf{p}) = 0 \\ (\mathbf{p} - \mathbf{p}_0) \times \nabla f(\mathbf{p}) = \mathbf{0} \end{cases}$$

that can be expanded and simplified to give the system of three non-linear equations:

$$\begin{cases} F_0 = c_0 + c_1 x + c_2 y + c_3 z + c_4 x^2 + c_5 xy + c_6 xz + c_7 y^2 + c_8 yz + c_9 z^2 = 0 \\ F_1 = (x - x_0)(c_2 + c_5 x + 2c_7 y + c_8 z) - (y - y_0)(c_1 + 2c_4 x + c_5 y + c_6 z) = 0 \\ F_2 = (y - y_0)(c_3 + c_6 x + c_8 y + 2c_9 z) - (z - z_0)(c_2 + c_5 x + 2c_7 y + c_8 z) = 0 \end{cases}$$

This system is solved by standard iterative Newton-Raphson procedure as in [347]. The initial point $\mathbf{p}_0$ is sufficiently close to the quadric to ensure the fast convergence of the algorithm. It is iteratively updated following the rule

$$\mathbf{p}^{j+1} = \mathbf{p}^j + \Delta\mathbf{p}^j$$

where $\Delta\mathbf{p}^j$ is obtained by solving the linear system

$$\Delta\mathbf{p}^j = \mathbf{J}^{-1}(\mathbf{p}^j)\mathbf{F}(\mathbf{p}^j)$$

composed of the original system equation $\mathbf{F} = \begin{bmatrix} F_0 & F_1 & F_2 \end{bmatrix}^\intercal$ and the inverse of its Jacobian matrix $\mathbf{J}$. The normal at each origin, given by the first row of the Jacobian matrix, is exploited to rotate the ray directions generated on the unit hemisphere to the local coordinates system at each origin. This ensures that the curvature of the quadric is taken into account in the direction sampling. This can be considered as an expansion (contraction) of the unit hemisphere for convex (concave) shapes.

Figures 5.4(a) and (b) compare the FE face perpendicular projection to the quadric normal projection, respectively. They provide a close-up view of the parabola mesh presented in Figure 5.1 that is fitted with a quadric and sampled with 10^5 points for each underlying FE face. Although faster, the perpendicular projection shown in Figure 5.4(a) does not ensure a continuous sampling of the quadric and leaves gaps between adjacent FE faces.

Figure 5.5(a) presents a side view of that same region showing also the original origins on the FE faces before being projected onto the quadric whose shape is clearly visible. The distance between the original and projected samples decreases close to the vertices since the quadric fitting is based on the vertices. Figure 5.5(b) shows the angular deviation generated by the rotation of the original direction produced by the Halton sampling. For this particular mesh, the correction is larger close to the vertices of the mesh, where the

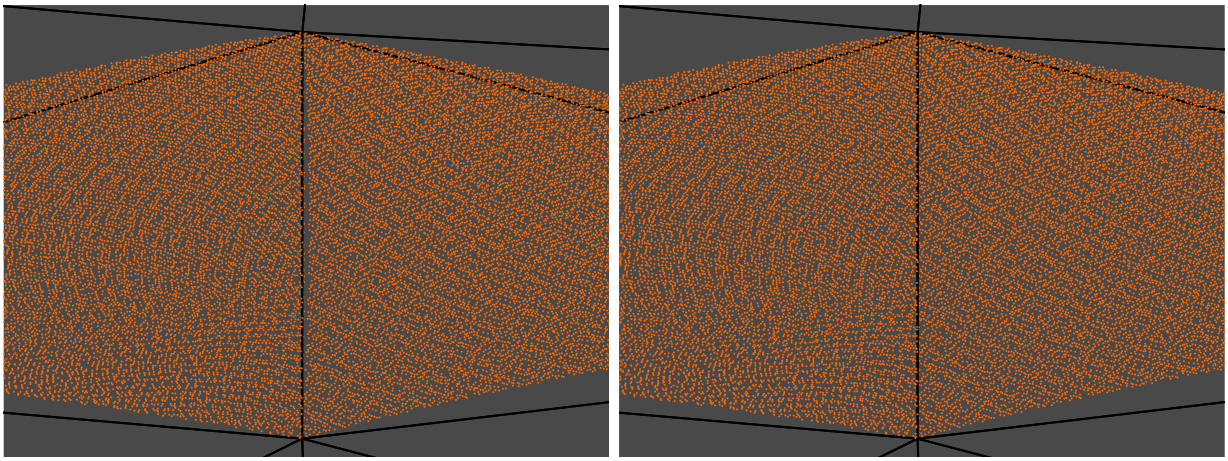

(a) (b)

Figure 5.4 – Projecting the surface samples onto the quadric along the FE faces normal produces gaps between adjacent faces (a). Projecting along the quadric normal ensures continuous sampling across FE faces (b).

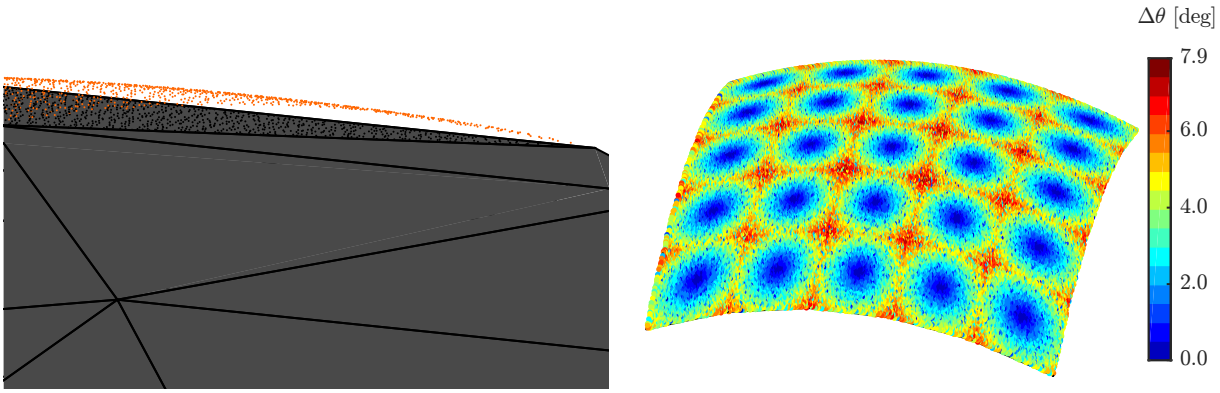

(a) (b)

Figure 5.5 – The original FE face surface samples are shown in black and their projection in orange in this side view (a). The colour scale of the origins represents the deviation between the original directions and the modified ones with the largest difference occurring close to the vertices (b).

difference between FE face normal and quadric normal is largest. The relatively coarse mesh gives rise to corrections ranging from 0 to almost 8 degrees.

Concerning the planetary heat fluxes computation and the strategy developed in Section 2.4, the same procedure is followed. Planet focused Halton sampling (PFHS) is carried out at FE face level and the samples are projected back onto the quadrics. The sampling is performed in two steps. First, just the origins are sampled to find the minimum angle γ (see Figure 2.25) between the planet direction and the quadric normal. Knowing γ, the directions are then generated. This time, the directions are not rotated but the scalar product with the quadric normal is computed for each origin to check that the rays do not penetrate the quadric. If this is the case, the penetrating rays are discarded. The ratio between the initial number of rays and the number of discarded ones

is computed. It is then exploited to ensure that the proper ray density is applied by re-sampling the FE face with a number of rays increased proportionally to the calculated ratio. The penetrating rays are again discarded but the number of remaining rays now almost respects the desired ray density. Figure 5.6 shows the resulting planet sampling strategy applied to the perpendicular cylinders. The sampling of only one super face is displayed here for clarity. The super face is composed of the rightmost three FE faces. In the bottom right corner, Figure 5.6 highlights the fact that origins that have no view factor with the planet if left on the flat FE faces can actually contribute to the planet heat flux if projected onto the quadric exploiting the correct normal.

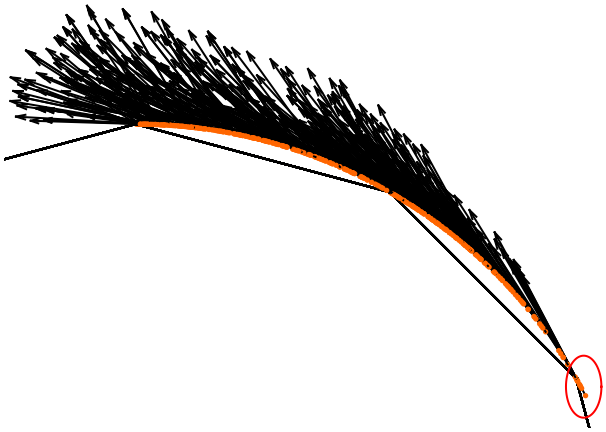

Figure 5.6 – Side view of the planet sampling strategy applied to the quadric fitting the cylinder. The orange dots represent the origin of the rays and correctly follow the recovered cylindrical shape. The red circle highlights the origins that can now see the planet.

5.2.3 Ray-quadric intersection

To compute the intersection between a ray and the quadric, Equation 2.48 describing the ray is inserted into Equation 5.2 defining the quadric shape. It results in a second order equation in t:

$$a_q t^2 + b_q t + c_q = 0 \tag{5.6}$$

where the coefficients a_q, b_q and c_q are

$$\begin{aligned}
a_q &= c_4 r_x^2 + c_5 r_x r_y + c_6 r_x r_z + c_7 r_y^2 + c_8 r_y r_z + c_9 r_z^2 \\
b_q &= c_1 r_x + c_2 r_y + c_3 r_z + 2c_4 r_x x_0 + c_5 r_y x_0 + c_6 r_z x_0 + c_5 r_x y_0 + \dots \\
&\quad 2c_7 r_y y_0 + c_8 r_z y_0 + c_6 r_x z_0 + c_8 r_y z_0 + 2c_9 r_z z_0 \\
c_q &= c_4 x_0^2 + c_5 x_0 y_0 + c_6 x_0 z_0 + c_1 x_0 + c_7 y_0^2 + c_8 y_0 z_0 + c_2 y_0 + c_9 z_0^2 + c_3 z_0 + c_0
\end{aligned}$$

Unfortunately, there is not a lot of room for optimising the calculation of these coefficients [158]. In [348], a slight optimisation is performed by taking advantage of parallel computations enabled by hardware such as GPUs (graphic processing units) or SSE[1] instruction sets.

[1]streaming SIMD extensions with SIMD standing for single input multiple data.

The rules of thumb presented in Section 2.5.3 are here again applied and the intersection is computed sequentially. The discriminant $b_q^2 - 4a_q c_q$ is first computed. If it is negative, there is no intersection. If it is positive, Equation 5.6 has two real roots and the ray intersects the quadric twice. The sign of t indicates if the intersection lies ahead or behind the origin of the ray. If both roots are positive, one might intuitively only check the closest one. This strategy is however inadequate when the quadric super face presents holes. In that particular case, the first intersection might fall in the hole and be discarded and the second intersection must be considered.

Once the intersection point is known, the problem consists in checking if it falls inside or outside the current super face. Projecting the FE face edges onto the quadric and exploiting the projected curves for this check would be extremely computationally expansive. The alternative strategy is to project back the intersection onto the underlying mesh. Projecting perpendicularly to the FE faces might again be attractive for its simpler implementation and faster execution but the problem encountered in sampling arises again. Figure 5.7(a) depicts the issue of perpendicular projection when the intersection is close to the edge of the FE face: it might incorrectly fall outside each FE face. Instead, the normal to the quadric at the intersection point is exploited, as represented in Figure 5.7(b). The intersection is projected normally to the quadric and the FE faces constituting the super faces are checked, starting from the closest one and considering only the few FE faces within reach of the intersection point. This strategy is more expansive since it can be considered as a secondary ray-intersection computation but it offers robustness.

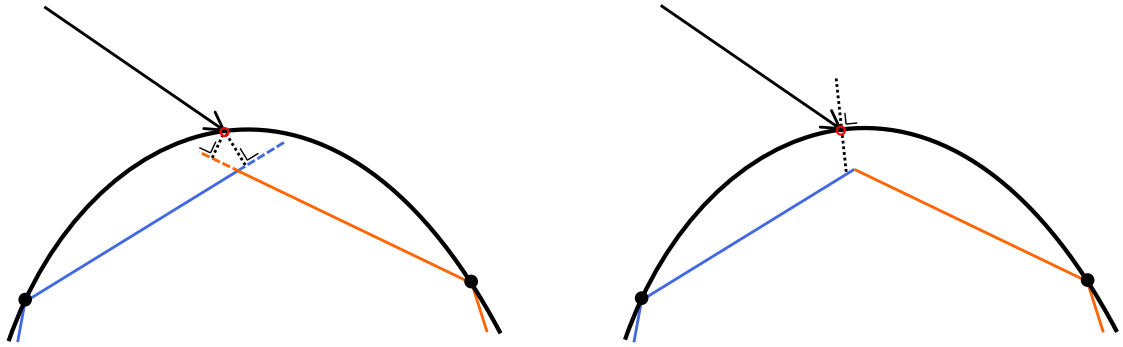

(a) (b)

Figure 5.7 – If the intersection is projected onto the underlying FE mesh normally to each FE face, the projection might fall outside both faces (a). To avoid such degenerated cases, the intersection is projected along the quadric normal onto the closest FE face (b).

Ray-quadric intersection checks are more computationally expansive than ray-triangle and space subdivision techniques present the drawback of potentially repeating the same intersection computation several times [304]. This occurs when two super faces with the same quadric equation are present in one voxel, or if the quadric spans several voxels crossed by the same ray. As introduced in Chapter 2, the mailboxing technique consists in attaching a mailbox to each face, storing the results of the intersection check with a ray counter that is incremented each time a ray is reflected or a new ray is emitted. This technique was introduced by Arnaldi *et al.* [307] and is further detailed in [303, 306, 311, 349]. The technique was implemented but again did not significantly improve the

performances because the number of times the mailbox is useful during the whole ray tracing is relatively small and because the additional checks to be performed balance the gain related to the computation of the quadric intersection. The mailboxing technique also does not avoid checking whether or not it falls inside the super face.

5.3 Planar super faces

The second kind of super faces consists in clusters of co-planar FE faces. As for the quadric super faces, sampling is performed at FE faces level to ensure uniform sampling. Concerning the intersection check, computing the intersection point itself is straightforward since it comes down to a ray-plane intersection, being the first step in the triangle intersection scheme. Determining if the intersection point lies within the irregular polygon is more complicated. First, the problem is again reduced to two dimensions by discarding the coordinate corresponding to the largest component of the normal. A robust and efficient strategy described in [308, 350], introduced in 1962 [351] and corrected in [352] is the crossing test. The philosophy is presented in Figure 5.8. It relies on the fact that if a ray from this point in an arbitrary direction crosses an odd number of times the polygon boundary, then the point is inside the polygon. The test is simplified by considering the ray parallel to one axis. In that case, only the edges having one vertex on each side of that axis need to be checked.

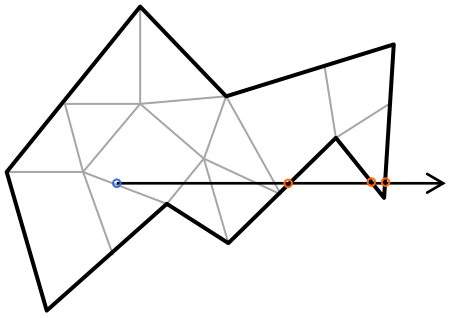

Figure 5.8 – Crossing test: an odd number of crossings indicates that the point is inside the polygon.

The boundary smoothing step performed at the end of the clustering process helps reducing the number of edges. This number is further reduced by checking if some edges are collinear. If this is the case, they are combined and only the extreme vertices are kept.

The third kind of super faces is composed of single FE faces that are not part of quadric fitted regions and do not have co-planar neighbours to be aggregated with. These faces are simply processed as classical FE face in the way described in the previous chapters.

5.4 Performance assessment

First, the perpendicular cylinders presented in Section 3.2 are considered to enable a comparison with ESARAD. Each cylinder is fitted with a quadric and clustered in 16 super nodes corresponding each to one super face in this case. Figure 5.9(a) presents the

32 identical super nodes resulting from the clustering. Because of their regular shape, the same subdivision can be applied to the cylinder primitive in ESARAD. Figure 5.9(b) gives the convergence of the RMS line sum error. The higher accuracy and convergence rate provided by the coupled Halton sampling is also present with the quadrics. This confirms the assumption that projecting the origins and rotating the directions according to the quadric normal does not jeopardise the uniformity of the coupled Halton sampling. The curves are almost identical to the one obtained with the detailed mesh and presented in Figure 3.1 and the performance gain remains limited for the same reasons *i.e.* only a few REFs contribute to the performance improvement since most of them only face the environment.

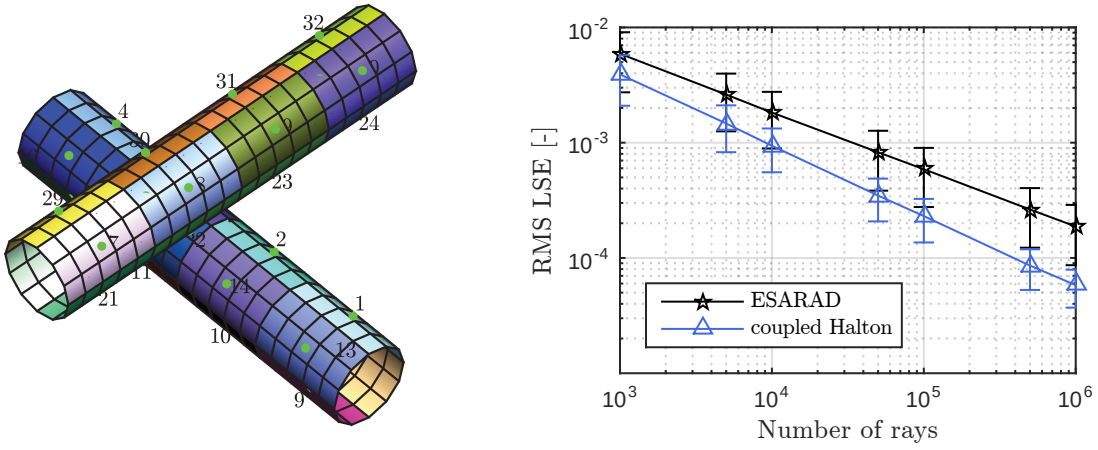

(a) (b)

Figure 5.9 – A quadric is fitted to each cylinder mesh that is then divided into 16 super faces (a). Convergence of the RMS LSE with the number of rays traced with ESARAD and the coupled Halton strategy applied to the super faces (b).

To assess the performance of the super face ray tracing, it was applied to three different structures, two of which were already presented in previous sections. The time to compute the detailed FE mesh REFs is compared to the super face REFs computation time. The first two structures are the EUI entrance baffle and the UVN CAA Sun baffle. They consist of only 2D elements and the FE meshes are divided into 50 and 118 super nodes, respectively. Because the mesh of the EUI entrance baffle is only composed of two cones and two planes, 100 (50 double sided) super faces are generated, one for each super node. For the UVN CAA Sun baffle, it results in 506 (253 double sided) super faces because some regions are neither planes nor fitted with a quadric. Figures 5.10(a) and (b) show the EUI entrance baffle and UV CAA Sun baffle super faces, respectively. In particular, Figure 5.10(b) shows the additional super faces located in the middle top part of the figure. It also shows that the mesh is subdivided into multiple regions clustered independently, the total required number of clusters being distributed proportionally not only to the area but also to characteristic length of each region.

The third example does not contain quadrics. It is the support structure of the back telescope assembly (BTA) that is part of the infrared sounder instrument of MTG. Figure 5.10(c) shows the FE mesh partitioned into 100 3D super nodes. Because the FE mesh contains many details such as screw holes and chamfers, many FE faces cannot be grouped

into planar regions. The 3D clusters also lead to separate super faces on each side. This explains why 12081 super faces are generated. They are represented in Figure 5.10(d).

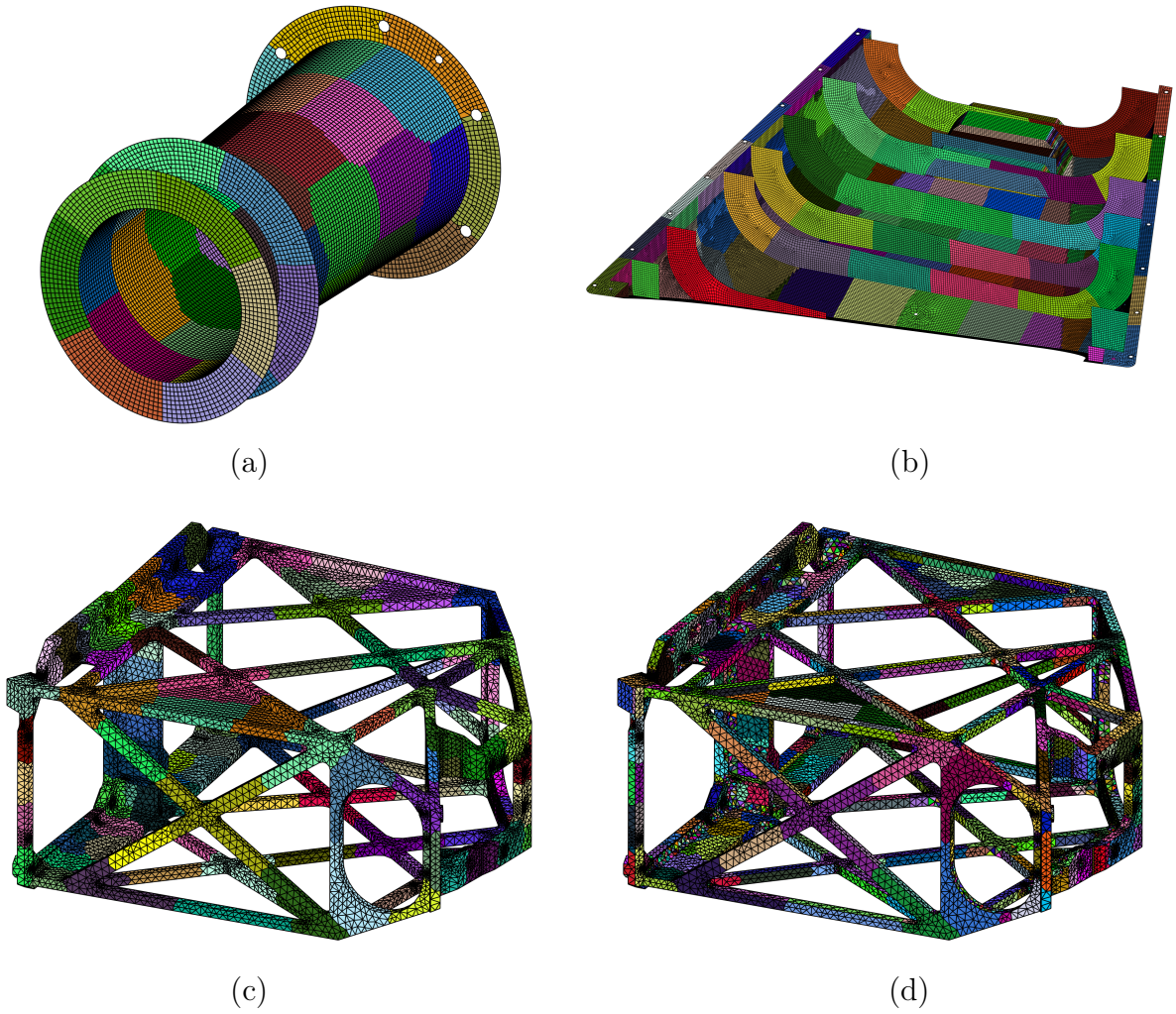

(a) (b)

(c) (d)

Figure 5.10 – EUI entrance baffle clustered into 100 super faces from 50 super nodes (a). UVN CAA Sun baffle top part divided into 506 super faces (b). BTA structure FE mesh clustered into 100 super nodes (c) and the resulting 12081 super faces (d).

Ray tracing is performed on both the detailed and reduced meshes and the computation times are compared. The same ray density is applied in both cases so that the total numbers of rays traced are almost identical. Table 5.1 summarises the results. In all three cases, computing the reduced REFs takes only a few minutes while it takes one or several hours with the detailed mesh. hence, more than one order reduction of the computation time is achieved.

The times mentioned in Table 5.1 are not to be compared with ESARAD computation times because the major part of the ray tracing algorithm is still implemented in Matlab®. For instance, tracing 5000 rays from each 100 faces composing an ESARAD GMM of the EUI entrance baffle exploiting the cone primitives will take less than 2.5min.

	n_f	ρ_{rays} [m^{-2}]	$n_{r,t}$	t_{FE} [min]	n_{SN}	n_{SF}	t_{SF} [min]	gain $t_{\text{FE}}/t_{\text{SF}}$
EUI baffle	36920	1 10^7	0.5 10^6	72	50	100	2.5	29
UVN baffle	172532	1 10^7	3.9 10^6	227	118	506	15	15
MTG BTA	49566	1 10^8	30.2 10^6	235	100	12081	12.5	19

Table 5.1 – Super face REFs computation time for various structures compared to original mesh. The columns give the number of active FE faces n_f, the ray density ρ_{rays}, the total number of rays traced in the model $n_{r,t}$, the time to compute the FE faces REFs t_{FE}, the number of super nodes n_{SN}, the number of active super faces n_{SF}, the time to compute the super faces REFs t_{SF} and finally computation time reduction factor.

5.5 Concluding remarks

.

This chapter discussed the super face concept derived from the external surfaces of the super nodes generated by the clustering presented in Chapter 4. To better capture the original geometry behind the FE mesh, an algorithm fitting quadrics to specific regions of the FE mesh was presented. The procedure gives excellent results and recovers the original shape provided that the region to fit is actually a quadric or close to a quadric. The coupled Halton direction and surface sampling strategy developed in Chapter 2 was adapted to the quadric super faces. Sampling is performed at FE face level and the ray origins are projected normally onto the quadric. The directions are also rotated according to the local quadric normal at the origin. The planet sampling strategy was also adapted. Planar super faces were also discussed. In particular the crossing algorithm, well known in the computer graphics community, is exploited to determine if the intersection lies inside the super face.

Finally the adapted ray tracing procedure was applied to the perpendicular cylinders mesh. Each cylinder mesh was fitted with a quadric and partitioned. The identical geometry was processed with ESARAD. Error convergence curves demonstrated that the superiority of the coupled Halton sampling strategy could be extended to quadrics ray tracing.

The time to obtain the REFs between the super faces with the adapted ray tracing algorithm was compared to the computation time of the original detailed FE REFs, considering the same ray density. Three space structures were considered and more than one order of magnitude reduction was achieved in all three cases.

Radiative-conductive thermal model reduction applied to space structures

6

Abstract

This chapter combines the developments of the global reduction methodology introduced in previous chapters, namely the FE mesh clustering, the super faces quasi-MCRT, the super nodes definition, the conductive reduction and temperature recovery. The performance of the global reduction and recovery process is demonstrated using two space structures, namely the EUI entrance baffle and MTG back telescope assembly. Several orders of magnitude reduction is achieved in model size and computation time without significant loss of accuracy.

6.1 Introduction

Figure 6.1 shows how the different building blocks developed in the previous chapters are integrated in the proposed global reduction process.

Starting from the structural FE mesh, small adaptations are inevitable such as adding MLI, defining contacts between parts and all the thermal and thermo-optical properties of the model. From that point, the thermal engineer selects the critical surfaces of the model to be fitted with quadrics and defines the number of super nodes for each part of the model, as he would define the nodal breakdown of a classical thermal LPM model. Then, the clustering is carried out following the procedure described in Chapter 4 along with the conductive reduction. In parallel, the quasi-MCRT developed in Chapter 2 and adapted to super faces in Chapter 5 is carried out on the partitioned mesh.

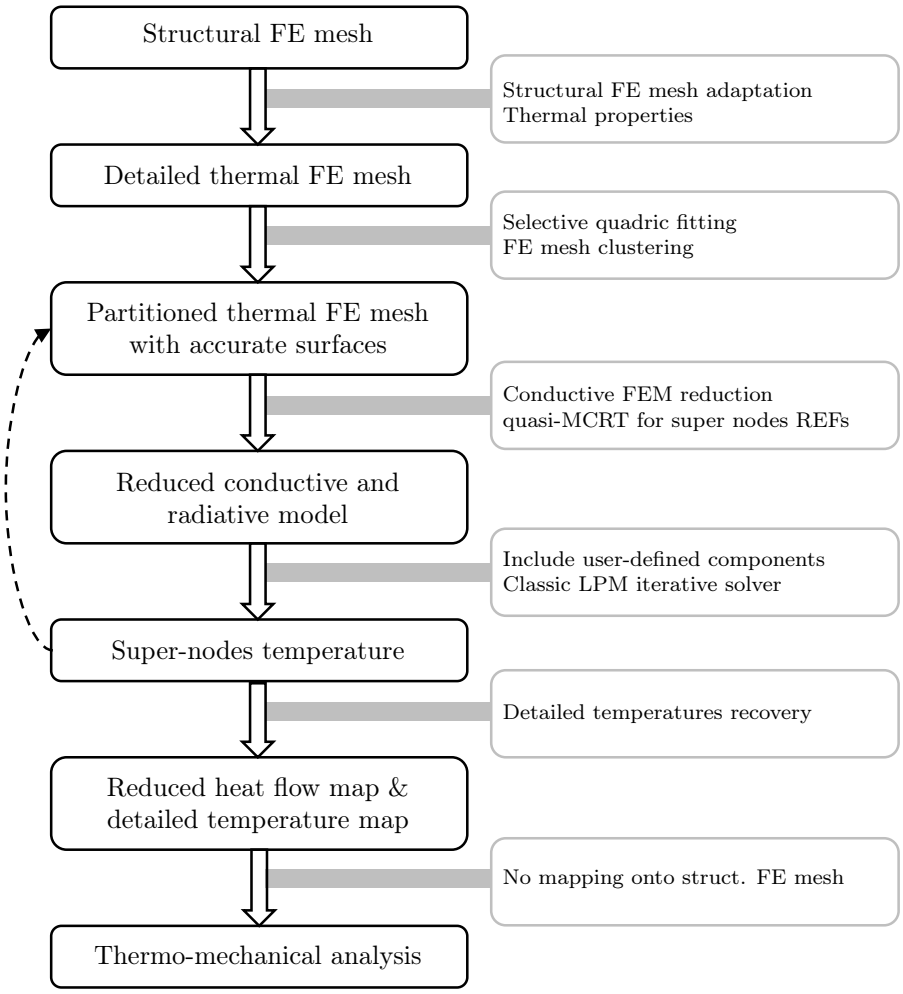

Figure 6.1 – Proposed global reduction process workflow.

From the resulting super faces REFs, the super nodes radiative couplings are derived. To the resulting reduced LPM model consisting of the super nodes with their radiative and conductive couplings, the thermal engineer may add user logic or specific components such as heat pipes. The reduced non-linear model is solved with standard algorithm similar to the `SOLVFM` routine of ESATAN, iteratively linearising the radiation terms and solving the

linear model. An iterative step can be envisaged to assess the error and locally modify the clustering accordingly. This loop is represented by the dashed arrow in Figure 6.1. Once the super node temperatures are computed, the approximate detailed temperature field can be recovered and in parallel the heat flow maps can be generated. The detailed temperatures can then be straightforwardly handed over to the structural engineer to perform the necessary coupled analyses.

The price to pay for this framework to be followed is a more collaborative work between the thermal and mechanical engineers early on from the model creation step.

This chapter is first devoted to the structure of the back telescope assembly. Section 6.3 discusses the global reduction process behaviour with the EUI entrance baffle already introduced several times across this document. For both applications, different reduction levels are assessed and compared to the detailed solution. Conclusions of the present chapter are eventually drawn in Section 6.4.

6.2 MTG BTA

In this section, the Back Telescope Assembly (BTA) that is part of the Meteosat Third Generation (MTG) Infrared Sounder (IRS) instrument is considered. Because it supports 4 mirrors, the temperatures of the BTA must be controlled and computed very accurately to guarantee that the mirrors remain aligned during the mission.

The BTA is made of Aluminium and the radiative environment is set to $-100\,°C$ for this test case. To reduce the computation time and number of REFs of the detailed solution, the emittance is assumed to be 1. Figure 6.2(a) shows the detailed mesh composed of 35217 nodes along with the location of the boundary conditions. The temperature is fixed to $20\,°C$ at the location depicted in red and $10\,W$ are applied at the opposite mounting interface. Figure 6.2(b) shows the resulting detailed mesh temperatures. The temperature drops down to almost $-25.9\,°C$ in the central region of the structure before rising to $-9.8\,°C$ where the dissipation is applied.

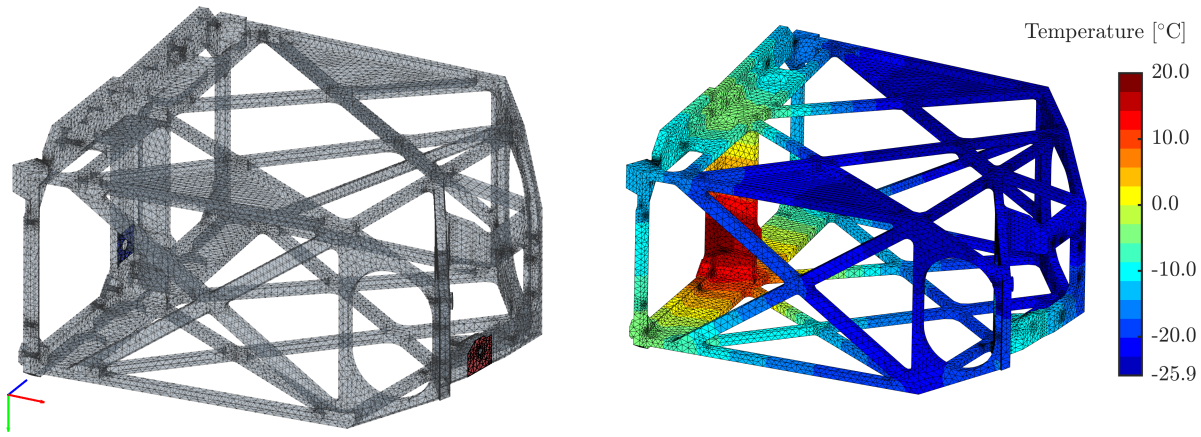

(a) (b)

Figure 6.2 – Detailed mesh showing the boundary condition location: $20\,°C$ fixed temperature in blue and $10\,W$ load in red (a). Reference solution obtained solving the detailed model (b).

In the frame of the BTA project, a dedicated ESATAN-TMS model had to be developed. A dedicated CAD-independent mesh was created and because of the complicated structure, no automatic conductive links computation was possible in ESATAN-TMS. They were computed manually and therefore subjected to approximations based on simple geometrical configurations [33]. The ESATAN-TMS model is composed of 422 LP nodes and Figure 6.3 presents the temperature map corresponding to the same boundary conditions. The minimum observed temperature is now $-28.4\,°C$ instead of$-25.9\,°C$ and the heat load application area rises up to $-7.2\,°C$ leading to an error of $2.6\,K$.

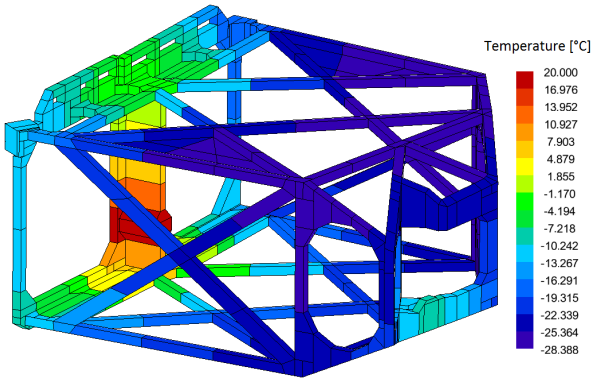

Figure 6.3 – MTG BTA structure ESATAN-TMS LPM model subjected to the same thermal environment described in Figure 6.2.

Based on this observation, it was decided to use the FE conductive reduction method to generate a new set of conductive links and replace the ones calculated manually. To this aim, the ESARAD and FE meshes were superimposed and identified. A modified version of the clustering algorithm was then applied to generate the more accurate reduced conductive links [353].

The global conductive radiative reduction method avoids creating a dedicated LPM mesh and directly exploits the FE mesh for both conductive and radiative aspects. It might be argued that the conduction reduction generates many non-physical, *i.e.* negative, conductive links, even between non-adjacent nodes in the model. Figure 6.4 shows the magnitude of the conductive links associated with the super node represented in magenta. Even though it exhibits non-zero conductive link with distant super nodes, the magnitude of the conductive link decreases rapidly as the conductive path between the two super nodes increases. Only a few super nodes in the vicinity of the considered one share a significantly large conductive coupling with it, the rest being minor corrections. This underlines that the reduced conductive links must be considered as a whole set and cannot be treated separately.

As performed with the EUI entrance baffle, the mesh was partitioned in 10 and 100 clusters. Figures 6.5(a-f) present the corresponding results to be compared with the detailed solution given in Figure 6.2. Figure 6.5(a) shows that each of the ten clusters contains a large portion of the mesh including several beams of the truss while with 100 clusters, each beam is separated in two or three super nodes. Figures 6.5(c) and (d) give the recovered detailed temperatures and, together with Figures 6.5(e) and (f), they highlight the fact that 10 super nodes already capture a large part of the thermal behaviour of the structure with errors ranging from $-1.1\,K$ to $1.2\,K$. The corresponding

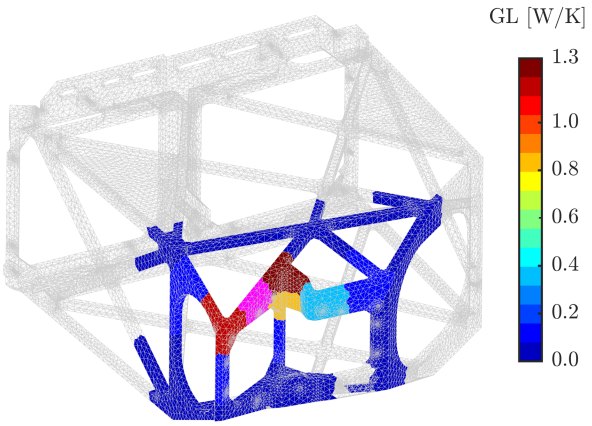

Figure 6.4 – The BTA structure is partitioned in 100 clusters. The magnitude of the conductive links related to the super node highlight in magenta decreases with the distance to the super node of interest.

RMS error is only 0.62 K and drops down to 0.06 K with 100 super nodes. Compared to the initial ESATAN model, the proposed global reduction method gives with 4 times less nodes a maximum error that is less than 0.3 K instead of 2.6 K.

6.3 EUI ENTRANCE BAFFLE

The first example consists of the EUI entrance baffle that is made of a 1 mm thick Aluminium shell. Composed of 18460 elements and 18590 nodes, the structural mesh is illustrated in Figure 6.6. It is mounted onto the EUI door mechanism and fixed by 6 screws and two pins located at the back of the baffle. To better highlight the performances of the method, the thermal environment the baffle is exposed to is slightly modified. As depicted in Figure 6.6, the temperature around the 6 screw holes is fixed to 20 °C and the baffle is surrounded by a radiative environment at −100 °C. The 0.28 A.U. perihelion solar heat flux (17.4 kW m^{-2}) impinges the whole surface of the baffle with a 45 degrees off-pointing angle, *i.e.* the Sun direction is given by the [–1, 1, 0] vector expressed in the axes displayed in Figure 6.6. In reality, the instrument is enclosed in the S/C and is protected from the major solar heat flux by its 400 mm thick heat shield that is equipped with feedthroughs providing the strictly necessary field of view.

Figure 6.7(a) presents the resulting absorbed heat flux, assuming that the solar absorptance and reflectance of Aluminium are 0.2 and 0.8, respectively, with the reflectance being entirely specular. Shadowing and multiple reflections effects are clearly observed. In particular, the multiple reflections produce concentration of the absorbed solar flux close to the middle and back annular interfaces. The flat nature of the FE faces also generates non-physical discrete concentration lines inside the baffle as well as on the annular interfaces. The latter effect highlights the need for accurate surface normal representation in the ray tracing process.

Figure 6.7(b) shows the detailed baffle temperature distribution resulting from the aforementioned boundary conditions and environmental heat fluxes. This distribution constitutes the reference solution to which the different reduced models will be compared.

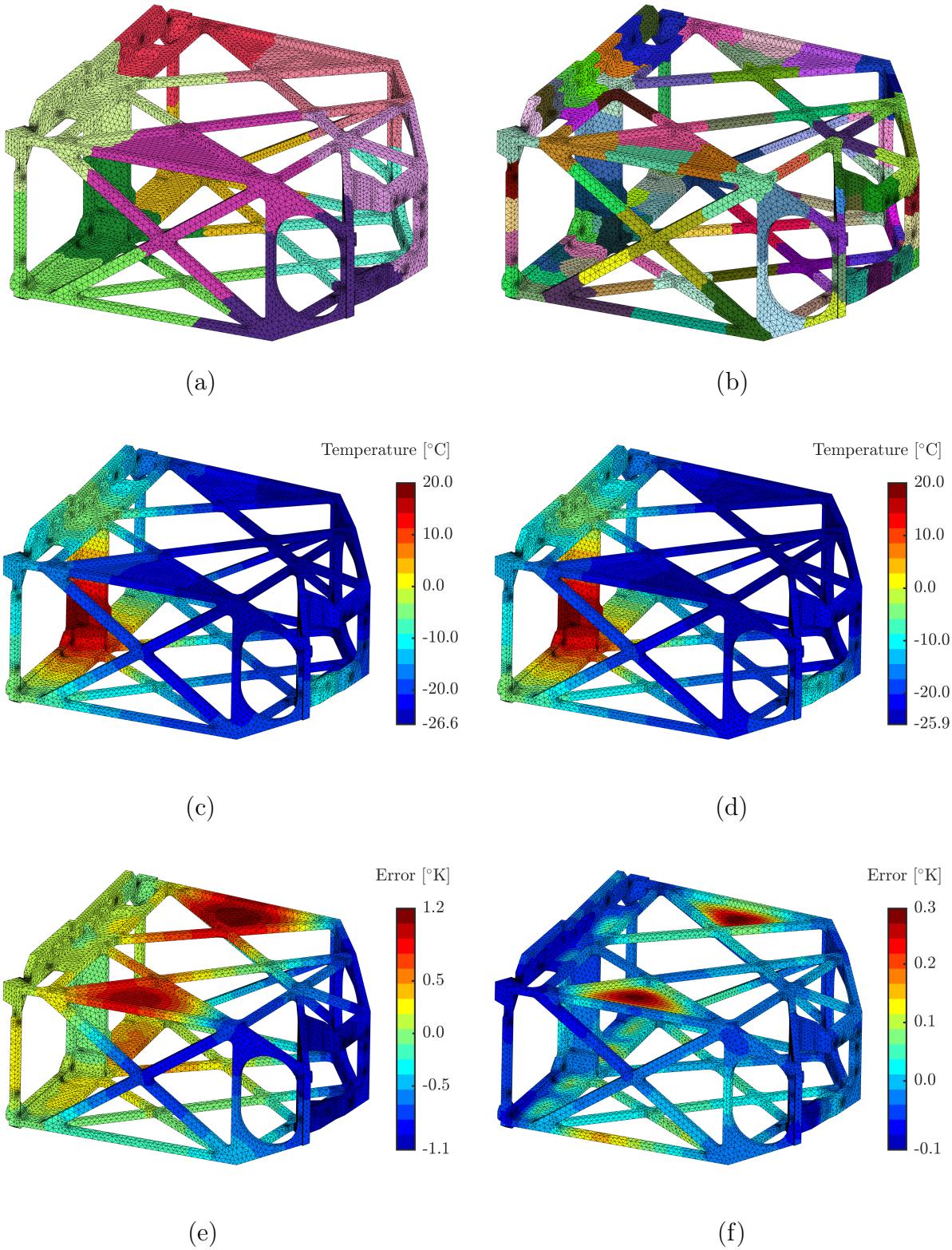

Figure 6.5 – The left (a,c,d) and right (b,d,f) column figures correspond to 10 and 100 super nodes, respectively. Top (a-b): region growing clustering results. Centre (c-d): recovered detailed temperature distribution. Bottom (e-f): recovered detailed temperature error.

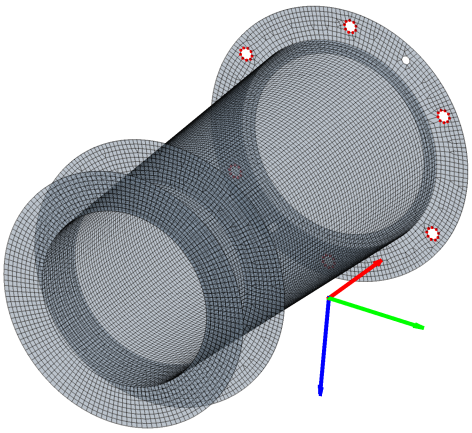

Figure 6.6 – EUI entrance baffle structural FE mesh with the x, y, and z coordinate axes represented by the red, green and blue vectors, respectively. The temperature around the fixation screw holes, depicted in red, is fixed.

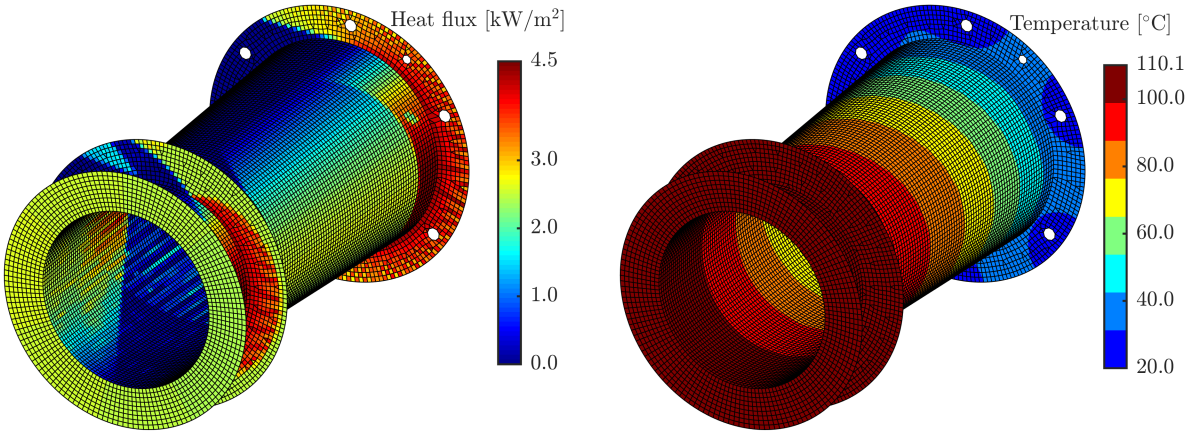

(a) (b)

Figure 6.7 – Absorbed solar heat fluxes with a 0.2 solar absorptance and 0.8 specular solar reflectance (a). Reference temperature distribution (b).

The computation of the absorbed solar heat fluxes and temperature with the present FE mesh took several hours. From a thermal point of view, such a detailed model is not necessary. The global reduction process is thus applied to decrease the number of faces and nodes while keeping accurate conductive links. It is worth mentioning that for 10 super nodes, computing the reduced conduction matrix takes less than 10 seconds with the local matrix inversion scheme developed in Section 4.3 while it takes around 215 seconds to invert the whole augmented conduction matrix $\mathbf{M}$ and obtain the exact same results.

As in the previous chapter, two quadrics are fitted to the model, *i.e.* one for the front and one for the tube, to correctly model the surface normals. Figure 6.8 presents the mesh partitioned into 100 clusters and shows the differences between the absorbed solar heat rate of each super face and the one obtained from the detailed flat FE faces presented

in Figure 6.7 and integrated over each super face. Even if the differences amount to a few mW and remain insignificant in this case, Figure 6.8 highlights the differences in the distribution due to the multiple reflections inside the baffle and close to the external annular interfaces. It also shows the effect of taking into account the quadric not only for the normal but also for the intersection and sampling. In this specific case, it means taking the actual conical surface area which is larger than the FE face area to derive the ray energy. This effect is more observed in the regions where the solar flux impinges the surface at near grazing angles for which the actual cross section of the surface exposed to the solar flux is larger. Figure 6.8 shows this effect with the orange super faces aligned along the baffle axis and exhibiting a small positive difference.

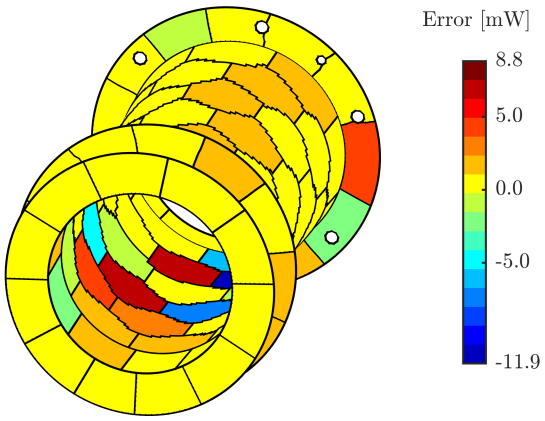

Figure 6.8 – Differences between the absorbed solar heat flux obtained from the quadric and flat FE faces ray tracing, integrated over each super face $Q_{\mathrm{SF}} - Q_{\mathrm{FE}}$ [mW].

Figures 6.9(a-f) present the global reduction process results, for 10 and 100 super nodes. Figures 6.9(a) and (b) show that the mesh is subdivided into 6 regions clustered independently, the total number of clusters being distributed proportionally to the area and characteristic length of each region. With 10 clusters, 5 of the 6 regions are left undivided and only the central part of the cone is partitioned. If the part needs to be divided into 100 clusters, the partitioning algorithm leads the annular regions to be divided only angularly while the central cone clearly exhibits the Voronoi-like shaped clusters. Figures 6.9(c) and (d) give the results of the solar ray tracing. Coming from the super node definition, heat fluxes are averaged over the whole super face area. Shadowing and concentration effects are inherently lost if the number of clusters is too small and can only be recovered by increasing it.

Figures 6.9(e) and (f) directly present the error between the recovered detailed temperatures obtained from the super nodes and the reference solution given in Figure 6.7(b). The 10 super nodes reduced model, *i.e.* involving almost a 200 reduction factor, already gives promising results with an RMS error of 1.4 K and a maximum error of 3.0 K. Largest errors arise where the uniform heat flux assumption is most violated: on the second annular interface, that is almost half in sunlight, half in shadow. Increasing the number of super nodes to 100 reduces the RMS and maximum errors down to 0.21 K and 0.77 K, respectively.

The whole procedure is automatised and varying the number of clusters does not take

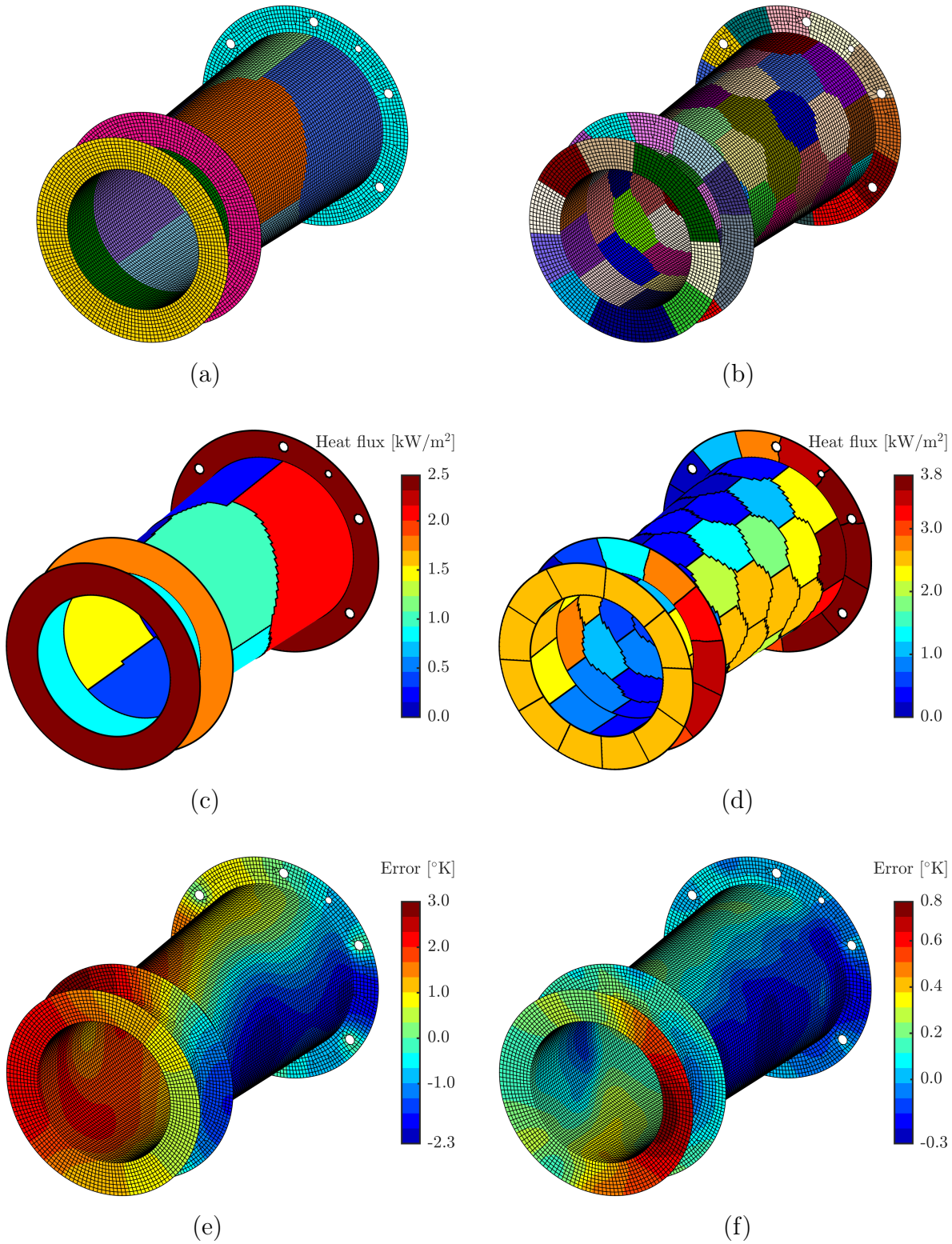

Figure 6.9 – The left (a,c,d) and right (b,d,f) column figures correspond to 10 and 100 super nodes, respectively. Top (a-b): region growing clustering results. Centre (c-d): average solar heat flux absorbed by the super face. Bottom (e-f): recovered detailed temperature error.

much time. Hence, increasing the number of super nodes is straightforward and a new FE mesh partition can be generated from which the conductive and radiative links REFs and solar heat fluxes can be recomputed. Figure 6.10 presents the convergence of the RMS temperature error with respect to the detailed solution. The convergence is almost linear in function of the number of super nodes, meaning that doubling the number of super nodes reduces the error by a factor 2. Some regions are however more useful to refine than others, such as regions subjected to large temperature gradients or where abrupt changes of the external heat fluxes are expected.

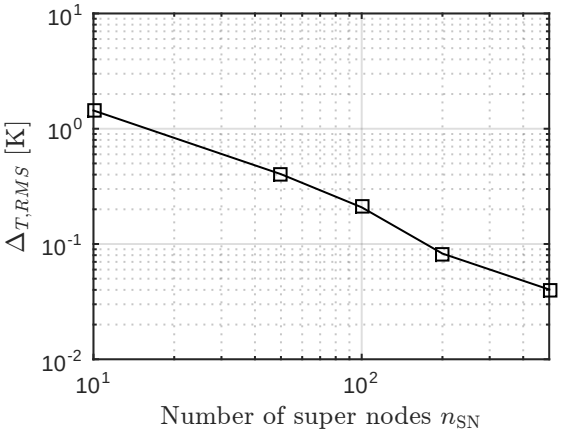

Figure 6.10 – Convergence of the RMS temperature error.

6.4 Concluding remarks

This chapter validated the global reduction methodology with two real space structures. Starting from the detailed FE mesh, two or three orders of magnitude reduction of the number of nodes was achieved without significant loss of accuracy. Table 6.1 summarises the size of the conductive and radiative coupling matrices. It highlights how large the detailed model radiation matrix can be. As explained in the previous sections and in Chapter 4, the proposed conductive reduction strategy tends to generate reduced conduction matrices with very low sparsity level. For the reduced model, the size of the matrices is obtained by adding the number of super nodes to the number of detailed nodes kept for the boundary conditions. For instance, to allow a fair comparison with the detailed model, the EUI entrance baffle required the 6×9 nodes around the screw hole and the environment node to be included in the reduction process, meaning that the size of the reduced conduction matrix is 65×65 with ten super nodes.

In practice, a dedicated super node representing the average temperature would be defined instead. It could be linked by a thermal contact conductance to another dedicated super node representing its footprint on the door mechanism onto which the baffle is mounted. These interfaces or boundary condition super nodes (like the red surface where the heat flux is applied in the BTA example) are not considered in the clustering algorithm and are defined separately. They are taken into account in the reduction process and only need to be linearly independent, like all super nodes. For the reduced matrices, the kept

interface nodes explain why there are more conductive couplings than radiative couplings. The kept interface nodes do not participate radiatively since they are part of super nodes already participating and the radiation exchanges are not counted twice.

From the numbers given in Table 6.1, only half of the values need to be stored and processed in the solver since the matrices are symmetric. Even with 100 super nodes, the reduction of the number of radiative couplings is huge: almost a factor 5000 for the BTA structure and a factor 30000 for the EUI entrance baffle. As for the REFs in Chapter 5, this drastic matrix reduction reduces the computation time of the temperatures significantly, from several tens of minutes up to a few hours for the detailed models to a few seconds for the reduced models.

		detailed	10 SNs	100 SNs
EUI baffle	$\mathbf{K}_L$	165918 (99.9%)	4096 (3.1%)	23716 (1.3%)
	$\mathbf{K}_R$	192295140 (44.4%)	119 (97.2%)	6490 (73.0%)
MTG BTA	$\mathbf{K}_L$	416827 (99.9%)	4489 (2.9%)	24649 (1.3%)
	$\mathbf{K}_R$	46375025 (96.3%)	127 (97.3%)	9797 (61.0%)

Table 6.1 – Number of non-zeros elements of the conduction and radiation matrices of the full and reduced models. The level of sparsity of each matrix is given in parentheses.

The global reduction approach is particularly suited for detailed space instrument and component design that are usually composed of complex shapes for which thermo-mechanical analyses are mandatory. Performing both analyses in the same modelling environment would ease model data exchanges. The proposed method however does not intend to replace the LPM for reduced LPM models exchanges between parties. ESATAN and SINDA formalisms are indeed particularly adapted when various reduced models of instruments or components need to be integrated into a higher level thermal model.

The proposed approach may be deemed inappropriate for early-phase S/C level analyses where a high degree of abstraction is needed with electronic boxes for instance modelled with only one node for thermal model or one lumped mass in the structural model. Yet, due to the short time scale often required by these pre-study analyses, specific early thermal and thermo-mechanical assessments could benefit from the automatic meshing strategies provided by the FEM and the proposed reduction method avoiding the time consuming creation of a dedicated LPM model.

The rapidly growing additive manufacturing techniques now enable manufacturing the complex shapes generated by topology optimisation [354]. During the several European Space Thermal Analysis Workshops I had the chance to attend, I discussed with space industry actors about the thermal analysis challenges hidden behind topology optimised structures. Today's space thermal analysis techniques are inappropriate to model complex shapes and additive manufacturing coupled to topology optimisation is calling for new methods [355]. The proposed global reduction method is perfectly adapted to the study of such complex shapes.

In the context of space instrument design, the purpose of thermo-mechanical analyses is twofold: first verify the integrity of the structure across the whole thermal environment it is submitted to and second to check optical elements remain aligned [356, 357]. Because the proposed method offers the possibility to fit quadric to specific surfaces, this feature

could be exploited to retrieve the change of curvature of mirrors and lenses during thermo-elastic analyses.

Conclusions

The present doctoral thesis constitutes a new attempt to re-unify the finite element and lumped parameter methods for space thermal analysis. Based on their respective advantages and drawbacks described in Table 1 of the introduction, we propose a new global non-linear radiative-conductive *a priori* model reduction technique. The *space thermal analysis through finite element modelling* (STARFEM) framework brings together LPM and FEM and bridges the gap between thermal and structural analyses. Figure 7.1 summarises the proposed framework which relies on the strengths of both methods.

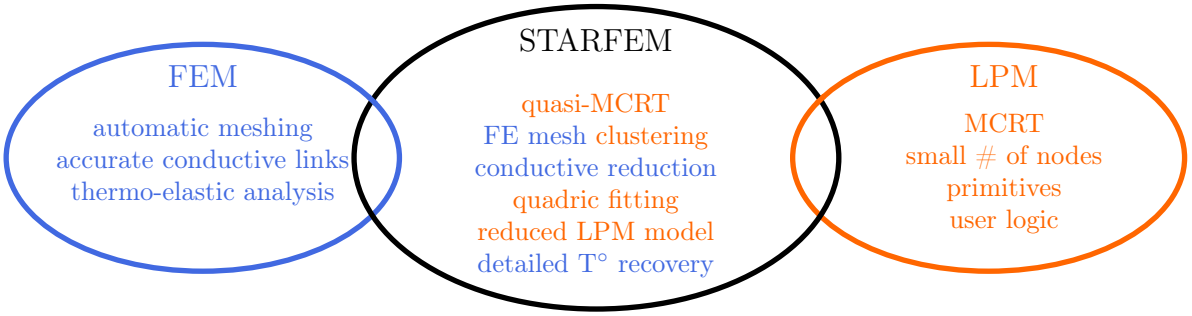

Figure 7.1 – Re-unification of the FEM and LPM with the STARFEM framework.

To combine the LPM with the FEM and achieve the global reduction method, several building blocks are developed in the different chapters of this thesis.

- In Chapter 2, the Monte Carlo ray tracing method, one of the foundations of space radiative analysers, is improved by introducing the new coupled Halton sampling strategy. The proposed quasi-MCRT scheme significantly reduces the number of rays required for a given accuracy[1]. Chapter 2 also improves the orbital heat fluxes computation. In particular, the planet-focused Halton sampling strategy is developed. Instead of relying on visible or infrared REFs, only useful rays are traced in the direction of the planet. In Chapter 3, the performances of the proposed methodologies in terms of accuracy and convergence rate are demonstrated using real space structures.

[1] After attending my presentations during the past ESA Thermal Analysis Workshops, the developers of THERMICA, T. Soriano and C. Théroude from Airbus Defence and Space Toulouse, were convinced to integrate my developments in THERMICA [358].

- In Chapter 4, the second approach to decrease the REFs computation time is addressed *i.e.* reducing the number of faces. Through FE mesh clustering, the concept of super node is defined and lays down the foundations of the reduced thermal model. Chapter 4 also exploits the second advantage of FEM (after automatic meshing) to generate accurate reduced conductive links. Combined with the super nodes definition, the detailed FE mesh conduction matrix is reduced through an innovative local inversion scheme.
- The conductive reduction being handled, the quasi-MCRT algorithm developed in Chapter 2 needs to be adapted to the partitioned mesh. In particular, the primitives from the classical space thermal analysis software are advantageously replaced by fitting quadrics to the FE mesh. This process is developed in Chapter 5. The super node external surfaces are divided into super faces classified as quadrics, planar clusters or single FE faces. The sampling and intersection strategies are updated in Chapter 5 to handle the super faces. From these, the REFs are computed and the super node radiative couplings are derived. No performance degradation of the updated quasi-MCRT algorithm is observed, therefore enabling both REFs computation time reduction techniques to complete each other.
- Chapter 6 finally brought together the previous developments building the non-linear reduced model from the super nodes and associated reduced radiative and conductive couplings. The reduced model can be treated as any LPM model and the temperatures can be computed with standard iterative solvers. It therefore allows the integration of any user logic or component like standard LPM models, picking the last advantage from the LPM list.

The proposed global conductive-radiative reduction strategy leads to several orders of magnitude reduction of the computation time of the radiative couplings and temperatures, without significant loss of accuracy compared to the detailed model. Besides, it avoids the time consuming task of creating dedicated GMM and TMM when a structural FE mesh is available and most of the CAD simplifications were already performed. It further smooths the interactions between the structural and thermal analyses, making the evermore critical coupled analyses easier to be carried out.

Perspectives for future research

The developments presented in this doctoral thesis give rise to several paths for improvements and generalisation of the method.

Error control and iterative reduction

Non-uniform heat fluxes are the root of reduction errors. As discussed in the thesis, there are several sources of non-uniformity among which there are radiative heat exchanges or environmental heat fluxes.

Because it is less computationally expensive than the REFs computation, performing the OHFs ray tracing on the detailed mesh and exploiting the shadowing and concentration locations in the clustering process could be envisaged. This may help generating more uniform heat fluxes on the super nodes. While this may seem attractive for steady-state

analysis, this strategy may become complicated for transient cases with spatially varying external heat fluxes.

To illustrate this iterative procedure, the one-dimensional radiative beam example presented in Chapter 4 is considered. A first reduced model is generated with two super nodes from which the detailed temperature profile is recovered. The gradient in each element is computed and input as the weight of the k-means clustering initialisation. This way, large gradient regions are more densely populated with cluster seeds. Figure 7.2 presents the results with two super nodes. The updated clustering reduces the size of the left super node where the temperature gradient is largest. Even if the error at the tip is almost identical, the global RMS error decreases from 2.76 K to 1.86 K for the same number of super nodes.

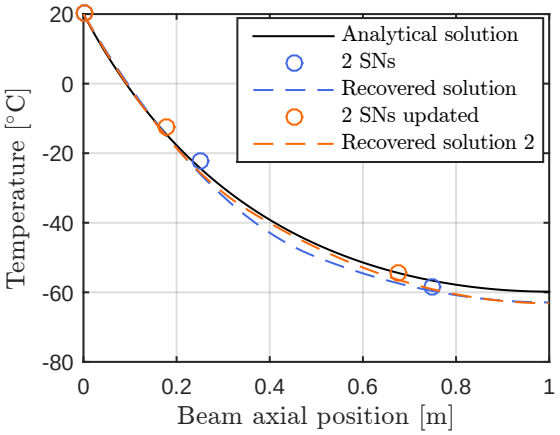

Figure 7.2 – Iterative clustering method applied to the radiative beam. The detailed and initial reduced models are compared to the updated reduced model.

An alternative would be to exploit again the recovered temperatures from the initial reduced model not only to update the position of the clusters but also to modify the number of super nodes. If the thermal engineer specifies a maximum temperature gradient per cluster, the greedy region growing algorithm could take into account the recovered temperature profile. The algorithm would stop to add adjacent elements to a region when the gradient threshold is achieved, and start with new regions.

For large models, only specific regions might require an update and one may desire to avoid the REFs re-computation. In such cases, the clustering could be applied locally to the clusters to be modified and the new super nodes radiative links might be derived from the already computed ones assuming a re-distribution proportional to the area of each new cluster.

There is a lot of room to generalise these iterative concepts to three dimensions. Great care must be taken in the iterative procedure, considering how it applies to transient analyses. It is also worth mentioning that temperature gradients are not necessarily synonym of reduced model errors. As demonstrated in Chapter 4, applying a uniform heat flux over the super node gives rise to a temperature gradient that is perfectly captured by the reduced model. The temperature gradient only becomes a source of error in the presence of radiative heat transfer or transients.

Parallel computing

Throughout this manuscript, we showed that there was a lot to learn from the computer graphics community, such as clustering algorithms or ray tracing acceleration techniques.

It is therefore important to mention a third way to reduce the computation time of the REFs *i.e.* to take advantage of the inherent parallelism of the ray tracing process. Parallel computing [36, 359, 360], in particular using Graphics Processing Units (GPUs) [361–363] is another field where the many developments are already performed by the computer graphics community. Exploiting GPUs to accelerate scientific computation is often referred to as General-Purpose GPU or GPGPU and has already been applied to a wide variety of problems [364].

Although the actual performance gain provided by the GPUs over CPUs was subject to discussions [365, 366], substantial reduction of the computation time is nevertheless achieved in industrial applications [367]. The main drawback of GPUs is that they require highly optimised memory management, depending on their specific architecture. Efforts are undertaken to simplify coding in CUDA (the programming language of NVIDIA GPUs) [368], and open programming languages such as OPENCL are developed to handle hybrid CPU and GPU architectures [369].

Convection and participating media

Although convective heat transfer was not considered in this thesis, the proposed method could be coupled with CFD analyses where the surface super nodes would act as thermal bridges to which convective heat transfer would be applied. Adapting the ray-tracing to include bulk absorption and participating media as described in [35] would also allow reducing the computational burden associated with thermal modelling of exhaust nozzles or combustion chambers [370, 371].

Integration limits for orbital heat fluxes computation

A

A.1 Introduction

To derive the planetary infrared and albedo heat fluxes, Equations 2.23 and 2.24 defined in Section 2.4 need to be integrated over the domains $\mathcal{S}_e$ and $\mathcal{S}_a$ defined as

$$\mathcal{S}_a = \mathcal{S}_1 \cap \mathcal{S}_2 \cap \mathcal{S}_3$$
$$\mathcal{S}_e = \mathcal{S}_1 \cap \mathcal{S}_2$$

where $\mathcal{S}_1$, $\mathcal{S}_2$ and $\mathcal{S}_3$ are

- the spacecraft field of view limited by the S/C FoV footprint $\mathcal{C}_1$,
- the surface of the planet located above the face plane footprint $\mathcal{C}_2$,
- and the sunlit side of the planet limited by the terminator $\mathcal{C}_3$, respectively.

This appendix gives the equations of the three footprints along with their potential intersection. The notations in this appendix are described in Figure 2.25.

A.2 The three footprint equations

A.2.1 S/C field of view

The spacecraft field of view is defined as the cone subtended by the S/C and tangent to the planet. Its footprint $\mathcal{C}_1$ is a z-axis centred circle in the plane $z = \cos\theta_{z,\max} = 1/h_r$ with a radius $\sin\theta_{z,\max} = \sqrt{h_r^2 - 1}/h_r$:

$$\mathcal{C}_1(\theta_z, \phi_z) = 1/h_r \begin{bmatrix} \sqrt{h_r^2 - 1}\cos\phi_z & \sqrt{h_r^2 - 1}\sin\phi_z & 1 \end{bmatrix} \tag{A.1}$$

A.2.2 The S/C face plane

The face plane equation, defined by its unit normal $\vec{\mathbf{n}} = \begin{bmatrix} \sin\gamma & 0 & -cos\gamma \end{bmatrix}$ in the local frame, becomes:

$$x\sin\gamma - z\cos\gamma + h_r\cos\gamma = 0 \tag{A.2}$$

If $|\gamma >| \theta_{z,\max}$, the face plane intersects the planet along a circle symmetric with respect to the $x-z$ plane. The equation of the intersection is obtained by rotating a circle of radius $r_n = \sqrt{1-h_r^2\cos^2\gamma}$ centred on z axis in the plane $z = h_r\cos\gamma$ by an angle $-\gamma$ around the y axis:

$$\begin{aligned}\mathcal{C}_2(\theta_z,\phi_z) &= \begin{bmatrix} r_n\cos\phi & r_n\cos\phi & \cos\gamma h_r\end{bmatrix}\begin{bmatrix}\cos\gamma & 0 & \sin\gamma\\ 0 & 1 & 0\\ -\sin\gamma & 0 & \cos\gamma\end{bmatrix}\\ &= \begin{bmatrix} r_n\cos\phi\cos\gamma - \sin\gamma\cos\gamma h_r & r_n\sin\phi & r_n\cos\phi\sin\gamma + \cos^2\gamma h_r\end{bmatrix}\end{aligned} \tag{A.3}$$

The face plane footprint vector equation then need to be translated in a θ_z-ϕ_z relationship. Identifying $\cos\theta_z$ as the z component and $\tan\phi_z$ as the ratio between y and x components of each vector, the face planet footprint becomes:

$$\begin{aligned}\cos\theta_z &= \cos\phi\sin\gamma\sqrt{1-h_r^2\cos^2\gamma} + \cos^2\gamma h_r\\ \tan\phi_z &= \frac{\sin\phi\sqrt{1-h_r^2\cos^2\gamma}}{\cos\phi\cos\gamma\sqrt{1-h_r^2\cos^2\gamma} - \sin\gamma\cos\gamma h_r}\end{aligned}$$

Extracting $\cos\phi$ from the first equation to plug it into the second expresses the FoV footprint as a θ_z function of ϕ_z:

$$\theta_{z,\mathcal{C}_2}(\phi_z) = \arccos\left(\frac{h_r\cos^2\gamma\sec^2\phi_z + \sin\gamma\sqrt{(1-h_r^2)\cos^2\gamma\sec^2\phi_z + \sin^2\gamma}}{1+\cos^2\gamma\tan^2\phi_z}\right) \tag{A.4}$$

A.2.3 The terminator

The third footprint to be defined is the terminator defined as the line dividing the day (sunlit) side of the planet from the dark night side. The normalized Sun position vector $\hat{\vec{\mathbf{r}}}_{\oplus\to\odot}$ can be expressed with the angle $\theta_\odot \in [0,\pi]$ and $\phi_\odot \in [0, 2\pi[$

$$\hat{\vec{\mathbf{r}}}_{\oplus\to\odot} = \begin{bmatrix}\cos\phi_\odot\sin\theta_\odot & \sin\phi_\odot\sin\theta_\odot & \cos\theta_\odot\end{bmatrix}$$

The terminator equation is obtained by rotating the great circle represented by the vector $\begin{bmatrix}\cos\phi & \sin\phi & 0\end{bmatrix}$ in the $x-y$ plane (corresponding to the terminator when the Sun is located in the $+z$ direction, $\theta_\odot = 0$) by an angle $\theta_\odot$ around y axis and by $\phi_\odot$ around z axis.

$$\begin{aligned}\mathcal{C}_3(\theta,\phi) &= \begin{bmatrix}\cos\phi & \sin\phi & 0\end{bmatrix}\begin{bmatrix}\cos\theta_\odot & 0 & -\sin\theta_\odot\\ 0 & 1 & 0\\ \sin\theta_\odot & 0 & -\cos\theta_\odot\end{bmatrix}\begin{bmatrix}\cos\phi_\odot & \sin\phi_\odot & 0\\ -\sin\phi_\odot & -\cos\phi_\odot & 0\\ 0 & 0 & 1\end{bmatrix}\\ &= \begin{bmatrix}\cos\phi_\odot\cos\theta_\odot\cos\phi - \sin\phi_\odot\sin\phi & \sin\phi_\odot\cos\theta_\odot\cos\phi + \cos\phi_\odot\sin\phi & -\sin\theta_\odot\cos\phi\end{bmatrix}\end{aligned} \tag{A.5}$$

Similarly to the face plane footprint, the terminator vector equation is translated in a θ_z-ϕ_z relationship:

$$\begin{aligned} \cos\theta_z &= -\sin\theta_\odot \cos\phi \\ \tan\phi_z &= \frac{\sin\phi_\odot \cos\theta_\odot \cos\phi + \cos\phi_\odot \sin\phi}{\cos\phi_\odot \cos\theta_\odot \cos\phi - \sin\phi_\odot \sin\phi} \end{aligned} \tag{A.6}$$

and ϕ is eliminated to get the θ_z as a function of ϕ_z for the terminator:

$$\theta_{z,\mathcal{C}_3}(\phi_z) = \arccos\left(\frac{-\sin\theta_\odot}{\sqrt{1+\cos^2\theta_\odot \tan^2(\phi_\odot - \phi_z)}}\right) \tag{A.7}$$

A.3 Intersection between the footprints

Because multiple footprints might be involved in the integration of Equations 2.23 and 2.24, their intersections need to be computed.

Many different intersection configurations can occur and Figure A.1 gives a representative configuration where all three footprints intersect. The S/C field of view $\mathcal{S}_1$ is represented by the hashed area, the integration domain above the face plane footprint $\mathcal{S}_2$ is represented by the red transparent area and the sunlit integration domain $\mathcal{S}_3$ by the yellow transparent area. The global albedo integration domain $\mathcal{S}_a$ is therefore represented by the hashed orange (red+yellow) area. Integrating over this domain is reduced, in this particular case, in splitting the integration of Equation 2.23 into four regions:

- up to the S/C field of view footprint (black line) from $\phi_{z,22}$ to $\phi_{z,21}$,
- up to the terminator footprint (yellow line) from $\phi_{z,21}$ to $\phi_{z,31}$,
- up to the face plane footprint (red line) from $\phi_{z,31}$ to $\phi_{z,32}$,
- and finally again up to the terminator footprint (yellow line) from $\phi_{z,32}$ to $\phi_{z,22}$.

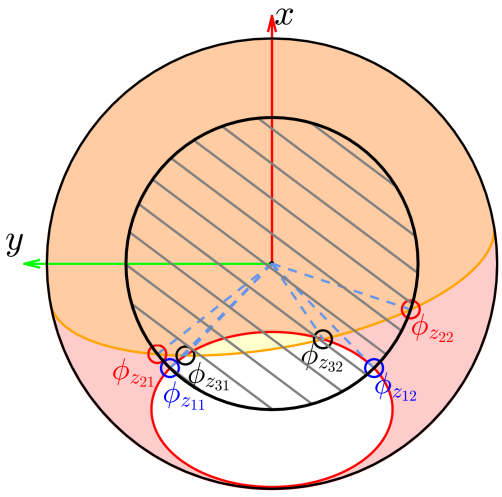

Figure A.1 – Representative footprint intersection configuration and integration domain, viewed from the S/C.

The face plane intersects the S/C FoV footprint symmetrically with respect to $x-z$ plane at an angle $\phi_{z,1}$ found by inserting the components of the S/C FoV limit given by Equation A.1 into the face plane equation:

$$\sin\gamma\sin\theta_{z,\max}\cos\phi_z - \cos\gamma\cos\theta_{z,\max} + h_r\cos\gamma = 0$$

from which $\cos\phi_{z,1}$ is extracted

$$\cos\phi_{z,1} = \cot\gamma\frac{\cos\theta_{z,\max} - h_r}{\sin\theta_{z,\max}} = -\cot\gamma\sqrt{h_r^2 - 1} \tag{A.8}$$

The azimuthal angle $\phi_{z,2}$ at which the terminator intersects the FoV footprint is obtained by equating the z component of the vector given by Equation A.5 to the z component of the FoV footprint plane (which is perpendicular to z axis)

$$\cos\theta_{z,\max} = -\sin\theta_\odot\cos\phi$$

The ϕ angle is then plugged into Equation A.6 giving $\tan\phi_z$ and $\phi_{z,\mathcal{C}_1-\mathcal{C}_3}$

$$\phi_{z,2} = \arctan\left(\frac{\cos\phi_\odot\sqrt{h_r^2 - \csc^2\theta_\odot} - \cot\theta_\odot\sin\phi_\odot}{\sin\phi_\odot\sqrt{h_r^2 - \csc^2\theta_\odot} + \cot\theta_\odot\cos\phi_\odot}\right)$$

To derive the azimuthal angle $\phi_{z,3}$ at which the face plane intersects the terminator, the components of Equation A.5 are inserted into Equation A.2.

$$\cos\phi\underbrace{(\sin\gamma\cos\phi_\odot\cos\theta_\odot + \cos\gamma\sin\theta_\odot)}_{c_1} - \sin\phi\underbrace{\sin\gamma\sin\phi_\odot}_{c_2} + \underbrace{h_r\cos\gamma}_{c_3} = 0$$

It can be transformed to a second degree equation in terms of $\tan(\phi/2)$ to find the local angle ϕ

$$\phi = 2\arctan\left(\frac{c_2 \pm \sqrt{c_1^2 + c_2^2 - c_3^2}}{c_3 - c_1}\right)$$

with the constants c_1, c_2 and c_3 as defined above. $\phi_{z,\mathcal{C}_2-\mathcal{C}_3}$ is finally derived through Equation A.6:

$$\phi_{z,3} = \arctan\left(\frac{\cos\theta_\odot\sin\phi_\odot\cot\phi + \cos\phi_\odot}{\cos\theta_\odot\cos\phi_\odot\cot\phi + \sin\phi_\odot}\right)$$

For each configuration, Equations A.4 and A.7 and their intersections $\phi_{z,1}$, $\phi_{z,2}$ and $\phi_{z,3}$ define the proper integration domain to compute the albedo and infrared heat fluxes. As depicted in Figure A.1, each intersection gives two azimuth angles $\phi_{z,11}$ and $\phi_{z,12}$ for the FoV and face plane, $\phi_{z,21}$ and $\phi_{z,22}$ for the FoV and terminator and $\phi_{z,31}$ and $\phi_{z,32}$ for the face plane and the terminator.

Bibliography

[1] Thornton, E. A., "Thermal structures - Four decades of progress," *Journal of Aircraft*, 29(3), pp. 485–498, May 1992. (Quoted page 1.)

[2] Buwalda, E. P. and Hibbs, A. R., "Satellite temperature measurements for 1958 alpha - explorer I," , Tech. Rep. DA-04-495-ORD-18, Jet Propulsion Lab., California Inst. of Tech., Pasadena, CA, United States, Apr. 1958. (Quoted page 1.)

[3] Boley, B. A. and Weiner, J. H., *Theory of Thermal Stresses*, Wiley, New York, (1960). (Quoted page 1.)

[4] Thornton, E. A. and Paul, D. B., "Thermal-structural analysis of large space structures - An assessment of recent advances," *Journal of Spacecraft and Rockets*, 22(4), pp. 385–393, Jul. 1985.

[5] Thornton, E. A., *Aerospace Thermal Structures and Materials for a New Era*, American Institute of Aeronautics and Astronautics, Washington DC, Jan. 1995.

[6] Ramesh B. Malla and Anindya Ghoshal, Jan. 1995. "On Thermally-Induced Vibrations of Structures in Space," , *Aerospace Thermal Structures and Materials for a New Era*. Earl A. Thornton (Ed.). Progress in Astronautics and Aeronautics. American Institute of Aeronautics and Astronautics, pp. 68–95.

[7] Nowacki, W., *Thermoelasticity*, 2nd Edition, Pergamon Press ; PWN-Polish Scientific Publishers, Oxford ; New York : Warszawa, (1986).

[8] Hetnarski, R. B. and Eslami, M. R., *Thermal Stresses: Advanced Theory and Applications*, no. v. 158 in Solid mechanics and its applications, Springer, Dordrecht, (2009). (Quoted page 1.)

[9] Hoff, N. J., "High Temperature Effects in Aircraft Structures.," , Tech. rep., North Atlantic Treaty Organizatio, (1958). (Quoted page 1.)

[10] Poelaert, D. and Burke, W. R., "Hubble Space Telescope solar array: A thermally induced disturbance torque," , Tech. Rep. NASA STI/Recon Technical Report 29387, ESA ESTEC, Mar. 1987. (Quoted page 1.)

[11] Beere, G. and Turner, R. G., "Thermal Orbital Performance of the Hubble Space Telescope Solar Arrays," *Proceedings of the 24th International Conference On Environmental Systems*, SAE International, Friedrrichshafen, Germany, p. 941568, Jun. 1994.

[12] Foster, C. L., Tinker, M. L., Nurre, G. S., and Till, W. A., "Solar-array-induced disturbance of the Hubble Space Telescope pointing system," *Journal of Spacecraft and Rockets*, 32(4), pp. 634–644, Jul. 1995. (Quoted page 1.)

[13] Courant, R., Friedrichs, K., and Lewy, H., "On the Partial Difference Equations of Mathematical Physics," *IBM Journal of Research and Development*, 11(2), pp. 215–234, Mar. 1967, originally published in Mathematische Annalen, 100, pp.32-74 (1928). (Quoted page 1.)

[14] Dusinberre, G. M., *Heat-Transfer Calculation by Finite Differences*, International textbooks in mechanical engineering., Scranton, Pa., International Textbook Co, (1961). (Quoted pages 1, 30, and 106.)

[15] Turner, M. J., Clough, R. W., Martin, H. C., and Topp, L. C., "Stiffness and Deflection Analysis of Complex Structures," *Journal of the Aeronautical Sciences*, 23(9), pp. 805–823, Sep. 1956. (Quoted page 1.)

[16] Clough, R. W., "The finite element method after twenty-five years: A personal view," *Computers & Structures*, 12(4), pp. 361–370, Oct. 1980. (Quoted page 1.)

[17] Visser, W., The Finite Element Method in Deformation and Heat Conduction Problems, Phd thesis, TU Delft, Delft University of Technology, Delft, The Netherland, (1968). (Quoted page 1.)

[18] Emery, A. F. and Mortazavi, H. R., "A comparison of the finite difference and finite element methods for heat transfer calculations," *Proceedings of the Symposium Computational Aspects of Heat Transfer in Structures*, NASA Langley Research Center, Hampton, Virginia, USA, pp. 51–82, (Nov. 5-8, 1981). (Quoted page 1.)

[19] Thornton, E., Dechaumphai, P., and Wieting, A., "Integrated finite element thermal-structural analysis with radiation heat transfer," *Proceedings of the 23rd Structures, Structural Dynamics and Materials Conference*, American Institute of Aeronautics and Astronautics, New Orleans,LA, pp. 188–196, May 1982. (Quoted pages 1 and 10.)

[20] Sein, E., Toulemont, Y., Safa, F., Duran, M., Deny, P., de Chambure, D., Passvogel, T., and Pilbratt, G. L., "A Φ 3.5 m diameter Sic telescope for Herschel mission," *Astronomical Telescopes and Instrumentation*, International Society for Optics and Photonics, pp. 606–618, (2003). (Quoted page 1.)

[21] Bagnasco, G., Kolm, M., Ferruit, P., Honnen, K., Koehler, J., Lemke, R., Maschmann, M., Melf, M., Noyer, G., Rumler, P., Salvignol, J.-C., Strada, P., and Te Plate, M., "Overview of the near-infrared spectrograph (NIRSpec) instrument on-board the James Webb Space Telescope (JWST)," *Proc. SPIE 6692, Cryogenic Optical Systems and Instruments XII*, Vol. 6692, San Diego, CA, USA, p. 66920M, Sep. 2007.

[22] Fishwick, N., Barraclough, S., and Warren, C., "High Accuracy Thermal Modelling applied to LISA Pathfinder Thermal Noise Analysis," *Proceedings of the 40th International Conference on Environmental Systems*, American Institute of Aeronautics and Astronautics, Barcelona, Spain, pp. AIAA 2010–6142, Jul. 2010.

[23] de Bruijne, J. H. J., "Science performance of Gaia, ESA's space-astrometry mission," *Astrophysics and Space Science*, 341(1), pp. 31–41, Sep. 2012.

[24] Halain, J.-P., Rochus, P., Appourchaux, T., Berghmans, D., Harra, L., Schühle, U., Auchere, F., Zhukov, A., Renotte, E., Defise, J.-M., Rossi, L., Fleury-Frenette, K., Jacques, L., Hochedez, J.-F., and Ben Moussa, A., "The technical challenges of the Solar-Orbiter EUI instrument," *Proc. SPIE 7732, Space Telescopes and Instrumentation 2010: Ultraviolet to*

Gamma Ray, 77320R, Vol. 7732, Society of Photo-Optical Instrumentation Engineers, San Diego, USA, pp. 77320R–77320R–10, (2010). (Quoted pages 1 and 93.)

[25] Giesen, P. and Folgering, E., "Design guidelines for thermal stability in optomechanical instruments," *Proceedings of SPIE, Optomechanics*, Vol. 5176, Society of Photo-Optical Instrumentation Engineers, San Diego, CA, USA, pp. 126–134[, Oct. 2003. (Quoted page 1.)

[26] Yoder, P. and Vukobratovich, D., *Opto-Mechanical Systems Design.*, 4th Edition, Crc Press, Boca Raton, (2015). (Quoted page 1.)

[27] Zhang, H. L., Baeyens, J., Degrève, J., and Cacères, G., "Concentrated solar power plants: Review and design methodology," *Renewable and Sustainable Energy Reviews*, 22, pp. 466–481, Jun. 2013. (Quoted page 1.)

[28] Ho, C. K. and Iverson, B. D., "Review of high-temperature central receiver designs for concentrating solar power," *Renewable and Sustainable Energy Reviews*, 29, pp. 835–846, Jan. 2014. (Quoted page 1.)

[29] Cook, G. M., Hodgetts, C., Stock, N. J., and Almazan, P. P., "Using Finite Element Discretisation for Spacecraft Thermal Analysis," *Proceedings of the 25th International Conference on Environmental Systems*, SAE International, San Diego, CA, USA, p. 951608, Jul. 1995. (Quoted page 1.)

[30] Panczak, T. D., "The Failure of Finite Element Codes for Spacecraft Thermal Analysis," *Proceedings of the 26th International Conference On Environmental Systems*, SAE International, Monterey, CA, USA, p. 961450, (8-11 July 1996).

[31] Etchells, J., "YGT Report: Integrating Finite Element Analysis into the Spacecraft Thermal Analysis Process," , Tech. Rep. YGT_Report_150705_1630, European Space Agency, ESTEC, Noordwijk, The Netherlands, Jul. 2005. (Quoted pages 2, 6, 29, 32, 33, and 92.)

[32] Peabody, H., "Introduction to FEMAP for Thermal Model Generation," *Proceedings of the Thermal and Fluids Analysis Workshop*, College Park, Maryland, USA, p. 6, Aug. 2006. (Quoted pages 2 and 10.)

[33] Gilmore, D. G. (Ed.), *Spacecraft Thermal Control Handbook*, 2nd Edition, Aerospace Press, El Segundo, Calif, (2002). (Quoted pages 1, 2, 6, 7, 8, 9, 29, 106, and 137.)

[34] Howell, J. R., "The Monte Carlo method in radiative heat transfer," *Transactions-American Society Of Mechanical Engineers Journal Of Heat Transfer*, 120(3), pp. 547–560, (1998). (Quoted page 2.)

[35] Howell, J. R., Siegel, R., and Mengüç, M. P., *Thermal Radiation Heat Transfer*, 6th Edition, CRC Press, Boca Raton, Fla., (2015). (Quoted pages 22, 31, 118, and 149.)

[36] Modest, M. F., *Radiative Heat Transfer*, third edition Edition, Academic Press, New York, (2013). (Quoted pages 2, 21, 23, 46, and 149.)

[37] Chin, J. H., Panczak, T. D., and Fried, L., "Spacecraft thermal modelling," *International Journal for Numerical Methods in Engineering*, 35(4), pp. 641–653, Sep. 1992. (Quoted pages 2 and 82.)

[38] Panczak, T. D., Ring, S., and Welch, M., "True Concurrent Thermal Engineering Integrating CAD Model Building with Finite Element and Finite Difference Methods," *Proceedings of the 9th Thermal and Fluids Analysis Workshop Proceedings*, NASA Glenn Research Center, Cleveland Ohio, pp. 217–232, (Aug. 31 - Sept. 4, 1998).

[39] Panczak, T. D. and Welch, M., "Integrating Thermal and Structural Analysis with Thermal Desktop^{TM}," *Proceedings of the 29th International Conference On Environmental Systems*, SAE International, Denver, Colorado, p. 2126, Jul. 1999.

[40] Cullimore, B., Panczak, T., Baumann, J., Genberg, V., and Kahan, M., "Integrated analysis of thermal/structural/optical systems," *Proceedings of the 32nd International Conference on Environmental Systems*, SAE International, San Antonio, Texas, p. 2444, (2002).

[41] ITP Engines UK Ltd., "ESATAN-TMS Thermal Engineering Manual," , Tech. rep., ITP Engines UK Ltd., Whetstone, Leicester United Kingdom, Aug. 2015. (Quoted page 2.)

[42] Gould, D. C., "Radiation Heat Transfer Between Diffuse-Gray Surfaces Using Higher Order Finite Elements," *Proceedings of the 34th AIAA Thermophysics Conference*, American Institute of Aeronautics and Astronautics, Denver, Colorado, pp. AIAA 2000–2371, (19-22 June 2000). (Quoted pages 2 and 10.)

[43] Peabody, H., "A Hybrid Solution Method Using ThermalDesktop and TMG to Solve LISA and other Large Thermal Models," *Proceedings of the 35th International Conference on Environmental Systems*, SAE International, Rome, Italy, p. 3055, Jul. 2005. (Quoted page 2.)

[44] May, C. P. and Costello, F. A., "Accuracy of Various Methods for Reducing the Number of Radiation Factors," *Proceedings of the 28th International Conference On Environmental Systems*, SAE International, Danvers, Massachusetts, USA, p. 981637, Jul. 1998. (Quoted page 2.)

[45] Kornberg, O. and Popok, D., "New Methods to Solve for Radiation from Finite Element Modelers," *Proceedings of the Thermal and Fluids Analysis Workshop*, College Park, Maryland, USA, p. 10, Aug. 2006. (Quoted pages 2 and 103.)

[46] Lemieux, C., *Monte Carlo and Quasi-Monte-Carlo Sampling*, Springer, (2009). (Quoted pages 3, 26, and 38.)

[47] Niederreiter, H., *Random Number Generation and Quasi-Monte Carlo Methods*, Vol. 63 of *CBMS-NSF regional conference series in applied mathematics*, Society for Industrial and Applied Mathematics, Philadelphia, Pa, (1992). (Quoted page 38.)

[48] Owen, A. B., "Quasi-monte carlo sampling," *ACM SIGGRAPH 2003 Course 44*, San Diego, CA, USA, pp. 69–88, (2003). (Quoted pages 3, 24, and 38.)

[49] Cumber, P. S., "Accelerating ray convergence in incident heat flux calculations using Sobol sequences," *International Journal of Thermal Sciences*, 48(7), pp. 1338–1347, (2009). (Quoted pages 3 and 39.)

[50] Kersch, A., Morokoff, W., and Schuster, A., "Radiative heat transfer with quasi-Monte Carlo methods," *Transport Theory and Statistical Physics*, 23(7), pp. 1001–1021, Sep. 1994. (Quoted pages 3, 38, and 44.)

[51] Arvo, J., Hanrahan, P., Jensen, H. W., Mitchell, D., Pharr, M., Shirley, P., and Fajardo, M., *State of the Art in Monte Carlo Ray Tracing for Realistic Image Synthesis*, acm siggraph 2001 course 29 Edition, ACM Press, New York, (2001). (Quoted page 3.)

[52] Beckers, B. and Beckers, P., "A general rule for disk and hemisphere partition into equal-area cells," *Computational Geometry*, 45(7), pp. 275–283, Aug. 2012. (Quoted pages 3, 41, and 49.)

[53] Vueghs, P., Innovative Ray Tracing Algorithms for Space Thermal Analysis, PhD thesis, University of Liège, Mar. 2009. (Quoted pages 3, 20, 23, 38, 39, 40, 41, 47, 49, and 80.)

[54] Vujičić, M. R., Lavery, N. P., and Brown, S. G. R., "View factor calculation using the Monte Carlo method and numerical sensitivity," *Communications in Numerical Methods in Engineering*, 22(3), pp. 197–203, Sep. 2005, *. (Quoted page 3.)

[55] Jeffers, A. E., "Heat transfer element for modeling the thermal response of non-uniformly heated plates," *Finite Elements in Analysis and Design*, 63, pp. 62–68, Jan. 2013. (Quoted page 3.)

[56] Martin, S., Etchells, J., and Appel, S., "Updates to the SINAS tool for mapping of lumped parameter temperatures onto a structural FE models," *Proceedings of the 23rd European Workshop on Thermal and ECLS Software*, ESA, Noordwijk, The Netherlands, pp. 193–208, Oct. 2009. (Quoted pages 3, 6, and 109.)

[57] McMurchy, R. R., "Thermal Network Modelling Handbook," , contract 9-10435 NASA-CR-144418, TRW Systems Group, Redondo Beach, CA, United States, (1972). (Quoted pages 6 and 29.)

[58] Etchells, J. and Bonnafous, B., "Guidelines for Space Thermal Modelling and Analysis," , Tech. Rep. TEC-MTV/2011/3562/ln, European Space Agency, ESTEC, Noordwijk, The Netherlands, Nov. 2012. (Quoted pages 6 and 7.)

[59] Robson, A., Heller, C., and Sdunnus, H., "Space Systems Thermal Analysis Software - A User's View," *Proceedings of the 35th International Conference on Environmental Systems*, SAE International, Rome, Italy, p. 3052, Jul. 2005. (Quoted page 6.)

[60] Terhes, C. and Appel, S., "Thermal mapping on Bepicolombo's Mercury Planetary Orbiter (MPO) using SINASIV," *Proceedings of the 30th European Space Thermal Analysis Workshop*, Noordwijk, The Netherlands, p. 1, May 2016. (Quoted pages 6 and 109.)

[61] Wise, R. A. and Mcelroy, P. M., "Finite Difference (FD) to Finite Element (FEA) Temperature Translation Using "Sinda Temperature Translator (STT)"," *Proceedings of the 31st International Conference on Environmental Systems*, SAE International, Orlando, Florida, USA, p. 3052, Jul. 2001. (Quoted page 6.)

[62] Rossi, F. N. and Pelletier, L., "Application of Thermal Software CORATHERM to Provide Thermo-Elastic Inputs," *Proceedings of the 38th International Conference On Environmental Systems*, SAE International, Danvers, Massachusetts, USA, p. 981578, Jul. 1998. (Quoted page 29.)

[63] Basset, T., Dudon, J.-P., and Vernay, C., "Applications of Thermal Software Coratherm to Provide Spacecraft Thermo-Elastic Inputs," *Proceedings of the 31st International Conference on Environmental Systems*, SAE International, Orlando, Florida, USA, p. 2439, Jul. 2001. (Quoted pages 9 and 29.)

[64] Zhukov, A., Czupalla, M., Kuisl, A., and Bleicher, G., "The KT Thermal Mapping Tool: A semi-automated temperature transfer between structural and thermal models," *Proceedings of the 27th European Space Thermal Analysis Workshop*, European Space Agency, Noordwijk, The Netherlands, pp. 119–136, (3-4 Dec 2013). (Quoted page 6.)

[65] Hengeveld, D. W., Braun, J. E., Groll, E. A., and Williams, A. D., "Hot- and Cold-Case Orbits for Robust Thermal Control," *Journal of Spacecraft and Rockets*, 46(6), pp. 1249–1260, Nov. 2009. (Quoted page 6.)

[66] Arduini, C., "Model uncertainties and approximations in large space system thermal analysis," *Acta Astronautica*, 10, pp. 51–53, (1983). (Quoted page 7.)

[67] Siebes, G., Kingery, C., Farguson, C., White, M., Blakely, M., Nunes, J., Avila, A., Man, K., Hoffman, A., and Forgrave, J., "Review and Assessment of JPL's Thermal Margins," *Proceedings of the 42nd International Conference on Environmental Systems*, American Institute of Aeronautics and Astronautics, San Diego, CA, USA, pp. AIAA 2012–3603, Jul. 2012. (Quoted page 7.)

[68] Gaski, J. D. and Lewis, D. R., "Chrysler Improved Numerical Differencing Analyzer," , Tech. Rep. TN-AP-66-15, Chrysler Corporation Space Division, New Grleans, Louisiana, Apr. 1966. (Quoted page 8.)

[69] Ishimoto, T. and Fink, L. C., "Systems Improved Numerical Differencing Analyzer (SINDA): Engineering-program manual," , NASA contract 9-10435 NASA-CR-134272,, TRW Systems Group, Redondo Beach, CA, United States, (1971). (Quoted pages 8 and 29.)

[70] Cullimore & Ring Technologies, "C&R Tech. - SINDA/FLUINT User's manual," , Tech. rep., Cullimore & Ring Technologies, May 2013. (Quoted page 8.)

[71] Creel, R., "LUROVA - From Render Engine to Thermal Model," *Proceedings of the Thermal and Fluids Analysis Workshop*, (Aug 4-8, 2014). (Quoted page 8.)

[72] Rathjen, H., "A personal look back on Thermal Software evolution within the past 36 years," *Proceedings of the 28th European Space Thermal Analysis Workshop*, European Space Agency, Noordwijk, The Netherlands, pp. 127–140, (14-15 Oct 2014). (Quoted pages 8 and 9.)

[73] Jensen, C. L. and Goble, R. G., "Thermal Radiation Analysis System (TRASYS)," , Nasa-cr-134391, mcr-74-100, Martin Marietta Corporation for NASA NASA Johnson Spacecraft Center, Denver, Colorado, Jun. 1974. (Quoted page 8.)

[74] Marshall Space Flight Center, "Large Space Telescope Phase A Final Report - Volume V - Support Systems Module," , Technical memorandum NASA TM X-64726, NASA, Alabama, Dec. 1972. (Quoted page 8.)

[75] Fleck, J. J., "The calculation of nonlinear radiation transport by a monte carlo method.," , Tech. Rep. UCRL–6698(Del.), 4466389, Lawrence Radiation Lab., Univ. of California, Livermore, Livermore, Jan. 1961. (Quoted pages 9 and 23.)

[76] Howell, J. R. and Perlmutter, M., "Monte Carlo Solution of Thermal Transfer Through Radiant Media Between Gray Walls," *Journal of Heat Transfer*, 86(1), pp. 116, (1964). (Quoted page 9.)

[77] Howell, J. R., "Application of Monte Carlo to Heat Transfer Problems," *Advances in Heat Transfer*, 5, pp. 1–54, (1969). (Quoted pages 9 and 23.)

[78] Turner, R., Spencer, G., Baumeister, J., and Rigby, P., "NEVADA - A Comprehensive and Proven Radiation Heat Transfer Computer Software Package," *Proceedings of the 27th International Conference On Environmental Systems*, SAE International, Lake Tahoe, Nevada, p. 972440, Jul. 1997. (Quoted page 9.)

[79] Modest, M. F., "Three-dimensional radiative exchange factors for nongray, nondiffuse surfaces," *Numerical Heat Transfer*, 1(3), pp. 403–416, Jul. 1978. (Quoted page 9.)

[80] Voigt, R. A., "Recent Developments in Thermal Radiation System Analyzer (TRASYS)," , *Proceedings of the Symposium on Computational Aspects of Heat Transfer in Structures*Adelman, H. M. (Ed.), NASA Langley Research Center, NASA Langley Research Center, pp. 243–251, (3-5 Nov 1981). (Quoted page 9.)

[81] Baumeister, J. F., Beach, D. E., and Armand, S. C., "Comparative Thermal Analysis of the Space Station Freedom Photovoltaic Deployable Boom Structure Using Trasys, Nevada, and Sinda Programs," *Proceedings of the 19th Intersociety Conference on Environmental Systems*, SAE International, San Diego, CA, USA, p. 891563, Jul. 1989. (Quoted page 9.)

[82] Raney, P. J., Weidman, D. J., and Adelman, H. M., "NASTRAN: Status, maintenance and future development of new capability," *Proceedings of the 1st NASTRAN Users' Colloquim*, NASA Langley Research Center, Hampton, Virginia, USA, pp. 1–7, (September 13-15, 1971). (Quoted page 9.)

[83] Lee, H.-P., "Structural-Thermal-Optical Program (STOP)," *Significant Accomplishments in Technology*, Goddard Space Flight Center, Greenbelt, Maryland, United States, pp. 36–40, Jan. 1971. (Quoted page 9.)

[84] Lee, H. and Mason, J. B., "NASTRAN thermal analyzer: A general purpose finite element heat transfer computer program," *Proceedings of the 2nd NASTRAN Users' Colloquium*, Hampton, VA; United States, pp. 443–454, (11-12 Sep. 1972).

[85] Lee, H.-P., Jan. 1973. "Application of Finite-Element Method in the Computation of Temperature with Emphasis on Radiative Exchanges," , *AIAA Progress in Astronautics and Aeronautics: Thermal Control and Radiation*. Tien, C. L. (Ed.). Vol. 31. MIT Press, Cambridge, MA, pp. 491–520.

[86] Lee, H.-P., "NASTRAN thermal analyzer: Theory and application including a guide to modeling engineering problems, volume 1," , Tech. Rep. NASA TM X-3503, NASA Goddard Space Flight Center, Greenbelt, Maryland 20771, Apr. 1977.

[87] Lee, H.-P., "NASTRAN thermal analyzer in a unified finite-element treatment of thermostructural analyses," *Proceedings of the Conference on Computational Aspects of Heat Transfer in Structures*, NASA Goddard Space Flight Center, Hampton, VA; United States, pp. 1–22, (3-5 Nov. 1981). (Quoted page 9.)

[88] Dijkstra, E. W., (1969). "Structured Programming," . *Software Engineering Techniques*. NATO Science Committee, Rome, Italy, pp. 88–93. (Quoted page 9.)

[89] Mills, H., "Structured Programming: Retrospect and Prospect," *IEEE Software*, 3(6), pp. 58–66, Nov. 1986. (Quoted page 9.)

[90] Loughhead, J. N., Miles, G. A., and Turner, J. R., "The ESATAN Thermal Network Analysis Computer Program," *Proceedings of the 14th Intersociety Conference on Environmental Systems*, SAE International, San Diego, CA, USA, p. 840967, Jul. 1984. (Quoted page 9.)

[91] Rebis, J. J. and Stroom, C. J. M., "ESATAN, A Review After Four Years in Use," *Proceedings of the 19th Intersociety Conference on Environmental Systems*, SAE International, San Diego, CA, USA, p. 891558, Jul. 1989.

[92] Stock, N. J. and Stroom, C. J. M., "The Development of Windowed Interfaces to the ESATAN/FHTS Thermal Analysis System," *Proceedings of the 23rd International Conference on Environmental Systems*, SAE International, Colorado Springs, Colorado, USA, p. 932257, Jul. 1993.

[93] Thomas, J., "Aerospace Thermal Analysis Tools - The State of the Art," *Proceedings of the 29th International Conference On Environmental Systems*, SAE International, Denver, Colorado, p. 2157, Jul. 1999. (Quoted page 9.)

[94] Rebis, J. J., Koeck, C., and Jeanne, P., "ESARAD, Software for View Factor, Radiative Exchange Factor and Heat Flux Calculation," *Proceedings of the 19th International Conference on Environmental Systems*, Vol. 1, SAE International, San Diego, CA, USA, p. 891560, Jul. 1989. (Quoted page 9.)

[95] Rebis, J. J. and Jeanne, P., "The Implementation of the ESARAD User Interface, Database and Geometric Modelling Facilities," *Proceedings of the 20th International Conference On Environmental Systems*, SAE International, Williamsburg, Virginia, p. 901377, Jul. 1990.

[96] Rebis, J. and Jeanne, P., "ESARAD - The European Space Agency's Radiative Analyser," *Proceedings of the 21st International Conference On Environmental Systems*, SAE International, San Francisco, CA, USA, p. 911587, Jul. 1991.

[97] Hampshire, I. M., Flett, D. C., Cook, G. M., Planas-Almazan, P., and Norris, R. D., "Esarad–Improvements to the European Space Agency Radiative Analyses," *Proceedings of the 26th International Conference On Environmental Systems*, SAE International, Monterey, CA, USA, p. 961374, (8-11 July 1996).

[98] Flett, D. C. and Almazan, P. P., "ESARAD 3.2 and its applications," , *Sixth European Symposium on Space Environmental Control Systems*Guyenne, T.-D. (Ed.), Vol. 400 of *ESA Special Publication*, p. 649, Aug. 1997. (Quoted page 9.)

[99] Davidson, A. M. and Stroom, C., "MANIP and MINIP, new modeling tools for the thermal engineer," , *ESA Environmental and Thermal Control Systems for Space Vehicles*Guyenne, T. D. and Hunt, J. J. (Eds.), Vol. 200 of *ESA Special Publication*, pp. 243–248, Dec. 1983. (Quoted page 9.)

[100] Stock, N. J. and De Koning, H. P., "Integrating the Thermal Analysis Process," *Proceedings of the 30th International Conference On Environmental Systems*, SAE International, Toulouse, France, p. 2445, (10-13 July 2000). (Quoted page 9.)

[101] Thomas, J., "Recent Advances in Shortening the Thermal Analysis Life-Cycle," *Proceedings of the 33rd International Conference on Environmental Systems*, SAE International, Vancouver, Canada, p. 2607, Jul. 2003. (Quoted page 9.)

[102] Theroude, C., Soriano, T., and M. Baucher, "THERMICA version 4.5.1 User Manual," , User Manual ASTRI.UM.757138.ASTR iss2.1, EADS Astrium, Toulouse, May 2012. (Quoted pages 9, 30, 53, 66, 80, and 109.)

[103] Behee, R., "The THERMICA-SINDA/G Integrated Graphical Environment for Spacecraft Thermal Modeling," *Proceedings of the 27th International Conference on Environmental Systems*, SAE International, Lake Tahoe, NE, USA, p. 972444, Jul. 1997. (Quoted page 9.)

[104] Basset, T., Dudon, J.-P., and Brunetti, F., "Thales Alenia Space thermal software suite," *Proceedings of the 22nd European Workshop on Thermal and ECLS Software*, European Space Agency, Noordwijk, The Netherlands, pp. 289–302, (28-29 Oct 2008). (Quoted page 9.)

[105] Basset, T. and Hugonnot, P., "E-Therm Policy," *Proceedings of the 27 Th European Space Thermal Analysis Workshop*, European Space Agency, Noordwijk, The Netherlands, pp. 221–234, (3-4 Dec 2013). (Quoted pages 9 and 109.)

[106] Perotto, V. and Mareschi, V., "ALTAN, a New Tool for Spacecraft Thermal Simulation," *Proceedings of the 34th International Conference On Environmental Systems*, SAE International, Colorado Springs, Colorado, USA, p. 2317, Jul. 2004. (Quoted page 9.)

[107] Fogerson, P. E., Welch, M. J., and Lepore, J. M., "Spacecraft Thermal Modeling Using the Thermal Synthesizer System," *Proceedings of the 26th International Conference On Environmental Systems*, SAE International, Monterey, CA, USA, p. 961377, (8-11 July 1996). (Quoted page 10.)

[108] Panczak, T. D. and Ring, S. G., "RadCAD: Integrating Radiation Analysis with Modern CAD Systems," *Proceedings of the 26th International Conference On Environmental Systems*, Monterey, CA, USA, p. 961375, (8-11 July 1996). (Quoted page 10.)

[109] Lucas, S., "RadCAD: Validation of a New Thermal Radiation Analyzer," *Proceedings of the 27th International Conference On Environmental Systems*, SAE International, Lake Tahoe, NE, USA, p. 972442, Jul. 1997. (Quoted page 10.)

[110] Noravian, H., "Integrated Thermal Analysis System (ITAS)," *Proceedings of the 26th International Conference On Environmental Systems*, SAE International, Monterey, CA, USA, p. 961376, (8-11 July 1996). (Quoted page 10.)

[111] Gartling, D., "COYOTE: A finite-element computer program for nonlinear heat-conduction problems.," , Tech. Rep. SAND–77-1332, Sandia National Laboratories, Albuquerque, New Mexico, Jun. 1978. (Quoted page 10.)

[112] Gartling, D. K., Hogan, R. E., and Glass, M. W., "COYOTE - A Finite Element Computer Program for Nonlinear Heat Conduction Problems Part I - Theoretical Background," , Tech. Rep. SAND2009-4926, Sandia National Laboratories, Albuquerque, New Mexico, Apr. 2010. (Quoted page 10.)

[113] Glass, M. W., "CHAPARRAL: A library for solving large enclosure radiation heat transfer problems," , Tech. Rep. SAND–95-2049, 120875, Sandia National Laboratories, Albuquerque, New Mexico, Aug. 1995. (Quoted page 10.)

[114] Noor, A. K., "Survey on Computer Programs for Heat Transfer Analysis," *Proceedings of the Symposium on Computational Aspects of Heat Transfer in Structures*, NASA Langley Research Center, pp. 487–561, (3-5 Nov 1981). (Quoted page 10.)

[115] Noor, A. K., "Survey of computer programs for heat transfer analysis," *Finite Elements in Analysis and Design*, 2(3), pp. 259–312, Oct. 1986. (Quoted page 10.)

[116] Kadaba, P. V., "Thermal radiation view factor: Methods, accuracy and computer-aided procedures," , Tech. Rep. NGT-01-002-099, Georgia Institute of Technology, Aug. 1982. (Quoted pages 10, 23, and 80.)

[117] Zarda, P. R., Anderson, T., and Baum, F., "FEM/SINDA: Combining the strengths of NASTRAN, SINDA, I-DEAS, and PATRAN for thermal and structural analysis," *Proceedings of COSMIC, The Twenty-First NASTRAN (R) Users' Colloquium*, pp. 41–59, Sep. 1993. (Quoted page 10.)

[118] Behee, R., "FEMAP for SINDA/G, a Transparent Integration of SINDA/G into the FEMAP Modeling System," *Proceedings of the 29th International Conference on Environmental Systems*, SAE International, Denver, Colorado, p. 2127, Jul. 1999. (Quoted page 10.)

[119] Fogerson, P. E., "Introduction of the Finite Element Method into the Thermal Synthesizer System," *Proceedings of the 27th International Conference On Environmental Systems*, SAE International, Lake Tahoe, Nevada, p. 972447, Jul. 1997. (Quoted page 10.)

[120] Kirtley, C. J. and Bouquet, H., "ESATAN Thermal Modelling Suite - Product Developments & Demonstrations," *Proceedings of the 24th European Thermal & ECLS Software Workshop*, ESA/Estec, Noordwijk, the Netherlands, pp. 111–134, (16-17 Nov 2010). (Quoted page 10.)

[121] Kirtley, C. J., "ESATAN Thermal Modelling Suite - product status," *Proceedings of the 25th European Thermal & ECLS Software Workshop*, ESA/Estec, Noordwijk, the Netherlands, pp. 145–166, Nov. 2011.

[122] Brouquet, H., "ESATAN Thermal Modelling Suite - product status," *Proceedings of the 26th European Thermal & ECLS Software Workshop*, ESA/Estec, Noordwijk, the Netherlands, pp. 137–154, Nov. 2012. (Quoted page 10.)

[123] Gould, D. C., "Thermal analysis of a high-speed aircraft wing using P-Version finite elements," *Proceedings of the 39th AIAA Aerospace Sciences Meeting & Exhibit*, American Institute of Aeronautics and Astronautics, Reno, Nevada, pp. 2001–0369, (2001/01/8-11). (Quoted page 10.)

[124] Imhof, M., Caire, K., Fagot, A., and Rooijackers, H., "ESATAP: A Post-Processing Tool for Thermal Analysis," *Proceedings of the 35th International Conference On Environmental Systems*, SAE International, Rome, Italy, p. 3054, Jul. 2005. (Quoted page 10.)

[125] Marechal, C., "GAETAN: A General and Automated Environment for Thermal Analysis Network," *Proceedings of the 32nd International Conference on Environmental Systems*, SAE International, San Antonio, Texas, p. 2448, Jul. 2002. (Quoted page 10.)

[126] de Koning, H. P., de Wolf, H., Almazan, P. P., and van Oosten, R., "Integrated Communication Environment for Thermal Analysis Software - Phase 2," *Proceedings of the 24th International Conference On Environmental Systems*, SAE International, Friedrrichshafen, Germany, p. 941424, Jun. 1994. (Quoted page 10.)

[127] de Koning, H. P. and Almazan, P. P., "Solutions for the Exchange of Models and Results of Analysis and Tests in the Space Domain - STEP-TAS and STEP-NRF," *Proceedings of the 27th International Conference On Environmental Systems*, SAE International, Lake Tahoe, NE, USA, p. 972448, Jul. 1997.

[128] Lebègue, E., Siebes, G., and Stroom, C., "Thermal Analysis Data Exchange Between ESA and NASA with STEP," *Proceedings of the 29th International Conference On Environmental Systems*, SAE International, Denver, Colorado, p. 2125, Jul. 1999. (Quoted page 10.)

[129] Ruel, C., Fourmond, J.-J., and Peabody, H., "A New Spacecraft Radiative Thermal Model Exchange System," *Proceedings of the 33rd International Conference on Environmental Systems*, SAE International, Vancouver, Canada, p. 2604, Jul. 2003. (Quoted page 10.)

[130] Sharp, J. R. and Page, A. T., "Ablation Modeling of Ares-I Upper State Thermal Protection System Using Thermal Desktop," *Proceedings of the 18th Thermal/Fluids Analysis Workshop (TFAWS)*, Cleveland, OH, US, p. 13, (14-14 Sept. 2007). (Quoted page 11.)

[131] Boulier, E., Pinaud, G., and Bugnon, P., "Thermal issues related to ExoMars EDLS performance," *Proceedings of the 28th European Space Thermal Analysis Workshop*, Noordwijk, The Netherlands, pp. 117–126, Oct. 2014.

[132] Leyland, P., Sheikh, U., Duval, B., Hermann, T. A., Loehle, S., McIntyre, T., Morgan, R. G., Lewis, S., Wei, H., Bouilly, J.-M., and Marraffa, L., "The ESA ARC Project: Ablation Radiation Coupling for hypervelocity re-entry with low density type ablators," *Proceedings of the 46th AIAA Thermophysics Conference*, American Institute of Aeronautics and Astronautics, Washington DC, USA, p. 3234, Jun. 2016. (Quoted page 11.)

[133] Turner, J. R., Swift, T. J., Andrews, T. M., and Lebru, A., "ESATAN FHTS Fluid Network Analysis," *Proceedings of the 19th Intersociety Conference on Environmental Systems*, SAE International, San Diego, CA, USA, p. 891559, Jul. 1989. (Quoted page 11.)

[134] Cullimore, B. A., "Advances in SINDA/FLUINT and SINAPS," *Proceedings of the International 26th Conference On Environmental Systems*, SAE International, Monterey, CA, USA, p. 961447, Jul. 1996. (Quoted page 11.)

[135] Kirchhoff, G., "Über das Verhältniss zwischen dem Emissionsvermögen und dem Absorptionsvermögen der Körper für Wärme und Licht," *Annalen der Physik*, 185(2), pp. 275–301, (1860). (Quoted pages 14 and 18.)

[136] Wien, W., "Über die Energievertheilung im Emissionsspectrum eines schwarzen Körpers," *Annalen der Physik*, 294(8), pp. 662–669, (1896). (Quoted page 14.)

[137] Planck, M., "Über das gesetz der energieverteilung im normalspectrum," *Annalen der physik*, 309(3), pp. 553–563, (1901). (Quoted page 15.)

[138] "Standard Solar Constant and Zero Air Mass Solar Spectral Irradiance Tables," , Tech. Rep. ASTM E490-00a(2014), ASTM International, West Conshohocken, PA, USA, (2014). (Quoted pages 15 and 65.)

[139] Stefan, J., "Über die Beziehung zwischen der Wärmestrahlung und der Temperatur," *Sitzungsberichte der mathematisch-naturwissenschaftlichen Classe der kaiserlichen Akademie der Wissenschaften*, 79, pp. 391–428, (1879). (Quoted page 16.)

[140] Boltzmann, L., "Ableitung des Stefan'schen Gesetzes, betreffend die Abhängigkeit der Wärmestrahlung von der Temperatur aus der electromagnetischen Lichttheorie," *Annalen der Physik und Chemie*, 22, pp. 291–294, (1884). (Quoted page 16.)

[141] Lambert, J. H., *Photometria, sive, De mensura et gradibus luminis, colorum et umbrae (On the Measure and Gradations of Light, Colors, and Shade)*, V.E. Klett, Augustae Vindelicorum, (1760). (Quoted page 16.)

[142] Kauder, L., "Spacecraft Thermal Control Coatings References," , Tech. Rep. TP-2005-212792, NASA Goddard Space Flight Center, Greenbelt, Maryland, (2005). (Quoted page 18.)

[143] ECSS Executive Secretariat, "Measurements of thermo-optical properties of thermal control materials," , Tech. Rep. ECSS-Q-ST-70-09C, European Space Agency - European Coordination for Space Standardization, Noordwijk, The Netherlands, Jul. 2008. (Quoted page 18.)

[144] Sparrow, E. M., (1963). "On the Calculation of Radiant Interchange between Surfaces," , *Modern Developments in Heat Transfer*. Ibele, W. (Ed.). Academic Press, New York, p. 181. (Quoted page 20.)

[145] Hottel, H. C., (1954). "Radiant heat transmission," , *Heat Transmission*. McAdams, W. H. (Ed.), 3rd Edition. Chapter 3. McGraw-Hill Inc., pp. 55–125. (Quoted page 20.)

[146] Eckert, E. R. G. and Drake, R. M., *Heat and Mass Transfer*, McGraw-Hill Inc, (1959). (Quoted page 20.)

[147] Gebhart, B., *Unified Treatment for Thermal Radiation Transfer Processes: Gray, Diffuse Radiators and Absorbers*, Papers - American Society of Mechanical Engineers, American Society of Mechanical Engineers, (1957). (Quoted pages 20 and 31.)

[148] Gebhart, B., "Surface temperature calculations in radiant surroundings of arbitrary complexity—for gray, diffuse radiation," *International Journal of Heat and Mass Transfer*, 3(4), pp. 341–346, Dec. 1961. (Quoted pages 20 and 31.)

[149] Oppenheim, K., "Radiation Analysis by the Network Method," *Transactions of the ASME.*, 54, pp. 725–735, (1956). (Quoted pages 20 and 103.)

[150] Almazan, P. P., "Accuracy of Monte Carlo ray-tracing thermal radiation calculations: A practical discussion," *Proceedings of the 6th European Symposium on Space Environmental Control Systems*, European Space Agency, Noordwijk, The Netherlands, pp. 579–591, (20-22 May, 1997). (Quoted pages 22, 24, 27, and 38.)

[151] Cohen, M. F. and Greenberg, D. P., "The Hemi-cube: A Radiosity Solution for Complex Environments," *SIGGRAPH Comput. Graph.*, 19(3), pp. 31–40, Jul. 1985. (Quoted page 23.)

[152] Hanrahan, P., Salzman, D., and Aupperle, L., "A rapid hierarchical radiosity algorithm," *Computer Graphics*, 25(4), pp. 197–206, (1991). (Quoted page 23.)

[153] Metropolis, N. and Ulam, S., "The Monte Carlo Method," *Journal of the American Statistical Association*, 44(247), pp. 335, Sep. 1949. (Quoted page 23.)

[154] Metropolis, N., "The beginning of the Monte Carlo method," *Los Alamos Science*, 15(584), pp. 125–130, (1987).

[155] Hammersley, J. M. and Handscomb, D. C., *Monte Carlo Methods*, London Methuen and Co. Ltd., (1964). (Quoted page 23.)

[156] Kelvin, L., "Nineteenth century clouds over the dynamical theory of heat and light," *Philosophical Magazine Series 6*, 2(7), pp. 1–40, Jul. 1901. (Quoted page 23.)

[157] Bernoulli, J., (1713). "Pars Quarta tradens Usum & Applicationem Praecedentis Doctrinae in Civilibus, Moralibus & Oeconomicis, (Chapter 4: The Use and Application of the Previous Doctrine to Civil, Moral and Economic Affairs)," . *Ars Conjectandi*. Impensis Thurnisiorum, Fratrum, Basileae, pp. 210–239, translated into English by Oscar Sheynin. (Quoted page 24.)

[158] Glassner, A. S., *An Introduction to Ray Tracing*, Academic Press, London, (1989). (Quoted pages 24, 38, and 128.)

[159] Koeck, C., Coffinier, P., Auberger, X., and Rebis, J.-J., "Kernel Algorithms document - ESARAD," , Tech. rep., ESA ESTEC; MATRA/ERC, (1994). (Quoted pages 24, 38, 51, 53, 66, 80, and 82.)

[160] Shirley, P. and Marschner, S., *Fundamentals of Computer Graphics*, 4th Edition, CRC Press, (2015). (Quoted page 26.)

[161] Pharr, M. and Humphreys, G., *Physically Based Rendering: From Theory to Implementation*, 2nd Edition, Elsevier/Morgan Kaufmann, Amsterdam, (2010). (Quoted pages 26, 39, 40, and 51.)

[162] Almazan, P. P., "Accuracy control in Monte Carlo radiative calculations," *Proceedings of the 5th Thermal and Fluids Analysis Workshop*, pp. 47–62, Nov. 1993. (Quoted pages 27 and 38.)

[163] Almazan, P. P., "Statistical Error Control for Radiative Software Based on Monte Carlo Methods," *Proceedings of the 23rd International Conference on Environmental Systems*, SAE International, Colorado Springs, Colorado, USA, p. 932258, (12-15 July 1993). (Quoted page 27.)

[164] Desaunettes, B., Charvet, D., and Renard, P., "Statistical Accuracy Control in THERMICA," *Proceedings of the 25th International Conference on Environmental Systems*, SAE International, San Diego, CA, USA, p. 951611, Jul. 1995. (Quoted page 27.)

[165] Reddy, J. N. and Gartling, D. K., *The Finite Element Method in Heat Transfer and Fluid Dynamics*, 3rd Edition, CRC series in computational mechanics and applied analysis, CRC Press, Boca Raton, FL, (2010). (Quoted pages 28 and 30.)

[166] Chambré, P. L., "Nonlinear Heat Transfer Problem," *Journal of Applied Physics*, 30(11), pp. 1683, (1959). (Quoted page 29.)

[167] Abarbanel, S. S., On Some Problems in Radiative Heat Transfer, Phd thesis, - Massachusetts Institute of Technology, Dept. of Aeronautical Engineering,, (1959). (Quoted page 29.)

[168] Liebmann, G., "A new electrical analog method for the solution of transient heat-conduction problems," *Transactions of the ASME*, 78(3), pp. 655–665, (1956). (Quoted page 29.)

[169] Karplus, W. J., *Analog Simulation: Solution of Field Problems.*, no. 434 p. in McGraw-Hill series in information processing and computers, McGraw-Hill, New York, (1958). (Quoted page 29.)

[170] Fourier, J., *Théorie Analytique de La Chaleur*, Firmin Didot, Paris, (1822). (Quoted page 29.)

[171] Doenecke, J. and Hartmann, G., "Conductive Shape Factors Allowing Node Reduction," *Proceedings of the 30th International Conference On Environmental Systems*, SAE International, Toulouse, France, p. 2485, Jul. 2000. (Quoted page 29.)

[172] Fradin, J. P. and Desaunettes, B., "Automatic Computation of Conductive Conductances Intervening in the Thermal Chain," *Proceedings of the 25th International Conference on Environmental Systems*, SAE International, San Diego, CA, USA, p. 951610, (10-13 Juy 1995). (Quoted page 29.)

[173] Fradin, J. P., Desaunettes, B., and Lacaze, C., "Rebeca-3D, The Software for Conductive Fluxes and Temperature Fields Prediction," *Proceedings of the 26th International Conference On Environmental Systems*, SAE International, Monterey, CA, USA, p. 961451, (8-11 July 1996). (Quoted page 29.)

[174] Chelotti, J. N., Pelletier, L., and Giovannini, R., "Application of EQUIVALE Software to the ESATAN Conductive Model Reduction," *Proceedings of the 23rd International Conference on Environmental Systems*, SAE International, Colorado Springs, Colorado, USA, p. 932132, Jul. 1993. (Quoted pages 29 and 109.)

[175] Dudon, J., Basset, T., and Peyrard, M., "A New Method for 3D Thermal Modeling With Coratherm," *Proceedings of the 33rd International Conference on Environmental Systems*, SAE International, Vancouver, Canada, p. 2665, Jul. 2003. (Quoted page 29.)

[176] Appel, S., Patrício, R., de Koning, H. P., and Pin, O., "Automatic Conductor Generation for Thermal Lumped Parameter Models," *Proceedings of the 34th International Conference On Environmental Systems*, SAE International, Colorado Springs, Colorado, USA, pp. SAE Technical Paper 2004–01–2397, Jul. 2004. (Quoted pages 29 and 109.)

[177] Kirtley, C. J., Stock, N. J., De Koning, H. P., and Appel, S., "Automatic Linear Conductor Generation Solution for Lumped Parameter Models," *Proceedings of the 35th International Conference On Environmental Systems*, SAE International, Rome, Italy, pp. SAE Technical Paper 2005–01–3059, Jul. 2005.

[178] Strutt, J. H., Stock, N. J., and Kirtley, C. J., "Lumped Parameter Thermal Conductor Generation for 3D Geometry," *Proceedings of the 44th International Conference on Environmental System*, AIAA, Tucson, AZ, USA, p. 297, (2014, July). (Quoted page 29.)

[179] Soriano, T., "THERMICA-THERMISOL 4.3.4," *Proceedings of the 24th European Thermal & ECLS Software Workshop*, Noordwijk, The Netherlands, pp. 151–168, (16-17 Nov. 2010). (Quoted page 30.)

[180] Kennelly, A. E., "The equivalence of triangles and three-pointed stars in conducting networks," *Electrical world and engineer*, 34(12), pp. 413–414, (1899). (Quoted page 33.)

[181] Hurty, W. C., "Vibrations of structural systems by component mode synthesis," *Journal of the Engineering Mechanics Division*, 86(4), pp. 51–70, (1960). (Quoted page 35.)

[182] Hurty, W. C., "Dynamic analysis of structural systems using component modes," *AIAA Journal*, 3(4), pp. 678–685, Apr. 1965. (Quoted page 35.)

[183] Guyan, R. J., "Reduction of stiffness and mass matrices," *AIAA journal*, 3(2), pp. 380–380, (1965). (Quoted pages 35 and 112.)

[184] Bampton, M. C. C. and Craig, Jr., R. R., "Coupling of substructures for dynamic analyses.," *AIAA Journal*, 6(7), pp. 1313–1319, Jul. 1968. (Quoted page 35.)

[185] MacNeal, R. H., "A hybrid method of component mode synthesis," *Computers & Structures*, 1(4), pp. 581–601, Dec. 1971. (Quoted page 35.)

[186] Botto, D., Zucca, S., Gola, M., Troncarelli, E., and Pasquero, G., "Component modes synthesis applied to a thermal transient analysis of a turbine disc," *Proceedings of the Worldwide Aerospace Conference & Technology Showcase,*, Vol. 10, Toulouse, France, p. 3, (2002). (Quoted page 35.)

[187] Botto, D., Zucca, S., and Gola, M. M., "A methodology for on-line calculation of temperature and thermal stress under non-linear boundary conditions," *International journal of pressure vessels and piping*, 80(1), pp. 21–29, (2003). (Quoted page 35.)

[188] Botto, D., Zucca, S., and Gola, M. M., "Reduced-Order Models for the Calculation of Thermal Transients of Heat Conduction/Convection FE Models," *Journal of Thermal Stresses*, 30(8), pp. 819–839, Jul. 2007. (Quoted page 35.)

[189] Shore, C. P., "Reduction method for thermal analysis of complex aerospace structures," , Tech. Rep. NASA-TP-2373, L-15777, NAS 1.60:2373, NASA Langley Research Center, (1985). (Quoted page 35.)

[190] Cardona, A. and Idelsohn, S., "Solution of non-linear thermal transient problems by a reduction method," *International Journal for Numerical Methods in Engineering*, 23(6), pp. 1023–1042, (1986). (Quoted page 35.)

[191] Noor, A. K., Balch, C. D., and Shibut, M. A., "Reduction methods for nonlinear steady-state thermal analysis," *International Journal for Numerical Methods in Engineering*, 20(7), pp. 1323–1348, Jul. 1984. (Quoted page 35.)

[192] Wang, Y., Song, H., Pant, K., Peabody, H., Ku, J., and Butler, C. D., "A projection-based model order reduction simulation tool for spacecraft thermal analysis," *Proceedings of the Thermal and Fluids Analysis Workshop (TFAWS11)*, NASA Langley Research Center, p. 19, (2011/08/15-19). (Quoted page 35.)

[193] Petit, D. and Pasquetti, R., "Réduction de modèle par identification de modes dominants : Application à un modèle bidimensionnel de diffusion thermique," *Revue de Physique Appliquée*, 25(8), pp. 831–842, (1990). (Quoted page 35.)

[194] Petit, D., Hachette, R., and Veyret, D., "A modal identification method to reduce a high-order model: Application to heat conduction modelling," *International Journal of Modelling & Simulation*, 17(3), pp. 242–250, (1997). (Quoted page 35.)

[195] Broussely, M., Bertin, Y., and Lagonotte, P., "Reduction and optimisation of thermal models using Kirchhoff network theory," *International Journal of Thermal Sciences*, 42(8), pp. 795–804, Aug. 2003. (Quoted page 35.)

[196] Oulefki, A. and Neveu, A., "Réduction par amalgame modal d'un modèle thermique," *Journal de Physique III*, 3(2), pp. 303–320, Feb. 1993. (Quoted page 35.)

[197] Girault, M. and Petit, D., "Identification methods in nonlinear heat conduction. Part I: Model reduction," *International Journal of Heat and Mass Transfer*, 48(1), pp. 105–118, Jan. 2005. (Quoted page 35.)

[198] Balima, O., Favennec, Y., and Petit, D., "Model Reduction for Heat Conduction with Radiative Boundary Conditions using the Modal Identification Method," *Numerical Heat Transfer, Part B: Fundamentals*, 52(2), pp. 107–130, Jun. 2007. (Quoted page 35.)

[199] Kerschen, G., Golinval, J.-c., Vakakis, A. F., and Bergman, L. A., "The method of proper orthogonal decomposition for dynamical characterization and order reduction of mechanical systems: An overview," *Nonlinear dynamics*, 41(1-3), pp. 147–169, (2005). (Quoted page 35.)

[200] Aling, H., Kosut, R., Emami-Naeini, A., and Ebert, J., "Nonlinear model reduction with application to rapid thermal processing," *Decision and Control, 1996., Proceedings of the 35th IEEE Conference on*, Vol. 4, IEEE, pp. 4305–4310, (1996). (Quoted page 35.)

[201] Banerjee, S., Cole, J., and Jensen, K., "Nonlinear model reduction strategies for rapid thermal processing systems," *IEEE Transactions on Semiconductor Manufacturing*, 11(2), pp. 266–275, May 1998.

[202] Fic, A., Białecki, R. A., and Kassab, A. J., "Solving Transient Nonlinear Heat Conduction Problems by Proper Orthogonal Decomposition and the Finite-Element Method," *Numerical Heat Transfer, Part B: Fundamentals*, 48(2), pp. 103–124, (2005).

[203] Bialecki, R. A., Kassab, A. J., and Fic, A., "Proper orthogonal decomposition and modal analysis for acceleration of transient FEM thermal analysis," *International Journal for Numerical Methods in Engineering*, 62(6), pp. 774–797, (2005).

[204] Pinnau, R. and Schulze, A., "Model reduction techniques for frequency averaging in radiative heat transfer," *Journal of Computational Physics*, 226(1), pp. 712–731, Sep. 2007.

[205] Falkiewicz, N. J. and Cesnik, C. E. S., "Proper Orthogonal Decomposition for Reduced-Order Thermal Solution in Hypersonic Aerothermoelastic Simulations," *AIAA Journal*, 49(5), pp. 994–1009, May 2011.

[206] Qian, J., Wang, Y., Song, H., Pant, K., Peabody, H., Ku, J., and Butler, C. D., "Projection-Based Reduced-Order Modeling for Spacecraft Thermal Analysis," *Journal of Spacecraft and Rockets*, 52(3), pp. 978–989, May 2015. (Quoted page 35.)

[207] Hickey, D., Masset, L., Kerschen, G., and Brüls, O., "Proper orthogonal decomposition for nonlinear radiative heat transfer problems," *Proceedings of the ASME International Design Engineering Technical Conferences*, Washington, pp. DETC2011–48339, Aug. 2011. (Quoted page 35.)

[208] Udagedara, I., Helenbrook, B., Luttman, A., and Mitchell, S. E., "Reduced order modeling for accelerated Monte Carlo simulations in radiation transport," *Applied Mathematics and Computation*, 267, pp. 237–251, Sep. 2015. (Quoted page 35.)

[209] Balima, O., Favennec, Y., Girault, M., and Petit, D., "Comparison between the modal identification method and the POD-Galerkin method for model reduction in nonlinear diffusive systems," *International Journal for Numerical Methods in Engineering*, 67(7), pp. 895–915, Aug. 2006. (Quoted page 35.)

[210] Lin, W. Z., Lee, K. H., Lim, S. P., and Liang, Y. C., "Proper orthogonal decomposition and component mode synthesis in macromodel generation for the dynamic simulation of a complex MEMS device," *Journal of Micromechanics and Microengineering*, 13(5), pp. 646, (2003). (Quoted page 35.)

[211] Binion, D. and Chen, X., "A Krylov enhanced proper orthogonal decomposition method for efficient nonlinear model reduction," *Finite Elements in Analysis and Design*, 47(7), pp. 728–738, Jul. 2011. (Quoted page 36.)

[212] Neveu, A. and EL Khoury, K., "Réduction d'un modèle thermique non linéaire par modes de branche. Application à un cable chauffant : Analyse vibratoire non linéaire sur base modale," *Revue française de mécanique*, 2, pp. 115–124, (2000). (Quoted page 36.)

[213] Quemener, O., Neveu, A., and Videcoq, E., "A specific reduction method for the branch modal formulation: Application to a highly non-linear configuration," *International Journal of Thermal Sciences*, 46(9), pp. 890–907, Sep. 2007.

[214] Videcoq, E., Quemener, O., Lazard, M., and Neveu, A., "Heat source identification and on-line temperature control by a Branch Eigenmodes Reduced Model," *International Journal of Heat and Mass Transfer*, 51(19-20), pp. 4743–4752, Sep. 2008. (Quoted page 36.)

[215] Laffay, P. O., Quéméner, O., Neveu, A., and Elhajjar, B., "The Modal Substructuring Method: An Efficient Technique for Large-Size Numerical Simulations," *Numerical Heat Transfer, Part B: Fundamentals*, 60(4), pp. 278–304, Oct. 2011. (Quoted page 36.)

[216] Nouy, A., "A priori model reduction through Proper Generalized Decomposition for solving time-dependent partial differential equations," *Computer Methods in Applied Mechanics and Engineering*, 199(23-24), pp. 1603–1626, Apr. 2010. (Quoted page 36.)

[217] Chinesta, F., Ammar, A., and Cueto, E., "Recent Advances and New Challenges in the Use of the Proper Generalized Decomposition for Solving Multidimensional Models," *Archives of Computational Methods in Engineering*, 17(4), pp. 327–350, Dec. 2010.

[218] Chinesta, F., Ladeveze, P., and Cueto, E., "A Short Review on Model Order Reduction Based on Proper Generalized Decomposition," *Archives of Computational Methods in Engineering*, 18(4), pp. 395–404, Nov. 2011.

[219] Chinesta, F., Keunings, R., and Leygue, A., *The Proper Generalized Decomposition for Advanced Numerical Simulations: A Primer*, Springer, (2014). (Quoted page 36.)

[220] Ladevèze, P., "Sur une famille d'algorithmes en mécanique des structures," *Comptes Rendus de l'Académie des Sciences*, 300(2), pp. 41–44, (1985). (Quoted page 36.)

[221] Ladevèze, P., Passieux, J.-C., and Néron, D., "The LATIN multiscale computational method and the Proper Generalized Decomposition," *Computer Methods in Applied Mechanics and Engineering*, 199(21-22), pp. 1287–1296, Apr. 2010.

[222] Ladevèze, P., "On reduced models in nonlinear solid mechanics," *European Journal of Mechanics - A/Solids*, 60, pp. 227–237, Nov. 2016. (Quoted page 36.)

[223] Aguado, J. V., Huerta, A., Chinesta, F., and Cueto, E., "Real-time monitoring of thermal processes by reduced-order modeling," *International Journal for Numerical Methods in Engineering*, 102(5), pp. 991–1017, May 2015. (Quoted page 36.)

[224] Hengeveld, D. W., "Reduced-Order Modeling for Rapid Thermal Analysis and Evaluation of Spacecraft," *Proceedings of the 46th AIAA Thermophysics Conference*, American Institute of Aeronautics and Astronautics, Washington DC, USA, pp. AIAA 2016–3698, Jun. 2016. (Quoted page 36.)

[225] Romijn, R., Özkan, L., Weiland, S., Ludlage, J., and Marquardt, W., "A grey-box modeling approach for the reduction of nonlinear systems," *Journal of Process Control*, 18(9), pp. 906–914, Oct. 2008. (Quoted page 36.)

[226] Molina, M. and Clemente, C., "Thermal Model Automatic Reduction: Algorithm and Validation Techniques," *Proceedings of the 36th International Conference On Environmental Systems*, SAE International, Norfolk, VA, United States, p. 2112, (17-20 July 2006). (Quoted page 36.)

[227] Gorlani, M. and Rossi, M., "Thermal Model Reduction with Stochastic Optimisation," *Proceedings of the 37th International Conference on Environmental Systems*, SAE International, Chicago, IL, USA, p. 3119, (9-12 July 2007). (Quoted page 36.)

[228] Bernard, M., Basset, T., Leroy, S., Brunetti, F., and Etchells, J., "TMRT - A thermal model reduction tool," *Proceedings of the 23rd European Workshop on Thermal and ECLS Software*, Noordwijk, The Netherlands, pp. 53–68, (6-7 Oct 2009). (Quoted page 36.)

[229] Bernard, M., Basset, T., and Etchells, J., "TMRT," *Proceedings of the 24th European Workshop on Thermal and ECLS Software*, Noordwijk, The Netherlands, pp. 169–180, (16-17 Nov 2010).

[230] Bernard, M., Etchells, J., Basset, T., and Brunetti, F., "Thermal Model Reduction – Theory & Application," *Proceedings of the 40th International Conference on Environmental Systems*, American Institute of Aeronautics and Astronautics, Barcelona, Spain, pp. AIAA 2010–6084, Jul. 2010.

[231] Ferrier, M. and Valentini, D., "TMRT Module Software - Use of an Industrial Application," *Proceedings of the 28th European Space Thermal Analysis Workshop*, Noordwijk, The Netherlands, pp. 105–116, (14-15 Oct 2014).

[232] Hugonnot, P., Basset, T., Connil, P., Brunetti, F., and Ferrier, M., "TMRT (Thermal Model Reduction Tool): Presentation of the tool and application on satellite model reduction for launcher coupled analysis," *Proceedings of the 46th International Conference on Environmental Systems*, Vienna, Austria, p. 132, Jul. 2016. (Quoted page 36.)

[233] Fishman, G. S., *Monte Carlo Concepts, Algorithms, and Applications*, Springer Series in Operations Research, Springer New York, New York, NY, (1996). (Quoted page 38.)

[234] Cochran, W. G., *Sampling Techniques.*, John Wiley, Oxford, England, (1953). (Quoted page 38.)

[235] Keller, A., (2013). "Quasi-Monte Carlo Image Synthesis in a Nutshell," , *Monte Carlo and Quasi-Monte Carlo Methods 2012*. Kuo, F. Y., Peters, G. W., Sloan, I. H., and Dick, J. (Eds.). Vol. 65. Springer Berlin Heidelberg, Berlin, Heidelberg, pp. 213–249. (Quoted page 38.)

[236] Cook, R. L., Porter, T., and Carpenter, L., "Distributed ray tracing," *Computer Graphics*, 18(3), pp. 137–145, Jul. 1984. (Quoted page 38.)

[237] Cook, R. L., "Stochastic sampling in computer graphics," *ACM Transactions on Graphics*, 5(1), pp. 51–72, Jan. 1986.

[238] Jensen, H. W., Arvo, J., Dutré, P., Keller, A., Owen, A. B., Pharr, M., and Shirley, P., "Course 44: Monte Carlo Ray Tracing," *ACM SIGGRAPH 2003*, Jul. 2003. (Quoted page 38.)

[239] Shirley, P., Dissertation.pdf, Phd thesis, University of Illinois at Urbana-Champaign, Urbana, Illinois, USA, (1991). (Quoted page 38.)

[240] Carpentier, A. and Munos, R., "Adaptive Stratified Sampling for Monte-Carlo integration of Differentiable functions," *ArXiv e-prints*, Machine Learning (stat.ML), pp. arXiv:1210.5345, Oct. 2012. (Quoted page 38.)

[241] McKay, M. D., Beckman, R. J., and Conover, W. J., "Comparison of Three Methods for Selecting Values of Input Variables in the Analysis of Output from a Computer Code," *Technometrics*, 21(2), pp. 239–245, May 1979. (Quoted page 38.)

[242] Richtmyer, R. D., "The evaluation of definite integrals, and a quasi-Monte-Carlo method based on the properties of algebraic numbers," , Tech. Rep. LA-1342, 4405295, Los Alamos Scientific Laboratory, Oct. 1951. (Quoted page 38.)

[243] Sobol, I., "On the distribution of points in a cube and the approximate evaluation of integrals," *USSR Computational Mathematics and Mathematical Physics*, 7(4), pp. 86–112, Jan. 1967. (Quoted pages 38 and 44.)

[244] Halton, J., "On the efficiency of certain quasi-random sequences of points in evaluating multi-dimensional integrals," *Numerische Mathematik*, 2(1), pp. 84–90, (1960). (Quoted pages 38 and 43.)

[245] Radiant ZEMAX LLC, "Zemax Optical Design Program User's Manual," , Tech. rep., ZEMAX LLC, Jul. 2011. (Quoted page 38.)

[246] Keller, A., "The Fast Calculation Of Form Factors Using Low Discrepancy Sequences," *In Proc. Spring Conference on Computer Graphics (SCCG '96*, Comenius University Press, pp. 195–204, (1996). (Quoted page 39.)

[247] Faure, H. and Lemieux, C., "Generalized Halton sequences in 2008: A comparative study," *ACM Transactions on Modeling and Computer Simulation*, 19(4), pp. 1–31, Oct. 2009. (Quoted pages 39 and 44.)

[248] Arvo, J. and Kirk, D., (1989). "A Survey of Ray Tracing Acceleration Techniques," , *An Introduction to Ray Tracing*. Glassner, A. S. (Ed.). Academic Press Ltd., London, UK, pp. 201–262. (Quoted pages 39 and 81.)

[249] Nusselt, W., "Graphische bestimmung des winkelverhaltnisses bei der wärmestrahlung," *Zeitschrift des Vereines Deutscher Ingenieure*, 72(20), pp. 673, (1928). (Quoted page 40.)

[250] Malley, T. J., A Shading Method for Computer Generated Images, Master's thesis, University of Utah, (1988). (Quoted page 40.)

[251] Vueghs, P., "Innovative Ray Tracing Algorithms for Space Thermal Analysis," *Proceedings of the 22nd European Workshop on Thermal and ECLS Software*, Noordwijk, The Netherlands, pp. 139–152, (28-29 October 2008). (Quoted page 40.)

[252] Masset, L., Brüls, O., and Kerschen, G., "Partition of the circle in cells of equal area and shape," , Tech. rep., University of Liège, (2012). (Quoted pages 41, 43, and 47.)

[253] van der Corput, J. G., "Verteilungsfunktionen. I. Mitt.," *Proceedings. Akadamie van Wetenschappen Amsterdam*, 38, pp. 813–821, (1935). (Quoted page 43.)

[254] Halton, J. H. and Smith, G. B., "Algorithm 247: Radical-inverse quasi-random point sequence," *Communications of the ACM*, 7(12), pp. 701–702, Dec. 1964. (Quoted page 44.)

[255] Kocis, L. and Whiten, W. J., "Computational investigations of low-discrepancy sequences," *ACM Transactions on Mathematical Software*, 23(2), pp. 266–294, Jun. 1997. (Quoted page 44.)

[256] Voronoi, G., "Nouvelles applications des paramètres continus à la théorie des formes quadratiques. Premier mémoire. Sur quelques propriétés des formes quadratiques positives parfaites," *Journal für die Reine und Angewandte Mathematik*, 133, pp. 97–102, (1908). (Quoted page 45.)

[257] Arvo, J., (2001). "Stratified Sampling of 2-Manifolds," . *State of the Art in Monte Carlo Ray Tracing for Realistic Image Synthesis*. Vol. SIGGRAPH 2001 Course Notes vol. 29. ACM Press. (Quoted page 51.)

[258] Arvo, J., "Stratified sampling of spherical triangles," *Proceedings of the 22nd Annual Conference on Computer Graphics and Interactive Techniques*, ACM Press, pp. 437–438, (1995). (Quoted page 51.)

[259] Legendre, A.-M., "Recherches sur l'attraction des sphéroïdes homogènes," *Mémoires de Mathématiques et de Physique, Présentés À l'Académie Royale Des Sciences, Par Divers Savants, et Lus Dans Ses Assemblées*, Vol. 10, Paris, pp. 411–435, (1785), published as M. Le Gendre and submitted to the Academy in 1782. (Quoted page 55.)

[260] Gauss, C. F., "Methodus nova integralium valores per approximationen inveniendi," *Proceedings of the Royal Society of Sciences*, Göttingen, pp. 1–40, Sep. 1814. (Quoted page 55.)

[261] Gauss, C. F., *Werke*, Vol. 3, Königlichen Gesellschaft der wWssenschaften zu Göttingen, Göttingen, (1876). (Quoted page 55.)

[262] Heine, E., *Handbuch Der Kugelfunktionen*, 2nd Edition, Georg Reimer, Berlin, (1881). (Quoted page 55.)

[263] Hobson, E. W., *The Theory of Spherical and Ellipsoidal Harmonics*, Cambridge University Press, Cambridge, (1931). (Quoted page 55.)

[264] Lowan, A. N., Davids, N., and Levenson, A., "Table of the zeros of the Legendre polynomials of order 1-16 and the weight coefficients for Gauss' mechanical quadrature formula," *Bulletin of the American Mathematical Society*, 48(10), pp. 739–743, (1942). (Quoted page 55.)

[265] Archibald, R. C. and Lehmer, D. H., "Recent Mathematical Tables," *Mathematics of Computation*, 1(2), pp. 45–56, May 1943. (Quoted page 55.)

[266] Cowper, G. R., "Gaussian quadrature formulas for triangles," *International Journal for Numerical Methods in Engineering*, 7(3), pp. 405–408, (1973). (Quoted page 55.)

[267] Lyness, J. N. and Cools, R., "A Survey of Numerical Cubature over Triangles," *Proceedings of Symposia in Applied Mathematics*, Vol. 48, American Mathematical Society, pp. 127–150, (1994).

[268] Wandzurat, S. and Xiao, H., "Symmetric quadrature rules on a triangle," *Computers & Mathematics with Applications*, 45(12), pp. 1829–1840, (2003). (Quoted page 55.)

[269] Cools, R. and Rabinowitz, P., "Monomial cubature rules since "Stroud": A compilation," *Journal of Computational and Applied Mathematics*, 48(3), pp. 309–326, (1993). (Quoted page 55.)

[270] Cools, R., "An encyclopaedia of cubature formulas," *Journal of Complexity*, 19(3), pp. 445–453, Jun. 2003. (Quoted page 55.)

[271] Stroud, A., *Approximate Calculation of Multiple Integrals*, Prentice-Hall series in automatic computation, Prentice-Hall, (1971). (Quoted page 55.)

[272] Clay, J. M. and Rodriguez, J., "Comparison of two Saturn Ring Models for Analyzing the Cassini Spacecraft Orbiting Saturn using TSS," *Proceedings of the Spacecraft Thermal Control Workshop*, The Aerospace Corporation, El Segundo, CA, USA, p. 21, Mar. 2015. (Quoted page 64.)

[273] Knocke, P., Ries, J., and Tapley, B., "Earth radiation pressure effects on satellites," *Proceedings of the AIAA/AAS Astrodynamics Conference*, American Institute of Aeronautics and Astronautics, Minneapolis, Aug. 1988. (Quoted page 65.)

[274] Taylor, V. R. and Stowe, L. L., "Reflectance characteristics of uniform Earth and cloud surfaces derived from NIMBUS-7 ERB," *Journal of Geophysical Research: Atmospheres*, 89(D4), pp. 4987–4996, Jun. 1984. (Quoted page 65.)

[275] ECSS Executive Secretariat, "Space environment," , Tech. Rep. ECSS-E-ST-10-04C, European Space Agency - European Coordination for Space Standardization, Noordwijk, The Netherlands, Nov. 2008. (Quoted page 65.)

[276] du Laurens d'Oiselay, F., "ESARAD V4.3," *Proceedings of the 15th Thermal and ECSL Software Workshop*, European Space Agency, Noordwijk, The Netherlands, pp. 119–142, (9-10 October 2001). (Quoted page 66.)

[277] Levin, E., "Reflected Radiation Received by an Earth Satellite," *ARS Journal*, 32(9), pp. 1328–1331, Sep. 1962. (Quoted page 67.)

[278] Levin, E., "Solar radiation pressure perturbations of earth satellite orbits.," *AIAA Journal*, 6(1), pp. 120–126, Jan. 1968. (Quoted page 67.)

[279] Cunningham, F., "Earth reflected solar radiation input to spherical satellites," *ARS Journal*, 32(7), pp. 1033–1036, (1962). (Quoted page 67.)

[280] Borderies, N. and Longaretti, P.-y., "A new treatment of the albedo radiation pressure in the case of a uniform albedo and of a spherical satellite," *Celestial Mechanics and Dynamical Astronomy*, 49(1), pp. 69–98, (1990). (Quoted page 67.)

[281] Dennison, A., "Illumination of a space vehicle surface due to sunlight reflected from earth," *ARS JOURNAL*, 32(4), pp. 635–637, (1962). (Quoted page 67.)

[282] Fitz, C. D., Lukasik, S. J., Mayer, E. A., and Simon, D. R., "Albedo and Planet Radiation Intercepted by an Earth Satellite," , Tech. Rep. AEDC-TOR-63-92, Vitro Laboratories, West Orange, New Jersey, USA, May 1963. (Quoted page 67.)

[283] Fontana, A., "The effect of planetary albedo on solar orientation of spacecraft," , Tech. Rep. NASA TN D-4133, National Aeronautics and Space Administration, (1967). (Quoted page 67.)

[284] Borderies, N., "A general model of the planetary radiation pressure on a satellite with a complex shape," *Celestial Mechanics and Dynamical Astronomy*, 49(1), pp. 99–110, (1990). (Quoted page 67.)

[285] Bhanderi, D. D. V., Spacecraft Attitude Determination with Earth Albedo Corretted Sun Sensor Measurements, PhD thesis, Department of Control Engineering, Aalborg University, Aalborg, (2005). (Quoted page 67.)

[286] Pavlis, N. K., Holmes, S. A., Kenyon, S. C., and Factor, J. K., "An earth gravitational model to degree 2160: EGM2008," Vienna, Austria, (13-18 April 2008), presented at the General Assembly of the European Geosciences Union. (Quoted page 76.)

[287] Pavlis, N. K., Holmes, S. A., Kenyon, S. C., and Factor, J. K., "The development and evaluation of the Earth Gravitational Model 2008 (EGM2008)," *Journal of Geophysical Research: Solid Earth*, 117(B4), pp. n/a–n/a, Apr. 2012. (Quoted page 76.)

[288] Ortiz Longo, C. R. and Rickman, S. L., "Method for the calculation of spacecraft umbra and penumbra shadow terminator points," , Tech. Rep. Technical Paper 3547, NASA Johnson Space Center, Washington DC, USA, Apr. 1995. (Quoted page 76.)

[289] Montenbruck, O. and Gill, E., *Satellite Orbits: Models, Methods and Applications*, Springer Science & Business Media, (2012). (Quoted page 76.)

[290] Taylor, R. P., Luck, R., Hodge, B. K., and Steele, W. G., "Uncertainty analysis of diffuse-gray radiation enclosure problems: A hypersensitive case study," *Proceedings of the 5th Thermal and Fluids Analysis Workshop*, pp. 27–40, Nov. 1993. (Quoted page 79.)

[291] van Leersum, J., "A method for determining a consistent set of radiation view factors from a set generated by a nonexact method," *International Journal of Heat and Fluid Flow*, 10(1), pp. 83 – 85, (1989).

[292] Lawson, D. A., "An improved method for smoothing approximate exchange areas," *International Journal of Heat and Mass Transfer*, 38(16), pp. 3109 – 3110, (1995).

[293] Sowell, E. F. and O'Brien, P. F., "Efficient Computation of Radiant-Interchange Configuration Factors within the Enclosure," *Journal of Heat Transfer*, 94(3), pp. 326, (1972). (Quoted page 79.)

[294] Vercammen, H. A. J. and Froment, G. F., "An improved zone method using monte carlo techniques for the simulation of radiation in industrial furnaces," *International Journal of Heat and Mass Transfer*, 23(3), pp. 329 – 337, (1980). (Quoted page 79.)

[295] Larsen, M. E. and Howell, J. R., "Least-Squares Smoothing of Direct-Exchange Areas in Zonal Analysis," *Journal of Heat Transfer*, 108(1), pp. 239, (1986).

[296] Loehrke, R. I., Dolaghan, J. S., and Burns, P. J., "Smoothing Monte Carlo Exchange Factors," *Journal of Heat Transfer*, 117(2), pp. 524, (1995). (Quoted page 79.)

[297] Daun, K. J., Morton, D. P., and Howell, J. R., "Smoothing Monte Carlo Exchange Factors Through Constrained Maximum Likelihood Estimation," *Journal of Heat Transfer*, 127(10), pp. 1124, (2005). (Quoted page 79.)

[298] Taylor, R. P. and Luck, R., "Comparison of reciprocity and closure enforcement methods for radiation view factors," *Journal of Thermophysics and Heat Transfer*, 9(4), pp. 660–666, Oct. 1995. (Quoted page 79.)

[299] Clarksean, R. and Solbrig, C., "Minimization of the effect of errors in approximate radiation view factors," *Nuclear Engineering and Design*, 149(1-3), pp. 431–440, Sep. 1994. (Quoted page 80.)

[300] Zeeb, C. N., Performance and Accuracy Enhancements of Radiative Heat Transfer Modeling via Monte Carlo, PhD thesis, Colorado State University, (2002). (Quoted pages 80, 81, and 82.)

[301] Desaunettes, B. and Puillet, C., "Monte-Carlo radiative software statistical accuracy control," *Proceedings of the 7th European Thermal and ECLS Software Workshop*, Toulouse, France, Oct. 1993. (Quoted page 80.)

[302] Fujimoto, A., Tanaka, T., and Iwata, K., "ARTS: Accelerated Ray-Tracing System," *IEEE Computer Graphics and Applications*, 6(4), pp. 16–26, (1986). (Quoted page 82.)

[303] Amanatides, J. and Woo, A., "A Fast Voxel Traversal Algorithm for Ray Tracing," *In Eurographics '87*, pp. 3–10, (1987). (Quoted pages 82 and 129.)

[304] Glassner, A. S., "Space subdivision for fast ray tracing," *IEEE Computer Graphics and Applications*, 4(10), pp. 15–24, (1984). (Quoted pages 82 and 129.)

[305] Zeeb, C. N., Burns, P. J., Branner, K., and Dolaghan, J., "USERS'MANUAL for MONT3D-Code Version 2.4," , Tech. rep., Colorado State University, (1999). (Quoted page 82.)

[306] Arvo, J., *Graphics Gems II*, Academic Press, Boston, (1991). (Quoted pages 82 and 129.)

[307] Arnaldi, B., Priol, T., and Bouatouch, K., "A new space subdivision method for ray tracing CSG modelled scenes," *The Visual Computer*, 3(2), pp. 98–108, Aug. 1987. (Quoted pages 82 and 129.)

[308] Akenine-Möller, T., Haines, E., and Hoffman, N., *Real-Time Rendering*, 3rd Edition, Peters, (2008). (Quoted pages 83 and 130.)

[309] Havel, J. and Herout, A., "Yet Faster Ray-Triangle Intersection (Using SSE4)," *IEEE Transactions on Visualization and Computer Graphics*, 16(3), pp. 434–438, May 2010. (Quoted page 84.)

[310] Wald, I., Realtime Ray Tracing and Interactive Global Illumination, PhD thesis, Computer Graphics Group, Saarland University, (2004). (Quoted page 84.)

[311] Shevtsov, M., Soupikov, A., Kapustin, A., and Novorod, N., "Ray-triangle intersection algorithm for modern CPU architectures," *Proceedings of GraphiCon*, Vol. 2007, pp. 33–39, (2007). (Quoted page 129.)

[312] Kensler, A. and Shirley, P., "Optimizing Ray-Triangle Intersection via Automated Search," *Proceedings of the IEEE Symposium on Interactive Ray Tracing*, IEEE, pp. 33–38, Sep. 2006.

[313] Möller, T. and Trumbore, B., "Fast, Minimum Storage Ray-Triangle Intersection," *Journal of Graphics Tools*, 2(1), pp. 21–28, (1997). (Quoted page 84.)

[314] Lagae, A. and Dutré, P., "An Efficient Ray-Quadrilateral Intersection Test," *Journal of Graphics, GPU, and Game Tools*, 10(4), pp. 23–32, (2005). (Quoted page 86.)

[315] Halain, J.-P., Rochus, P., Renotte, E., Appourchaux, T., Berghmans, D., Harra, L., Schühle, U., Schmutz, W., Auchère, F., Zhukov, A., Dumesnil, C., Delmotte, F., Kennedy, T., Mercier, R., Pfiffner, D., Rossi, L., Tandy, J., BenMoussa, A., and Smith, P., "The EUI instrument on board the Solar Orbiter mission: From breadboard and prototypes to instrument model validation," , *Proc. SPIE 8443, Space Telescopes and Instrumentation 2012: Ultraviolet to Gamma Ray,*Takahashi, T., Murray, S. S., and den Herder, J.-W. A. (Eds.), p. 844307, Sep. 2012. (Quoted page 93.)

[316] Halain, J.-P., Rochus, P., Renotte, E., Hermans, A., Jacques, L., Mazzoli, A., Auchère, F., Berghmans, D., Harra, L., Schühle, U., Schmutz, W., Aznar Cuadrado, R., Dumesnil, C., Gyo, M., Kennedy, T., Verbeeck, C., and Smith, P., "The qualification campaign of the EUI instrument of Solar Orbiter," *Proceedings of SPIE - The International Society for Optical Engineering - Space Telescopes and Instrumentation 2016: Ultraviolet to Gamma Ray*, Vol. 9905, Society of Photo-Optical Instrumentation Engineers, Edinburgh, United Kingdom, p. 99052X, Jul. 2016. (Quoted page 93.)

[317] Gulde, S. T., Kolm, M. G., Smith, D. J., Maurer, R., Courrèges-Lacoste, G. B., Sallusti, M., and Bagnasco, G., "Sentinel 4: A geostationary imaging UVN spectrometer for air quality monitoring–status of design, performance and development," *Proceedings of the International Conference on Space Optics*, Tenerife, Canary Islands, Spain, p. 8, (7-10 Oct. 2014). (Quoted page 97.)

[318] Lahoz, W. A., Peuch, V.-H., Orphal, J., Attié, J.-L., Chance, K., Liu, X., Edwards, D., Elbern, H., Flaud, J.-M., Claeyman, M., and El Amraoui, L., "Monitoring Air Quality from Space: The Case for the Geostationary Platform," *Bulletin of the American Meteorological Society*, 93(2), pp. 221–233, Feb. 2012. (Quoted page 97.)

[319] Jackson, C., Harris, A., and Duffy, K., "Coarse Radiation Patches for Element-Based Thermal Analysis," *Proceedings of the 33rd International Conference on Environmental Systems*, Vol. 1, SAE International, Vancouver, p. 2664, Jul. 2003. (Quoted page 103.)

[320] Karypis, G. and Kumar, V., "A Fast and High Quality Multilevel Scheme for Partitioning Irregular Graphs," *SIAM Journal on Scientific Computing*, 20(1), pp. 359–392, Jan. 1998. (Quoted page 104.)

[321] Karypis, G., "Multi-constraint mesh partitioning for contact/impact computations," *Proceedings of the 2003 ACM/IEEE Conference on Supercomputing*, ACM, p. 56, (15-21 Nov. 2003).

[322] Buluc, A., Meyerhenke, H., Safro, I., Sanders, P., and Schulz, C., "Recent Advances in Graph Partitioning," , ArXiv e-prints 1311.3144, Computational Research Division, Lawrence Berkeley National Laboratory,, Feb. 2015. (Quoted page 104.)

[323] Shamir, A., "A survey on Mesh Segmentation Techniques," *Computer Graphics Forum*, 27(6), pp. 1539–1556, Sep. 2008. (Quoted pages 104 and 123.)

[324] Bezdek, J. C. (Ed.), *Fuzzy Models and Algorithms for Pattern Recognition and Image Processing*, no. 4 in The handbooks of fuzzy sets series, Springer, New York, (2005), oCLC: 636057416. (Quoted page 104.)

[325] Celenk, M., "A color clustering technique for image segmentation," *Computer Vision, Graphics, and Image Processing*, 52(2), pp. 145–170, Nov. 1990. (Quoted page 104.)

[326] Yan, D.-M., Wang, W., Liu, Y., and Yang, Z., "Variational mesh segmentation via quadric surface fitting," *Computer-Aided Design*, 44(11), pp. 1072–1082, Nov. 2012. (Quoted pages 104, 108, 122, and 123.)

[327] Jain, A. K., "Data clustering: 50 years beyond K-means," *Pattern Recognition Letters*, 31(8), pp. 651–666, Jun. 2010. (Quoted page 105.)

[328] Steinhaus, H., "Sur la division des corp materiels en parties," *Bull. Acad. Polon. Sci.*, 4(12), pp. 801–804, (1956). (Quoted page 105.)

[329] Lloyd, S. P., "Least squares quantization in PCM," *IEEE Transactions on Information Theory*, 28(2), pp. 129–137, Mar. 1982, originally as an unpublished Bell laboratories Technical Note (1957). (Quoted page 105.)

[330] Sparks, D. N., "Algorithm AS 58: Euclidean Cluster Analysis," *Applied Statistics*, 22(1), pp. 126, (1973). (Quoted page 105.)

[331] Hartigan, J. A. and Wong, M. A., "Algorithm AS 136: A K-Means Clustering Algorithm," *Applied Statistics*, 28(1), pp. 100, (1979). (Quoted page 105.)

[332] Greig, D. M., Porteous, B. T., and Seheult, A. H., "Exact maximum a posteriori estimation for binary images," *Journal of the Royal Statistical Society*, 51(2), pp. 271–279, (1989). (Quoted page 108.)

[333] Boykov, Y. and Kolmogorov, V., "An experimental comparison of min-cut/max- flow algorithms for energy minimization in vision," *IEEE Transactions on Pattern Analysis and Machine Intelligence*, 26(9), pp. 1124–1137, Sep. 2004. (Quoted page 108.)

[334] Lin, L., Yang, C., Meza, J. C., Lu, J., Ying, L., and E, W., "SelInv-An Algorithm for Selected Inversion of a Sparse Symmetric Matrix," *ACM Transactions on Mathematical Software*, 37(4), pp. 1–19, Feb. 2011. (Quoted page 112.)

[335] Sharma, G., Agarwala, A., and Bhattacharya, B., "A fast parallel Gauss Jordan algorithm for matrix inversion using CUDA," *Computers & Structures*, 128, pp. 31–37, Nov. 2013. (Quoted page 115.)

[336] Anderson, E. (Ed.), *LAPACK Users' Guide*, Society for Industrial and Applied Mathematics, Philadelphia, (1992). (Quoted page 115.)

[337] Muñoz-Rojas, P. A., Odorczyk, M. F., Cardoso, E. L., and Vaz Jr, M., "A superconvergent temperature patch procedure for nodal flux recovery in finite element computations," *Mecánica Computacional*, 29(56), pp. 5705–5727, Nov. 2010. (Quoted page 116.)

[338] Zienkiewicz, O. C. and Zhu, J. Z., "The superconvergent patch recovery and a posteriori error estimates. Part 1: The recovery technique," *International Journal for Numerical Methods in Engineering*, 33(7), pp. 1331–1364, (1992). (Quoted page 116.)

[339] Kraus, A. D., Aziz, A., and Welty, J., *Extended Surface Heat Transfer*, John Wiley & Sons, Inc., Hoboken, NJ, USA, Dec. 2000. (Quoted page 118.)

[340] Sander, P. V., Snyder, J., Gortler, S. J., and Hoppe, H., "Texture mapping progressive meshes," *Proceedings of the 28th Annual Conference on Computer Graphics and Interactive Techniques (SIGGRAPH 2001)*, ACM Press, Los Angeles, CA, USA, pp. 409–416, (12-17 August 2001). (Quoted page 120.)

[341] Yan, D.-M., Liu, Y., and Wang, W., (2006). "Quadric surface extraction by variational shape approximation," . *Geometric Modeling and Processing-GMP 2006*. Springer, pp. 73–86. (Quoted pages 122 and 123.)

[342] Petitjean, S., "A survey of methods for recovering quadrics in triangle meshes," *ACM Computing Surveys*, 34(2), pp. 211–262, Jun. 2002. (Quoted page 123.)

[343] Várady, T., Martin, R. R., and Cox, J., "Reverse engineering of geometric models—an introduction," *Computer-Aided Design*, 29(4), pp. 255–268, Apr. 1997. (Quoted page 123.)

[344] Mencl, R. and Müller, H., "Interpolation and Approximation of Surfaces from Three-dimensional Scattered Data Points," *Proceedings of the Scientific Visualization Conference (Dagstuhl 97)*, IEEE Computer Society, Washington, DC, USA, pp. 223–232, (9-13 June 1997). (Quoted page 123.)

[345] Taubin, G., "Estimation of planar curves, surfaces, and nonplanar space curves defined by implicit equations with applications to edge and range image segmentation," *IEEE Transactions on Pattern Analysis and Machine Intelligence*, 13(11), pp. 1115–1138, (1991). (Quoted page 123.)

[346] Taubin, G., "An improved algorithm for algebraic curve and surface fitting," *Proceedings of the Fourth International Conference on Computer Vision*, IEEE Computer Society Press, pp. 658–665, (11-14 May 1993). (Quoted page 123.)

[347] Martínez Morera, D. and Estrada Sarlabous, J., "On the distance from a point to a quadric surface," *Revista Investigacion Operacional*, 24(2), pp. 153–161, (2003). (Quoted page 126.)

[348] Skala, V., "A new approach to line – sphere and line – quadrics intersection detection and computation," *Proceedings of the International Conference on Numerical Analysis and Applied Mathematics (ICNAAM-2014)*, Vol. 1648, AIP Publishing LLC, Rhodes, Greece, Sep. 2014. (Quoted page 128.)

[349] Hunt, W. A., "Corrections to the surface area metric with respect to mail-boxing," IEEE, pp. 77–80, Aug. 2008. (Quoted page 129.)

[350] Haines, E., (1994). "Point in Polygon Strategies," . *Graphics Gems IV*. Academic Press, Inc ., pp. 24–46. (Quoted page 130.)

[351] Shimrat, M., "Algorithm 112: Position of point relative to polygon," *Communications of the ACM*, 5(8), pp. 434, Aug. 1962. (Quoted page 130.)

[352] Hacker, R., "Certification of Algorithm 112: Position of point relative to polygon," *Communications of the ACM*, 5(12), pp. 606, Dec. 1962. (Quoted page 130.)

[353] Jacques, L., Masset, L., Thibert, T., Jamotton, P., Dalibot, C., and Kerschen, G., "Finite element model reduction for the determination of accurate conductive links and application to MTG IRS BTA," *Proceedings of the 28th Space Thermal Analysis Workshop*, Noordwijk, The Netherlands, pp. 285–298, Oct. 2014. (Quoted page 137.)

[354] Zhu, J.-H., Zhang, W.-H., and Xia, L., "Topology Optimization in Aircraft and Aerospace Structures Design," *Archives of Computational Methods in Engineering*, Apr. 2015. (Quoted page 144.)

[355] Connil, P., Dudon, J. P., Basset, T., Hugonnot, P., and Brunetti, F., "THERM3D / e-Therm GMM (conductive) and TMM generation of thermo-mechanical antenna support designed for ALM," *Proceedings of the 30th European Space Thermal Analysis Workshop*, Noordwijk, The Netherlands, (5-6 October 2016). (Quoted page 144.)

[356] Mazzoli, A., Saint-Georges, P., Orban, A., Ruess, J.-S., Loicq, J., Barbier, C., Stockman, Y., Georges, M., Nachtergaele, P., Paquay, S., and De Vincenzo, P., "Experimental validation of opto-thermo-elastic modeling in OOFELIE multiphysics," *Proceedings of SPIE - Optical Design and Engineering IV*, Society of Photo-Optical Instrumentation Engineers, Marseille, France, p. 81671I, Sep. 2011. (Quoted page 144.)

[357] Young-Soo, K., Eung-Shik, L., and Sun-Hee, W., "System trade-off study and opto-thermo-mechanical analysis of a sunshield on the MSC of the KOMPSAT-2," *Journal of Astronomy and Space Sciences*, 20(4), pp. 393–402, (2003). (Quoted page 144.)

[358] Soriano, T. and Caugant, A., "SYSTEMA & THERMICA," *Proceedings of the 30th European Space Thermal Analysis Workshop*, Noordwijk, The Netherlands, (5-6 October 2016). (Quoted page 146.)

[359] Gibson, D., "Parallel thermal analysis with Linux clusters," *Proceedings of the 21st European Workshop on Thermal and ECLS Software*, ESA, Noordwijk, ESTEC, Oct. 2007. (Quoted page 149.)

[360] Marakis, J., Chamiço, J., Brenner, G., and Durst, F., "Parallel ray tracing for radiative heat transfer: Application in a distributed computing environment," *International Journal of Numerical Methods for Heat & Fluid Flow*, 11(7), pp. 663–681, (2001). (Quoted page 149.)

[361] Takizawa, H., Yamada, N., Sakai, S., and Kobayashi, H., "Radiative Heat Transfer Simulation Using Programmable Graphics Hardware," *5th IEEE/ACIS International Conference on Computer and Information Science and 1st IEEE/ACIS International Workshop on Component-Based Software Engineering,Software Architecture and Reuse*, IEEE, Honolulu, pp. 29–37, (10-12 July 2006). (Quoted page 149.)

[362] Godoy, W. F. and Liu, X., "Introduction of Parallel GPGPU Acceleration Algorithms for the Solution of Radiative Transfer," *Numerical Heat Transfer, Part B: Fundamentals*, 59(1), pp. 1–25, Jan. 2011.

[363] Fazanaro, F. I., Soriano, D. C., Suyama, R., Madrid, M. K., de Oliveira, J. R., Muñoz, I. B., and Attux, R., "Numerical characterization of nonlinear dynamical systems using parallel computing: The role of GPUs approach," *Communications in Nonlinear Science and Numerical Simulation*, 37, pp. 143–162, Aug. 2016. (Quoted page 149.)

[364] Owens, J. D., Luebke, D., Govindaraju, N., Harris, M., Krüger, J., Lefohn, A. E., and Purcell, T. J., "A survey of general-purpose computation on graphics hardware," *Computer Graphics Forum*, Vol. 26, Wiley Online Library, pp. 80–113, (2007). (Quoted page 149.)

[365] Lee, V. W., Kim, C., Chhugani, J., Deisher, M., Kim, D., Nguyen, A. D., Satish, N., Smelyanskiy, M., Chennupaty, S., Hammarlund, P., and others, "Debunking the 100X GPU vs. CPU myth: An evaluation of throughput computing on CPU and GPU," *ACM SIGARCH Computer Architecture News*, 38(3), pp. 451–460, (2010). (Quoted page 149.)

[366] Gregg, C. and Hazelwood, K., "Where is the data? Why you cannot debate CPU vs. GPU performance without the answer," IEEE, pp. 134–144, Apr. 2011. (Quoted page 149.)

[367] Browell, R., "Bigger, Better, Faster: HPC Technology Leadership," *Excellence in Engineering Simulation*, p. 6, (2011). (Quoted page 149.)

[368] Han, T. D. and Abdelrahman, T. S., "hiCUDA: High-Level GPGPU Programming," *IEEE Transactions on Parallel and Distributed Systems*, 22(1), pp. 78–90, Jan. 2011. (Quoted page 149.)

[369] Stone, J. E., Gohara, D., and Shi, G., "OpenCL: A Parallel Programming Standard for Heterogeneous Computing Systems," *Computing in Science & Engineering*, 12(3), pp. 66–73, May 2010. (Quoted page 149.)

[370] Rana, H. and Passaro, A., "Thermal modelling of thruster nozzles & plumes," *Proceedings of the 30th European Space Thermal Analysis Workshop*, Noordwijk, The Netherlands, Oct. 2016. (Quoted page 149.)

[371] Shan, Y. and Zhang, J.-z., "Numerical investigation of flow mixture enhancement and infrared radiation shield by lobed forced mixer," *Applied Thermal Engineering*, 29(17-18), pp. 3687–3695, Dec. 2009. (Quoted page 149.)

List of Journal Publications

1. Jacques L., Masset L., and Kerschen G., "Direction and Surface Sampling in Ray Tracing for Spacecraft Radiative Heat Transfer", *Aerospace Science and Technology*, 47 (December 2015), pp. 146–153, doi:10.1016/j.ast.2015.09.034.

2. Jacques L., Béchet E., and Kerschen G., "Finite element model reduction for space thermal analysis", *Finite Elements in Analysis and Design*, in review.

List of Conference Publications

1. Jacques L., Masset L. and Kerschen G., "Enhancement of ray tracing method for radiative heat transfer with new Isocell quasi-Monte Carlo technique and application to EUI space instrument baffle", In *Proceedings of the* 27^{th} *Space Thermal Analysis Workshop*, pp. 291-302, ESA-ESTEC, Noordwijk, The Netherlands, 3-4 December 2013.

2. Jacques L., Masset L. and Kerschen G., "Ray tracing Enhancement for space thermal analysis: Isocell method", In *Proceedings of the* 3^{rd} *International Conference on Computational Methods for Thermal Problems, THERMACOMP2014*, pp. 399-402, Massarotti N., Nithiarasu P. and Sarler B. (Eds.), Lake Bled, Slovenia, 2-4 June 2014.

3. Jacques L., Masset L. and Kerschen G., "Enhancement of ray tracing method for radiative heat transfer with new Isocell quasi-Monte Carlo technique and application to EUI space instrument", In *Proceedings of the* 10^{th} *International Conference on Heat Transfer, Fluid Mechanics and Thermodynamics*, Orlando, FL, 14-16 July 2014.

4. Jacques L., Masset L., Thibert T., Jamotton P., Dalibot C., Kerschen G., "Finite Element Model Reduction for the Determination of Accurate Conductive Links and Application to MTG IRS BTA", In *Proceedings of the* 28^{th} *Space Thermal Analysis Workshop*, pp. 285-298, ESA-ESTEC, Noordwijk, The Netherlands, 14-15 October 2014.

5. Jacques L., Masset L. and Kerschen G., "Finite element model reduction of thermal Systems with Conductive and Radiative heat transfers", In *Proceedings of the* 26^{th} *Spacecraft Thermal Control Workshop*, The Aerospace Corporation, El Segundo, CA, 24-26 March 2014.

6. Jacques L., Masset L. and Kerschen G., "Enhancement of ray tracing method for radiative heat transfer: application to EUI space instrument", In *Proceedings of the* 15^{th} *International Heat Transfer Conference, IHTC-15*, IHTC15-1234, Kyoto, Japan, 10-15 August 2015.

7. Jacques L., Masset L. and Kerschen G., "Finite element model reduction for spacecraft thermal analysis", In *Proceedings of the* 29^{th} *Space Thermal Analysis Workshop*, pp. $227 - 242$, ESA-ESTEC, Noordwijk, The Netherlands, 3-4 November 2015.